Preparation and evaluation of hybrid gold-iron oxide nanoparticles as a multifunctional platform for diagnosis and therapy of pancreatic cancer

Maryam Malekigorji

A thesis submitted in partial fulfilment of the

requirements of

Keele University

for the degree of Doctor of Philosophy

June 2016

Abstract

Pancreatic ductal adenocarcinoma (PDAC) is the most common epithelial, exocrine pancreatic malignancy. Gemcitabine, as the only chemotherapy clinically available for pancreatic cancer, proves effective only in 23.8% of patients. Recently, iron oxide-gold hybrid nanoparticles (HNPs) have received significant attention in cancer therapy, which exploit the surface chemistry and SPR of the gold with magnetic character of the iron oxide, offering imaging, heating and drug delivery potentials.

In this work HNPs were synthesised using a multi-step coating process of iron oxide cores. Particles were characterised by different techniques, in terms of their size, zeta potential, morphology and their magnetic properties. Laser irradiation on HNPs was used in order to obtain optimal temperature increase, needed for drug release. It is postulated that nanoparticulate irradiation at lower temperatures can trigger drug release from the surface of the vehicle before cellular hyperthermia was initiated. Different bisnaphtalamide based anticancer drugs were conjugated onto the surface of the HNPs. Drug loading, stability and drug release studies were carried out. A pancreatic cancer targeting peptide (c(RGDfC)) was conjugated to the formulations to increase drug specific delivery and anticancer activity. *In vitro* biological studies were performed on two pancreatic cancer cell lines and a human monocyte cell line.

Hybrid formulations (specially targeted formulation) have shown higher cytotoxicity compared with free drugs and gemcitabine on pancreatic cancer cells. Drug uptake pattern was dose responsive and time dependant on all cell lines, and hybrid formulations internalised at significantly higher concentrations than the free drugs. AFM topography images were in agreement with cellular uptake. Moreover, HNPs possessed thermoresponsive drug delivery potentials *in vitro*.

This is the first time these novel drugs were conjugated to iron oxide-gold HNPs, which demonstrated the interesting potential of these nanoparticles to act as thermoresponsive drug carriers.

Key words: Iron oxide-gold nanoparticles, Pancreatic cancer, Thermoresponsive drug delivery

ACKNOWLEGDEMENTS

I would like to express my deepest appreciation to my two excellent supervisors, those who provided scientific guidance. Dr Clare Hoskins, thank you so much for everything. Your supervision and advice helped me in all the time of research and writing of this thesis. I hope that I could be as lively, enthusiastic, and energetic as you. Dr Anthony Curtis, you provided insightful discussions about the research, unflinching encouragement and support in various ways.

I gratefully acknowledge my colleagues, Wejdan Nazar, Adeolu Oluwasanmi, Mohanad Alfahad, Ali Alsuraifi and Vaibhav Khare for their advices and crucial contribution, which made them a backbone of this research and so to this thesis.

I would also like to thank my very patient parents, my sister and my brother, for being such a huge mental and financial support through my PhD! I couldn't have made it without you all.

My special gratitude also goes to my husband and my little prince, Mahan, for their encouragement and love. Ehsan, thank you for being a good husband and Dad, for listening to my frustrations and complains and for believing in me.

And last but not least, completing this project would have been all the more difficult were it not for the support and friendship provided by the other members of the School of pharmacy and life science at Keele University. I am indebted to them for their help.

Maryam

Contents

List of Tables

List of figures

List of abbreviations

5FU	Fluorouracil
6-TG	6-thioguanine
AFM	Atomic force microscopy
AuNPs	Gold nanoparticles
BCRP	Breast cancer resistance protein
BNIDi	Bis(naphthalimido)-1,20-diaminoicosane
BNIPd	Bis(naphthalimido)-1,12-diaminododecane
BNIPDaoct	Bis(naphtalimido propyl) diamino octane
BNIPds	Bis (naphthamimidopropyl) -3, 3-(butane-1,4-diylbis (sulfanediyl)) bis(propan-1-amine)
BNIPDSpm	Bis(naphthalimidopropyl) spermine
Ch5	Cholesteryl pendant
C(RGDfC)	Cyclo(-Arg-Gly-Asp-D-Phe-Cys) peptide
DMSO	Dimethyl sulfoxide
Dox	Doxorubicin
EPR	Enhanced permeability and retention
FCC	Field cooling curve
FCW	Field-cooled-warming
FTIR	Fourier Transform Infrared spectroscopy
HNPs	Hybrid nanoparticles

HPLC	High performance liquid chromatography
IVIVC	In vitro in vivo correlations
MNPs	Magnetic nanoparticles
MPS	Mononuclear phagocyte system
MRI	Magnetic resonance imaging
MTO	Mitoxantrone hydrochloride
MTT	3-(4,5-dimethylthiazol-2-yl)-2,5-diphenyltetrazolium bromide
NIR	Near Infrared
NLDCs	Lipid-dextran sulphate hybrid carriers
NPs	Nanoparticles
PAA	Poly (acrylic acid)
PCS	Photon correlation spectroscopy
PDAC	Pancreatic ductal adenocarcinoma
PDI	Polydispersity index
PEG	Polyethylene glycol
PEI	Poly (ethyleneimine)
PXRD	Powder x-ray diffraction
RES	Reticuloendothelial System
RME	Receptor mediated endocytosis
SERS	Surface-enhanced Raman Scattering
SPIONs	Super paramagnetic iron oxide nanoparticles
SPM	Scanning probe microscopy
SPR	Surface plasmon resonance

SQUID	Superconducting quantum interference device
TEM	Transmission electron microscopy
uPAR	Urokinase plasminogen activator receptor
ZFCW	Zero-field-cooled warming

Chapter One
Introduction

1.1. Cancer

Cancer is described as one of the most hazardous class of disease categorised by uncontrolled cell growth (Stewart and Wild, 2014) and the third leading cause of death (after heart disease and stroke) in developed countries as well as the second leading cause of death (after heart disease) in the United States (ACS, 2014). Studies have revealed that there were about 8.2 million deaths and 14.1 million patients living with cancer worldwide in the year 2012 (World Cancer Report, 2014). This complex genetic disease has the potential to invade or spread through the bloodstream and lymphocytic system to other parts of the body. The incidence rate for all cancers was higher in developed countries compared to developing countries. Moreover, the most common causes of cancer related deaths in the world are lung, liver, bowl, breast, prostate and pancreatic cancer (ACS, 2011).

1.1.1. Pancreatic cancer

Pancreatic cancer is the twelfth most common cancer worldwide (same position with kidney cancer) with 338,000 new cases diagnosed in 2012 (Ferlay *et al.* 2013). It is also the tenth most common cancer in the UK, where about 8,800 people were diagnosed with pancreatic cancer; equals 24 people every day (Cancer Research UK, 2014).

Pancreatic cancer symptoms include pain in the upper or middle abdomen and back, jaundice, unexplained weight loss, loss of appetite and fatigue. Unfortunately, pancreatic cancer cannot be detected at early stages and most patients with localised disease have no detectable symptoms or signs. Therefore, it is not diagnosed until late stages, when cancer has metastasised to other organs. This leads to poor prognosis and incidence equalling mortality (5 years survival rate). Pancreatic cancer is highly related to the age and the peak incidence of the disease takes place between 65-75 year age group (Lankisch *et al.* 2002).

This type of cancer is divided into two main groups: Exocrine tumours, which are associated with enzyme producing cell and endocrine tumours, for hormone producing cells such as insulin, glucagon and somatostatin.

Exocrine pancreatic cancer is the most common form of pancreatic cancer (95 %), which can occur anywhere along the length of the pancreas (Thompson, 1988). But endocrine tumours are very rare and they grow more slowly than exocrine tumours (Tomassetti *et al.* 2005). The risk factors for both types of pancreatic cancers are smoking, drinking alcohol, carcinogens and chronic pancreatitis.

1.1.1.1. Pancreatic ductal adenocarcinoma (PDAC)

Pancreatic ductal adenocarcinoma (PDAC) is the most prevalent epithelial, exocrine pancreatic cancer, which shows for more than 80 % of the malignant neoplasms of the pancreas (Alexakis *et al.* 2004). It is developed from cells lining the ducts that carry the digestive juices into the main pancreatic duct and then on into the duodenum. Clinical research has revealed slight improvement in the median overall survival of patients since 20 years ago (Lockhart *et al*. 2005).

PDAC influences more developed countries than other parts of the world with more than 8000 cases diagnosed in the UK each year (Keane *et al.* 2014). Patients who do not receive any treatment usually live for of 3-5 months and 6-10 months for locally advanced disease (O'Sullivan and Kocher, 2007). Over the past decade, gemcitabine alone or combined with fluoropyrimidine, fluorouracil (5FU) or erlotinibis has been the only chemotherapy available clinically for pancreatic cancer (Walker and Ko, 2014). Gemcitabine is a nucleoside analogue that mimics physiological nucleosides in terms of uptake and metabolism and is incorporated into newly synthesised DNA resulting in synthesis inhibition and chain termination. Unfortunately, this chemotherapeutic agent proves effective in only 23.8 % of patients with the only alternative being surgical removal of the localised tumour (Figure 1) (Cunha *et al.* 2005).

Like many solid tumours PDAC has mass transport properties which are different from normal tissues (Neesse *et al*. 2011). Many physical barriers may affect efficient PDAC drug delivery which results from numerous pathological features. These barriers are leaky and disorganised with non-functional vasculature (Farrell *et al*. 2009), characteristically dense stroma (Neesse *et al*. 2011) and deregulated cellular transport proteins (Farrell *et al*. 2009). The permeable vasculature of PDAC may result in high interstitial

fluid pressure (Frieboes *et al*. 2011), which inhibits the transition of drug from the vasculature to the extracellular section. The extracellular section of PDAC is normally a dense stromal, called desmoplastic, which has been demonstrated to affect drug delivery and reaction to gemcitabine in preclinical models (Neesse *et al*. 2011). Thus, there is a need to increase the efficacy of this treatment as well as exploring alternative therapies.

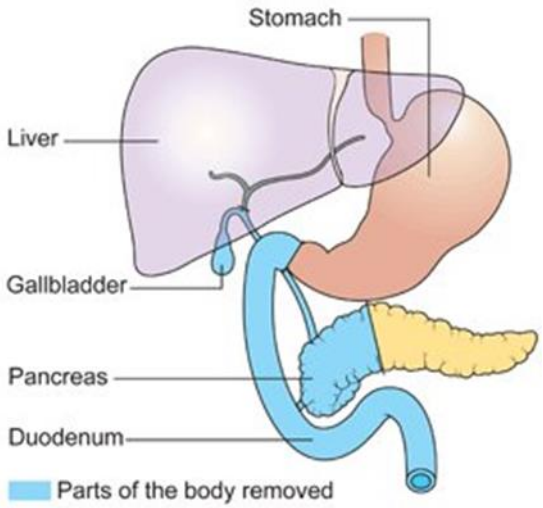

Figure 1. Diagram showing the area to be removed for pylorus preserving pancreatic duodenectomy (Cancer Research UK, 2012).

1.2. Nanotechnology in medicine

The concept of nanotechnology was first considered by Richard Feynman, in his 1959 lecture. By saying "There's plenty of room at the bottom", he defined the value of employing individual atoms using larger machines to creating smaller machines (Feynman, 1959).

Nanotechnology is derived from the Greek word, which means dwarf or one billionth. This is one of the fastest growing technologies of our time and is a multidisciplinary field, which includes chemistry, engineering, biology and medicine. Moreover, it has become a versatile and promising platform for creating novel materials with enhanced properties and potential applications in cancer therapy. This technology has revolutionised healthcare and

medical therapies. Nanoparticles (NPs) are commonly smaller than hundred nanometres in size; therefore, they can represent many interactions with biological molecules on the surface of the cells as well as inside the cells.

This technology suggests the possibility for constructing smart therapies capable of targeting specific cancers. The particles themselves may possess multifunctional properties that can be used for early detection, accurate diagnosis and personalised treatment (Cai and Chen, 2007). Although progress of therapies is still in the early phases, the use of NPs is becoming prevalent in diagnostic applications and will probably involve all areas of medicine in the future for the treatment of certain diseases such as cancer. Research into NPs is in its infancy for liver, upper gastrointestinal and pancreatic cancers, and their use is becoming increasingly popular as contrast media for radiological researches (Andrén-Sandberg, 2012). However, more advanced technologies capable of active targeting are still in the early phases of evaluation for clinical use and small fraction of NP-based therapies are in the clinic.

Nanomedicine platforms suggest many advantages for sensing, delivery and image-targeting agents. The first study in cancer therapy by nanomedicine goes back to 1974, when Gregoria *et al.* prepared liposomes as drug carriers for the first time (Gregoria *et al*. 1974). The size, shape, structure and chemical properties of engineered NPs open a vast range of technical applications and novel approaches in medical research (Yang *et al.* 2009).

In nanomedicine, the most widely researched NPs are quantum dots (Cai *et al.* 2007), carbon nanotubes (Liu *et al.* 2007), magnetic NPs (Thorek *et al.* 2006), liposomes (Park *et al.* 2004), gold NPs (Huang *et al.* 2011a), polymeric (Thompson *et al*.2008), lipid and silver NPs (Ferrari, 2005; Grodzinski *et al.* 2006).

Quantum dots have been used in detection and biological labelling because of their size-dependent fluorescence properties (Bruchez *et al.* 1998; Chan and Nie, 1998; Lee, 2001). Magnetic NPs are useful in cell sorting (Liberti *et al.* 2001), MRI (Lawaczeck *et al.* 1997; Meyers *et al*. 1963; Schleich *et al.* 2014), drug delivery (Goodwin *et al.* 1999; Joubert, 1997; Koppolu *et al.* 2012) and magnetic hyperthermia therapy (Andra *et al*. 1999; Hilger *et al.* 2000; Kruse *et al.* 2014). Polymeric and lipid and NPs have been investigated to encapsulate therapeutic agents in order to enhance drug safety, solubility, and delivery efficiency due to the enhanced permeability and retention

(EPR) effect of the cancerous tissues (Farokhzad and Langer 2006; Moses *et al*. 2003). Carbon-based NPs have been exploited for photothermal therapy (Kam *et al.* 2005) and drug delivery (Bekyarova *et al.* 2005; Bianco *et al.* 2005; Lin *et al.* 2004).

1.2.1. Metallic nanoparticles

Metallic NPs have received great attention for over a century and are now extensively utilised in biomedical sciences (Conde *et al.* 2012; Hu *et al.* 2009; Lin *et al.* 2014). Metallic NPs have shown unique and unusual chemical, physical and biological properties due to their quantum size, in comparison with other NPs. This capability allows them to be used in a range of biomedical applications (Kogan *et al*. 2007). Metallic NPs can be simply synthesised with a high level of control of their shape, size and composition (Kawamura *et al.* 2013). Two simple methods, bottom-up and the top-down techniques, have been suggested for the fabrication of metal NPs. Top-down technique uses traditional methods to guide the synthesis of nanoscale materials. The paradigm proper of its definition generally shows that in the top-down method it all starts from bulk piece of material, which is then gradually or step-by-step removed to form objects in nano scale. This approach for nanofabrication is the one first suggested by Feynman (Feynman, 1959). However, top-down techniques for nanofabrication have critical limit in the ability to miniaturise components. Therefore, several bottom-up techniques have been used to synthesise nanostructures one atom at a time, in the most efficient and precise way possible (Pattekari *et al*. 2011).

Metals such as nickel and cobalt are extremely magnetic but also highly cytotoxic, which limits their biomedical applications (Denkhaus and Salnikow, 2002; Haynes *et al*. 2000). On the other hand, iron oxide, gold and silver have a long history of safe clinical use. Because of their inherent instability, surface engineering of these particles before introduction into biological environments is highly demanded (Auffan *et al.* 2009; Häfeli *et al.* 2009). The specific attention of this thesis is on the use of iron oxide and gold metallic hybrid nanostructures.

1.2.2. Iron oxide metallic nanoparticles

In recent years magnetic iron oxide NPs (MNPs) have attracted considerable attention of the researchers due to their vast biomedical applications from utilising in the recovery of metal ions and dyes to drug delivery, hyperthermia and imaging (Figure 2) (Comoucka *et al.* 2010; Neuberger *et al.* 2005). Studies have highlighted MNPs offer the benefit of utilising both EPR effect (passive targeting) whilst also allowing for a direct, externally guided delivery to the tumour (active targeting) (Arruebo *et al*. 2007).

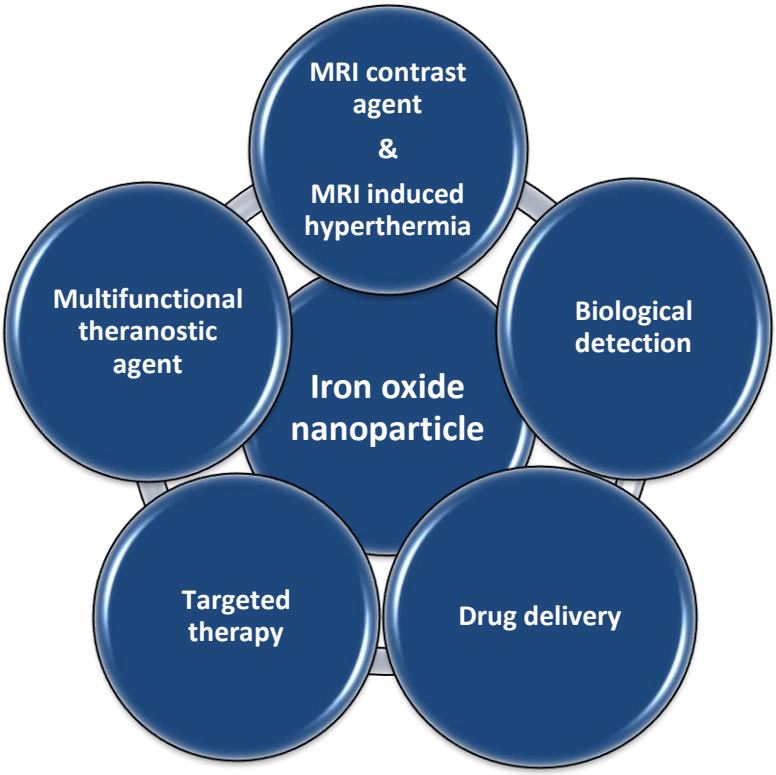

Figure 2. Schematic diagram showing biomedical applications of iron oxide nanoparticles.

Magnetic separation of iron oxide NPs (with a single magnet instead of centrifugation or precipitation) is a rapid and advantageous method with high efficacy and cost-effectiveness. Superparamagnetic properties of MNPs allow them to interact with numerous biological molecules in different ways. They also have large surface area to volume ratios (because of their nano-size), wide choice of surface functionalisation and low surface charge at physiological pH. However, they tend to aggregate in aqueous solution and biological systems due to their inherent magnetic nature. This unwanted

behaviour possibly reduces the long term stability of formulations and results in large nanoparticle clusters that are not acceptable for biomedical applications (Chan, 2007). Furthermore, it has been well documented that iron oxide may degrade into free ions in physiological environments (Stroh *et al*. 2004). This degradation can enhance the production of free radical in cells which leads to cell damaging and finally cell death (Hoskins *et al.* 2012a; Hoskins *et al.* 2012c; Minotti and Aust, 1987).

In order to eliminate the potential of degradation of iron oxide NPs, they are usually coated with materials such as poly (acrylic acid) PAA (Mak and Chen, 2005), Dextran (Ciobanu *et al.* 2012) and poly (ethyleneimine) (PEI) (Wang *et al.* 2009) or coatings such as silica (Santra *et al.* 2001), carbon (Mendes *et al.* 2014) or precious metals (e.g. gold or silver) (Mandal *et al.* 2005).

As mentioned above, in order to increase biocompatibility, impart colloidal stability and avoid to uptake by the reticuloendothelial system (RES), iron oxide NPs can be coated with polymers such as polyethylene glycol (PEG) and polyacrylamide. During systemic administration, a significant quantity of NPs are non-specifically cleared from the blood by the mononuclear phagocytic system (MPS) (the liver, spleen, and lymph nodes) and the efficiency of this process depends on NPs` size and surface chemistry. Therefore, HNPs composed of multiple nanocomponents must be engineered to exhibit a long residence time in the bloodstream if *in vivo* circulation is needed to be effective. The polymeric coating also allows for addition of functional ligands, such as radioactive ions for PET imaging and fluorophores for fluorescent imaging.

Furthermore, this functionalisation and modification of MNPs may improve their magnetic properties and affect their behaviour *in vivo* (Gupta and Gupta 2005; Tartaj *et al.* 2003). MNPs have been extensively explored as contrast enhancement agents in magnetic resonance imaging (MRI) applications due to their capacity to increase the proton relaxation of specific tissue. Investigations are also underway utilising them in MRI induced cellular hyperthermia (Wabler *et al.* 2014); such phenomenon can be observed when these particles are placed inside an altering magnetic field resulting in rapid fluxing between polarised and relaxed states which leads to localised heating of the NPs. Additionally, MNPs have been exploited widely as a nanomedicine platform for the targeted delivery of therapeutic agent through magnetic drug delivery

(Neuberger *et al*. 2005) and via the attachment of high-affinity ligands (Zhang *et al*. 2002; Torchilin, 2006).

However, recent studies have emerged detailing the flaws of such flexible coatings for long term application, whereby core exposure leads to free radical cellular damage (Hoskins *et al.* 2012a; Hoskins *et al.* 2012c). Recent investigations have shown toxicity and cellular fate of polymer coated iron oxide NPs. As a result, most of them such as Feridex IV® and Luminex®, which were exploited as contrast agents in clinic, have been removed from use in humans. Currently, designing highly rigid coatings which make nano-sized formulations biocompatible and keep the unique contrast ability of their predecessors is being sought.

The main concerns in chemically fabricated hybrid assemblies include the numerous synthesis steps that may produce a vast range of structures with ill-controlled configurations. For example, coating step may not achieve successfully in synthesis process and instead of producing uniform HNPs, many different NPs in shape and size may be fabricated. Another problem is lack of understanding about the details of particle formation. This might be due, to a large extent, to the lack of adequate techniques to precisely control the shell structures of HNPs (Prabhu and Hudson, 2009; Chen *et al.* 2009).

1.2.2.1. Super paramagnetic iron oxide nanoparticles (SPIONs)

Iron oxide NPs are usually divided in two main groups (in terms of their size): super paramagnetic and ferromagnetic NPs. Nearly all of investigations in nanomedicine are based on super paramagnetic NPs (Neuberger *et al.* 2005) but few studies have also emphasised the potential of ferromagnetic NPs (Kita *et al.* 2010).

The term superparamagnetism is referred to a form of magnetism, which appears in small (20 nm or less) ferromagnetic or ferrimagnetic NPs. The concept of SPIONs magnetism is mentioned in the mid-1950s for the first time (Bean, 1956), which explains the capability of a ferrimagnetic or ferromagnetic particle to be magnetised with an external magnetic field and to completely lose this magnetisation when the magnetic field is removed

(Dunlop, 1973; Bate, 1980). Then, in 1970s, Freeman and colleagues proposed the use of magnetism in biomedicine (Freeman *et al*. 1960).

Super paramagnetic iron oxide nanoparticles (SPIONs) are small synthetic α-Fe_2O_3 (hematite), γ-Fe_2O_3 (maghemite) or Fe_3O_4 (magnetite) particles with a core diameter between 10-20 nm. Among this group only maghemite and magnetite can be used for biomedical applications. Moreover, mixed oxides of iron with transition metal ions such as manganese, cobalt, copper and nickel have superparamagnetic characteristics and also included in the SPIONs category. SPIONs are biocompatible, biodegradable and facilely tunable with rapid removal through extravasation and renal clearance. They have been shown to have high suspensibility, well reactive surface, consistent particle size distribution, and the possibility of further modifications (Kemshead and Ugelstad, 1985).

SPIONs have been utilised as targeted magnetic resonance contrast agents for MRI, with advanced progression in diagnosis of diseases such as cancer in their early stages (Amstad *et al*. 2009). The nonspecific uptake of SPIONs in the mononuclear phagocyte system (MPS) or reticuloendothelial system (RES) after administration made it feasible to use in clinical diagnostic of many organs.

In drug delivery, targeted cancer therapy, in order to deliver radio therapeutics and chemotherapeutics, is the one of most considered areas (Bae and Park, 2011; Moghimi *et al.* 2001). Nevertheless, photothermal ablation (cell death by using local hyperthermia) (Zhigilei *et al.* 2009), peptides (Zuo *et al*. 2014), antibodies (Pathak and Benita, 2012) and gene delivery (Cheong *et al.* 2009) by SPIONs have received increasing attention recently (Yen *et al.* 2013).

Over the past three decades, the synthesis of SPIONs by different synthetic routes has been well documented. SPIONs can be fabricated by physical approaches such as mechanical grinding and bio-mineralisation processes or through chemical methods such as co-precipitation methods, thermal decomposition methods, micro emulsion methods, flame-assisted methods, hydrothermal syntheses, polyol methods, sol-gel syntheses, sono-chemical reactions, electrochemical methods, etc (Chaudhuri *et al.* 2012; Wahajuddin and Arora, 2012). Compared with the physical methods and the bio-mineralisation processes, chemical methods, especially co-precipitation technique, are common methods to make iron oxide NPs for MRI application. Because, they represent high potential in controlling fundamental parameters, such as, size, size distribution, phase purity and

degree of crystallinity in MRI applications. For example, in co-precipitation technique, the size of the particles can be adjusted by base concentration, temperature, and presence of surfactants (Levy *et al.* 2002).

SPIONs are one of the few particles injected into the human body which are simply incorporated into the body`s natural metabolism. In general, SPIONs can be removed from circulation prematurely by two pathways, which are taking by the RES (> 200 nm) or via renal clearance system (< 5.5 nm). Therefore, particles between 10-100 nm in diameter exhibit the highest circulation time (Gupta and Gupta, 2005) as their small surface area (compared with large SPIONs) reduces the area accessible for adsorption of RES proteins and they are still large enough to avoid renal filtration.

In order to create stealthy NPs, the chemical nature of the particles` surface must be considered. For example, in terms of RES uptake, some studies propose that for SPIONs with less than 40 nm in diameter, surface properties of the particles are more important than their size. While a surface with negative charge enhances the attachment of plasma proteins that results higher uptake, positively charged surface may allow the SPIONs to attach to cells in a non-specific behaviour (Wahajuddin and Arora, 2012). As a result, hydrophilic and neutral surface are more ideal to reduce opsonisation and clearance (Köseoğlu *et al.* 2002). It has been proposed that pinocytosis was the main mechanism of SPIONs internalisation with tumour cells as SPIONs drug uptake was not plateau (Zhang *et al.* 2009a). Plateau would be expected in the case of receptor mediated endocytosis due to the decreased availability of free receptors overtime.

AmionSPARK® and Feraheme® are two clinically available form of iron oxide NPs, which have been chemically modified to present a specific function (Chen, 2010). AminoSPARK® is NIR fluorescent NPs consist of an iron oxide core with a biocompatible, amine-functionalised surface suitable for further chemistry and conjugation to a variety of amine reactive molecules. So far it has been used in laboratory for animal research. Feraheme® or ferumoxytol is used to treat iron deficiency anaemia in people with chronic kidney disease.

1.2.2.2. Ferromagnetic iron oxide nanoparticles

Ferromagnetic iron oxide nanoparticles have potential in biomedical applications. Their particle size can be controlled and a vast range of size can be fabricated (from a few nanometres up to tens of nanometres). The small size of ferromagnetic iron oxide NPs proves that they can enter to the living cells. As with SPIONs, these NPs may be coated with biomolecules, which allow them to bind to or interact with other molecules for creating a controllable addressing or tagging tool (Pankhurst *et al.* 2003). Furthermore, ferromagnetic NPs are under Coulomb's law, which indicates that they can be affected by external magnetic fields, where energy can be shifted from the exciting fields to the nanoparticle. As a result, ferromagnetic iron oxide NPs can be synthesised to resonantly react with a time-changing magnetic field. For example, particles can be prepared for heating purposes, which can be used as hyperthermia agents; transferring toxic amounts of thermal energy to desirable area such as tumours; or as radiotherapy and chemotherapy improvement agents, which applies moderate warming to be more efficient on cancer therapy.

They also present greater magnetic potential than their SPION counterparts, which is desirable for external magnetic guidance and enhanced contrast-ability. Ferromagnetic iron oxide preparations, combined with MRI, have the potential to revolutionise a number of investigative and treatment procedures. This would be attained by the combination of the benefits delivered by iron oxide NPs together with MRI, which leads to superior and safer imaging alternatives (Gneveckow *et al.* 2005; Hilger *et al.* 2005; Rudolf *et al.* 2006).

Ferromagnetic iron oxide NPs are usually fabricated by co-precipitation methods (Kandpal *et al.* 2014). As same as SPIONs, their shape, size and crystallinity can be designed based on reaction conditions. Although SPIONs are less magnetic, they are still more preferred than ferromagnetic iron oxide NPs, which is related to the relative instability of ferromagnetic NPs and difficulties in suspending due to their aggregation.

1.2.2.3. Iron oxide for MRI

Liver tumour was the first cancer clinically diagnosed by iron oxide imaging agent (Saini *et al.* 1987). Recently, multi-functional iron oxide NPs are considered to be used for measuring tumour volumes and improving the delineation of brain tumour boundaries (Mehdorn *et al.* 2011; Senft *et al.* 2010; Willems *et al.* 2006). There are several examples of SPIONs in experimental study or first phase of clinical trials (Vu-Quang *et al.* 2012; Wang *et al.* 2014a; Wang *et al.* 2014b). Many formulations have already been used in clinic for medical imaging and therapeutic applications. For example, Lumirem® has been used for bowel imaging (Wang *et al.* 2001). Also, using Feridex IV® for spleen and liver imaging (Bonnemain, 1998), Combidex® for lymph node metastases imaging (Harisinghani *et al.* 2003), and Ferumoxytol® for iron replacement therapy has been reported (Provenzano *et al.* 2009). Although designing this new class of diagnosing agents has been a huge achievement in modern nanomedicine, the theoretical models of iron oxide NPs and the electron structure of the complex compounds with diagnosing molecules are not well described.

MRI has been used for *in vivo* cell tracking due to its great spatial resolution. This can be achieved by changing the proton relaxation time, when hydrogen protons align and come back to their initial state. MR image is generated by two independent processes, longitude relaxation (T_1 recovery) and transverse relaxation (T_2 decay). SPIONs can change the relaxation time extensively through transferring their magnetic relaxation to the surrounding nuclei. As a result, significant delay of the signals between contrasted and non-contrasted areas can be monitored (Figure 3).

Investigations are also underway utilising SPIONs in clinic to visualise cell migration, in order to monitor cellular therapies with MRI. The detection threshold for SPION-labelled cells is affected by magnetic field strength and acquisition parameters. One of the problems using MRI is that it needs high concentrations of contrast agents due to its low sensitivity. A high concentration of iron oxide enhances toxicity, which is highly concerned in biomedical applications. Fabricating aggregated particles may be an alternative method to enhance the sensitivity. Aggregated forms have stronger magnetic field, thus high concentration of iron oxide NPs is not necessarily needed (Bystrejewski *et al.* 2007).

Figure 3. Standard MR image of a healthy canine brain by T_2 imaging agent presenting difference in contrast between various areas (Malekigorji *et al*. 2014).

In an interesting study, Wu and co-workers explored MR imaging of human pancreatic cancer xenograft labelled with SPIONs in nude mice (Wu *et al.* 2012). Tumour xenografts were induced in nude mice through the injection of human pancreatic cancer cells labelled with SPIONs. The unlabelled cancer cells served as a control. MR imaging was achieved by a 1.5 T MR scanner for the tumour xenograft at the first, second and third week after the injection. They revealed that the tumour xenograft was induced in 100 % nude mice on MR imaging for both groups in the first week after the injection. In the SPION category, the tumours presented homogeneous hypo intensity on T_1 - and T_2 -weighted and FIESTA images 1 week after injection. Two and three weeks after injection, the centre of the tumours was still hypo intense on all the above sequences. The tumour periphery is intense on T_1 -weighted, and hyper intense on T_2 -weighted and FIESTA images. The tumours in the control group were homogeneously hypo intense or is intense on T_1 -weighted, and hyper intense on T_2 -weighted and FIESTA images in the first, second and third week after the injection. The signal to-noise ratio and size of the tumour centre in the group injected with the SPIONs decreased in all T_1 - and T_2 -weighted images and FIESTA. These outcomes emphasise that human pancreatic cancer cells labelled with SPIONs can induce tumour xenograft in nude mice and MRI can display the kinetics of SPIONs distribution in tumour xenografts (Wu *et al*. 2012).

1.2.2.4. Iron oxide for magnetic hyperthermia

Magnetic thermotherapy of cancers is a fourth treatment technique, after surgery, radiotherapy, and chemotherapy in the world. This novel technique can be utilised on its own or in combination with chemotherapy and/or radiotherapy. Iron oxide NPs have the capacity to produce heat when exposed to strong magnetic fields (Rosensweig, 2002); the magnetic moments of the iron oxide NPs completely or partially align in the direction of the field, upon usage of an electromagnetic field. At a unique frequency to the NPs, the magnetic moments delay behind the field can cause a delay in the magnetic response. Therefore, the magnetic moments do not follow the same line throughout the reversal of orientation of the used magnetic field. A hysteresis loop is produced that is evident when the reversal is hindered and related energy loss is dissipated in the form of heat energy (Figure 4).

Magnetic moment can alter unsystematically in single domain materials through thermal fluctuation at high temperatures. But the thermal energy is decreased at lower temperatures leading to a blocking of the magnetic moments. This is identified as the blocking temperature which is related to the shape and size of NP. Small NPs have smaller volumes, thus they represent a lower energy barrier and lower blocking temperature. Magnetic crystal suspensions of iron oxide NPs deposit the energy of alternating magnetic fields and release this energy as heat, which triggers hyperthermic stress in cancer cells (Kossatz *et al.* 2014). In targeted magnetic hyperthermia treatment of cancers, MNPs act as thermal seeds under an alternating magnetic field (Figure 5) (Gneveckow *et al.* 2005; Hergt *et al.* 2006; Hilger *et al.* 2005). Increasing temperature more than 40 °C improves the radiation effect and causes thermoablation of the cancer cells. This heating is supposed to induce enhanced vibrational, translational and rotational motion of molecules in the cells. Moreover, heating has the ability to increase metabolism and transition (structural transformation from an ordered to a disordered state) of cellular structures, such as proteins, DNA and RNA (Hilger and Kaiser, 2012).

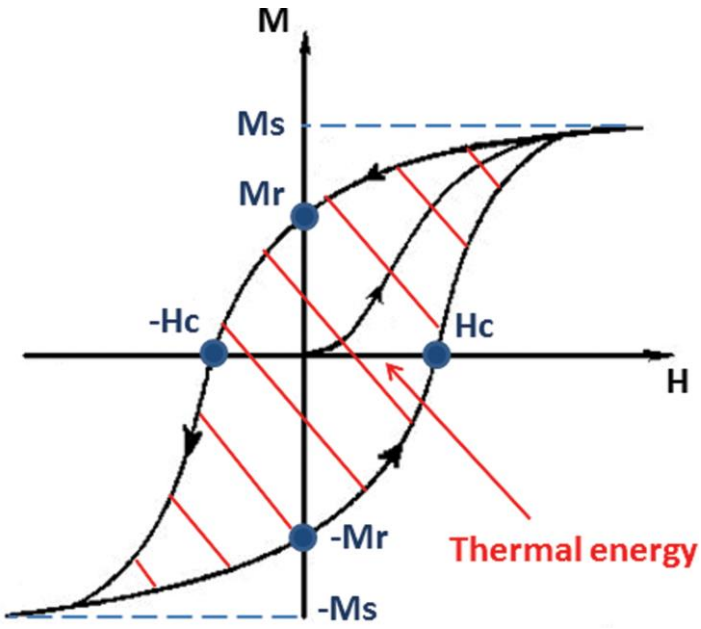

Figure 4. Hysteresis loop of iron oxide NPs. The area of the hysteresis loop represents the energy dissipated during a magnetisation cycle (Hervault and Thanh, 2014).

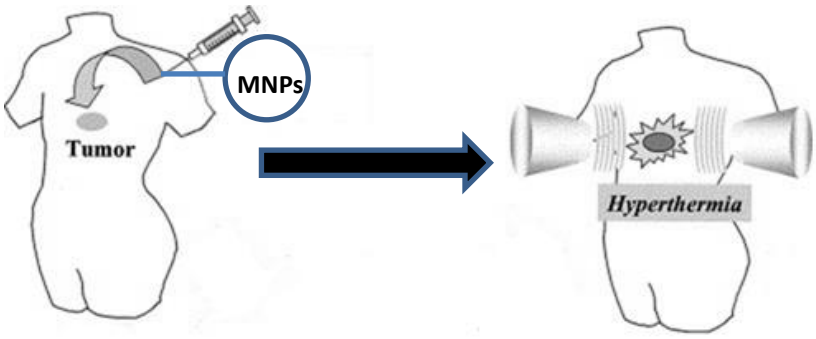

Figure 5. Schematic illustration of hyperthermia treatment of cancers inside an altering magnetic field.

Recently, Kossatz *et al.* studied the therapeutic outcomes of magnetic hyperthermia therapy with SPIONs on pancreatic cancer (BxPC-3) xenografts in mice *in vivo*. Iron oxide NPs were injected into the pancreatic tumour before applying cumulative heating to 43 ˚C. Histological study of magnetic hyperthermia treated tumour tissue revealed changes in cell viability (apoptosis and necrosis) and demonstrated a reduced cell proliferation, in

comparison with the control cells. This study emphasises the capability of iron oxide NPs for magnetic hyperthermia application in pancreatic cancer therapy (Kossatz *et al.* 2014).

In another interesting piece of research, Basel and co-workers injected MNPs into mouse monocyte macrophage like (RAW264.7) cells. These cells are well-known for their tumour homing activity. In order to develop a murine xenograft model of disseminated peritoneal pancreatic cancer, they injected Pan 02 cells intraperitoneally (IP). After tumour growth, monocyte/macrophage like cells (loaded with MNPs) were injected IP and let to transfer into the tumour. After three days, the mice were located in an alternating magnetic field for 20 min to induce hyperthermia. This treatment procedure was performed three times. A survival study showed that this treatment considerably enhanced survival in this murine pancreatic cancer model and the average post-tumour insertion life expectancy improved to 31 %. Therefore, this technology is really promising method in actively delivering NPs for local hyperthermia therapy of cancer (Basel *et al.* 2012).

However, there are still inconsistencies between experimental results and predictions of the amount of heat produced by the MNPs based on the current simple models, which has been a main problem to optimise the design of magnetic particles for clinical application (Manfred *et al*. 2010).

1.2.2.5. Iron oxide nanoparticles as vehicles for chemotherapy

Iron oxide NPs have been highly studied for their potential as drug delivery means for chemotherapeutic applications (Hedgire *et al.* 2014; Jain *et al.* 2005; Yallapu *et al.* 2013). Incorporating cytotoxic agents with NPs has shown to passively target pancreatic adenocarcinomas and enhance drug efficacy (Hoskins *et al.* 2010). This is supposed to be due to the accumulation of drug by EPR effect, which leads to deeper tissue penetration. This localised delivery, in combination with the rapid diagnosis and treatment leads to an interesting approach with excellent potentials to act as a selective treatment with lowered dosages, therefore reducing side effects and improves clinical results for patients suffering from pancreatic cancer.

Therapeutic agents, such as drugs, proteins, peptides and nucleic acids, can be incorporated in the iron oxide NPs by either conjugating on the surface of particles or trapping within

the NPs themselves. Many chemical strategies have been used for the conjugation of targeting, therapeutic and imaging agents with NPs surfaces. These can be categorised into covalent linkage methods, such as direct NP conjugation, covalent linker chemistry (conjugation of biomolecules to the surface of NPs by a linker) and click chemistry (biocompatible reactions intended primarily to join substrates of choice with specific biomolecules); and physical interactions, which are electrostatic, hydrophilic/hydrophobic interactions (forces between molecules or atomic groups do not arise from a covalent bond). Functional groups of the NPs` coating, ligands and physicochemical properties of them can directly affect the choice of chemistry. The main goal is to incorporate the therapeutic, targeting or imaging agent without changing its functionality. Functionality in such formulations is imposed by the nature of the ligand (e.g. conformation of biomolecules) and the method by which it is conjugated. For example, if an antibody is attached to the NPs` surface but its detection site is covered by proteins, it may lose its ability to bind or reach to its site of action. Surface modification of NPs with biocompatible materials such as polyethylene glycol (PEG) can reduce the adsorption of plasma proteins and avoid the formation of protein corona (Gref *et al.* 2000).

The surface of iron oxide NPs has been amended with anticancer drugs such as doxorubicin (Dox) (Kievit *et al.* 2011), Catechin-dextran (Vittorio *et al.* 2014) and Paclitaxel (Hwu *et al.* 2009). Catechin-dextran conjugated Endorem NPs (dextran coated iron oxide NPs) enhance the intracellular concentration of the drug, in comparison with the drug alone. Inside a magnetic field, this nano-sized formulation caused apoptosis in 98 % of human pancreatic cancer cell line (MIA PaCa-2). The authors proposed that the attachment of catechin-dextran with Endorem improves the anticancer activity of the drug and offers a novel way of targeted drug delivery to cancerous cells with the help of magnetic fields *in vitro*. It is suggested that this remote control drug delivery of the catechin-dextran by a magnetic field makes it a potential agent in cancer therapy (Vittorio *et al.* 2014).

Sometimes the surface of iron oxide NPs, as a chemotherapeutic carrier, contains a targeting ligand that can find the receptors overexpressed on the external surface of tumour cells (Kievit and Zhang, 2011). As an example, Lee *et al*. (Lee *et al*. 2013) fabricated urokinase plasminogen activator receptor (uPAR)-targeted magnetic iron oxide NPs delivering gemcitabine as a chemotherapeutic agent for targeted delivery into uPAR-expressing tumour and stromal cells. This novel assembly was designed by grafting

iron oxide NPs with the amino-terminal fragment peptide of the receptor-binding domain of uPA (naturally occurring ligand of gemcitabine and uPAR, through a lysosomal cleavable tetrapeptide linker). These multifunctional NPs were synthesised not only to induce intracellular release of gemcitabine following receptor-mediated endocytosis into cancer cells, but also to offer contrast enhancement property in MRI of cancers. The data confirmed the lysosomal enzyme- and pH-dependent release of gemcitabine, which preserves the drug from enzymatic degradation and offering imaging capability.

1.2.3. Gold Nanoparticles

Among the category of metallic NPs, gold NPs (AuNPs) deserve close examination and discussion due to their biocompatibility, non-toxic properties, simple and fast preparation, ease of bioconjugation, physical, chemical, optical and electronic properties and the increasing number of publications in the literature for medical applications, from imaging and diagnosing to drug delivery and photothermal therapy (Li *et al.* 2010; Mikami *et al.* 2013).

There are many sub-types of AuNPs based on the size, shape, and physical properties, such as nanosphere, nanoshells, nanocages and nanorods (Figure 6). Each type has its own unique physical properties. The specific architecture is determined the synthetic route and chemical precursors used. The earliest studies of gold nanoparticles go back to gold nanospheres (although not exactly spherical in a strict sense) (Zsigmondy, 1926).

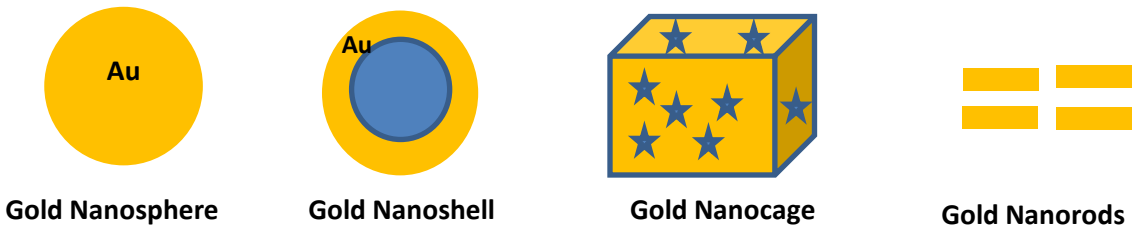

Figure 6. Schematic illustration of different types of gold nanoparticle.

Gold nanospheres between 2 nm and 100 nm in diameter can be synthesised by wet chemical method, which is controlled reduction of an aqueous chloroauric acid ($HAuCl_4$) solution with different reducing agents under varying conditions (Cai *et al.* 2008). Particles around 2 nm in diameter demonstrate distinctive chemical and physical properties, with interesting biomedical applications (Qian *et al.* 2008). AuNPs have been investigated for imaging (Zhang *et al.* 2009b), cancer therapy (Jain *et al.* 2012), and drug delivery (khan *et al*. 2014) in recent years. They also have been used for photothermal therapy and tumour ablation as one of the hottest areas (diagnosis, surgery and medicine) in current research due their enhanced optical properties (Iancu, 2013) (Figure 7). The capability to react as nanoheaters makes these particles potential agents in theranostics, which was presented by Loo *et al*. for the first time (for gold nanoshells) (Loo *et al.* 2004), Lapotko *et al.* (for gold nanospheres) (Lapotko *et al.* 2006), and Hleb *et al*. (for gold nanorods) (Hleb *et al.* 2008).

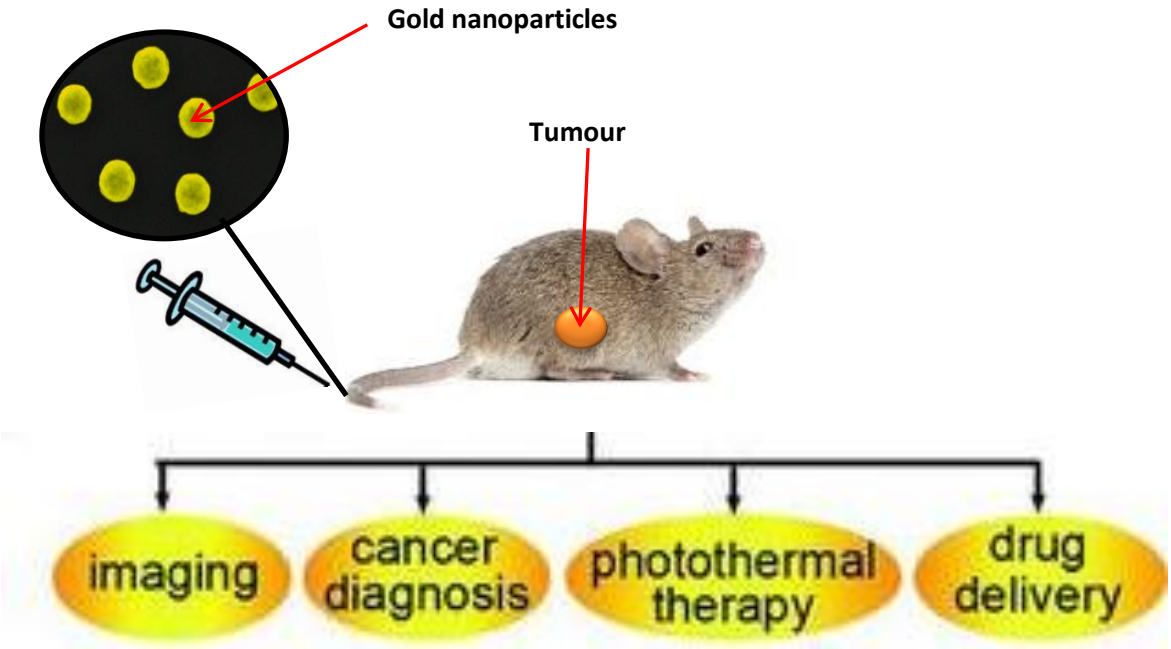

Figure 7. Applications of gold nanoparticles.

Multiple studies have highlighted AuNPs use as surface-enhanced Raman Scattering (SERS) substrates to investigate components in living cells (Li *et al.* 2014; Quaresma *et al.* 2014). In surface-enhanced Raman scattering (SERS), the Raman signals

can be enhanced by many orders of magnitude when the probed molecules are attached or in very close vicinity to noble metal nanostructures with their high local optical fields. SERS spectroscopy can offer the local chemical composition of biomolecules at very low concentrations, and detect the slight changes of the structure at sub-cellular level. Moreover, SERS spectroscopy can be exploited in physiological environment without fixation. AuNPs are able to evaluate the interaction of many chemotherapeutic agents with their pharmacological destinations, such as DNA, within living cancer cells (Alliain and Vo-Dinh, 2002; Alliain *et al.* 2002; Culha *et al.* 2003). Other studies contain cancer gene detection (Rivera *et al.* 2010) and cancer protein biomarker detection (Kosaka *et al.* 2014).

In addition to good synthetic control, gold is extremely biocompatible. This means that it does little to no harm when coming into contact with the human organism. *In vitro* studies suggest that AuNPs do not cause cytotoxicity in human cells (Mie, 1908). This study iterates the findings of many other studies previously described. Thus, Medical devices such as insulin pumps and peacemakers use gold because of both biocompatibility and reliability in electronic devices.

1.2.3.1. Light-scattering of gold nanoparticles

Recent medical applications of colloidal gold, particularly cancer diagnostics and photothermal therapy, have initiated generally from their intensely enhanced optical properties. When particles are exposed to light, many processes can happen: the incoming light might be adsorbed and/or scattered at the same frequency as the incoming light (Mie scattering (scattering of an electromagnetic plane wave by a homogeneous sphere) or Rayleigh scattering (elastic scattering of light by particles that is much smaller than the wavelength of the radiation)), the adsorbed light might be re-emitted (i.e., fluorescence) or the local electromagnetic field of the incoming light can be enhanced; thus increasing any spectroscopic signals from the molecules at the surface of particles, which is called surface-enhanced spectroscopy; such as surface-enhanced Raman scattering (Mie, 1908).

For AuNPs, all these processes are powerfully enhanced due to the unique interaction of light with the free electrons in the metal particles. When AuNPs are irradiated, conduction-band electrons at the surface of the particle start to oscillate due to the electron field of the

light (Sokolov *et al.* 2003). This coherent oscillation of the metal free electrons in resonance with the electromagnetic field is called the surface plasmon resonance (SPR). The SPR absorption related to the dielectric constant of the metal, the particle shape and size and the surrounding medium (Jensen *et al.* 1999). For small particles (< 25 nm), the absorption cross-section directly depends on the particle size and can be measured by Mie theory (Mie, 1908). SPR applications include evaluation of macromolecules in biological environments, equilibrium measurements (affinity and enthalpy), kinetic measurements and analysis of mutant proteins.

For AuNPs, the resonance takes place in the visible spectral area at around 520 nm, which is confirmed by the deep red colour of the NPs in solution. The high-scattering cross-section of AuNPs, with their high photostability (comparing with organic dyes), create a powerful tool for imaging guided drug delivery systems. The use of this light-scattering property for cellular imaging, particularly cancer imaging, has progressed recently (Gu *et al.* 2015; Ilovitsh *et al.* 2015).

AuNPs are used in optical labelling of the cancer biomarkers due to the strong scattering of them. Gold NPs of 30-100 nm diameters scatter strongly and can be distinguished easily by eye. Also the scattering from a gold nanoparticle (60 nm) is much higher than the emission of a fluorescence molecule (Jain *et al.* 2006). The drawback of light-scattering imaging is the interfering of scattered light from tissue (Huang *et al.* 2011a). Therefore, for highly scattering tissue using fluorescence-based imaging techniques can be helpful. While clinical investigations of MNPs have presented great potential in imaging, the use of AuNPs in light-scattering imaging or photon luminescence imaging is still in the first stage in the laboratories. Moreover, the light scattering imaging using AuNPs is simple (a conventional light microscope prepared with a dark field condenser is the only tool needed for the gold imaging system), in comparison with the requirements of MRI.

1.2.3.2. Tumour ablation using gold nanoparticles

To kill cancerous cells, researchers have focussed on exploiting the SPR effect of AuNPs as an alternative method to standard surgical therapies (especially for patients with contraindications), which results in cellular hyperthermia leading to tumour ablation

(Kodiha *et al.* 2015; Lee *et al.* 2014). The advantages of using thermal ablation are reduced morbidity and mortality compared with standard surgical resection and the ability to treat nonsurgical patients.

Photothermal ablation is a minimally invasive therapy, where a focussed laser beam of a specific wavelength (relating to the SPR of the NPs) is irradiated onto the nanoparticulates. Photothermal sensitizers are able to convert the adsorbed light from laser irradiation into heat. Therefore, NPs experience temperature increase (above 42 °C), which can be used to cause irreversible damage to the carcinoma.

Gold holds great potential as a pivotal material key to fighting cancer in future smart therapies. For light scattering and absorption it has been well documented that gold nanoshells and nanocages are preferential in biomedical application due to their SPR occurring at highly red-shifted wavelengths within the biological near infrared window. This window is a narrow range of wavelengths where light is highly transmittable through biological tissue. Hence, this leads to a highly localised therapy which causes minimal trauma to healthy tissue (Fiedler *et al.* 2001; Vogl *et al.* 2004; Weissleder *et al.* 2001*).*

Pitsilldes *et al*. first explained in 2003 the application of gold nanoparticle for photothermal therapy of lymphocytes *in vitro* using immunoconjugates coupled with a nanosecond Nd (Pitsillides *et al.* 2003). In this study laser induced solvent bubbles around the particles produced enough mechanical stress to cause cell death. Zharov and colleagues subsequently proposed the factors that influence the killing energy (thermal energy which causes cell death), for example particle size and the number of pulses per second, as well as the dynamics of the thermal events around the particles. These factors are crucial in order to realise the killing efficiency and mechanism involved. Additionally, nanorods (when the shape of gold NPs change from spheres to rods) (Popp *et al.* 2014), nanoshells (composed of a silica core around 100 nm and a thin shell of gold) (Gao *et al.* 2015), and nanocages (a type of hollow and porous gold nanostructures, which are formed by a galvanic replacement reaction between silver nanocubes and auric acid in aqueous solution) (Kessentini and Barchiesi, 2013) (Figure 6) have all been reported to be used as a nanoheater in biomedicine.

Puvanakrishnan demonstrated the feasibility of using the real-time narrow band imaging system of AuNPs to image breast and pancreatic tumour margins, intraoperatively. He also

showed the feasibility of performing image-guided therapy of pancreatic tumour margins, potentially guiding photo-thermal ablation of tumours (Puvanakrishnan, 2011).

In another study, Glazer *et al.* demonstrated a new cancer therapy by applying intracellular hyperthermia of AuNPs in a radio frequency field. This therapy is based on the specificity of the targeting antibody. Despite systemic treatment and whole-body radio frequency field exposure, healthy tissues were without toxicity. Pancreatic cancer cells showed higher apoptosis and cell viability reduced after treatment with cetuximab-conjugated AuNPs and radio frequency field exposure (Glazer *et al.* 2010*).*

1.2.3.3. Gold nanoparticles in drug delivery

AuNPs can be exploited to deliver drugs and imaging agents that have poor pharmacokinetics (Kim *et al.* 2009; Zhang *et al.* 2011). These nanoparticulates are able to deliver compounds, which are susceptible to enzymatic degradation, such as vaccines as well as those that have low intracellular penetration, for example siRNA (Lee *et al.* 2011b; Lu *et al.* 2010). AuNPs have the potential to be functionalised by active ligands, due to their large surface area, at densities (1.0×10^6 μm^{-2}) (Bard and Faulkner, 2001), which are 100 times higher than that achievable with conventional liposomes (Torchilin *et al.* 2001). This property allows the researchers to optimise AuNPs binding affinity for a specific disease type, stage or patient. Gold nanostructures can also engage multiple, adjacent receptor sites, due to their comparability in size to the distances between cell-surface targets, resulting higher selectivity in their uptake (Jiang *et al.* 2008).

Receptor mediated endocytosis (RME) has been proposed as the primary mechanism of AuNPs cellular entry (Shukla *et al.* 2005). AuNPs in around 1 nm in size can cross the cell membrane and nucleus to interact with DNA. In contrast, particles between 20-50 nm show excellent penetration in to cells without any cytotoxic effect (Gao *et al.* 2011).

Due to the optical and electronic properties of AuNPs, these particles recently have been used in thermorespomsive drug delivery as they can produce enough heat upon laser irradiation, which can be applied as a trigger for therapeutic agents to be released in their site of action (Dreaden *et al*, 2011) (Figure 8).

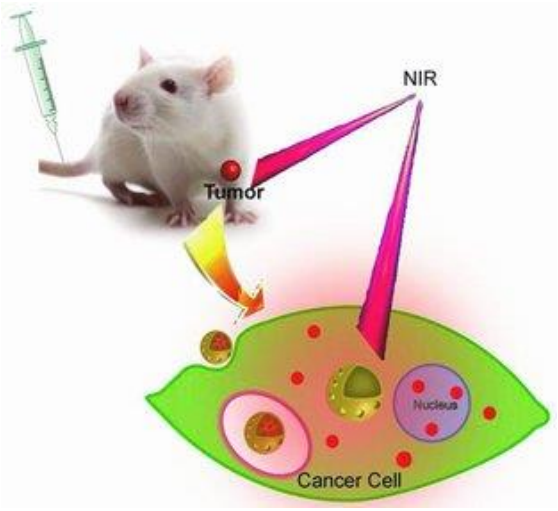

Figure 8. Laser driven anticancer drug delivery based on gold nanoparticles (Dong *et al.* 2013).

AuNPs can conjugate to other molecules by physical (electrostatic) interactions (Rayavarapu *et al.* 2007) and covalent interactions. The nature of AuNPs surface chemistry can help for easy and controlled attachment of different molecules particularly those with thiol functionalities (Lee *et al.* 2010). Moreover, conjugation with proteins (Aubin-Tam, 2013), carboxylic acid (DeLong *et al.* 2010) aptamers (Zhang *et al.* 2013) and disulfides (Letsinger *et al.* 2000) have been also reported.

1.3. Hybrid nanoparticles

Hybrid NPs (HNPs) consist of two or more types of material, such as liposomes, quantum dots, metals, mesoporous silica and polymers. In general, the term "hybrid" mostly used if the inorganic units are in situ by using sol-gel chemistry. The introduction of multifaceted hybrid system has the potential to improve upon the biocompatibility and stability encapsulation efficiency of non-hybrid system. For example, polymer-lipid HNPs have been demonstrated to enhance size or suspension stability of NPs in biological environments by controlling the molar ratio between lipid and polymer components (Wang *et al.* 2013). Moreover, it has been well demonstrated that by coating the surface of quantum dots with a lipid layer, biocompatibility was increased (Wang *et al.* 2012). By using this technology both organic and inorganic phases are formed together through the

simultaneous polymerisation of organic monomer and sol-gel precursors of the inorganic domains (Ochi and Takahashi, 2001).

Depending on the strength or level of interactions, two types of hybrid materials can be classified. Type 1, "non-covalent" hybrid materials, develop weak interactions between the two phases (organic and inorganic phases consist of interactions due to van der Waals, electrostatic and hydrogen bonding forces), whereas, type 2 hybrid materials show strong chemical interaction between the two materials phases to increase the phase coupling. The structural components of the HNPs are mainly classified based on the therapeutic function they deliver. For example, structural nano components such as polymers, liposome, mesoporous silica, micelle or viruses can mainly carry a drug cargo, while structural nanocomponent such as a gold nanoparticle or a carbon nanotube are useful for photoablation therapy (Sailor and Park, 2012).

Controlled drug release from hybrid nanostructure is the next challenge after encapsulating or conjugating the imaging and therapeutic agents onto the hybrid structure. It has been well documented that degradation and diffusion are the key factors for drug release process (Morales *et al.* 2012).

Hybrid nanostructures (NPs which consist of two or more types of material) can eliminate some of the problems required to overcome multidrug resistance due to their multi-functionality. Typically, by adding different functional ligands to a single module one can tackle a problem from different angles at the same time. For example, Zhang and colleagues fabricated novel nanostructured lipid-dextran sulfate hybrid carriers (NLDCs) for sustained delivery of water-soluble cationic mitoxantrone hydrochloride (MTO) and overcoming multidrug resistance. *In vivo* pharmacokinetics in rats after intravenous administration showed that MTO-loaded NLDCs (MTO-NLDCs) had longer half-life than free MTO. In the biodistribution study, NLDCs significantly improved the MTO levels in plasma, spleen, and brain, and reduced the distribution of MTO in heart and kidney. In comparison with free drug, MTO-NLDCs efficiently increased cytotoxicity through the higher accumulation of the drug in breast cancer resistance protein (BCRP)-overexpressing MCF-7/MX cells. MTO-NLDCs accumulated into the resistant cancer cells by the clathrin-mediated endocytosis pathway, which escaped the efflux induced by BCRP transporter and thereby overcame the multidrug resistance of MCF-7/MX cells (Zhang *et al*. 2012).

The idea of encapsulating imaging agents and susceptible drugs in order to avoid premature metabolism has been the focus of many investigations (Morales *et al.* 2012; Zhang *et al*. 2008). NPs that carry biomolecules as a cargo can release their payloads if they became unprotected. The release of imaging agent can be triggered by enzymatic degradation, changing the pH and temperature at the designated area.

The potential of HNPs to transport more than one SPION makes them easier to be seen by MRI, which leads to earlier detection of smaller tumours. The fact that this type of drug delivery vehicle can transfer very different cargos such as a fluorescence NP, a magnetic NP, quantum dot, and a small drug is really promising for the future of drug delivery.

1.4. Nanoparticles in biological environment

The suspension stability (dispersion ability of particulate solid to remain in a liquid matrix solution indefinitely) of NPs in physiological environment is one of the most crucial issues for their usage in biomedicine. This depends on the chemical and physical structure of the NPs and the surface charge of the particles.

In a complex environment NPs aggregation is a common phenomenon, which usually results in irreversible inter-particular adherence and leads to the formation of large and irregularly shaped clusters (Rausch *et al*. 2010). Therefore, understanding the factors that affect NPs colloidal stability and aggregation when introduced into biological environment is crucial to design safe and effective formulations for clinical use. NPs colloidal stability will control their pharmacokinetics, bio-distribution, and systemic toxicity *in vivo* (Nel *et al*. 2006). As an example, Aoki and co-workers revealed in an *in vivo* toxicity experiment that the cause of morbidity of Wistar rats administered at high doses intravenously nano-hydroxyapatite was NPs aggregation and subsequent capillary blockage in the lungs (Aoki *et al*. 2000). Moreover, researcher have revealed that NPs which are stable in blood have a prolonged circulation half-life in the body, and are less likely to be rapidly cleared by the body's reticuloendothelial system (RES) (Gref *et al*. 2000). Therefore, a fundamental understanding of NPs aggregation is required to rationally design NPs whereby it can be understood how they may behave at molecular, cellular, and systemic levels within biological systems.

Surface modification of NPs is one of the most preferred methods to improve colloidal stability (Albanese and Chan, 2011). Thus, it is important to have a good understanding of the mechanisms governing NP stability, and to apply these methodologies in biomedical applications. Modification techniques designed to improve colloidal stability in complex biological environments are electrostatic, steric, or electrosteric stabilisation (Jiang *et al*. 2010).

While characterisations of NPs such as surface area, surface charge and crystallinity have been increasingly investigated (Rivera *et al.* 2010), a deep recognition of the basic mechanisms such as interactions between NPs and proteins and their colloidal reaction in different physiological media is required (Warheit *et al.* 2008). When NPs enter into the biological environment, proteins and other biological molecules compete to attach to the surface of particles, which results in the creation of a protein corona (Figure 9). This phenomenon significantly describes the biological characteristics of the NPs and covering its original surface properties. The biophysical properties of this complex can be different from original formulated NPs. As a result, the biological properties and bio- distribution of the NPs are critically affected by the particle-protein complexes.

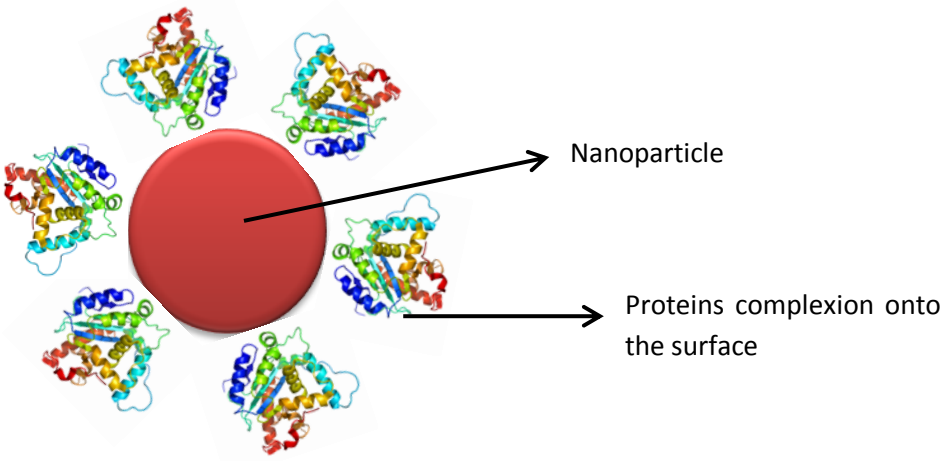

Figure 9. Schematic illustration of protein corona (NPs-Protein complex) created around an iron oxide nanoparticle in biological environment.

1.5. Theranostics in nanomedicine

The term "theranostics" used for first time in the literature in 2002 (Funkhouser, 2002). Theranostics combines diagnosis of disease with the therapeutic capability to treat the disease in one platform. This dual therapy could potentially lead to reduced treatments times and better patient prognosis (Sumer and Gao, 2009).

This novel technology is mainly used in cancer therapy and nanomedicine. In cancer therapy, it is important to detect and treat the tumour before it expands into different part of the organism, as well as image the tumour before, during and after treatment. Since theranostics combines two separate functions, diagnosis and therapy, it is necessary to have sufficient accumulation of agent within the diseased area. This can be achieved via EPR effect, which is first termed by Matsumura and Maeda in 1986 (Matsumura and Maeda, 1986), resulting in deeper drug penetration (Figure 10). This is associated with the damaged and leaky tumour vasculature due to the rapid angiogenesis related to tumour growth. Inside the tumour, the particles are hindered from returning to systemic blood circulation due to the poorly developed lymphatic drainage system presented by most tumours. Additionally, the use of targeting ligands has been studied to increase the accumulation of the NPs in the tumour tissue (Yu *et al.* 2012).

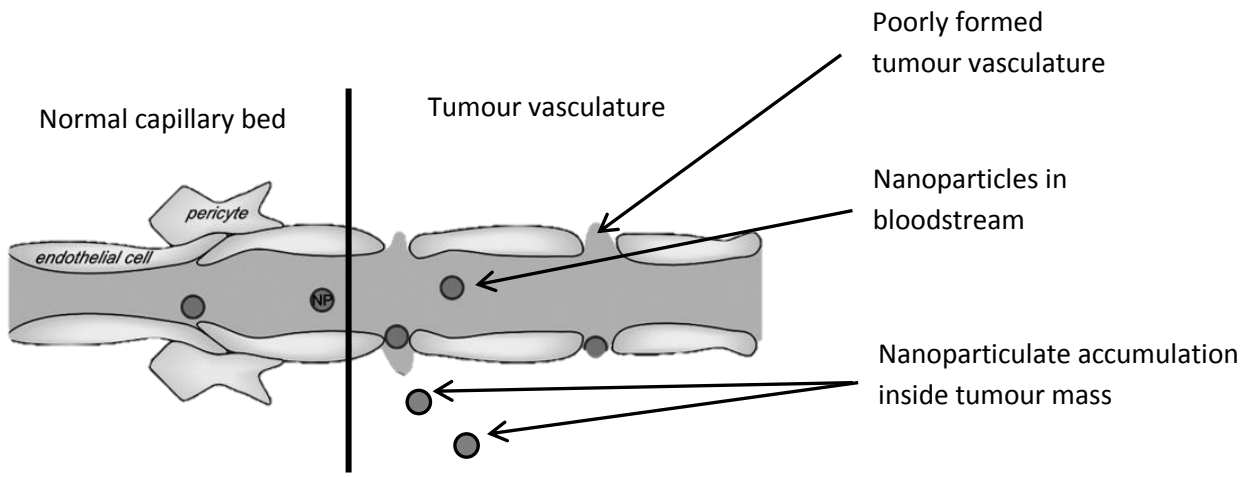

Figure 10. Schematic diagram of the enhanced permeability and retention effect.

In drug delivery technique the size of NPs plays an important role, which has to be large enough to avoid filtration via kidneys and small enough to prevent the capture by the liver

and spleen (Moghimi *et al.* 2001). NPs less than 100 nm in size can enter into the highly permeable blood capillaries which provided by the rapidly growing tumours (EPR effect) (Barenholz, 2012). This however does not happen in healthy tissue as the blood vessels are well developed and nonporous. Moreover, formulation with suitable NPs may increase physicochemical properties such as aqueous solubility, which can enhance therapeutic efficiency.

Nano-sized formulations of chemotherapeutic drugs have demonstrated to passively target pancreatic adenocarcinomas and increased drug efficacy (Yoshida *et al.* 2012). This is related to the accumulation by EPR effect, which leads to deeper drug penetration. One potential problem of using the EPR effect to target tumour is that macromolecule have accumulated in inflamed areas in a similar trend which is undesirable for cancer drug delivery (Vasir *et al.* 2008). Many different nanoparticulates have been used for theranosthic purposes, which are summarised in Table 1. Some NPs such as AuNPs, MNPs or carbon nanotubes have inherent diagnostic/therapeutic properties.

Targeted drug delivery is more advantageous than conventional drug therapy as in targeted drug delivery only a desirable area in the body is affected, which can minimise the side effects caused by conventional drug therapy. The purpose of drug chemotherapy is to transport a drug to the targeted area and treat the disease without affecting surrounding healthy tissue. Strong carrier-drug interactions might enhance the loading capacity and reduce the release rate of drug from the carrier; thus, choosing proper carrier-drug interactions is critical in design and preparation of nanocarriers for drug delivery.

A successful drug delivery carrier protects the drug from degradation or metabolism transit in the physiological environment. It is also essential to minimise the rate of drug release during transportation. Upon reaching the tumour tissue and entering the diseased cell, the system should release its payload quickly; thus promoting cell mortality. After delivering the drug at the target site, the carrier needs to be easy expelled from the body. Toxicity must be considered and reduced to avoid adverse effects in the organism (Poste and Kirsh, 1983).

Table 1. Different theranostic materials in biomedical applications.

Contrast agent	Drug used	Applications	References
Manganese oxide	siRNA	RNA delivery and MRI	Bae *et al.* 2011
Gold	Doxorubicin	Diagnosis, stimulus responsive drug release and photothermal therapy	Chen *et al.* 2013 Huang *et al.* 2011b
Iron oxide	siRNA, doxorubicin, docetaxel	Targeting, MRI and therapy	Lee *et al.* 2009 Yang *et al.* 2010 Ling *et al.* 2011
Silica	Pyropheophorbide (HPPH), doxorubicin	Drug carrier, CT and x-ray imaging and photodynamic therapy	Huang *et al.* 2011b Roy *et al.* 2003 Park *et al.* 2009
Carbon nanotubes	DNA plasmid, doxorubicin, paclitaxel	Diagnosis, DNA and drug delivery, self photolumines-cent and photothermal property	Pantarotto *et al.* 2004 Liu *et al.* 2008 Robinson *et al.* 2010b
Quantum dots	Doxorubicin, methotrexate	Imaging, therapy and sensing	Savla *et al.* 2011 Yuan *et al.* 2009

1.6. Iron oxide-gold hybrid nanoparticles

Functionalised iron oxides NPs (iron oxide as the core) with inorganic compounds are divided into five groups (Figure 11): mosaic, dumbbell, core-shell, shell-core and shell-core-shell (Wu *et al.* 2008).

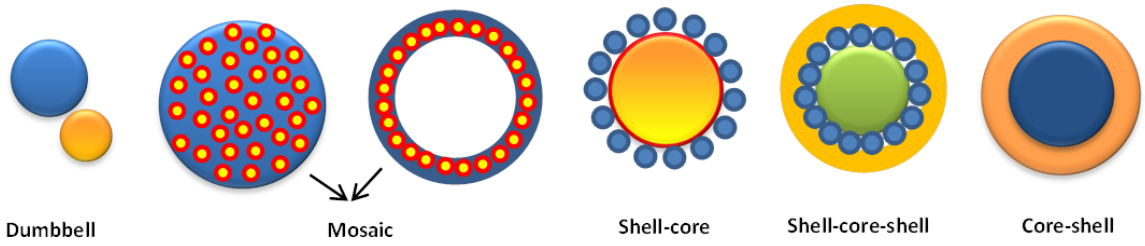

Figure 11. Schematic functionalised iron oxide nanoparticle (iron oxide assumed as the core).

Matrix-dispersed iron oxide NPs can be fabricated by a variety of different states and increase the size of naked iron oxide NPs. The mosaic assembly are usually synthesised in the hollow silica spheres with iron oxide NPs and the shell-core structure can be produced through individual iron oxides that are attached with their inner layer. Shell-core-shell structure can be formed via layer-by-layer strategy, which might overcome some limitations of iron oxide NPs such as degradation (producing free radicals, which lead to cell damage and cell death), aggregation (making clusters, which are undesirable for biomedical applications) and precipitation (reducing colloidal stability) (Jeong *et al.* 2007; Lyon *et al.* 2004; Yu *et al.* 2008). The outer shell can be a polymer, metal NPs and quantum dots, but the inner shell may be the same or different functional materials. This type of nano-composite is estimated to highly increase the range of application of iron oxide NPs. Dumbbell structure is usually fabricated by epitaxial growth of iron oxide on the inorganic compound.

Core-shell structural iron oxide hybrid NPs are remarkably promising materials. Coatings can stabilise magnetic NPs, which improve dispersion and biocompatibility, and the surface can be functionalised by different molecules for various applications. As mentioned above, iron oxide alone in physiological media is unstable. Moreover, limitations have been reported with the use of flexible polymer coatings, whereby core

exposure leads to free radical cellular damage. As a result, imaging agents (polymer coated iron oxide NPs) such as Feridex IV® and Luminex® have been removed from use in humans (Hoskins *et al.* 2012a; Hoskins *et al.* 2012c). To overcome these limitations, they are usually coated with materials such as silica, polymers or gold, which has allowed the synthesis and design of NPs of sophisticated structure and function for biomedical applications. Iron oxide-gold as hybrid nanoparticles (HNPs) (Figure 12) have recently been the focus of many investigations (Hoskins *et al.* 2012b; Seied Sajadi *et al.* 2014; Štarha *et al.* 2015) and are becoming increasingly applicable in biomedicine.

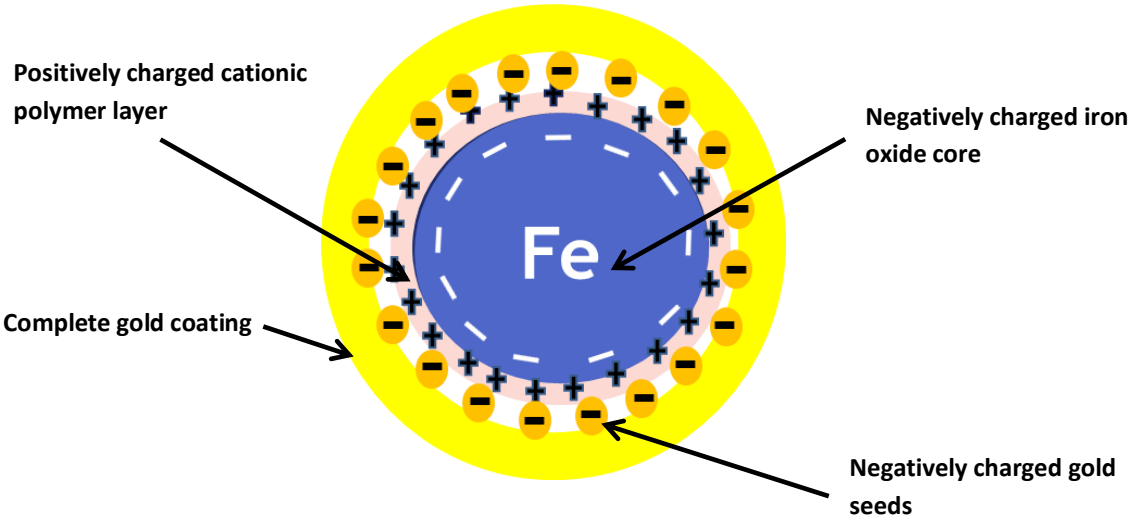

Figure 12. Schematic diagram of gold-iron oxide core-shell nanoparticle presenting electrostatic charges within each layer.

Gold surfaces have the affinity to bind with thiol groups (-SH) by dative covalent linkages (a kind of 2-center, 2-electron covalent bond in which the two electrons derive from the same atom), which means they can be easily modified to confer different functional groups (Figure 13). In particular, it accelerates the attachment of biomolecules with intrinsic self-assembly properties onto the surface of NPs. For instance, Wei *et al*. fabricated a reversible self-assembly of α-cyclodextrins capped AuNPs to vesicles, mediated by a guest (azobenzene) conjugated to the double hydrophilic block copolymers poly-isopropylacrylamide and poly dimethyl acrylamide. This assembly mechanism occurs in pure water under the stimulus of temperature. A possible mechanism is via the thermal responsive coil-to-globule transition of the poly-isopropylacrylamide block

(Wei *et al*. 2012). This shows novel approach for designing magnetic NPs with well-controlled and functional complexes (Robinson *et al.* 2010a).

By using hybrid structure of iron oxide/gold core-shell a multifunctional system can be designed which exploits the surface chemistry of the gold whilst retaining the magnetic character of the iron oxide, allowing for biologically sound drug delivery and imaging. This leads to a rigid nanoparticle structure which eliminates the potential of degradation of the iron oxide core into toxic free radicals. Hence, the overall system is more biocompatible.

Iglesias-Silva and colleagues used microemulsion method to synthesis iron oxide NPs (9 ± 2 nm) following by coating with gold. For gold coating, $HAuCl_4$ was reduced by glucose using a range of molar ratios (1:1 – 1:8) of $HAuCl_4$/glucose. The complete core-shell NPs were characterised via UV spectroscopy, TEM (Transmission electron microscopy), magnetometry measurements and x-ray powder diffraction (XRD) analysis. These characterisation tests of the NPs show that the initial nuclei were completely coated by the metal, and the ratio of reducing agent affected shells size. Moreover, magnetic properties demonstrated a large reduce of the magnetisation for the coated NPs in comparison with the uncoated ones (Iglesias-Silva *et al*. 2010).

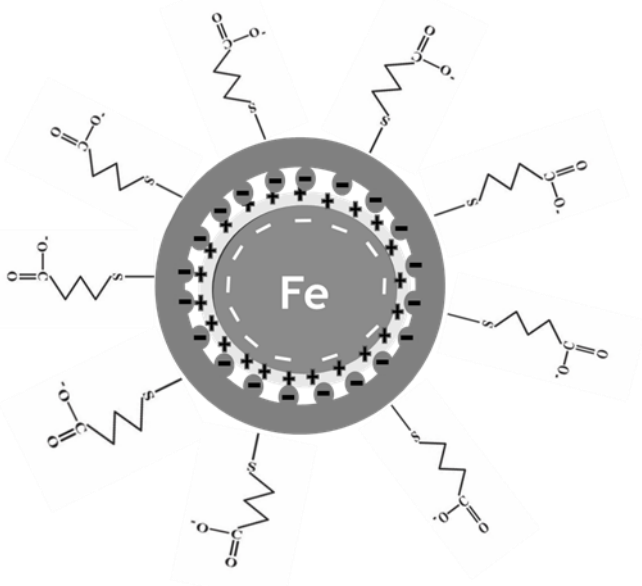

Figure 13. Schematic diagram of functionalising iron oxide-gold hybrid nanoparticles by Au-S chemistry.

Recently, Maleki *et al.* prepared gold coated iron oxide NPs. They used modified water-in-oil inverse nano-emulsion method to fabricate stable iron oxide NPs with high saturation magnetisation (Maleki *et al*. 2015). To achieve mono-dispersed iron oxide particles, molar ratio of iron salts, the concentration of ammonium hydroxide as reducing agent, and molar ratio of water to surfactant were optimised. The biocompatibility of the iron oxide NPs was tested by 3-(4, 5-dimethylthiazol-2-yl)-2, 5-diphenyltetrazolium bromide (MTT) assay, which disclosed that the produced NPs were non-toxic. The surface of iron oxide NPs was functionalised through conformal coating of the NPs with a thin shell of gold (~4 nm) via chemical reduction of attached gold salts at the surface of the iron oxide NPs. The final iron oxide core shell NPs show strong plasmon resonance. Results from physical and chemical characterisation of the changes in surface plasmon resonance, optical band particle size, core-shell surface composition, phase components, and magnetic properties proved the formation of iron oxide gold NPs.

Lin and colleague explained for the first time that gold shell did not degrade the magnetic properties of their iron oxide NPs (Lin *et al.* 2001). In another study doxorubicin was loaded onto gold-coated iron oxide NPs, which showed the same retention of magnetism of naked iron oxide NPs and a sustained release of the drug (Kayal and Ramanujan, 2010). Moreover, iron oxide and gold have been applied in drug delivery systems and imaging to form multifunctional particles. These studies confirmed the attachment of a variety of molecules to the NPs and sustained drug release outlines. As an example, in one study FePt-Au NPs were synthesised, which possessed multifunctional capabilities including catalytic growth effects, magnetic resonance (MR) contrast effects, optical signal enhancing properties with high colloidal stability and biocompatibility. Biological detection capabilities were validated through evaluating the particles in the patterned biochip based detection of avidin−biotin and in molecular MR imaging of neuroblastoma cells (Choi *et al.* 2006). In another interesting study, Xu and colleagues fabricated dumbbell-like iron oxide-gold NPs and coupled with Herceptin and a platin complex. The platin-gold-iron oxide-Herceptin complex as a target-specific nanocarrier was capable to deliver platin into Her2-positive breast cancer cells (Sk-Br3) with strong therapeutic effects (Xu *et al.* 2009). Moreover, literature has revealed that the oxidised maghemite form preferentially binds gold compared with the magnetite form and is more stable and biocompatible form of iron oxide (Lyon *et al.* 2004).

Iron oxide gold NPs have been used as a drug carrier to deliver chemotherapeutic agents into the tumour tissue. For example, Wagstaff and colleagues have synthesised cisplatin conjugated iron oxide gold NPs. To do this, Iron oxide core was synthesised by co-precipitation method following by gold reducing onto the surface. Cisplatin was conjugated to the NPs by a thiolated polyethylene glycol (PEG) linker. Characterisation of the particles was performed by scanning transmission electron microscopy, inductively coupled plasma mass spectrometry, dynamic light scattering, UV-Vis spectrophotometry, and electron probe microanalysis. They found that iron oxide NPs have low inherent cytotoxicity on ovarian cancer cell lines (A2780 and A2780/cp70) and cisplatin conjugated formulations are up to 110-fold more cytotoxic than the drug alone. This might be due to the differences in uptake mechanism as free drug internalises through cells` pores/ channels and particles are taken up by endocytosis, thus higher proliferation rate in cancerous cells resulted in greater cytotoxicity of conjugated cisplatin, in comparison with free cisplatin. Interestingly, they demonstrated that this nano-sized formulation could be accumulated in specific regions by using an external magnetic field, which showed cell growth inhibition area for the treated cells by novel formulation. This is mainly due to the higher accumulation of hybrid formulation in cells placed in magnetised area, which leads to higher internalisation and cytotoxicity of novel formulation compared to the cells treated without external magnetic field (Wagstaff *et al*. 2012).

Some studies have been focusing on the treatment of pancreatic cancer. Recently, Barnett *et al*. studied the attachment of 6-thioguanine (6-TG) onto iron oxide-gold HNPs (Barnett *et al.* 2013a). In this study, 6-TG was successfully conjugated onto the HNP surface and incubated with human pancreatic cancer cells (BxPC-3). A 10-fold decrease in half maximal inhibitory concentration (IC_{50}) and enhanced cellular uptake was reported with the 6-TG-conjugated HNPs in comparison with free drug. From the measurement of the SPR band of AuNPs, iron oxide-gold particles reportedly possessed SPR bands in the range of 535-750 nm depending on the core size and Au shell thickness. This band is characteristic of the optical properties of gold nano-structures, in contrast to the largely silent feature in the visible region for Fe_3O_4 particles. The observed SPR band showed a red shift in comparison with AuNPs. Interestingly, the core-shell NPs with a thicker Au shell displayed a smaller red shift than those with thinner Au shells. This finding is in fact consistent with theoretical calculation of the Fe_3O_4-Au core-shell morphology based on

Mie theory, suggesting that the optical properties are affected by the chemical nature of the oxide core (Wang *et al.* 2008).

Recently, Guo *et al.* investigated the Photothermal ablation of human pancreatic cancer cell line (PANC-1) with hybrid iron-oxide core gold-shell nanoparticles. They showed that GoldMag® (30 nm diameter, 50 μgmL^{-1}) nanoparticles were capable of cellular internalisation and temperature elevation after near infrared irradiation (7.9 Wcm^{-1}, 5 min). The temperature elevation achieved was as high as 79.51 ˚C which resulted in only 2.3 % cellular proliferation after 24 h compared with 47.0 % in the non-irradiated control (Guo *et al.* 2013).

Use of HNPs for thermo-responsive drug delivery is now a major focus. This technology benefits from magnetic properties reduced toxicities and the ability to target the drug release using focussed laser irradiation.

1.7. Bisnaphthalimide based anticancer agents

In order to find more efficient anticancer agents, using small molecules which have the affinity to bind to deoxyribonucleic acid (DNA) and demonstrating anticancer activities has been the focus of scientific interest recently (Gurova *et al.* 2009; Mohammadi *et al.* 2015; Wootton *et al.* 2015). Amongst these, bisnaphthalimide derivatives with photophysical properties have exhibited exciting potential as chemotherapeutic agents, which is due to their interactions with DNA by intercalation of the chromophore unit between the base pairs of the DNA double helix. Bisnaphthalimides consist of two chromophore units (naphthalimido rings), which are linked together through a linker chain. The linker should contain no less than one or two amine groups as amino group has been verified as a crucial part for cytotoxic activity (Figure 14A) (Brana *et al*. 1993). Many compounds with different substitutions in the chromophore and different length of the linker chain have been designed and synthesised (Brana *et al.* 1993).

DNA intercalators are held in place between the base pairs by van der Waal's interactions, thus creating a stable complex. As a result, the DNA becomes partially unwound and lengthens, which leads to the inhibition of DNA replication and transcription (Figure 14B). Bisnaphthalamide based drugs also inhibit topoisomerase II action (responsible for double

stranded breaks in DNA, catalyses DNA unwinding, and controls the processes required to untangle and unknot double stranded DNA), resulting in cell death. In addition, topoisomerase II has a key role in DNA replication and transcription, and also aids chromosomal organisation prior to mitosis (Banerjee *et al*. 2013; Barron *et al*. 2010).

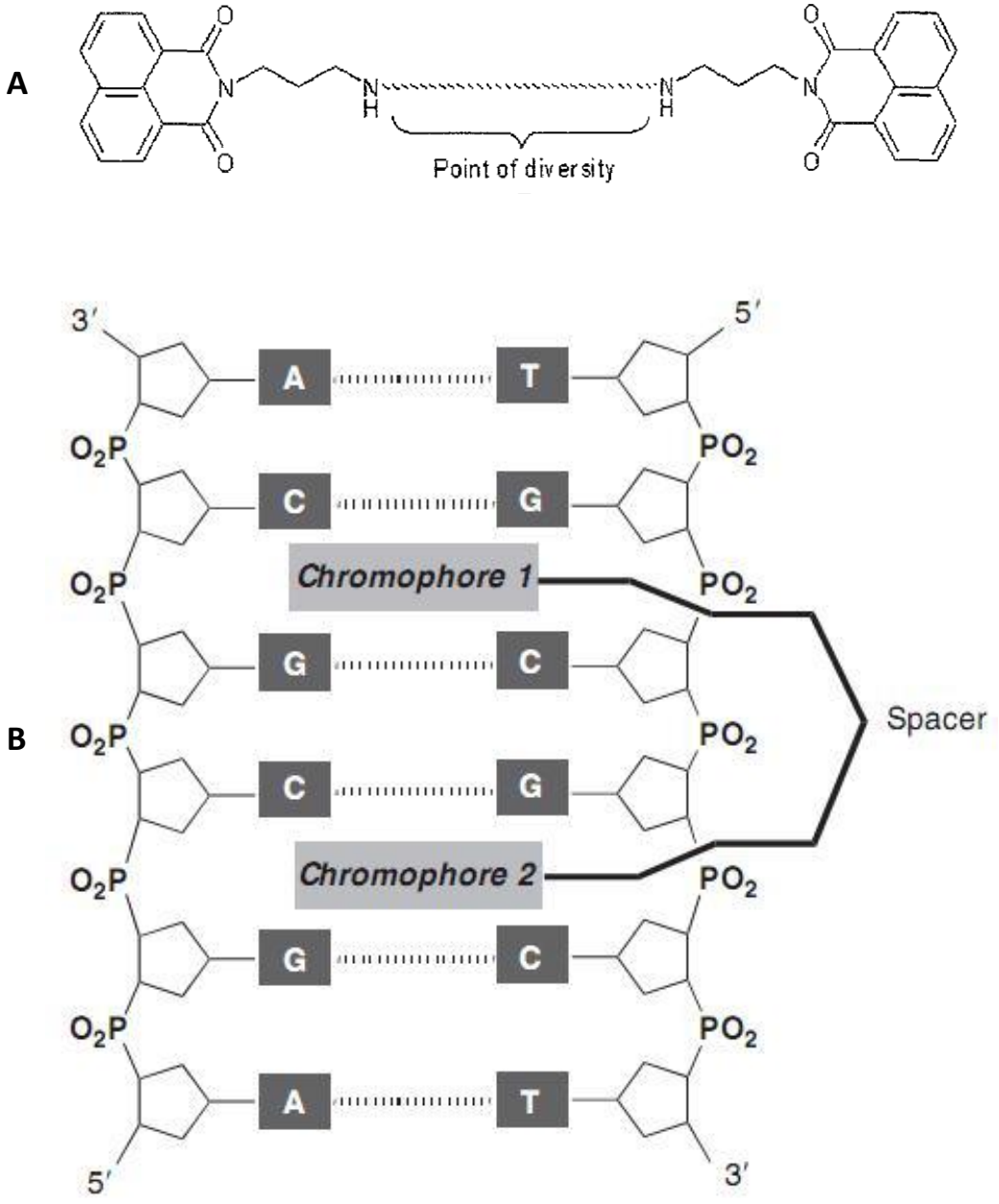

Figure 14. A) Basic bisnaphthalimide chemical structure and B) Schematic interaction between a bisnaphthalamide based drug and DNA (Karimi Goftar *et al*. 2014).

Brana and colleagues designed and synthesised a new symmetrical bis-intercalating series of bisnaphthalimides in the 1980s (Brana *et al*, 1980). These chemicals can be synthesised by nucleophilic reaction of 1,8-naphthalic anhydride with the corresponding alkyltetraamine. In contradiction of naphthalimides, bisnaphthalimides` structure increases DNA binding capacity, therefore, enhances their chemotherapeutic capability (Brana and Ramos, 2001).

Even though bisnaphthalimide series have considerable cytotoxicity, they have very limited solubility in aqueous solvents; thus, exploring alternative carrier to deliver them inside the tumour is essential (Brana *et al*. 1995). Poorly water-soluble anticancer agents normally have a tendency to distribute and accumulate in the peripheral tissues. Due to the nature of most chemotherapeutic agents, this will translate into significant systemic toxic effects. It was demonstrated that once an anticancer agent is conjugated with a nanocarrier, its biodistribution and pharmacokinetics will be dictated by the properties of the carriers rather than the drug molecules themselves (Chen *et al*. 2001). This gives researchers a new way to make poorly water-soluble anticancer drugs work better without the need to modify them.

1.8. Gemcitabine

Gemcitabine (2,2-difluorodeoxycytidine) as a novel nucleoside analogue, is an chemotherapeutic agent, which has been used for the treatment of many different type of tumour, such as pancreatic, ovarian, non-small-cell-lung, breast and bladder cancers. This cytotoxic agent can affect DNA replication in rapidly dividing cells, such as cancer cells. However, prior its action, gemcitabine must be activated by deoxycytidine kinase and other intracellular kinases. These enzymes can phosphorylate gemcitabine to produce gemcitabine diphosphate and triphosphate, which are the active forms of gemcitabine. Gemcitabine triphosphate incorporate into DNA throughout S-phase of cell cycle, which influences the termination of DNA synthesis and lead to single-strand breaks and finally cell apoptosis (Tiefenthaler *et al*. 2003; Veltkamp *et al*. 2008).

Patients with advanced or metastatic pancreatic cancer may be treated with gemcitabine as a first line treatment. However, it proves effective in 23.8 % of patients with the only

alternative being surgical removal of the localised tumour (Cunha *et al*. 2005). Moreover, it was demonstrated that elderly patients (with unresectable pancreatic cancer) were suffered from haematological and non-haematological adverse effects of gemcitabine (Takeuchi *et al*. 2004). In this thesis, all of the biological investigations will be compared with gemcitabine as a reference chemotherapeutic agent.

1.9. Aims

HNPs have interesting potential for theranostics; however, due to their relative age little literature is available. Hence this study exploited the use of the combined magnetic and optical properties in the thermoresponsive delivery of novel bisnaphthalamide based drugs in the treatment of pancreatic cancer. This was realised via nanoparticulate irradiation at lower temperatures which triggered drug release from the surface of the vehicle before cellular hyperthermia was initiated.

This research is based on the design, synthesis and characterisation of hybrid iron oxide-gold core-shell nanostructures, which possess strong magnetism and surface plasmon resonance (SPR) and consists of three parts: 1) synthesis and characterisation of HNPs, 2) drug loading (bisnaphthalimide based drugs) and characterisation of new formulations, and 3) biological investigations of novel formulations. Here, the drug loading is achieved via charge-charge interactions between the positively charged drug compound and negatively charged HNPs. It is postulated that these electrostatic interactions can be broken at high temperatures (Figure 15). Electrostatic bonds are weaker than covalent bonds. These bonds have bond energy (the energy required to break a bond) of only about 20 $kJmol^{-1}$, while covalent O-H bond has a bond energy of 460 $kJmol^{-1}$. By temperature increase, the vibration of electrostatic bonds results in breaking the interactions between differently charged molecules. The amount of energy required to break this interaction is supplied by laser irradiation (gold reacts as a nanoheater upon laser irradiation).

Statistical independent sample t.test (parametric test) was used throughout of the thesis to compare means of two independent groups within the Microsoft Excel software package.

This is the first time that drugs (bisnaphthalamide based drugs) conjugated to the surface of HNPs by charge-charge interactions, which possess thermoresponsive delivery potentials.

Moreover, this system is capable to be used in image guided heat triggered drug delivery in cancer diagnosis and therapy.

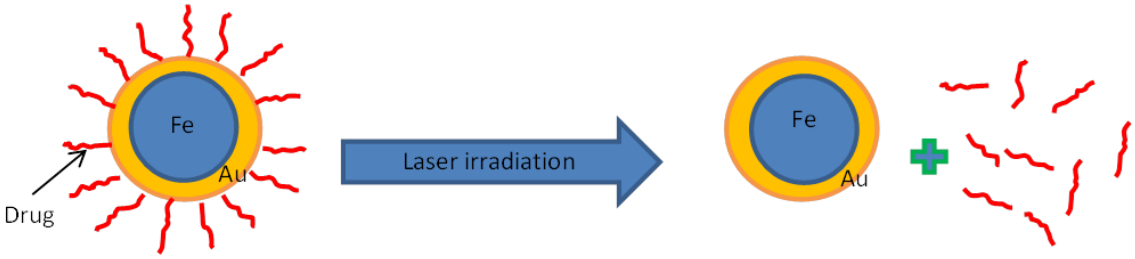

Figure 15. Schematic diagram of thermoresponsive drug delivery of HNP-Drug upon laser irradiation.

Chapter Two

Synthesis and characterisation of iron oxide-gold core-shell hybrid nanoparticles

2.1. Introduction

Iron oxide-gold hybrid nanoparticles (HNPs) have recently been the focus of a number of investigations and are becoming increasingly applicable in biomedicine (Hoskins *et al*. 2012b; Hoskins *et al*. 2012c; Seied Sajadi *et al.* 2014; Štarha *et al.* 2015). By using both iron oxide (Fe_3O_4) and gold (Au) within one drug delivery vehicle, a multifaceted and stable system can be fabricated (Barnett *et al*. 2013; Barnett *et al.* 2012). This exploits the surface chemistry and SPR of the gold coating whilst maintaining the magnetic character of the iron oxide core, offering imaging, heating and drug carrier potentials. Moreover, the presence of the gold shell surrounding the magnetic core makes it possible to functionalise the nanoparticles (NPs) with thiolated (-SH) molecules by exploiting the well described Au-S chemistry (Robinson *et al*. 2010a).

The binding energy of thiolates to the gold surfaces is experimentally determined by high-resolution x-ray photoelectron spectroscopy (Castner *et al.* 1996) and temperature-programmed desorption (Nuzzo *et al*, 1987) to be about 160 kJ/mol. X-ray absorption experiments (Roper *et al*. 2004) and early interpretation of photoelectron diffraction (Kondoh *et al*. 2003) suggested that the sulfur binds to the atop position of the Au surface.

While there are a number of strategies reported for the synthesis and fabrication of Fe_3O_4-Au NPs such as reverse micelle method and iterative seeding method (Carpenter *et al.* 1999; Cho *et al.* 2005; Lin *et al.* 2001; Lyon *et al.* 2004), they all highlight the importance of bottom-up synthesis and processing. One strategy involves sequential formation of the iron oxide core and Au shell, which was used for the synthesis of highly-monodisperse Fe_3O_4-Au NPs (Goon *et al.* 2009). This approach can produce iron oxide gold NPs in a core size range of 5-15 nm with a shell thickness range of 0.5-2.0 nm. Another strategy is thermally activated processing of iron oxide NPs and AuNPs as precursors in a mixed solution. This strategy expands the method of thermally-induced homo-interparticle coalescence of metal NPs (Schadt *et al.* 2006).

Goon and co-workers described the synthesis of Fe_3O_4-Au core-shell HNPs with an intermediate polymer, which separates the two entities (Goon *et al*. 2009). Incorporation of an organic intermediate layer between the Fe_3O_4 NPs and Au shell is proposed to avoid gold migration into the Fe_3O_4 core and enhance the saturation magnetisation and

relaxivity (Smolensky *et al*. 2011). Gold coating of the polymer coated Fe_3O_4 NPs can be fabricated by firstly attaching gold seeds (by electrostatic interactions between positively charged polymer and negatively charged gold NPs) to the nanoparticle surface, which is followed by subsequent reduction of Au onto the surface, in order to achieve a complete Au coat (Goon *et al*. 2009; Zhang *et al*. 2011). Moreover, this seeding technique is suitable method to achieve a higher degree of control over the Au shell thickness (around 10 nm). The shell thickness is an important factor as it affects the SPR of gold. Decreasing the thickness of the gold shell from 20 to 5 nm leads to SPR red shift (Goon *et al*. 2009; Zhang *et al*. 2011).

In another study, Barnett *et al*. synthesised Fe_3O_4-Au core-shell HNPs with the core diameter of 70 nm, using a polymer intermediate (PEI). These particles finally were PEGylated with PEG-thiol through dative covalent bonding between the thiol groups (-SH) on the polymer and the gold shell of the NPs. Particles were characterised by Fourier Transform infrared spectroscopy (FTIR) and transmission electron microscopy (TEM). The stability of HNPs was tested for six months and the size of particles, zeta potential, magnetic coercivity, T_2 relaxivity and nano-heating potentials were analysed to verify whether, any physical changes or degradation had happened since first measurement. The stability of particles was also tested in physiological conditions *in vitro* over a two week period. Therefore, HNPs were suspended in deionised water, placed inside the dialysis membrane and located into conical flasks containing 200 mL RPMI cell culture media (in sink condition). Media was pH adjusted to pH 7.2 and 4.5 to mimic blood and lysosomal physiological conditions, respectively. The hybrid formulation was subsequently analysed for Fe and Au content by inductively coupled plasma-optical emission spectroscopy (ICP-OES). The metal concentration in HNP formulation was calculated to be in a 3:1 ratio for Fe:Au (wt:wt). FTIR spectroscopy proved the presence of characteristic peaks attributed to the PEG coating. After six months, there were not any surface modification, morphology or diameter changes, confirmed by TEM, for the formulation. Zeta potential measurements also confirmed that the gold shell did not degrade or change during the stability test. Magnetic coercivity (Hc), determined by superconducting quantum interference device (SQUID) measurement, appeared to decrease after six months, showing that the magnetic properties of HNPs were modified over time. Physiological stability test showed an increase in Au content outside the dialysis chamber, which is indicative of particle degradation. No measureable degradation was observed for Fe, which is

reasonable, given, the rigid nature of the gold coating. The ΔT values (change in temperature) achieved upon laser irradiation appeared to be stable after six months, compared to the initial study (Barnett *et al*. 2013a).

This work describes the synthesis and characterisation of HNPs using the techniques Goon and colleagues reported for HNP assembly (Goon *et al*. 2009). This method is able to synthesis HNPs with the ability to engineer the coverage of gold on the magnetite particle surface, which utilises PEI for the dual functions of attaching gold nano-seeds onto magnetite particles as well as preventing the formation of large aggregates. Moreover, this seeding gives a higher degree of control over the Au shell thickness. Characterisation of the HNPs will be carried out using a number of analytical and microscopy techniques including, ICP-OES, UV/Visible spectroscopy, photon correlation spectroscopy, T_2 relaxivity measurement using magnetic resonance imaging, superconducting quantum interference analysis, x-ray diffraction analysis, laser irradiation and TEM. These methods are described below in relation to our work.

2.1.1. Inductively coupled plasma-optical emission spectroscopy

Inductively coupled plasma-optical emission spectroscopy (ICP/OES) is one of the most commonly used techniques in metal content analysis. The technique is related to the spontaneous emission of photons from ions and atoms that have been excited in a radio frequency discharge to identify, and quantify the elements present (Fassel and Kniesley, 1974). Solid samples need acid digestion or extraction before injection, therefore, the analytes will be presented in a solution but gas and liquid samples can be injected straight into the instrument (Mermet, 2005).

The ICP-OES is composed of two systems: the ICP and the optical spectrometer (Figure 16). Argon gas is mainly used to create the plasma which is directed by a torch consisting of three concentric tubes made of quartz. The sample solution is transformed to an aerosol and placed into the central channel of the plasma. The aerosol is rapidly vaporised at the centre of ICP due to the extremely high temperature (nearly 10000 K), where it is liberated as free atoms in the gaseous state. Required energy for promoting atoms to excited states is achieved by additional collisional excitation within the plasma

imparts. After excited state, atoms will relax to the ground state through the emission of a photon, which have specific energies. This energy can be identified via the quantised energy level structure for the atoms or ions. Therefore, the wavelength of the photons determines the elements from which they originated. Moreover, the concentration of the element in the sample can be calculated by the total number of photons (Hou and Jones, 2000).

By using ICP, the presence of gold and iron in our formulation can be confirmed; the concentration of them can be analysed and also the ratio of Fe:Au can be determined.

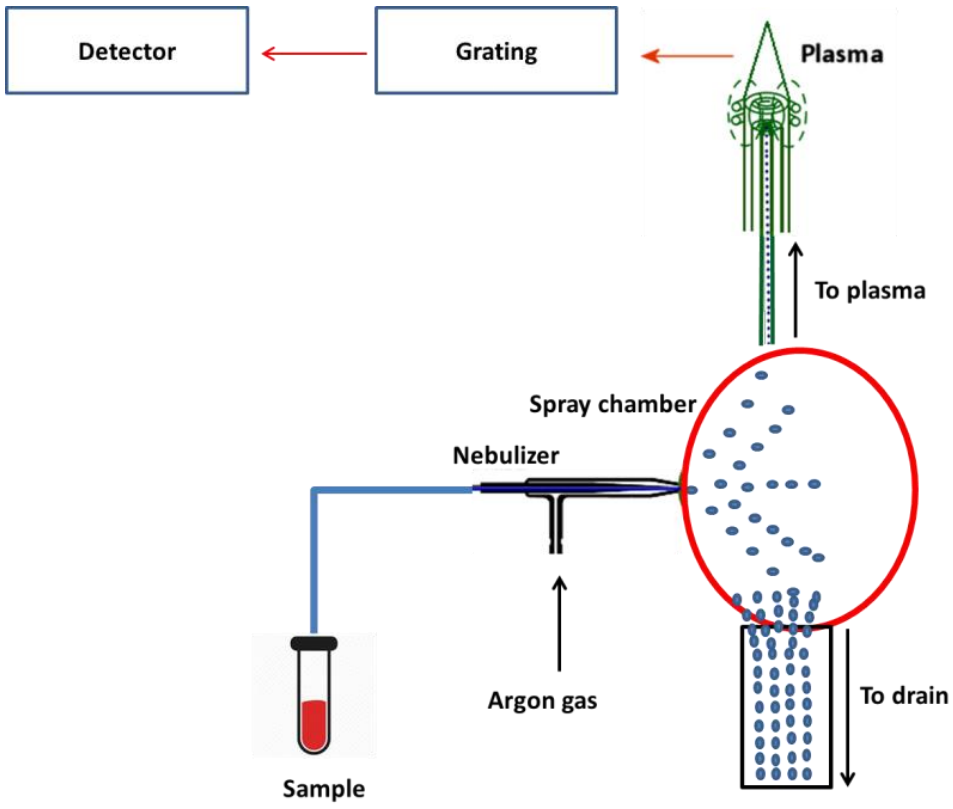

Figure 16. Schematic diagram of inductively coupled plasma-optical emission spectroscopy.

2.1.2. X-Ray Diffraction

X-ray diffraction (XRD) is a unique technique in determination of crystallinity of a compound and mainly applied to analyse solid substances in forensic science. In some cases, it is the only technique to achieve further differentiation of substances under laboratory environments. This method can analyse minute contact traces, smears, tiny sample areas, or small sample quantities, as well as large amounts of substances. XRD is generally worked by diffractometers, which is a piece of equipment to place samples and detector (Figure 17).

XRD method is based on constructive interference of a crystalline sample and monochromatic x-rays. The x-rays are produced via cathode ray tube and filtered to generate monochromatic radiation. The interaction of the incident rays with the sample results constructive interference when conditions obey Bragg's Law (Equation 1). This law correlates to the wavelength of electromagnetic radiation (λ) to the diffraction angle (θ) and the lattice spacing in a crystalline sample (d).

$$n\lambda = 2d \sin \theta \quad (1)$$

This distinctive x-ray diffraction pattern produced in a characteristic XRD analysis offers a unique "fingerprint" of the crystals in the sample, which allows recognising the crystalline form of sample by comparing with the standard reference patterns.

This technique allows us to compare the PXRD pattern of the fabricated Fe_3O_4 NPs with the reference sample of Fe_3O_4. Moreover, the purity of samples can be determined.

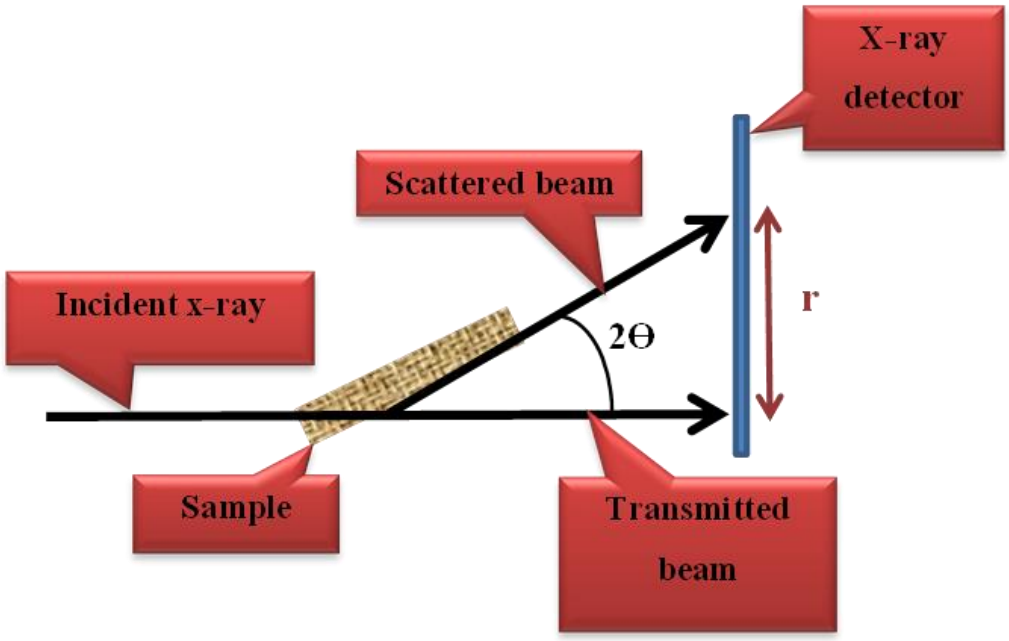

Figure 17. Schematic illustration of XRD technique.

2.1.3. UV/Visible spectroscopy

UV/Vis spectroscopy is routinely used in analytical chemistry for both qualitative and quantitative determination of different molecules (Deeney and Sinclair, 1997). Many analytes absorb light in the ultraviolet-visible spectral region, which causes objects to appear coloured. When light is adsorbed by a material, outer electrons are promoted from their ground states to excited states. This promotion of electrons to different energy levels leads to electromagnetic radiation in the visible part of the spectrum or in the ultraviolet region. The electrons are held strongly in single bonds, making them difficult to excite but the electrons involved in double and triple bonds are held less tightly and can be a lot more exited. This phenomenon can be used to produce well-defined absorption spectra (Deeney and Sinclair, 1997). UV/Vis spectrometer consists of a source of radiation of appropriate wavelengths, equipment for isolating light to a single wavelength and getting it to the sample (monochromator and optical geometry), a container for introducing the test sample into the light beam and finally a detector to measure the light intensity (Figure 18).

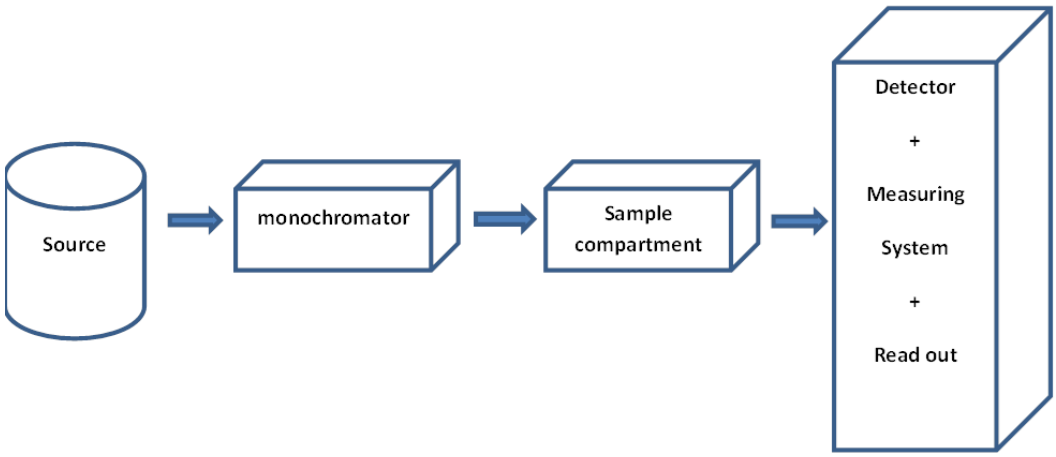

Figure 18. Schematic diagram of a UV/Vis spectrometer.

Each chemical has a unique spectral characteristic due to the location of the electrons with respect to the nucleus. In order to calculate the concentration of analytes a relationship must be created to achieve quantitative information. The fraction of light that passes through the sample (T) can be calculated by these equations:

$$T = I / I_0 \quad (2)$$

$$\% T = T \times 100 \quad (3)$$

I is the intensity of light, which passes through the sample solution and I_0 is the intensity of the light that passes through the solvent. Percent transmittance (% T) is the transmittance fraction multiplied by 100 (Equation 3). A more convenient quantity in analysing is the absorbance or the negative log of transmittance (Equation 4).

$$A = -\log T \quad (4)$$

The Beer-Lambert law explains that the absorbance of a solution is directly related to the concentration of the absorbing molecules in the solution (Equation 5) (Bouguer, 1729). Therefore, UV/Vis spectroscopy can be used to verify the concentration of the absorber in a solution. In this equation, ε is a molar absorptivity constant which based on both substance and wavelength, L is the length of the path travelled by light through the sample and c is the concentration. This linear equation between concentration and absorbance lets researchers to use spectroscopy for quantitative measurements of samples. A calibration

curve can be made by preparing standard solutions and the concentration of an unknown solution can be calculated by linear regression.

$$Abs = \log_{10} I / I_0 = \varepsilon L C \quad (5)$$

This test is useful for the determination of coating process in HNPs synthesis as each particle (naked iron oxide, seeded or coated particles) has a different UV spectrum. UV/ Vis spectroscopy also shows us the presence of gold and help us to measure the gold surface plasmon wavelength.

2.1.4. Photon correlation spectroscopy

Photon correlation spectroscopy (PCS) or dynamic light scattering (DLS) has been a useful light-scattering method for investigating the properties of solutions and suspensions of small particles, macromolecules and polymers (Berne, 2000). This technology is absolute, non-destructive and non-invasive. When small particles are exposed to the incoming light, the light will scatter in all directions. If the light supply is a laser (coherent and monochromatic), the scattering intensity randomly moves and vibrates over time. This oscillation is because of the fact that the small particles in solutions are experiencing Brownian motion, and thus the distance between the light scatters in the solution is continually fluctuating with time, leading to the development of a moving pattern. This random motion is modelled by the Stokes-Einstein equation. Below the equation is given in the form most often used for particle size analysis (Equation 6).

$$D_h = \frac{k_B T}{3\pi\eta D_t} \quad (6)$$

Where:

- D_h is the hydrodynamic diameter (particle size)
- D_t is the translational diffusion coefficient (found by dynamic light scattering)

- k_B is Boltzmann's constant
- T is thermodynamic temperature
- η is dynamic viscosity

This moving pattern is used to deduce particle size as the movement of smaller particles is faster than larger or heavier ones and scatter less light (Figure 19). The scattered light then undergoes destructive or constructive interference via the surrounding small particles, and within this intensity changing, data presents the time scale of movement of the scatters. The dynamic data of the particles is originated by an auto-correlation of the intensity trace recorded throughout the procedure.

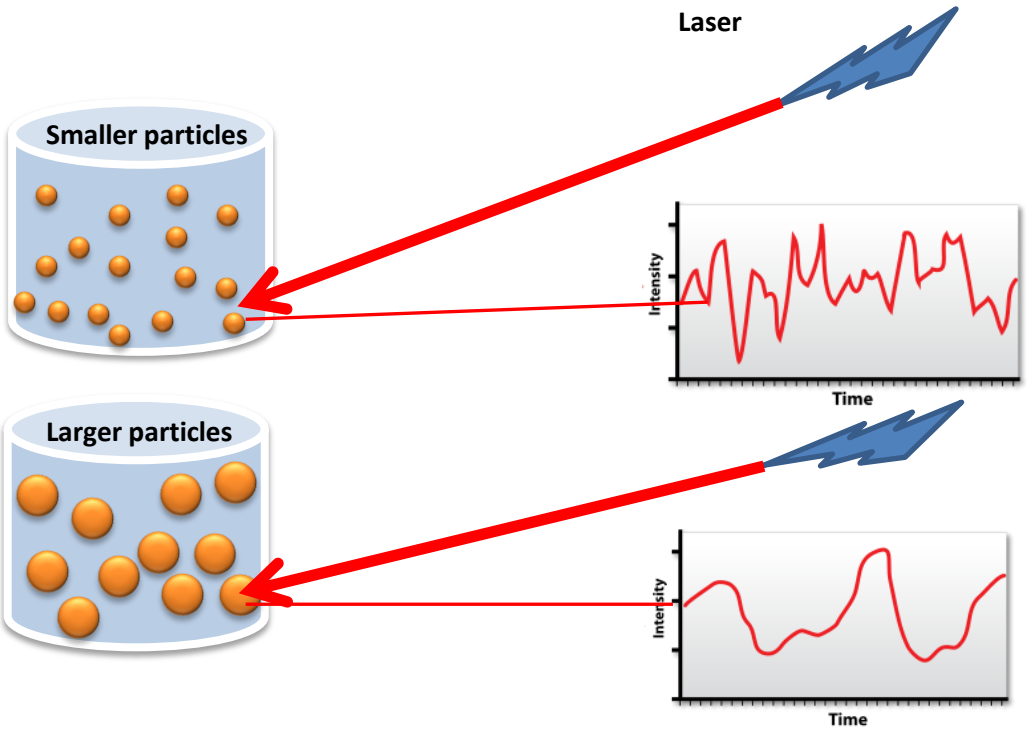

Figure 19. Schematic diagram of light scattering of two samples (small and large particles).

This technique is an indirect size measurement method as the measured quantity (the auto-correlation of fluctuations of the scattered light intensity) must undergo further mathematical processing to extract the quantity of interest (e.g. the particle size distribution or the diffusion coefficient distribution). Therefore, the actual size of the particles may differ from the one obtained by PCS (especially for aggregated NPs). Moreover, the size measurement gained is slightly larger than that of the actual sample particle size due to the

formation of a hydration layer surrounding the particles from the solvent (Sibilia, 1996). This method is very suitable for macromolecules as it can measure sample sizes from 3 nm to 3 µm (Sibilia, 1996).

PCS has been used to measure the size of different particles such as polymers, micelles, carbohydrates, proteins and other NPs. The mean effective diameter of the particles can be verified in monodisperse systems. This quantity depends on the size of surface structures, the particles` core size, the concentration of the particles, and the type of ions in the solution. PCS can also be equipped to determine the diffusion coefficient of the particles and the surface charge (zeta potential) of them in suspensions. PCS software usually shows the particle population (polydispersity index (PDI)) at different diameters. Therefore, in a mono-disperse system, software displays only one population (PDI = 0), but in a poly-disperse system, multiple particle populations are displayed (0 < PDI < 1). Moreover, PCS can be exploited for stability tests by periodical measurements of samples, which can determine aggregation and changing hydrodynamic radius of the particles over time.

Using PCS in our study can help us to determine the size of particles during the synthesis process, which can confirm the coating steps.

2.1.5. Transmission electron microscopy

The transmission electron microscope (TEM) is a very useful instrument that can be exploited to study the aggregation structure of a sample (Sibilia, 1996). TEM has been used to image nanomaterials, measuring of particle and/or grain size, size distribution, and morphology. The equipment passes a beam of electrons through a thin layer of sample resulting in interactions (Sibilia, 1996). These interactions produce a high resolution image of the aggregation architecture. Therefore, samples of less than 1 µm in size can be imaged by this technology (Sibilia, 1996). The quality of images depends on the contrast of the sample relative to the background. Samples are usually made by drying NPs on a copper grid, which is covered with a thin layer of carbon. Chemicals with high electron densities can be easily imaged compared with amorphous carbon. This involves most metals (e.g. aluminium, copper, gold and silver), metal oxides (e.g. 52uperpara oxide, silica,

titanium oxide), and other NPs such as carbon nanotubes, polymer NPs, quantum dots, and MNPs.

TEM help us to visualise our naked and coated particles and measure the size of the particles accurately as aggregation of particles cannot interfere the size measurement in this method.

2.1.6. Zeta potential measurement

Suspended NPs usually possess surface charge because of the chemistry at the particle surface. Counter ions can be attracted to the charged surface; thus, NPs will be surrounded by a cloud of counter ions. These counter ions are related to the particle close to the particle surface. As a result, this immobile layer of counter ions accumulates near to the surface of particle, which is termed the stern layer. Outside of this layer (toward to the centre of particles) the concentration of counter ions falls consistently, and because of the higher mobility of ions within this layer, it is usually called diffuse layer. Zeta potential defines the electrostatic potential between the stern and diffuse layer.

Zeta potential measurement is a standard technique to understand the stability of colloidal dispersions. The magnitude of the zeta potential shows the degree of electrostatic repulsion between adjacent, similarly charged particles in a formulation. For molecules and particles that are small enough, a high zeta potential will confer stability, i.e., the solution or dispersion will resist aggregation. When the potential is small, attractive forces may exceed this repulsion and the dispersion may break and flocculate. So, colloids with high zeta potential (negative or positive) are electrically stabilised, while colloids with low zeta potentials tend to coagulate or flocculate.

Zeta potential measurement can also be used to evaluate synthesis process. Low zeta potential demonstrates that the particles possess a weak surface charge; therefore, repulsive forces between particles in that suspension are weak. These particles will aggregate more, which leads to low stability. In contrast, high surface charge represents strong repulsive forces between particles, resulting less aggregation, and higher stability.

Zeta potential measurement can help us to determine the surface charge of the particles during the synthesis process, which can confirm the coating steps.

2.1.7. Magnetic resonance imaging and T_2 relaxivity measurement

Magnetic resonance imaging (MRI), as a non-invasive imaging technique, offers anatomical imaging system via measuring proton relaxation time of water and soft tissues (structure and function) in biological environments (Britton, 2010). MR images are obtained by manipulating the magnetic orientations of the hydrogen nuclei. Super paramagnetic materials possess a property called spin (rotation of the nucleus around its own axis), which can help the nucleus produces a magnetic field. This spin is returned to its resting state by two mechanisms, spin-lattice relaxation (T_1) and spin-spin relaxation (T_2). T_1 or longitudinal relaxation is returning of magnetisation in longitude and T_2 is returning of the transverse magnetisation. The enhanced transverse relaxivity (decreased T_2 signal) is detected as a darker area in an MRI scan (Figuerola *et al*. 2010). MR contrast agents are formulations injected intravenously in order to increase, or produce, differences in signal intensity between tissues in the MR image.

This technique allows us to compare the magnetic property of our fabricated iron oxide NPs with commercial superparamagnetic NPs, Feridex®.

2.1.8. Superconducting quantum interference

Superconducting quantum interference device (SQUID) sensors are highly sensitive devices to detect and localise superparamagnetic iron oxide NPs (SPIONs). They are sensitive detectors of time-varying magnetic fields. This time-varying magnetic field is produced by moving the sample relative to the pick-up coil of the sensor and an external field is utilised to retain the sample magnetisation. Relaxometry can detect NPs in a stationary sample and the time-varying magnetic field is generated via magnetising the NPs by a pulsed DC field following by removing the magnetic field, which allows the NP magnetisation to relax.

In this system, the SQUID sensors are switched on after a short delay before measuring the decaying field of the magnetised particles. This delay is needed to let transient fields, produced in conductive elements of the measuring system through the pulsed field, to decline appropriately, in order to organise process of the SQUIDs in their most sensitive range.

SQUID allows us to determine saturation magnetisation of our HNPs vs. applied field hysteresis loop.

2.1.9. Laser irradiation

When a laser is irradiated to a sample surface, the surface reflects a proportion of the energy, which highly depends on the material and the laser wavelength (Zhigilei *et al*. 2009). The adsorbed energy is transmitted from optical photons to electrons and subsequently to the lattice, resulting diffusion of the energy into the material (Liu, 2005). Extremely high energy pulses might result in photochemical reactions that detach atoms and molecules from the surface. The rest of the energy distributes into the material through heat transfer. These include the sequential excitation and relaxation of the metal electrons, its interaction with the lattice, i.e. the phonon-phonon thermalisation and the electron-phonon relaxation (Liu, 2005; Zhigilei *et al*. 2009). The heating effect can be applied for thermoresponsive drug delivery and photothermal ablation without affecting the surrounding healthy tissues.

By irradiating HNPs with a laser beam, the ability of particles to produce enough heat needed for drug release process can be examined.

2.1.10. Aims and objectives

The aim of this study is to synthesise hybrid iron oxide-gold core-shell NPs and characterise them in order to ensure the correct structures were fabricated. Chemical and physical characterisation will be carried out by ICP-OES, UV/Visible spectroscopy, photon correlation spectroscopy, zeta potential measurement, T_2 relaxivity measurement,

superconducting quantum interference analysis, x-ray diffraction analysis, laser irradiation and transmission electron microscopy. These techniques will be used to confirm the size, shape, surface charge, crystallinity, magnetic properties and the capability of HNPs to act as nano-heaters, ultimately indicating their use as drug carriers.

2.2. Materials and Methods

2.2.1. Materials used

Table 2. Materials used in synthesis and characterisation of HNPs.

Materials	Suppliers
Sodium hydroxide	Fisher Scientific Co., UK
Potassium nitrate	Sigma-Aldrich Co., UK
Iron sulphate	ACROS Organics Co., USA
Sulphuric acid	Sigma-Aldrich Co., UK
Poly(ethyleneimine) (PEI) (ave. Mw=2 kDa)	Sigma-Aldrich Co., UK
Poly(ethyleneimine) (PEI) (ave. Mw=750 kDa)	Sigma-Aldrich Co., UK
Chloroauric acid	Sigma-Aldrich Co., UK
Sodium borohydride	ACROS Organics Co., USA
Hydroxyl amine	Sigma-Aldrich Co., UK
Hydroxyl amine	Sigma-Aldrich Co., UK
Hydrochloric acid	Sigma-Aldrich Co., UK
Nitric Acid	Sigma-Aldrich Co., UK
Iron III standard	Sigma-Aldrich Co., UK
Iron oxide standard	Sigma-Aldrich Co., UK
Gold standard	Sigma-Aldrich Co., UK
Chloroform	Sigma-Aldrich Co., UK
Formvar	Agar Scientific Co., UK
Ethanol	Sigma-Aldrich Co., UK
Copper grid	Agar Scientific Co., UK

2.2.2. Methods

2.2.2.1. Synthesis of iron oxide nanoparticles

This work describes the synthesis and characterisation of HNPs using the techniques Goon and colleagues reported for HNP assembly (Goon *et al*. 2009). Iron oxide core was synthesised through co-precipitation method. Initially, 1.03 g sodium hydroxide and 1.82 g potassium nitrate were added to 180 mL deionised water and nitrogen was bubbled over at 90 °C for 1 h. The above solution was added to a mixture of iron sulphate (3.89 g) and sulphuric acid (20 mL, 0.01 M) and stirred at 90 °C under nitrogen gas for 24 h (Figure 20). The supernatant was removed after using a strong permanent magnet on the outside of a glass vial containing the iron oxide NPs to separate the magnetic material from the solvent. This magnetic fraction was washed 6 times and immediately re-suspended in 15 ml deionised water (the concentration of Fe was determined after gold coating step). Characterisation of iron oxide core was carried out within 1 week after synthesis of the particles.

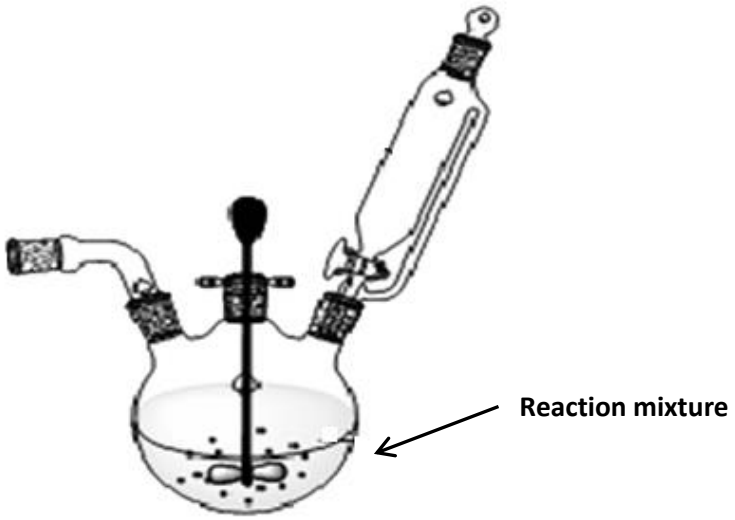

Figure 20. Schematic reaction on of synthesising iron oxide nanoparticles.

The concentration of the particles was determined using ICP-OES and zeta potential measurement was used to monitor their surface charge. The size of the particles was measured using photon correlation spectroscopy and transmission electron microscopy.

2.2.2.2. Polymer coating of iron oxide nanoparticles

Poly(ethylenimine) (PEI) was used to coat the surface of the iron oxide (Fe_3O_4) NPs (Figure 21) by electrostatic interaction between the negatively charged iron oxide and the cationic PEI. PEI used for the dual functions of attaching gold nano-seeds onto magnetite particles as well as preventing the formation of large aggregates. In this stage, 5 mL of Fe_3O_4 solution was added to a 50 mL solution of PEI in water (MW 750,000, 5 $mgmL^{-1}$) and sonicated using a probe sonicator (Soniprep 150 plus, MSE Co, MSS150.CX4.5) for 0.5 h. Particles were separated from the free PEI in solution using a high powered magnet and washed 6 times with deionised water. The final particles were re-suspended in 5 ml deionised water.

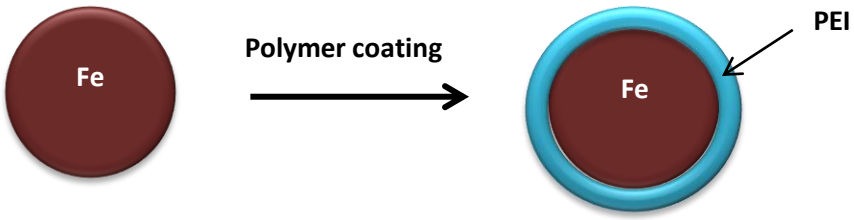

Figure 21. Schematic diagram of PEI coating on iron oxide nanoparticles.

The surface charge of the particles was monitored via zeta potential measurement. By this method, the presence of polymer around the iron oxide core can be confirmed since upon the PEI coating, the negative zeta potential of Fe_3O_4 core must shift from the negative value toward the positive charge due to the presence of PEI coating.

2.2.2.3. Gold seeding process

In order to fabricate gold seed NPs, chloroauric acid ($HAuCl_4$, 4 %, 375 µL) and sodium carbonate (Na_2CO_3, 500 µL, 0.2 M) were diluted to 100 mL of ice cold water. This solution was stirred for 10 min before the addition of sodium borohydride ($NaBH_4$, 0.5 $mgmL^{-1}$, 5 mL). At this time the solution turned a deep red colour and was stirred for another 10 min (Figure 22).

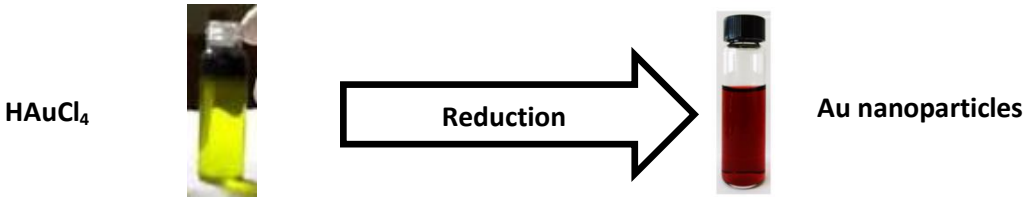

Figure 22. Colour changing of gold solution (5 mL) from yellow to deep red after reduction.

Gold seeding was achieved by electrostatic interaction of negatively charged gold NPs with cationic PEI coating (Figure 23). Fe_3O_4-PEI (2 mL) was added to the gold-seed solution (90 mL) previously prepared. The mixture was stirred at room temperature for 2 h. The magnetic particles were magnetically separated from solution and washed 6 times with deionised water. These particles stabilised by stirring in a solution of 1 $mgmL^{-1}$ PEI (MW 2000) for 10 min. Finally, the particles were washed extensively with deionised water and re-suspended in 5 mL deionised water.

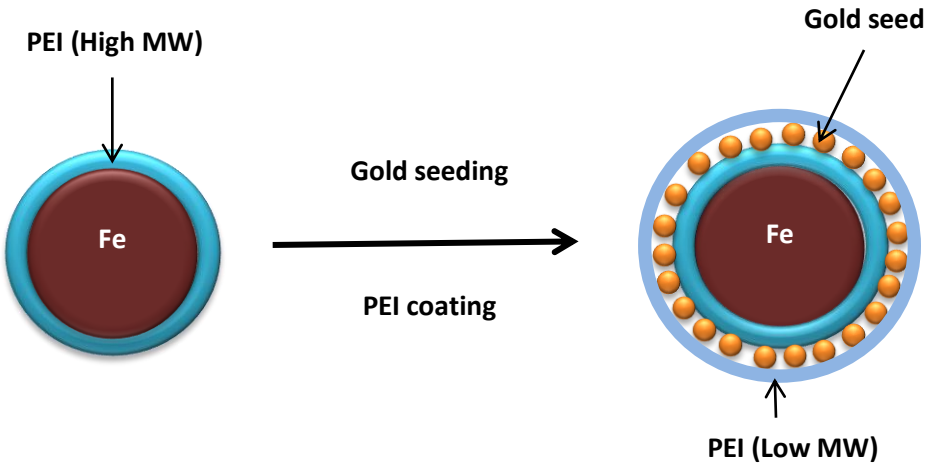

Figure 23. Schematic diagram of gold seeding process.

The gold seeding and PEI coating were monitored by zeta potential measurement in each step. This can show that whether the seeding and coating processes achieved as gold and PEI have negative and positive charge, respectively. These synthesis steps also monitored by UV/Vis spectroscopy as the presence of gold seeds in the formulation must change the Fe_3O_4-PEI spectrum due to the surface plasmon resonance of gold.

2.2.2.4. Gold coating process

In order to achieve a complete shell, gold was reduced onto the particle surface. To do this, particles were stirred with 110 mL sodium hydroxide (0.01 M) at 60 °C and 0.5 mL of 1 % $HAuCl_4$ was added followed by hydroxyl amine ($NH_2OH{\cdot}HCl$, 0.75 mL, 0.2 M). Two consecutive iterative reductions were carried out by addition of 1 % $HAuCl_4$ (0.5 mL) and 0.2 M $NH_2OH{\cdot}HCl$ (0.25 mL) with 10 min intervals. Final HNPs re-suspended in 5 ml of water after washing extensively and magnetically separating. Zeta potential and UV/Vis spectroscopy was recorded to investigate any changing in surface charge and UV/Vis spectrum upon the complete coating.

2.2.2.5. Characterisation of hybrid nanoparticles

2.2.2.5.1. Inductively coupled plasma-optical emission spectroscopy

Metal content of the HNPs was determined using inductively coupled plasma-optical emission spectroscopy (ICP-OES, Optima 7000V DV, PerkinElmer, Wokingham, UK). An acid digestion was carried out on the samples using a concentrated nitric acid: hydrochloric acid (1:1) solution with heating up to 100 °C (1:10 sample: acid). The samples were diluted (1:10) with deionised water prior to analysis. A calibration was run using iron and gold standard solutions 10-0.05 ppm (R^2 = 0.9999) (Barnett *et al*. 2013a). The concentration of HNPs used for all subsequent experiments indicates the concentration of Fe.

2.2.2.5.2. Powder x-ray diffraction (PXRD)

Iron oxide NPs in solution were sent for powder x-ray diffraction (PXRD) to the Lennard Jones Laboratories, Keele University. PXRD was carried out to verify the crystal structure of the fabricated Fe_3O_4 NPs (Hoskins *et al*. 2012b). PXRD patterns have been achieved by a Bruker D8 Advance x-ray diffractometer with these parameters (Norrish and Taylor, 1962):

1) A flat disc sample holder from 10˚ to 70˚ (2Θ)
2) Cu Kα radiation
3) A 0.04˚ (2 Θ) step size
4) A data collection time of 7s per step

The result compared to reference sample of Fe_3O_4.

2.2.2.5.3. UV/Visible spectroscopy

UV Peak absorbance of iron oxide NPs, gold seeds and HNPs in deionised water was measured using a Shimadzu UV-Vis spectrometer (UV-2600 UV–Vis (NIR) with an ISR-2600 Plus Integrated sphere, Shimadzu, Germany). Aqueous samples were analysed in quartz cuvettes, absorbance scans were carried out between 300-800 nm (Hoskins *et al*. 2012b). All measurements were run in triplicate at room temperature (25 °C) and recorded as average values.

2.2.2.5.4. Photon correlation spectroscopy and zeta potential measurement

Hydrodynamic diameters and zeta potential measurements were carried out using a photon correlation spectrometer (PCS, Zetasizer Nano-ZS, Malvern Instruments, UK). Samples were diluted in deionised water to make 1 $mgmL^{-1}$ of HNPs and sonicated for 30 s before

measuring the size and surface charge of the particles at 25 °C. 1 mL of samples was placed in screw-top glass vials and hydrodynamic radius, PDI and zeta potential of samples were measured during the synthesis process (Hoskins *et al*. 2012b).

2.2.2.5.5. TEM imaging

Transmission electron microscopy (TEM) was used to visualise the particles. Formvar®, known as polyvinyl formal appears to be the most widely used support film for TEM grids. In order to make Formvar® coated copper grids, commercially available copper grids (200 mesh, Agar Scientific Co, UK) were washed in chloroform in small beaker and transferred onto filter paper to dry. A glass slide was polished and wiped with lint-free cloth and then submerged (3/4 of height) 2 times in Formvar® solution (0.5 $mgmL^{-1}$). The slide was immediately removed from solution and air dried. The edges of the slide were scored with a sharp, ethanol-cleaned razor blade. The film was removed from the slide by floating it onto a water pool. The copper grids were laid (face down) on the film in the regions that are of the proper thickness and without wrinkles. Then the film with grids was picked up by covering them with a glass slide. The glass slide containing coated copper grids was air dried overnight. Samples were pipetted onto formvar coated copper grids (2 µL) and dried under a heat lamp for 4 h. The samples on the grids were directly imaged using a JEOL JEM-12 microscope with ANAlysis software (JEOL, Japan) (Barnett *et al*. 2013a).

2.2.2.5.6. Magnetic resonance relaxivity measurements

The HNPs were dispersed in agar as described below and sent to the University of Dundee for magnetic resonance imaging. Magnetic relaxivity of the HNPs was measured by a 1.5 T MRI scanner (Signa G=HDx, GE, USA) by means of GE's receive only HD 8-channel head coil. Feridex® (superparamagnetic NPs coated with dextran) and HNPs were dispersed in 2 % agar, with the concentration between 0.05 μgmL^{-1} and 50 μgmL^{-1}, and placed on plastic vials. Inversion Recovery Spin-Echo (IRSE) sequences has been applied,

in order to measure T_1 and T_2 relaxation times, respectively, on a single coronal slice intersecting the gel with NPs. The parameters for IRSE imaging were as described below:

1) Time repeating (TR) = 15s
2) Echo time (TE) = 9ms
3) Field of view (FOV) = 20 cm
4) Acquisition matrix = 128 × 128
5) Band width (BW) = 15.63 kHz
6) Slice thickness = 8 mm
7) Number of excitations (NEX) = 1
8) Inversion time (TI) = 100, 200, 400, 600, 800, 1000, 1200, 1400, 1600, 1800, 2000 and 2200 ms.

These parameters were applied as mentioned with 10, 20, 30, 50, 70, 100, 120, 150, 200, 250, 300, 350, 400, 450, 500, 550, 600, 650, 700, 750, 800, 850 and 900 ms. Areas of interest were chosen in each sample over the image set and then T*i*(*i*=1&2) values were determined by the 3-parameter non-linear least squares fit of the mean signal intensities vs. time (TI and TE respectively) data. The related relaxivities were calculated (r*i* in $Mm^{-1}S^{-1}$) through the gradient of the linear least squares fit of the relaxation rates (R*i*=1/T*i*) vs. concentration of Fe (mM) (Hoskins *et al*. 2012b).

2.2.2.5.7. Superconducting quantum interference device analysis

Iron oxide NPs were sent in solution to the University of Warwick for superconducting quantum interference device (SQUID) analysis as described below. Magnetic characterisation of NPs was performed by a Quantum Design MPMS-XL SQUID magnetometer. In this method, cooling (FCC) curves, field-cooled-warming (FCW) and zero-field-cooled warming (ZFCW) were determined in a field H = 8 kA/m, between 10 and 280 K. Magnetisation vs. applied field hysteresis loops were measured at 250 K in applied fields up to 4 MA/m. For the ZFC curves, the samples were first cooled to the basal temperature (10 K) without applied field. Next, a field was applied and the variation of magnetisation was measured by increasing the temperature up to T = 250 K (Barnett *et al*. 2013a).

2.2.2.5.8. Laser irradiation

HNPs were evenly suspended in a 2 % agar solution at concentrations of 50 μgmL^{-1} and 100 μgmL^{-1}. The dispersed HNPs in agar were allowed to cool to form gels in 35 mm diameter plastic petri dishes. Samples were stored in the fridge until analysis and allowed to equilibrate at room (25 °C) and human body temperature (37 °C) before irradiation. Samples were exposed to continuous wave laser beam (1000 V, 6 Hz) emitted by a solid state laser system (Ng:YAG pulsed 1064 nm).

Many of the reports to date have been carried out using a 532 nm green light source for laser irradiation of gold (Woods, 2010). However, light of this wavelength unfortunately does not pass through biological tissues. Instead it becomes adsorbed and this leads to heat discharge of NPs as well as the biological tissue rather than sole heating of NPs. The broad UV peak of HNPs (Figure 27) covers a large array of wavelengths in which laser irradiation would become adsorbed resulting in heating effects in the HNPs. It can be seen from the spectra that 532 nm does experience some absorbance which clarifies increasing of thermal energy described in the literature for gold nano-shells after irradiation (Figure 27) (Woods, 2010). It has been well documented that heating will occur at any point in the spectra where absorbance occurs due to the presence of gold (Curtis *et al*. 2015). Towards the red end of the spectra at 1064 nm it was detected that comparable absorbance to 532 nm occurs. Thus, it is assumed that laser irradiation at 1064 nm should cause localised heating of the HNPs without heating of biological tissues. Moreover, laser systems using 1064 nm pulsed sources are widely used both in the cosmetic industry for tattoo removal and hair removal and also in clinical settings for ophthalmic treatment (Tanaka *et al*. 2011). Thus, these systems are rather cheap, portable and penetrate biological tissues with no adverse effect. Other researches about heating of NPs via SPR utilisation have revealed that using pulsed laser irradiation is more efficient than continuous laser irradiation (Lukianova-Hleb, 2013).

In this study ultrafine thermocouples were used to monitor thermal change (inside and outside of the beam) in the gel (0.076 mm diameter, T-type, PFA coated, Omega, UK) coupled with a thermocouple logger (TC08 Pico Technology, UK). This transformed the voltage change to the real-time change in temperature. The gel samples were placed in the laser beam and irradiated by the beam for 60 s, which were timed by a stopwatch (Figure 24). A sample of 2 % agar (without NPs) was exploited to measure the temperature

change as a control sample. Changing temperature in the samples was calculated by Equation 7 and all statistical analyses were carried out using t.test analysis within the Microsoft Excel software package.

$$\Delta T = (T_{final} - T_{initial}) - T_{\Delta\, control} \quad (7)$$

Further studies incorporated HNPs into fresh raw chicken tissue which used to mimic that of human. The HNPs were dispersed using a fine needle into the tissue at a concentration of 100 μgmL^{-1}. This sample was exposed to the same laser beam as mentioned above, for 60 s at room temperature. Any thermal change resulting in tissue damage would be visually evident due to whitening of the tissue, as a result of cooking.

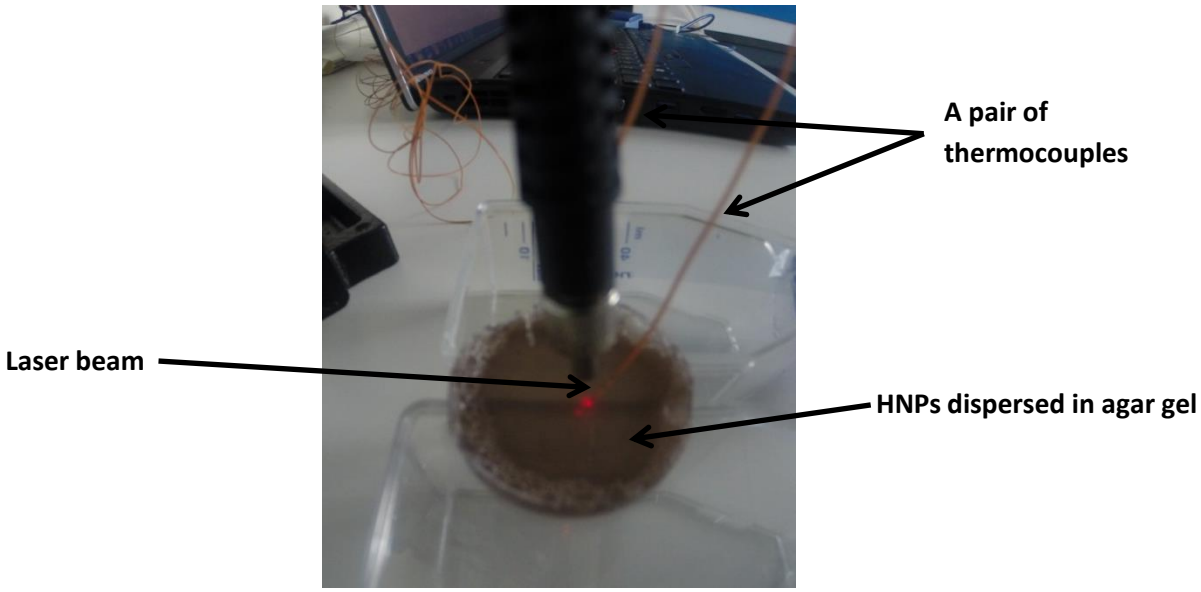

Figure 24. Laser irradiation of HNPs sample dispersed in agar gel.

Laser irradiation of HNPs in agar gel was previously used by Curtis *et al*. HNPs (500 μgmL^{-1}, 50 μgmL^{-1} 5 μgmL^{-1} and 0 μgmL^{-1}) were dispersed into a 2% agar phantom in 35 mm petri dishes and samples were irradiated by a laser beam at 1064 nm using a ML-LASER-YB5 Q-switched Nd:YAG Laser Treatment System. The gels were exposed to laser irradiation for 60 s and their cooling profile monitored by T-type thermocouples over 120 s. Temperature change was also measured using an thermal imaging Camera.

Data showed that HNPs experienced heating of up to 40°C with a total area of heat dissipation up to 132.73 mm^2 from the 1 mm diameter irradiation point after 60 s (Curtis *et al*. 2015).

2.3. Results

2.3.1. Photon correlation spectroscopy and zeta potential measurement

The Fe_3O_4 particles were successfully synthesised and coated with PEI and gold (the ratio of Fe:Au was 4:1) which has a percentage yield of 86 %. The fabrication of these structures was monitored closely through zeta potential measurement. The Fe_3O_4 possessed a negative surface charge of - 24.9 mV due to the surface sulphate associations from the synthetic procedure (Hoskins *et al*. 2012a) (Table 3). Subsequently the zeta potential shifted to + 47.5 mV after coating of the Fe_3O_4 core with PEI. This increase is due to the presence of the positively charged primary amine groups in the PEI backbone; hence indicating that coating was successful. The Fe_3O_4-PEI-Au_{seed} and Fe_3O_4-PEI-Au_{coat} NPs represented a decrease in surface charge, which is due to the negatively charged gold atoms (+ 33.9 mV and - 4.3 mV, respectively). The hydrodynamic radius of Fe_3O_4 core, Fe_3O_4-PEI and HNPs (1 $mgmL^{-1}$) was 1100 nm, 300 nm and 891 nm, respectively (Table 3). A large diameter was obtained due to the inherent magnetic properties of the iron oxide cores. However, Fe_3O_4-PEI had the smallest particle size in this group which could be due to the polymer coating that decreased the aggregation of the particles. After gold coating the apparent size increased probably due to the tendency of gold nanoparticles which are unfunctionalised to aggregate in solution.

PDI index of particles showed that they possess homogeneous distribution within the formulation as PDI of Fe_3O_4, Fe_3O_4-PEI and HNPs was less than 0.3. PDI of Fe_3O_4-PEI-Au_{seed} was around 0.394, which could be due to the presence of small fraction of free gold seeds in formulation (Table 3).

Table 3. Photon correlation spectroscopy showing hydrodynamic radius, polydispersity index and zeta potential of particles measured at 1 mgmL^{-1} in deionised water (n=3, ave ± SD).

Particle	Hydrodynamic Radius nm ± SD	Polydispersity Index ± SD	Zeta Potential mV ± SD
Fe_3O_4	1100±24.21	0.22±0.06	− 24.92±1.88
Fe_3O_4-PEI	300±11.75	0.27±0.03	+ 47.56±3.72
Fe_3O_4-PEI-Au_{seed}	433±8.83	0.39±0.06	+ 33.94±4.48
Fe_3O_4-PEI-Au_{coat} (HNP)	891±35.81	0.24±0.11	− 4.34±0.03

2.3.2. TEM imaging

TEM imaging represented a precise view of the Fe_3O_4 shape and size, which was approximately 30 nm (n = 20, SD = ± 4.23) (Figure 25A). Gold NPs (2 nm) (Figure 25B) were fabricated and seeded on to the surface of Fe_3O_4 NPs by charge-charge interactions, which changed the shape of particles to a unique 'bobbly' surface (Figure 25C). The TEM images of the fully coated HNPs displayed a small increase in particle size to around 40 nm (n = 20, SD = ± 6.61) (Figure 25D).

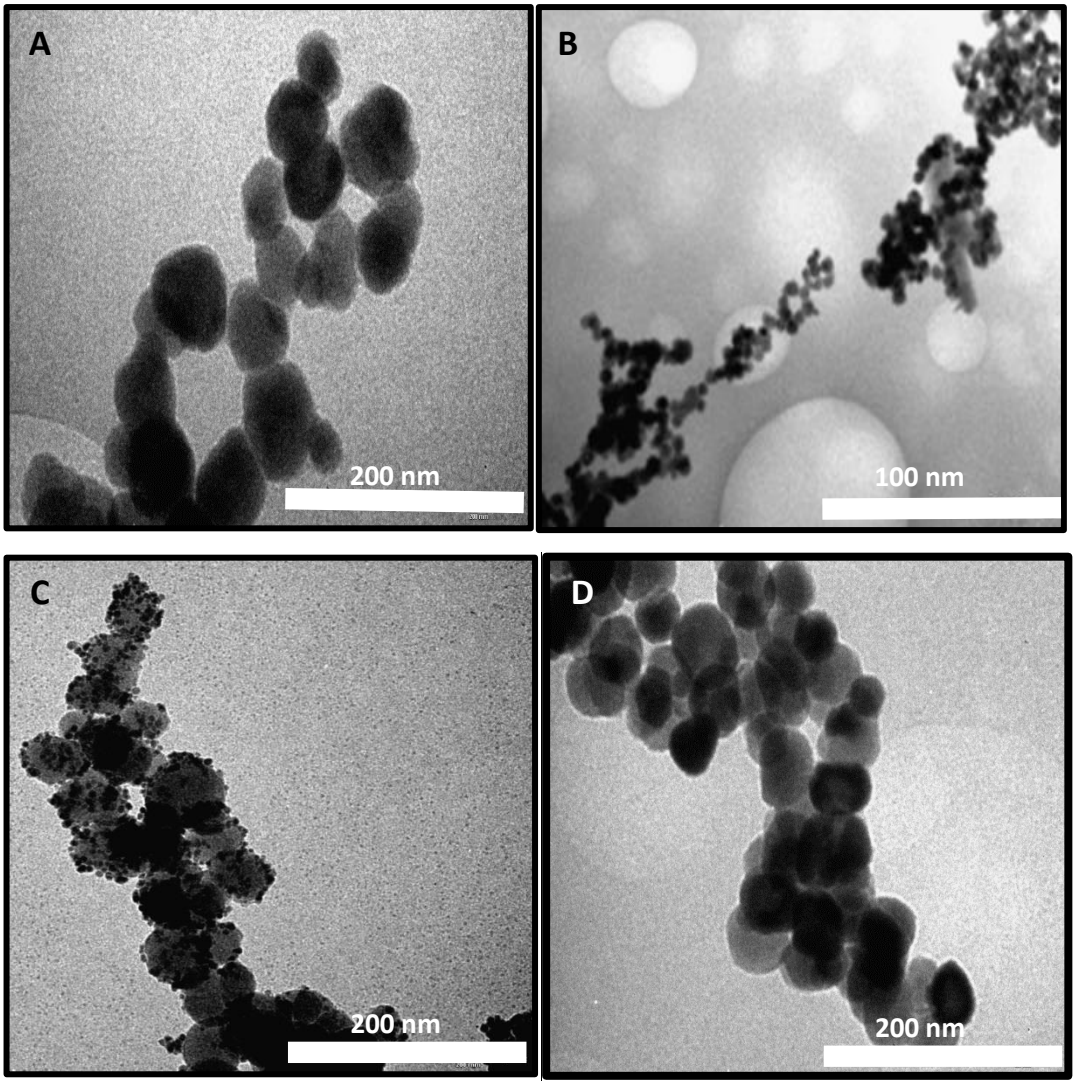

Figure 25. Size and shape estimations of NPs analysed by TEM: A) Fe_3O_4 nanoparticles, B) Gold nano-seeds, C) Fe_3O_4-Au_{seed} and D) HNPs.

2.3.3. Inductively coupled plasma-optical emission spectroscopy

ICP was used to deduce the concentration based on the total iron and gold content of the NPs. The concentration of iron and gold in formulation (calculate from the standard curves (Appendix, Figure 1)) were 2.65 ± 0.15 $mgmL^{-1}$ (R^2 = 0.999) and 0.68 ± 0.004 $mgmL^{-1}$ (R^2 = 0.998), respectively (calculated from the standard calibration equation). The ratio of Fe:Au in formulation was approximately 4 : 1. This ratio was in line with other studies of HNPs for biological applications (Barnett *et al*. 2013a; Hoskins *et al*. 2012b). ICP analysis

for Fe and Au was run 6 times for three different batches of HNPs showing that the standard deviations and means are reliable and the synthesis protocol is reproducible.

2.3.4. Powder x-ray diffraction analysis

Both synthesised Fe_3O_4 NPs and reference sample of Fe_3O_4 (Sigma-Aldrich Co., UK) were analysed by PXRD test. PXRD pattern of fabricated Fe_3O_4 NPs was compared with the reference sample of Fe_3O_4 (Figure 26). The diffraction peaks of synthesised sample (Figure 26A) are closely matched with the reference sample (Figure 26B), showing that our particles have a cubic crystal system (Itoh *et al*. 2003). Moreover, no specific peaks of impurities were detected. The small extra peaks observed in fabricated iron oxide sample are associated with signal/noise ratio.

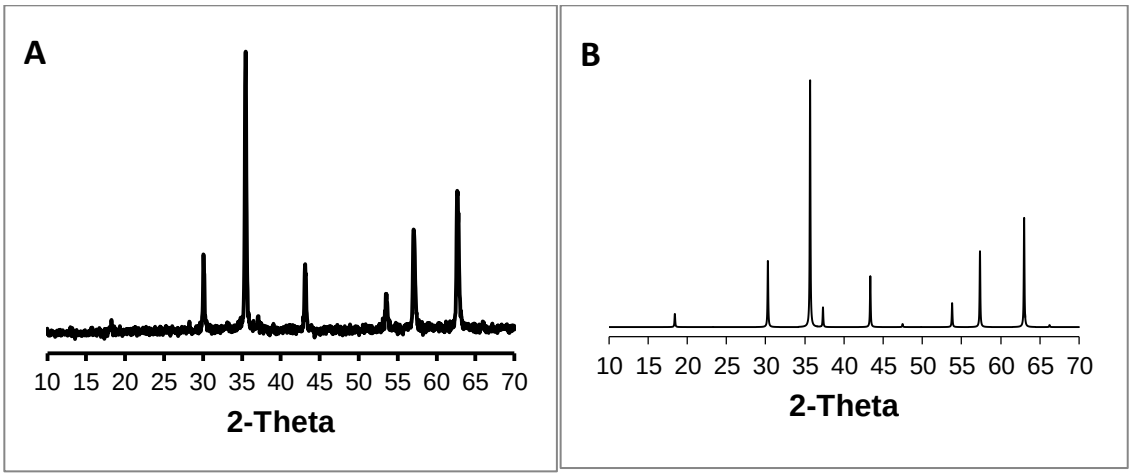

Figure 26. Powder x-ray diffraction of A) Fabricated Fe_3O_4 NPs compared to B) reference sample of Fe_3O_4.

2.3.5. UV/Visible spectroscopy

Colloidal gold NPs can absorb light and transform it into localised heat (photo-thermal therapy). UV-visible spectroscopy was used to obtain absorption spectra of the particles (Figure 27) in order to determine the wavelength at which the maximum absorbance

occurred (λ_{max}). λ_{max} value is used as an indication of the wavelength at which the SPR effect will be optimal. The scan of PEI-coated iron oxide cores showed featureless spectra, which indicated that no SPR occurred. This was expected since the particles did not consist of any gold. The gold seed solution possessed a λ_{max} of 480 nm, which was red shifted after seeding to the Fe_3O_4-PEI surface to 520 nm. After reducing gold onto the surface of particles (completing the coating process) a shift to 610 nm was achieved; this indicates that the gold coating was successful. However, this peak was rather broad, which might be due to the interaction between solute and solvent or gold shell and PEI polymer. The shift is mainly due to differences of size between gold nano-seed (2 nm) and HNPs (40 nm) as increasing the size of solid gold nanospheres shifts their absorption spectrum toward more penetrating red light (Hainfeld *et al*. 2014).

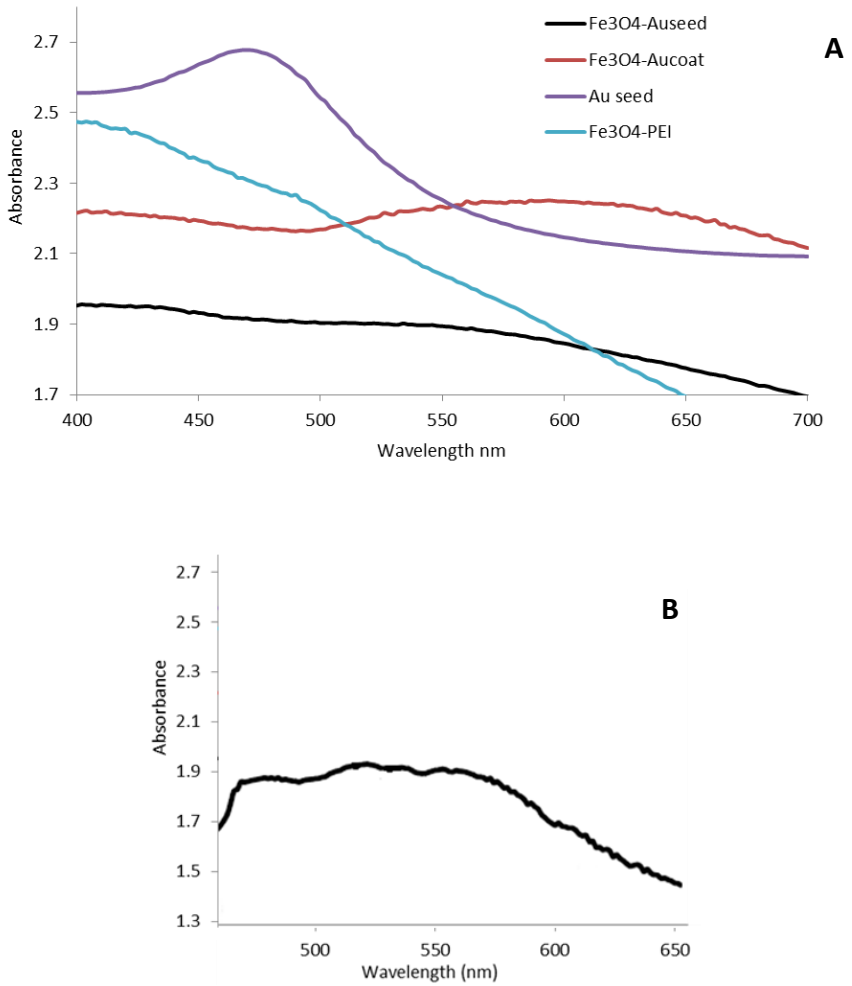

Figure 27. UV–Vis absorbance spectra of A) Fe_3O_4-PEI, Au seeds, Fe_3O_4-PEI-Au_{seeds} and Fe_3O_4-PEI-Au_{coat} (HNPs) and B) Second derivative peak of Fe_3O_4-PEI-Au_{seeds}.

2.3.6. T_2 MR relaxivity measurment of HNPs

Transverse relaxation (T_2) of HNPs and Feridex® as a function of concentration of Fe in mM were obtained (Figure 28). The transverse relaxivities (r_2) was measured with the gradient of the straight lines fitted to those data.

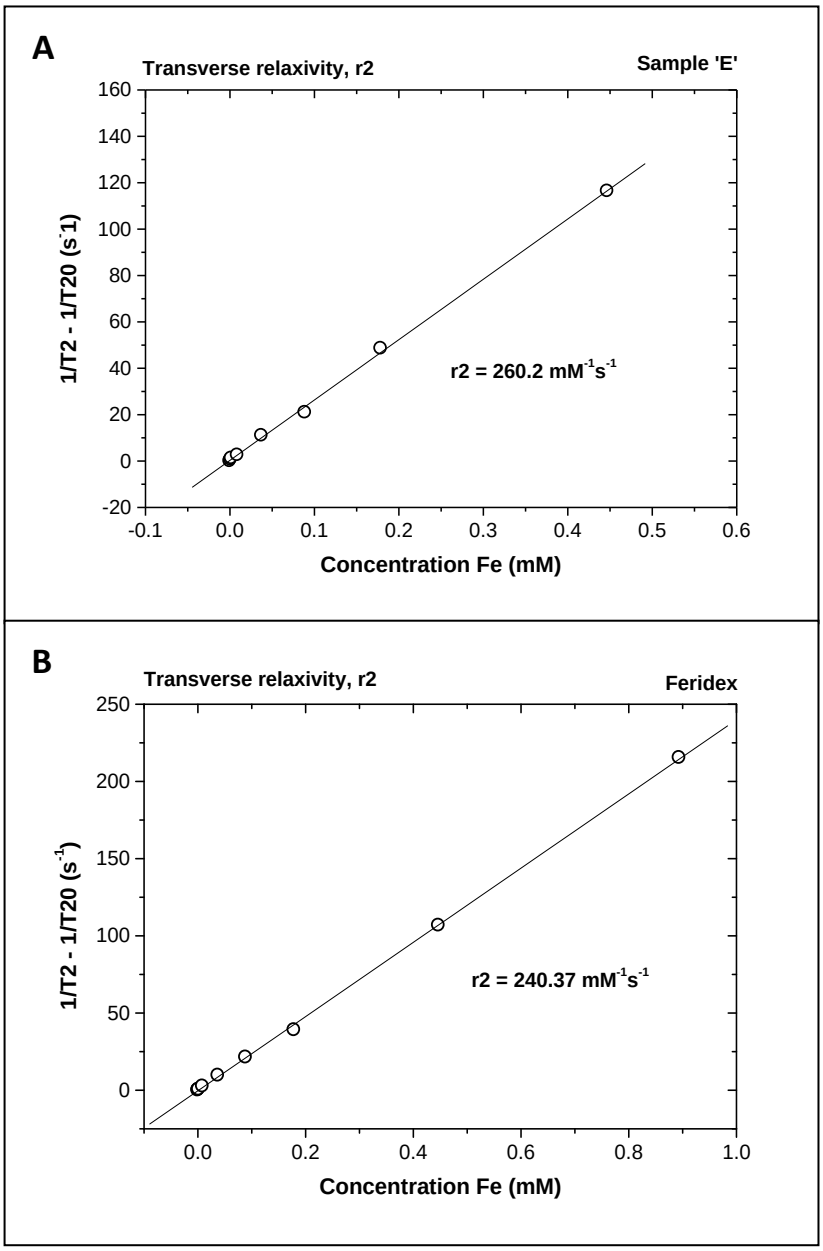

Figure 28. Transverse relaxation (T_2) rate of A) HNPs and B) Feridex® as a function of concentration of Fe. The dotted line represents the linear fit to the experimental data.

For both samples, the relaxation rates ($1/T_i$) with the highest concentration of iron (1.79 mM) had to be omitted due to the large deviation from the linear fit to the rest of the data, which could be because of the agglomeration of highly concentrated and/or the larger error presented in the calculation of the T_2 for that specific sample attributed to the very low signal-to-noise ratio of the MR images achieved at longer TE.

The transverse relaxivity of Fe_3O_4 NPs was 260.20 $mM^{-1} s^{-1}$ (Figure 28A), which was slightly higher than the relaxivity of previously clinically used Feridex® (240.37 $mM^{-1} s^{-1}$) ($p > 0.05$) (Figure 28B).

2.3.7. Magnetic characterisation of hybrid nanoparticles

The saturation magnetisation vs. applied field hysteresis loop (Figure 29A) of the HNPs was collected at 250 K. The saturation magnetisation and magnetic coercivity parameters at T = 250 K are indicative that the Fe_3O_4 core of the HNPs was highly crystalline and magnetically ordered at room temperature. The zero field cooled / field cooled curve (Figure 29B) indicates features characteristic of ferromagnetic NP. The absence of a maximum in this data shows that the ordering temperature is above room temperature.

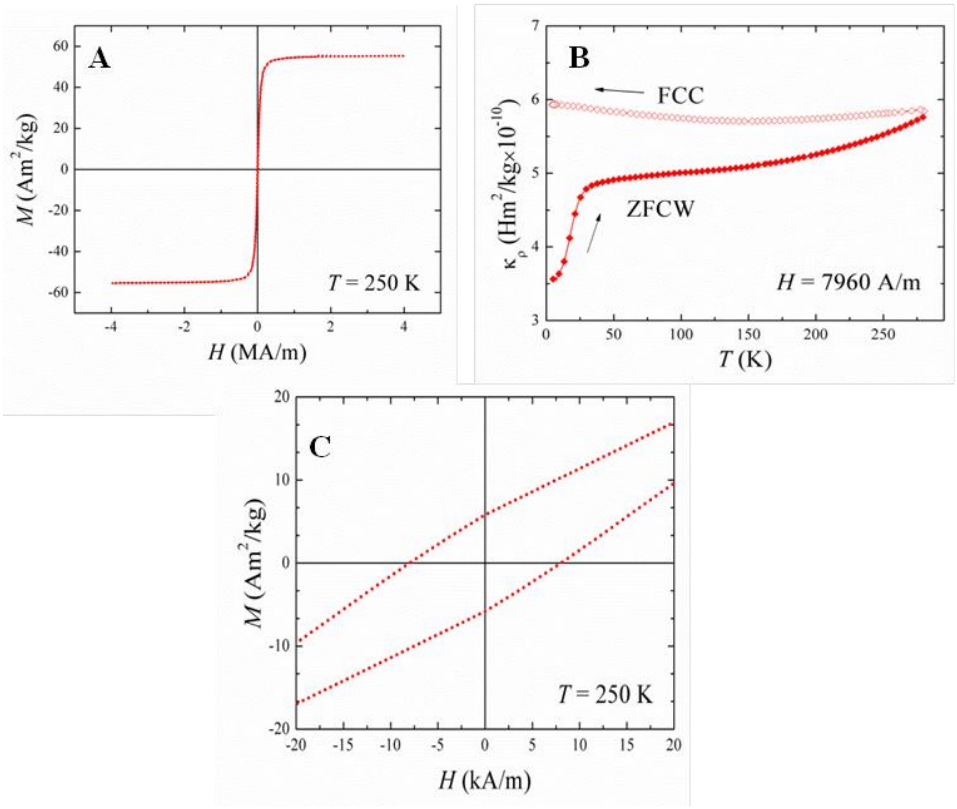

Figure 29. Magnetisation data of HNPs: A) M(T) curves determined in zero-field cooled warming (AFCW) and field-cooling mode, B) M(H) curves collected at 250 K between - 4 and 4 MA/m and C) M(H) curves measured at 250 K.

2.3.8. Laser irradiation

Incorporation of the unique properties of HNPs into thermally responsive carrier has great potential for future biomedical applications (thermoresponsive drug delivery). In this kind of treatment the surrounding normal tissues would not experience temperature increase, which may lead to unwanted damage (Zijlstra and Orrit, 2011). This is because the laser beam only focuses on the treated area and the temperature will not increase outside the laser beam (confirmed in our results below). To explore the potential of the HNPs as nano-heaters, HNPs (50 μgmL^{-1} and 100 μgmL^{-1}) were dispersed in agar gel and irradiated with continuous wave laser (Ng:YAG pulsed 1064 nm, 1000 V, 6 Hz) for 60 s.

The agar phantom was utilised to mimic physiological tissue. HNPs showed a time and concentration dependent heating effect and a localised heating of the sample was observed in the region exposed to laser radiation via thermocouple measurement (Figure 30). The first thermocouple was fixed at the centre of the gel (inside the laser focal point) and the second thermocouple was placed on the edge of the phantom sample, 14 mm away from the laser focal point.

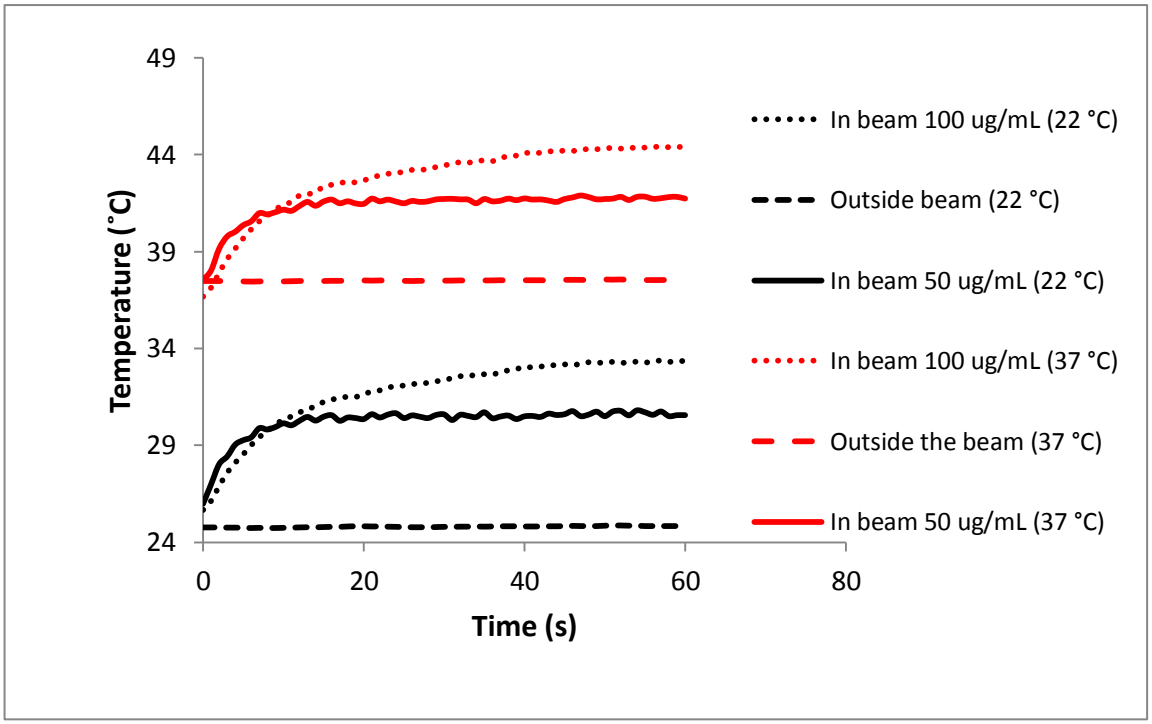

Figure 30. Diagram showing the heating effect of HNPs dispersed in 2 % agar gel upon laser irradiation in room and body temperature. All statistical analyses were carried out using t.test analysis within the Microsoft Excel software package.

After laser irradiation for 60 s, changing temperature in agar gel without HNPs as a reference sample and outside of the laser focal point (for samples containing HNPs) were negligible, showing that heating only took place for HNPs in the region exposed to the laser radiation.

Data demonstrated the change in temperature (ΔT) of the agar gels containing the HNPs (50 μgmL^{-1} and 100 μgmL^{-1}) at 22 °C and 37 °C. ΔT was calculated by any temperature change during laser irradiation, compared with the control sample (Equation 6).

At concentrations of 50 μgmL^{-1} at room temperature, ΔT was 5.57 °C ± 1.43 after 60 s laser irradiation, which was significantly higher than the temperature increase achieved outside the beam ($p < 0.05$) (Figure 30). A small time dependant increase in temperature was recorded upon longer laser exposure, which was insignificant ($p > 0.05$). At 100 μgmL^{-1}, ΔT significantly increased ($p < 0.05$) after 60 s (ΔT was 7.70 °C ± 0.80), comparing with the temperature changes outside the beam. Negatively skewed distribution of temperature increase was achieved for both concentrations (Appendix, Figure 2). The experiment was repeated at 37 °C and around the same ΔT was achieved for samples at this temperature ($p < 0.05$) (Figure 30).

In order to see visual heating effect of HNPs, 100 μgmL^{-1} of HNPs was injected into a raw chicken breast *in vitro* and exposed to the laser irradiation for 60 s, at room temperature (Figure 31). A control sample of raw chicken breast (without HNPs) was irradiated and imaged before and after irradiation (Figures 31A and 31B). After laser irradiation, the control sample did not change in case of colour and no heating effect was observed, confirming our previous studies on agar gel discussed before. However, the colour of the samples containing nano-formulation did change subtly as a result of temperature increase caused by HNPs (although it is not distinctive in the image) (Figures 31C and 31D).

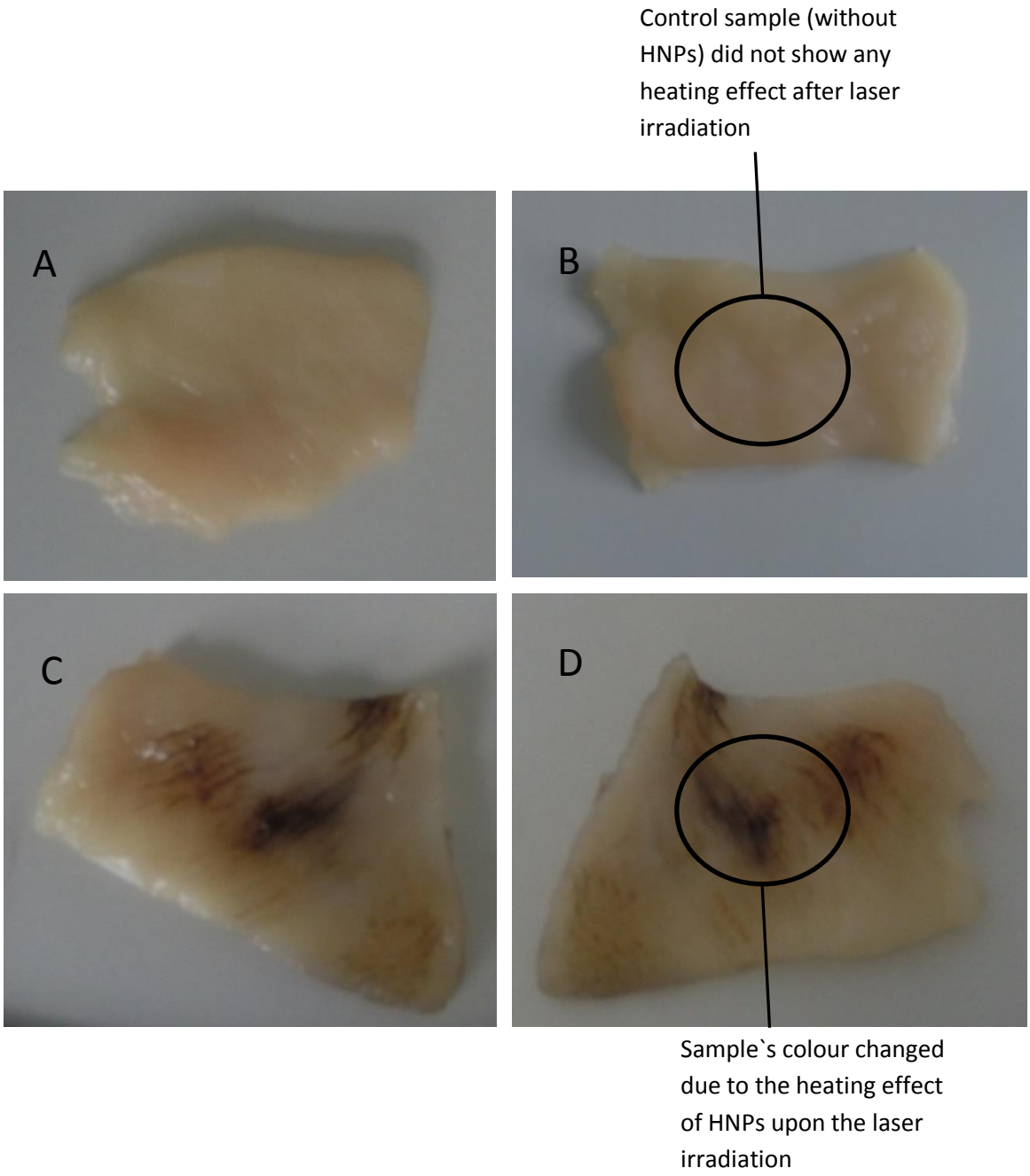

Figure 31. *In vitro* laser irradition of raw chicken breast: A) Control sample before irradiation, B) Control sample after irradiation, C) Sample containing HNPs before laser irradiation and D) Sample containing HNPs after laser irradition.

2.4. Discussion

Hybrid iron oxide-gold NPs were successfully synthesised. The formation of Fe_3O_4 core and/or the hybrid structure were characterised by T_2 MR relaxivity measurement, powder x-ray diffraction analysis, magnetic characterisation, ICP-OES, UV/Visible spectroscopy, PCS and TEM microscopy.

Both Powder x-ray diffraction analysis and magnetic characterisation confirmed that typical crystalline structure of Fe_3O_4 was achieved (by comparing with the control sample) (Figures 26 and 29). In general, UV/Vis spectroscopy and zeta potential measurement indicated that fully coated HNPs were synthesised (Figure 27 and Table 3, respectively). Naked iron oxide core was successfully coated with poly(ethylenimine) as an intermediate layer, which was proved by zeta potential measurements (Table 3). Changing the zeta potential from negative charge for iron oxide to positive value after coating with PEI is a suitable indication that polymer coating process was successful. Gold seeding was attained with 2 nm gold NPs and complete gold shell was achieved by consecutive gold reduction onto the surface of NPs. The gold shell thickness was around 10 nm, which can be increased or decreased to study the optimal physical properties for different purposes (Huang *et al*. 2011a; Pissuwan *et al*. 2006; Zijlstra and Orrit, 2011). Each stage in the synthesis process was examined with UV/Visible spectroscopy (Figure 27), TEM (Figure 25), and zeta potential measurement (Table 3).

Fe_3O_4-PEI-Au_{seed} particles had a lower positive zeta potential compared to Fe_3O_4-PEI and zeta potential shifted to negative range upon the complete gold coating. These shifts toward the negative value is due to the presence of gold, which possess negative charge, and can confirm that gold seeding and gold coating have been achieved during the synthesis process (Table 3). UV/Visible spectroscopy was carried out in order to identify the presence of colloidal gold in these constructs. The $\lambda_{max,}$ measured via UV/Visible spectroscopy, red shifted from 480 nm (gold NPs λ_{max}) to 520 nm and 610 nm, after gold seeding and gold coating, respectively (Figure 27). This result again indicates that complete coating was achieved. Earlier investigations on gold nano-shells have described that the λ_{max} can be red shifted toward the infrared region (800-1200 nm) (Pissuwan *et al*. 2006). However, fabricated HNPs in this study did not show such large shift. The spectrum achieved was very broad and covered from 500-700 nm. This wide absorbance peak, without high shifting toward the infrared region could be because of the

synthesis method, the presence of PEI polymer layer between the gold shell and iron oxide core and the size variations of shell thickness and/or final particles diameter. However, the UV/Visible spectrum of HNPs was in line with other studies (λ_{max} between 500-600 nm) (Curtis *et al*. 2015; Goon *et al*. 2009; Smolensky *et al*. 2011; Wang *et al*. 2005a; Wang *et al*. 2005b).

The inherent magnetic nature of iron oxide core resulted in particle aggregation in solution, which was reflected in the large hydrodynamic radius observed using PCS. Therefore, the size estimation from the PCS was higher than the size found using TEM and large particle size was observed in each synthesis step. Previous studies on HNPs showed large hydrodynamic radius caused by magnetic aggregation (Hoskins *et al*. 2012b). However, after polymer coating, particle size decreased, which can indicate that coated particles tend to aggregate less than naked iron oxide NPs; thus the PEI intermediate layer acted as a stabiliser (Table 3). Gold seeding and gold coating onto the Fe_3O_4-PEI also affected the particles size and larger diameter has been obtained upon the seeding and coating process (Table 3). These results from the PCS were not in agreement with the TEM data, because findings from the TEM microscopy showed that naked Fe_3O_4 seemed to be monodisperse and approximately 30 nm in size (Figure 25A).

The electron micrograph (Figure 25) showed that the iron oxide core is formed, seeded and coated with gold NPs. A slight increase in particles size was observed after complete gold coating to the surface of iron oxide NPs. Therefore, it is estimated that the shell thickness is around 10 nm. Shell thickness has a direct impact on SPR and heating properties. It was suggested that reducing the thickness of the Au shell from 20 nm to 5 nm results in SPR red shift about 300 nm, which is related to the enhanced coupling between the outer and inner shell surface plasmons for the particles with thinner shell (Prodan *et al*. 2003).

The results revealed that fabricated HNPs had an r_2 (260.2 mM^{-1} s^{-1}) fairly similar with previously clinically administered Feridex® (240.37 mM^{-1} s^{-1}) (Lee *et al*. 2011) (Figure 28). Previously, Smolensky and colleagues proposed that gold shell at the surface of iron oxide NPs leads to quenched contrast ability (Smolensky *et al*. 2011).

The findings suggest that the magnetic characteristics of the HNPs after gold coating process are in agreement with clinical standards and therefore have the capacity to use as contrast agents. These results in addition to the laser irradiation finding emphasise that the unique physical characteristics of the magnetic iron oxide NP and gold nano-shell, which

possesses SPR effect, are preserved by an intermediate polymer layer (PEI) that separates the core and shell.

Few investigations have been performed for the heating effects of iron oxide-gold HNPs. Previously Hirsh and colleagues fabricated HNPs (Hirsch *et al*. 2003). They injected their HNPs into a tumour tissue in mice, which was exposed to laser irradiation (820 nm, 4 Wcm^{-2}, 5 mm spot diameter) for around 6 min. The result demonstrated that irradiation of this novel particles inside the tumours increased the temperature to 37.4 °C after 4-6 min irradiation. Hirsh reported that this temperature increase was above the threshold temperature at which irreversible tissue damage occurs. In another study, Barnett *et al*. dispersed HNPs in 2 % agar gel and the samples were exposed to laser irradiation at 532 nm by a Q-switched Nd:YAG laser (10 ns pulse duration, 10 pulses s^{-1}). They reported that increasing the thickness of gold coating onto the iron oxide-PEI NPs resulted in reducing particles` ability to act as nano-heaters and decreased their magnetic properties, which is related to the enhanced coupling between the outer and inner shell surface plasmons for the particles with thinner shell (Barnett *et al*. 2012).

Synthesised HNPs demonstrated to act as nano-heaters upon the laser irradiation at 1064 nm, which was time and concentration dependant (Figure 30). In concentration of 100 μgmL^{-1} at 37 °C , the temperature of the particles increased up to 44.5 °C, which is enough for our therapeutic agent to be released inside the tumour cells (will be described in Chapter Three). Moreover, the increased temperature only occurred in laser irradiated area, which means that this technique will not affect or damage surrounding healthy tissues. Laser experiment was performed with HNPs dispersed in an agar phantom, although this was an *in vitro* assay, the agar was used to mimic *in vivo* tissue conditions. However, in order to achieve higher ΔT, optimisation of synthesis process for HNPs is needed as the maximum achieved ΔT was less than 8 degrees. Additionally, the visual heating effect of HNPs has been confirmed by *in vitro* injection of particles into the raw chicken breast by applying laser irradiation (Figure 31).

2.5. Conclusion

Novel hybrid iron oxide-gold core-shell NPs have been successfully synthesised and characterised by various techniques such as FTIR, PCS, UV–vis absorption, TEM, and PXRD, which all confirmed the formation of hybrid structure of the particles. Iron oxide NPs of core diameter 30 nm and gold coat (using the seeding method) were synthesised with a poly(ethylenimine) intermediate layer. The size of HNPs by TEM was approximately 40 nm. HNPs possessed a maximal absorbance at 610 nm. After laser irradiation in agar phantom a ΔT of 7.70 °C ± 0.80 was achieved after only 60 s exposure (100 μgmL^{-1}). The HNPs appeared to decrease T_2 values in line with previously clinically used MRI contrast agent Feridex®. Therefore, this study showed the potential of these HNPs as dual function MRI contrast agents and thermal switches in heat triggered drug delivery for thermo-responsive drug delivery.

Chapter Three

Drug conjugations and characterisation of new formulations

3.1. Introduction

NPs are usually described as aggregates or solid particles, which possess the core diameter between 10-1000 nm. This irreversible aggregation is the main indication of physical stability of NPs. The principle factors that influence the effect of aggregation are type of NPs, duration and temperature of storage, zeta potential and the presence of electrolytes. To prevent NPs from sticking together and setting out of suspension, NPs must be stabilised.

There are two main strategies to induce stability for NPs in suspension: electrostatic repulsion and steric hindrance. By electrostatic repulsion, the charged surface of two NPs repels each other, resulting in a stable suspension. Steric stabilisation can be achieved by the sorption of none-ionic molecules (usually large ones) onto the surface of NPs. The surface-grafted molecules have a tail that is soluble in the surrounding solvent, and an anchor unit that is ideally non-soluble. These molecules keep NPs away from each other, reducing the effects of attractive van der Waals forces.

In nanoparticulate drug delivery systems, the therapeutic or diagnostic agent can be encapsulated in or conjugated directly onto the NPs` surface. Recently, iron oxide-gold nanoparticles coated with hydrophilic polymer poly(ethylene glycol) (PEG) have been identified as long-circulating NPs which have potentials as drug delivery systems. The presence of the PEG coating makes the NPs becoming ‘stealth’ like resulting in longer systemic circulation compared with conventional therapies (Bhadra *et al.* 2002; Jokerst *et al.* 2011).

Aqueous based formulations are desirable for administration of therapies into biological environments. However, many formulations experience long term stability issues. As such, it is common for NP formulations to be freeze dried and stored as solid powders before use to enhance their shelf life. Often, aggregation of NPs or drug release occurs on storage and hence the need for such freeze drying processes.

The aggregation plays a pivotal role in their fate in aqueous environment. Many factors in human bodies such as pH and ionic composition can affect the interactions of nano-sized particles in biological environments (Guzman *et al.* 2006). Aggregated forms of NPs are usually poly-dispersed in solutions and their sizes may increase further when the pH reaches to the zero point of charge (pHzpc) (the pH where the concentration of protonated

and deprotonated surface groups are equal). Another important issue for understanding particles` behaviour is whether the dried NPs can disperse in a similar manner to the native solution upon reconstitution with water or biological media.

Moreover, release of therapeutic agents at their designated site of action in order to achieve targeting of the drug is one of the main concerns in designing NPs. To take full advantage of high specific NPs, there should be no drug release until HNPs reach target site; thus reducing adverse effects (Zeng *et al*. 2011). This can be achieved by designing a sophisticated drug delivery system which protects particles from early release and has to be triggered by an external stimulus (e.g. temperature or pH changes) to release the cargo at the final destination.

Measurement of drug release from formulations can be achieved using various methods including ultracentrifugation and ultrafiltration. More recently the use of dialysis tubing has grown dramatically (Johnston *et al*. 2006; Modi and Anderson, 2013). This entails trapping the formulation inside visking membrane of known pore size and exhaustively dialysing against water. As drug is released from the formulation, it permeates through the membrane into the surrounding media where it can be extracted and measured as a function of time. In comparison with the ultracentrifugation and ultrafiltration techniques, using the dialysis method means there is no need to set up an additional step of separating NPs from the free drug during the study. The external pressure utilised to separate NPs in other techniques may disturb the equilibrium, and partial separation can result in major errors (Wallace *et al*. 2012). Some of the advantages of using dialysis membrane for measuring drug release are one or more of the following: (1) assessing the effect of formulation factors and manufacturing methods on the drug product, (2) routine assessment of quality control to support batch release, (3) substantiating product label claims, and (4) establishing an *in vitro in vivo* correlation (IVIVC).

3.1.1. Bisnaphthalimide based drug

In 1993, Brana *et al.* suggested bisnaphthalimides as potent chemotherapeutic agents. The bistertiary derivatives of this substance are identified to possess great antitumor activity in both murine and human cancerous cells (Brana *et al.* 2001). Due to the planar aromatic moiety, these chemicals intercalate within the DNA by the major groove (Sami *et al*. 2000). Although mitonafide and amonafide as monomeric 3-nitro- and 3-amino-substituted compounds, respectively did not present sufficient anti-tumour activity in clinical trials (Taylor *et al*. 2002), elinafide and bisnafide as bissecondary analogues, (Figure 32), have shown remarkable *in vitro* anti-tumour activity. However, transferring elinafide to clinical trials for the treatment of solid tumours was not successful, because it showed a high toxicity without any marked therapeutic benefit (Brana *et al.* 2001).

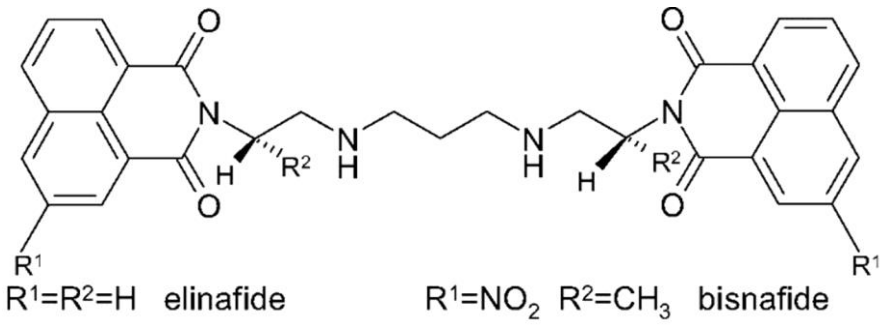

Figure 32. Chemical structure of the bisnaphthalimide based anti-cancers, elinafide and bisnafide.

Previous studies have evaluated the *in vitro* and *in vivo* pancreatic anticancer activity of a nano-sized formulation based on novel poly(allylamine) grafted with 5 % mole cholesteryl pendant groups (Ch5-PAA). Novel anticancer drug, bis(naphtalimido propyl) diamino octane (BNIPDaoct) (Figure 33) was loaded into Ch5-PAA polymeric self-assemblies. BNIPDaoct compounds are not soluble in aqueous solutions, thus toxic solvents such as dimethyl sulfoxide (DMSO) have been used to solubilise this drug. Ch5-PAA novel formulation was able to increase aqueous solubility of BNIPDaoct, which enhanced its

anticancer activity and efficacy. Ch5 showed the capability of solubilising 0.3 $mgmL^{-1}$ of BNIPDaoct in water (free drug was insoluble in water) with 1:1 initial drug:polymer mass ratio (concentration of the polymer was 1 $mgmL^{-1}$).

As previously described in Chapter One (Section 1.5), NPs are able to improve penetration/ internalisation of drugs into cancerous cells by EPR effect. Therefore, instead of active targeting, Ch5-PAA formulation accumulated passively in pancreatic cancer cells driven by EPR effect. This new formulation showed similar tumour reduction efficacy as the commercial drug, gemcitabine and an 8-fold reduction in concentration of free BNIPDaoct for the same cytotoxic result was achieved. The optimal formulations of Ch5 loaded with BNIPDaoct were tested for their cytotoxicity *in vitro* on Caco-2 and HEK293 cells. All formulations were capable of lowering the IC_{50} values when compared with the free drug, therefore enhancing their therapeutic effect. *In vivo* oral administration of Ch5 formulations demonstrated significant decrease of the tumour growth when treated on tumour bearing nude mice over a 4 week period (Hoskins *et al*. 2010).

BNIPDaoct possesses a chain with 14 carbons and two amine groups (eight carbons are between amines) between the bisnaphthalamide aromatic moieties (Figure 33). Many different compounds can be designed through changing this chain. For example, by increasing the number of carbon the hydrophobicity of the compound would increase, which makes it easier for the drug to cross the hydrophobic cell membrane. Moreover, by increasing the number of amine group, the drug would be more positively charged. This might able the drug to conjugate with the negatively charged NPs and since this interaction is not as robust as covalent bonding; the drug can be released by a trigger (temperature or pH changing) in a designated area.

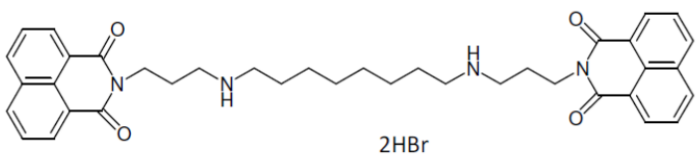

Figure 33. Chemical structure of bisnaphtalimido propyl diamino octane (BNIPDaoct).

This work will investigate the potential of using HNPs as thermally triggered drug carriers for pancreatic cancer. This novel technology will exploit the use of gold surface of the HNPs for the conjugation and delivery of novel chemotherapeutic drugs based on the bisnaphthalamide series. Four different bisnaphthalamide derivatives will be used in this study (Figure 34).

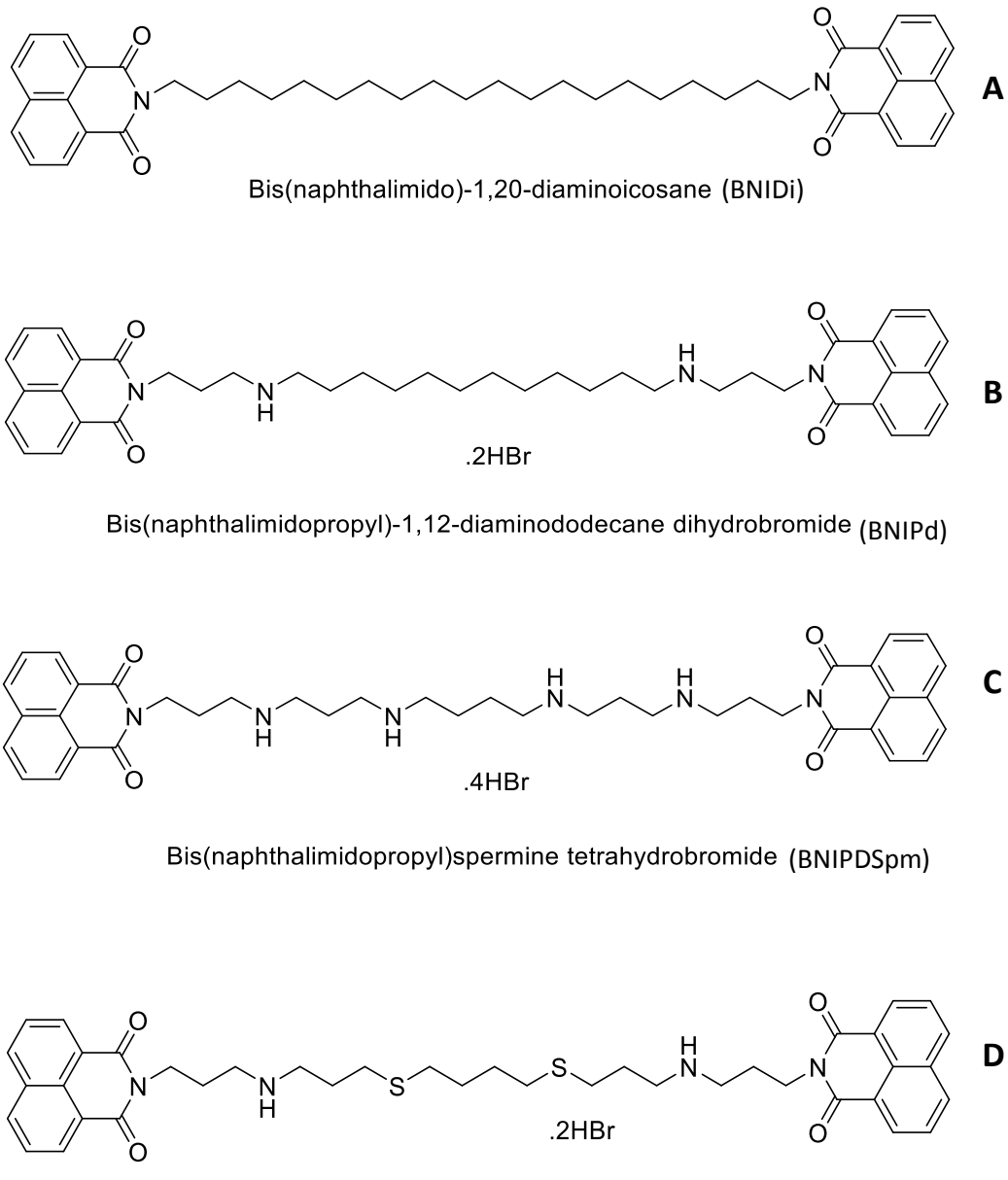

Figure 34. Chemical structure of A) BNIDi, B) BNIPd, C) BNIPDSpm and D) BNIPds

The first drug is bis(naphthalimido)-1,20-diaminoicosane (BNIDi) which possesses a chain, 20 carbons long between the bisnaphthalime moieties (Figure 34A). The second one is bis(naphthalimido)-1,12-diaminododecane (BNIPd) which possesses a chain of similar length, however two of the carbons was replaced with two amine groups (Figure 34B). The third derivative chain, bis(naphthalimidopropyl) spermine (BNIPDSpm), is of similar length with four substituted amines (Figure 34C) and finally, bis(naphthamimidopropyl)-3,3`-(butane-1,4-diylbis(sulfanediyl))bis(propan-1-amine) (BNIPds) is comprised of a chain of the same length which has two amine groups as well as two additional thiol groups (Figure 34D). These compounds have been selected for binding onto the HNPs in order to investigate the potential of electrostatic interaction of drugs and HNPs as stimuli responsive systems for drug release. It was assumed that BNIDi would not conjugate onto the surface of the HNPs due to the absence of any charge or driving force for attachment. However, it was postulated that the drugs with positive amine groups (BNIPd and BNIPDSpm) would possess the ability to conjugate onto the negative surface of HNPs via weak van der Waal's interactions. The final drug BNIPds has been added as a control as the thiol groups in the drug structure facilitate the attachment to the gold surface of HNPs by dative covalent bond (Au-S chemistry).

These novel formulations were characterised by different analytic instruments such as photon correlation spectroscopy (PSC), Fourier Transform Infrared Spectroscopy (FTIR), fluorescence spectroscopy (due to the presence of aromatic rings in bisnaphthalamide derivatives) and reverse phase high performance liquid chromatography (RP-HPLC) (with fluorescence detector). The loading concentration of each drug has been optimised and formulations were tested for their stability and drug release profiles.

Drug release study at various temperatures in water or culturing medium (in order to simulate physiological conditions) will be performed. It is suspected that the release pattern of the drugs with stronger interactions with HNPs, such as BNIPDSpm and BNIPds will be slower than formulation containing BNIPd which has only two amines in its structure. It is important to investigate the drug release pattern at different temperatures because the aim of this study is to trigger the release of drug in pancreatic cancer cells by laser irradiations. As described in Chapter Two (Section 2.3.8), these particles produced temperature increase up to 44 ºC upon the laser irradiation for 60 s. Therefore, it is crucial

to explore how much drug will be released from the formulations at different temperatures including 44 ºC.

3.1.2. Fourier Transform Infrared spectroscopy

FTIR is a sensitive and highly diverse molecular spectroscopy method and chemical analysis technique, which can identify organic chemicals in a whole range of applications in pharmaceutical industries related to drug discovery and structural elucidation.

The term "Fourier transform" comes from the fact that a mathematical process is needed to translate the raw data into the actual spectrum. Infrared (IR) spectroscopy has been used to identify unknown materials, recognise the quality/consistency of a sample, determine the amount of components in a mixture and identify the functional groups in a chemical compound (Griffiths and de Hasseth, 2007). Samples in any state can be analysed using this technique including solid, liquid and gaseous phase samples (Sibilia, 1996).

Each molecule has its own particular frequency resulting from the internal vibrations in the chemical bonds of the functional groups, which is used in IR spectroscopy (Banwell and McCash, 1994; Schwedt and Haderlie, 1997; Sibilia, 1996). IR spectroscopy works by passing infrared radiation (500-4000 cm^{-1}) through a sample. This radiation is adsorbed at frequencies related to the compound vibrational frequency and the remaining frequencies are transmitted (Sibilia, 1996; Stuart *et al*. 1996). Each chemical structure has specific vibration; thus it can be detected by the analysis of its unique IR spectrum (Sibilia, 1996). The difference between FTIR and IR is using an interferometer instead of a monochromator in FTIR, which measures the spectrum indirectly (Sibilia, 1996). The interferometer combines two waves together and due to this combination and amplification, it can digitise the data and generate a spectrum (Stuart *et al*. 1996). In comparison with IR spectra, FTIR spectra possess high resolution of the peaks, enhanced signal/noise ratio and reduced measuring time, which makes it a very useful and precise technique (Schwedt and Haderlie, 1997; Sibilia, 1996).

In this study, FTIR is an ideal tool to verify the presence of drug and analysis of drug conjugation to the surface of synthesised NPs.

3.1.3. Fluorescence spectrometry

Fluorescence spectroscopy (also known as fluorometry or spectrofluorometry) is an important investigational technique in many areas of analytical science, due to its extremely high sensitivity and selectivity. It is used in a broad range of chemical, biochemical and medical research and has become an essential investigational technique in the pharmaceutical industry. Fluorescence spectrometry can detect and quantify fluorescent chemicals by electromagnetic spectroscopy.

Compounds which have fluorescent characteristics have rigid molecular structures, such as aromatic ring systems, double and triple bonds (Schwedt and Haderlie, 1997). When a molecule absorbs a photon of light, the consequential excited electronic state leads to a change in the energy of that molecule. But when the molecule returns to its ground state the excess electronic energy is released as a photon of light, which is known as fluorescence (Hurtubise, 1990; White and Argauer 1970).

Bisnaphthalimide derivatives are fluorescent compounds due to the presence of aromatic rings. This characteristic can help to demonstrate bisnaphthalamide drugs are present (on the basis of their excitation and emission properties) within the hybrid nano-formulation by fluorescence spectrometry.

3.1.4. High performance liquid chromatography

High performance liquid chromatography (HPLC) is one of the main analytical techniques utilised in the pharmaceutical industry. It has been used for a vast range of applications, which starts from drug discovery to formulation improvement and beyond. This instrument has been used in analytic chemistry to separate, identify, quantify and qualify the components in a sample.

In normal phase HPLC, the separation technique occurs by the transportation of molecules through a non-polar mobile phase within a polar stationary phase, a column. This transportation relies on a pump that pressurises the liquid solvent containing the sample mixture (Kazakevich and LoBrutto, 2007). Each molecule in the solvent interacts with the adsorbent material in a different way, which produces different flow rates. Therefore,

components can be easily separated as they flow out the column. In reverse phased (RP) HPLC the column size is the same but non-polar stationary phase such as modified silica (long hydrocarbon chains are attached to its surface) and a polar mobile phase are utilised. In this method, compounds are separated due to their differences in hydrophobicity, which depends on polarity and size of the molecule (Kazakevich and LoBrutto, 2007). Non-polar and larger compounds in the mixture are retained on the column for longer as they tend to attach to the hydrocarbon chains in the column due to the van der Waal`s dispersion forces but the smaller polar molecules have strong attractions to the solvent and thus are eluted first. It means that increasing the polarity of the mobile phase will increases the retention time of non-polar molecules in the column. As a result, polar, non-polar and ionisable molecules will be separated by this method.

In this study RP-HPLC with fluorescence detection can help to verify /quantify the drugs inside hybrid formulations.

3.1.5. Aims and objectives

The aim of this work is to evaluate the ability of a series of bisnaphthalamide based drugs to conjugate onto the surface of HNPs. It is the first time that these drugs conjugated to the surface of HNPs to fabricate a thermoresponsive drug delivery system, which will be triggered by laser irradiation, enable them to release their cargo in the designated area. Different bisnaphthalamide based drugs will be introduced to the HNPs to investigate the properties of electrostatic and covalent bonds between the drugs and gold surface. Novel formulations will be PEGylated to increase biocompatibility and blood circulation time. These nano-formulation will be characterised by PCS, fluorescent spectroscopy, FTIR and RP-HPLC. The stability of formulation will be tested at different temperatures and forms (dispersed in water or freeze dried) for 4 weeks. Drug release studies will be carried out at different temperature, PH and in culturing medium.

3.2. Materials and Methods

3.2.1. Materials used

Table 4. Materials used in synthesis and characterisation of hybrid formulations.

Materials	Suppliers
Thiolated poly ethylene glycol (PEG-thiol)	Sigma-Aldrich Co., UK
PRMI Medium 1640(1X)	Life technologies Co., UK
HPLC Grade acetonitrile	Sigma-Aldrich Co., UK
Octane sulfonic acid	Sigma-Aldrich Co., UK
Sodium acetate	ACROS Organics Co., USA
HPLC Grade hydrochloric acid	Sigma-Aldrich Co., UK
HPLC Grade dimethyl sulfoxide	Sigma-Aldrich Co., UK
Bis(naphthalimido)-1,20-diaminoicosane (BNIDi)	Synthesised by Keele Nanopharmaceutics research group
Bis(naphthalimido)-1,12-diaminododecane (BNIPd)	Synthesised by Keele Nanopharmaceutics research group
Bis(naphthalimidopropyl)spermine (BNIPDSpm)	Synthesised by Keele Nanopharmaceutics research group
Bis(naphthamimidopropyl)-3,3`-(butane-1,4-diylbis(sulfanediyl))bis(propan-1-amine) (BNIPds)	Synthesised by Keele Nanopharmaceutics research group
Hybrid nanoparticles (HNPs)	Synthesised in Chapter Two

3.2.2. Methods

3.2.2.1. Drug conjugation

To a solution of HNPs (1 $mgmL^{-1}$, 5 mL) a certain amount of drug (dissolved in 5 mL deionised water) (Table 5) was added (based on the concentration of HNPs used in the literature for drug conjugation (Barnett *et al*. 2013a; Barnett *et al.* 2013b)). The solution was stirred for 3 h (optimum time for drug conjugation as no further attachment was achieved over this time) at room temperature (20 ºC) before being magnetically separated and extensively washing with deionised water. For the formulations containing

O-[2-(3-mercaptopropionyl amino) ethyl]-O′-methylpolyethylene glycol (PEG-thiol), 25 mg of powdered polymer (based on the concentration used in the literature for PEGylation (Barnett *et al*. 2013a; Barnett *et al*. 2013b)) was added simultaneously with drug (a mixture of drug and PEG was added to the HNP solution) and particles were washed after 3 h as previously described. It was postulated that PEG will coat the surface of HNPs completely if it was added before the drug, thus no free surface would be available for the drug attachment.

24 formulations (in conjugation with four different bisnaphthalamide derivatives) were prepared by this method and half of them were PEGylated by PEG-thiol (Table 5).

Table 5. Table presents the amount of loaded bisnaphthalamide derivatives and PEG-thiol (dissolved in 5 mL of water) in each formulation.

Formulation	Type of loaded drug	Amount of loaded drug (mg)	Amount of loaded PEG-thiol (mg)
1	BNIDi	6.25	-
2	BNIDi	6.25	25
3	BNIDi	12.5	-
4	BNIDi	12.5	25
5	BNIDi	25	-
6	BNIDi	25	25
7	BNIPd	6.25	-
8	BNIPd	6.25	25
9	BNIPd	12.5	-
10	BNIPd	12.5	25
11	BNIPd	25	-
12	BNIPd	25	25
13	BNIPDSpm	6.25	-
14	BNIPDSpm	6.25	25
15	BNIPDSpm	12.5	-
16	BNIPDSpm	12.5	25
17	BNIPDSpm	25	-
18	BNIPDSpm	25	25
19	BNIPds	6.25	-
20	BNIPds	6.25	25
21	BNIPds	12.5	-
22	BNIPds	12.5	25
23	BNIPds	25	-
24	BNIPds	25	25

3.2.2.2. Characterisation of novel formulations

3.2.2.2.1 Drug quantification

To find the optimal loading concentration of each drug onto the HNPs, the amount of attached drug was quantified by RP-HPLC (Prominence, DEGASSER, LC20AD, SHIMADZU) using a fluorescence detector at 234 nm (Excitation) and 394 nm (Emission) (Jasco, PU-980, Japan; column C18(2), 150×4.60 mm 5 micron, flow rate: 1 $mLmin^{-1}$, injection volume: 20 µL). The buffer used in HPLC mobile phase was prepared by adding 0.432 g octane sulfonic acid (to enhance the retention) and 1.64 g sodium acetate to 200 mL of deionised water. Then the pH of the solution was reduced to 4.5 by the addition of hydrochloric acid (1-2 mL). Mobile phase was prepared by mixing this buffer and acetonitrile at a ratio of 70:30, respectively. After drug conjugation the particles were separated from the supernatant (waste solution) by using a strong permanent magnet on the outside of a glass vial containing the formulation. One mL of the waste solution (in water) was diluted with 1 mL of dimethyl sulfoxide (DMSO) and drug concentrations were analysed via HPLC. A calibration was run using drug solutions dissolved in 50: 50 H_2O: DMSO with the concentration of 3.13-50 μgmL^{-1} (R^2 = 0.999) (Appendix, Figure 7). The addition of DMSO helps the drug to be dissolved without sonication. The amount of attached drug was calculated from the amount of free drug in waste solution, detected via HPLC. All measurements were run in triplicate and recorded as average values.

3.2.2.2.2. Zeta potential measurement

Zeta potential measurements of novel formulations were carried out using a photon correlation spectrometer (PCS, Zetasizer Nano-ZS, Malvern Instruments, UK) as described in Chapter Two (Section 2.2.2.5.4).

3.2.2.2.3. Fourier Transform Infrared Spectroscopy

HNP alone and formulations with the highest drug loading concentrations (5 mL) were freeze dried using Heto PowerDry LL3000, Thermo-Fisher UK. The freeze dried samples were analysed on the FTIR using a diamond tipped attenuated total reflectance attachment (Nicolet iS5 with iD5 ATR, Thermo-Fisher UK) and 64 scans were run at room temperature with background subtraction in order to qualitatively verify drug presence.

3.2.2.2.4. Fluorescent spectroscopy

Aqueous solution of free bisnaphthalamide based drugs and their hybrid formulations were run at room temperature on the Luminescence spectrometer (Varian, Cary Eclipse Fluorescence Spectrophotometer, USA) with Excitation wavelength set at 234 nm. The samples were scanned for Emission between 200-600 nm at 400 $nmsec^{-1}$ with the slit widths of 5 nm, and the spectra were collected and analysed by the provided software.

3.2.2.2.5. Stability study

The stability of formulations was tested in relation to the amount of released drug from the particles in aqueous solution. The formulations were either left suspended in water or dried powder. This study was run at both room temperature (20 ˚C) and 4 ˚C over the period of 4 weeks. For the aqueous formulations, 1 mL of each formulation (drug concentration = 0.5 $mgmL^{-1}$) was kept at room temperature or 4 ˚C and the supernatant was analysed each week with HPLC to find out the concentration of released drug. For studying the stability of powder formulations 1 mL of each formulation with the same mentioned concentration was freeze dried. Each week samples were reconstituted in deionised water and the concentration of released drug investigated via HPLC as previously described in Section 3.2.2.2.1. All samples were sonicated with a sonic bath prior the separation of particles from the supernatant. All measurements were run in triplicate and recorded as average values.

3.2.2.2.6. *In vitro* drug release study

In vitro drug release study in aqueous environments

Some studies revealed linear correlation model between *In vitro* drug release in water and *in vivo* absorption (Bose and Wui, 2013; Cardot *et al*. 2007). Formulations (2 mL, 0.5 $mgmL^{-1}$) were placed into visking tubing (12-14 KDa) and dialysed against 200 mL deionised water at room temperature (20 ˚C) with stirring. The volume of dialysis fluid was in excess to mimic the *'sink'* conditions experienced after injection into the blood stream (Barnett *et al*. 2013a). At selected time points (0.083 h, 0.17 h, 0.33 h, 0.5 h, 1 h, 4 h, 6 h, 8 h, 24 h, 48 h, 72 h, 144 h, 168 h and 216 h) a sample of the exterior solution (1 mL) was removed and replaced with 1 mL deionised water at the specified time points previously described. All samples were diluted with 1 mL of DMSO and drug concentrations were analysed via HPLC. The experiment was carried out in triplicate and the peak area was compared to a calibration of the free drug dissolved in DMSO/H_2O (50:50) (R^2 = 0.999) (Appendix, Figure 7).

In vitro drug release at varied temperatures

Drug release study for formulations was performed at different temperatures (20, 30, 40, 44, 50 & 60 ˚C) and the release of the drugs was monitored by HPLC as described in Section 3.2.2.2.1. This test was performed to mimic the temperature change upon the laser irradiation. Previously Jelveh and Chithrani used this approach to predict the release of drug from gold NPs after laser irradiation (Jelveh and Chithrani, 2011).

In vitro drug release in biological media

The release of BNIPDSpm drug from PNIPDSpm-HNP and PNIPDSpm-HNP-PEG was also tested in serum free culture media (RPMI) at different pH. RPMI is a form of medium used in cell culture and tissue culture to grow different type of human cells. This medium

contains a great deal of phosphate and is formulated for use in a 5% carbon dioxide atmosphere. Although it is not completely as same as the biological fluid, examining release of drug in RPMI may be useful to have better understanding of drug release in biological environments. The pH of culture media was 7.5, which was close to the intracellular pH (pHi =7.42) of pancreatic cancer cells (Preissler and Williams, 1981). We also investigated the drug release pattern at pH=4.6 and pH=3.6 to simulate endosome and lysosome environment. pH adjustment was carried out using concentrated hydrochloric acid (20 M). The release of the drug was tested by HPLC as described in Section 3.2.2.2.1.

3.3. Results

3.3.1. Drug conjugation

All four bisnaphthalamide based drugs were characterised using HPLC coupled to a fluorescence detector at Excitation 234 nm and Emission 394 wavelengths (Figure 35). The retention time for peak observation for all drugs was between 7-11 min, where sharp peaks were observed. In order to investigate drug concentration in our experiments, calibration curve, obtained from HPLC analysis (samples concentration between 3.13-50 μgmL^{-1}) for each drug was utilised (R^2 = 0.999) (Appendix, Figure 7).

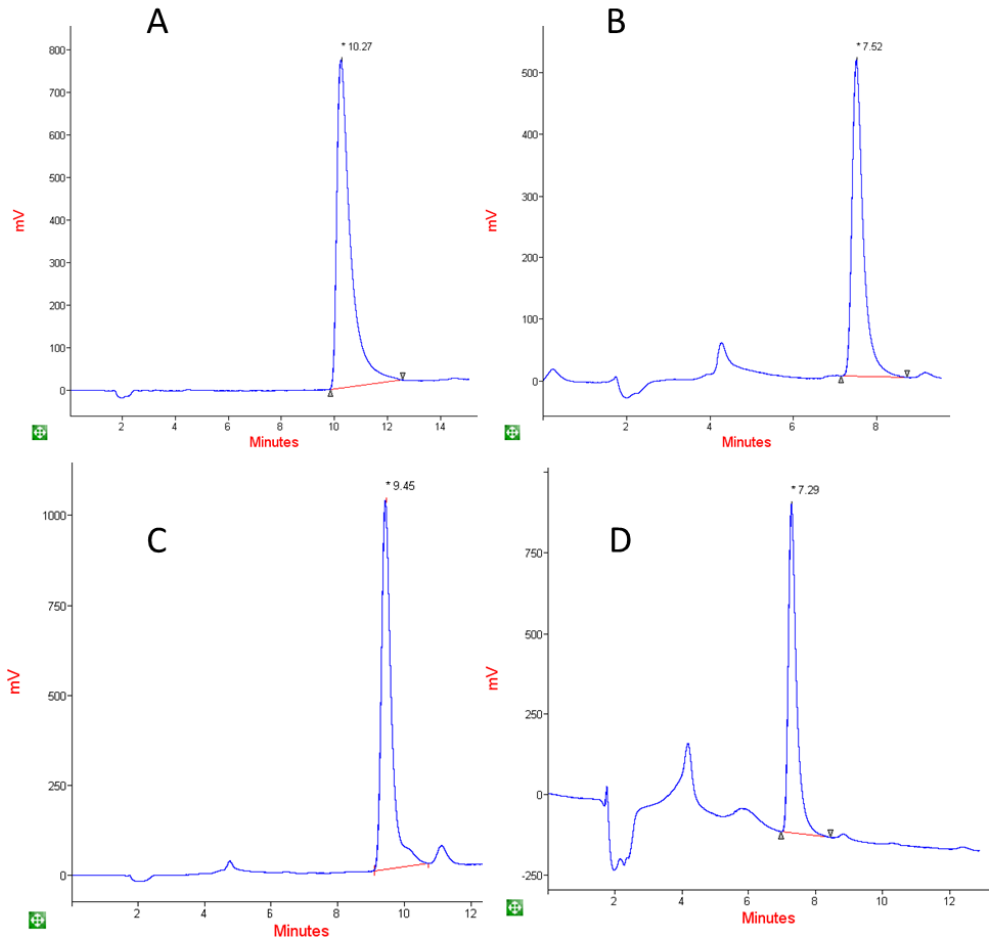

Figure 35. RP-HPLC analysis of 100 µgmL^{-1} A) BNIDi, B) BNIPd, C) BNIPDSpm and D) BNIPds, detected at 394 nm Emission. All drugs were dissolved in DMSO/H2O (50:50 v/v).

Data from HPLC analysis showed that BNIDi was not capable of conjugation onto the surface of HNPs and PEGylated HNPs (HNP-PEG) to form BNIDi-HNP and BNIDi-HNP-PEG (Figure 36). This was expected due to the absence of any positively charged amine group in BNIDi structure or other driving force for conjugation. The remaining drugs (BNIPd, BNIPDSpm, and BNIPds) all successfully conjugated onto the surface of HNP and HNP-PEG at varying degrees. Therefore six different formulations (BNIPd-HNP, BNIPd-HNP-PEG, BNIPDSpm-HNP, BNIPDSpm-HNP-PEG, BNIPds-HNP and BNIPds-HNP-PEG) were fabricated. The optimum loading concentration for each drug was investigated by HPLC analysis (Figure 36).

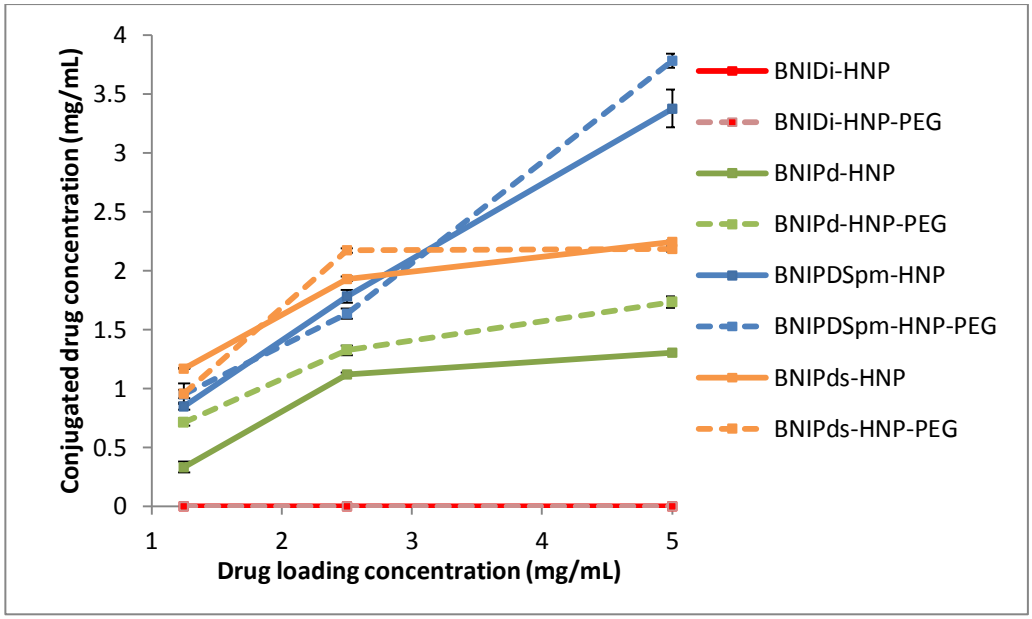

Figure 36. Drug loading of bisnaphthalamide based drugs onto HNPs at varied initial drug feed concentration (n=3, ave ± SD).

The loading concentrations for each drug were 1.25 mgmL^{-1}, 2.5 mgmL^{-1} and 5 mgmL^{-1} (Figure 36). Higher initial feed concentrations were not investigated due to the lack of aqueous solubility of drug compounds over 5 mgmL^{-1}. One way to increase the solubility of drug is using co-solvent such as DMSO during the formulation process. However, DMSO was not used in this study as it increases the cytotoxicity of the final product. In general, increasing drug loading concentration of BNIPDSpm resulted in greater drug attachment onto the nanoparticle surface. This could be due to the number of amine group in BNIPDSpm structure (4 amines), resulted in stronger electrostatic interactions between the drug and particle, in comparison with other drugs. As no plateau was observed in the graph, it would suggest that further conjugation could be possible and the HNP surface was not saturated; however, the physicochemical properties of the drug in solution hindered further attachment. For BNIPds the graph did plateau at higher drug feed ratios suggesting the particle surface was saturated and no more attachment was possible. Given, the nature of the permanent thiol linkage achieved with BNIPds drug (in addition to the electrostatic binding opportunities arising from the amines) compared with the sole ability for electrostatic attachment of the other drugs, it is postulated that a more rigid binding occurs with less flexibility, utilising greater surface area and hence leading to lower binding saturation concentrations.

The data showed that BNIPDSpm conjugated (with 5 $mgmL^{-1}$ loading concentration) to the surface of HNPs at higher concentration to the other drugs (Figure 36). Approximately, 3.4 $mgmL^{-1}$ and 3.8 $mgml^{-1}$ of BNIPDSpm (from 5 $mgmL^{-1}$ loading concentrations) attached to the HNP and HNP-PEG, respectively. This means that the binding efficiency of 68-76% was achieved. The addition of PEG appeared to increase BNIPd and BNIPDSpm loading slightly (Figure 36). This was unexpected given the PEG moiety was in competition with the drug for area on the gold surface; however, as evident in the drug loading data, the surface was possibly not saturated and also it is possible that small quantities of drug molecules could have been physically trapped within the polymer framework. At 2.5 $mgmL^{-1}$ loading concentration, BNIPds surpassed BNIPDSpm and attached slightly more to the surface of HNPs. However, when the loading concentration increased from 2.5 $mgmL^{-1}$ to 5 $mgmL^{-1}$, the concentration of conjugated BNIPds did not change significantly ($p > 0.05$) (Figure 36).

While BNIDi with no amine group (Figure 34A) did not attached to the HNP and HNP-PEG, the loading capacity of bisnphathalamide derivatives increased by increasing the number of amine group (from two amines in BNIPd to four amines in BNIPSDpm) (Figure 36). In all loading concentrations, BNIPd tended to conjugate to the particles less than BNIPDSpm and BNIPds drugs (Figure 36). This could be due to the number of amine groups (two amines) presents in its structure (Figure 34B), thus the electrostatic interaction between BNIPd and the HNPs is weaker than other formulations. BNIPDSpm possessed four amine groups (Figure 34C) , which allowed it to make strong electrostatic interactions with negatively charged gold at the surface of HNPs. BNIPds has two amine groups and two additional thiol groups (Figure 34D), therefore, it can attach to the particles` surface by covalent dative bond via Au-S chemistry and presumably by charge-charge interactions through amine groups. However, in 5 $mgmL^{-1}$ loading concentration BNIPds attached to the HNPs surface less than BNIPDSpm, which may be due to surface saturation as discussed (Figure 36).

3.3.2 Characterisation of novel formulations

3.3.2.1. Zeta potential measurement of novel formulations

Particles conjugated with different drugs were characterised by photon correlation spectrometer (Table 6). Zeta potential measurements showed that all the formulations possessed positive surface charges, excluding BNIDi-HNP and BNIDi-HNP-PEG. These results indicate that drug attachment was achieved as the amine functionalities within the majority of the drug molecules would infer positive charge.

The surface charge of BNIDi-HNP and BNIDi-HNP-PEG formulations was very similar to that of the HNP alone, which again confirms that drug conjugation was not achieved (Table 6).

Table 6. Zeta potential index of particles measured at 1 $mgmL^{-1}$ (concentration of conjugated drug) in deionised water (n=3, Ave ± SD).

*: Unknown concentration was used due to the lack of drug attachment.

Particle	Zeta Potential mV ± SD
HNP	− 4.32±0.03
* BNIDi-HNP	− 4.25±0.06
* BNIDi-HNP-PEG	− 6.97±0.01
BNIPDSpm-HNP	+28.48±0.14
BNIPDSpm-HNP-PEG	+13.43±0.07
BNIPd-HNP	+26.62±0.05
BNIPd-HNP-PEG	+9.25±0.18
BNIPds-HNP	+10.44±0.12
BNIPds-HNP-PEG	+1.12±0.05

The charge pattern for other unPEGylated formulations was BNIPDSpm-HNP > BNIPd-HNP > BNIPds-HNP. The BNIPDSpm-HNP formulation possessed the highest zeta potential in this group which is due to the BNIPDSpm molecule possessing the

greatest number of amine groups (four amines) compared with other drugs (Figure 34C). The surface charge of the BNIPd-HNP formulation was less than BNIPDSpm-HNP as it only possesses two amines groups. The reduced surface charge of the BNIPds-HNP (which also possesses two amine groups) compared to the BNIPd-HNP formulation is possibly due to the presence of the thiol (-SH) group in the drug structure. Thiol groups in water surroundings dissociate a proton, which makes the surface less positive (Václav *et al*. 2011). As a result of this, the decrease of zeta potential confirms also the binding of thiol groups on gold surface.

The data shows that all PEGylated formulations possessed lower surface charges, compared with unPEGylated formulations conjugated with the same drug, indicating further modification of PEG. This could be due to PEG chains shielding surface charge of gold coating.

Although, the absence of BNIDi in the formulations (BNIDi-HNP and BNIDi-HNP-PEG) was proposed before, the presence of PEG in BNIDi-HNP-PEG can explain the decrease of BNIDi-HNP zeta potential upon the PEGylation. Moreover, the same surface charge pattern for PEGylated formulations was achieved, which again proves the presence of different drug in each formulation, described before (BNIPDSpm-HNP-PEG > BNIPd-HNP- PEG > BNIPds-HNP-PEG) (Table 6).

3.3.2.2. Fourier Transform Infrared Spectroscopy of formulations

FTIR was used to qualitatively confirm the conjugation of drugs onto the HNPs. FTIR analysis of the samples (excluding BNIDi formulations) indicated that each drug conjugated to the surface of HNPs successfully (Figures 38-40). Before introducing the samples to FTIR, background spectrum was collected and subtracted. The series of characteristic Infrared (IR) bands for each formulation are summarised in detail in Tables 7-9.

FTIR Spectra of BNIDi-HNP and BNIDi-HNP-PEG indicated that BNIDi did not conjugate to the HNP, since there was not any difference between FTIR spectra of HNP (Figure 37A) and BNIDi-HNP (Figure 37B). Peaks at 1651 cm^{-1}, between 2950-2850 cm^{-1} and at 3442 cm^{-1} in figures 37A and 37B are associated with N-H bending, alkane C-H

stretching and N-H stretching (amine group) vibrations, respectively. These peaks confirm the presence of PEI polymer in formulations. Band around 2800 cm^{-1} for BNIDi-HNP-PEG is related to C-H stretching vibration (Figure 37C). Other Peaks observed at 1660 cm^{-1} (C=O stretching), 1341 cm^{-1} (C–H bending; −CH2 and −CH3) confirm the presence of bound PEG within BNIDi-HNP- PEG formulation.

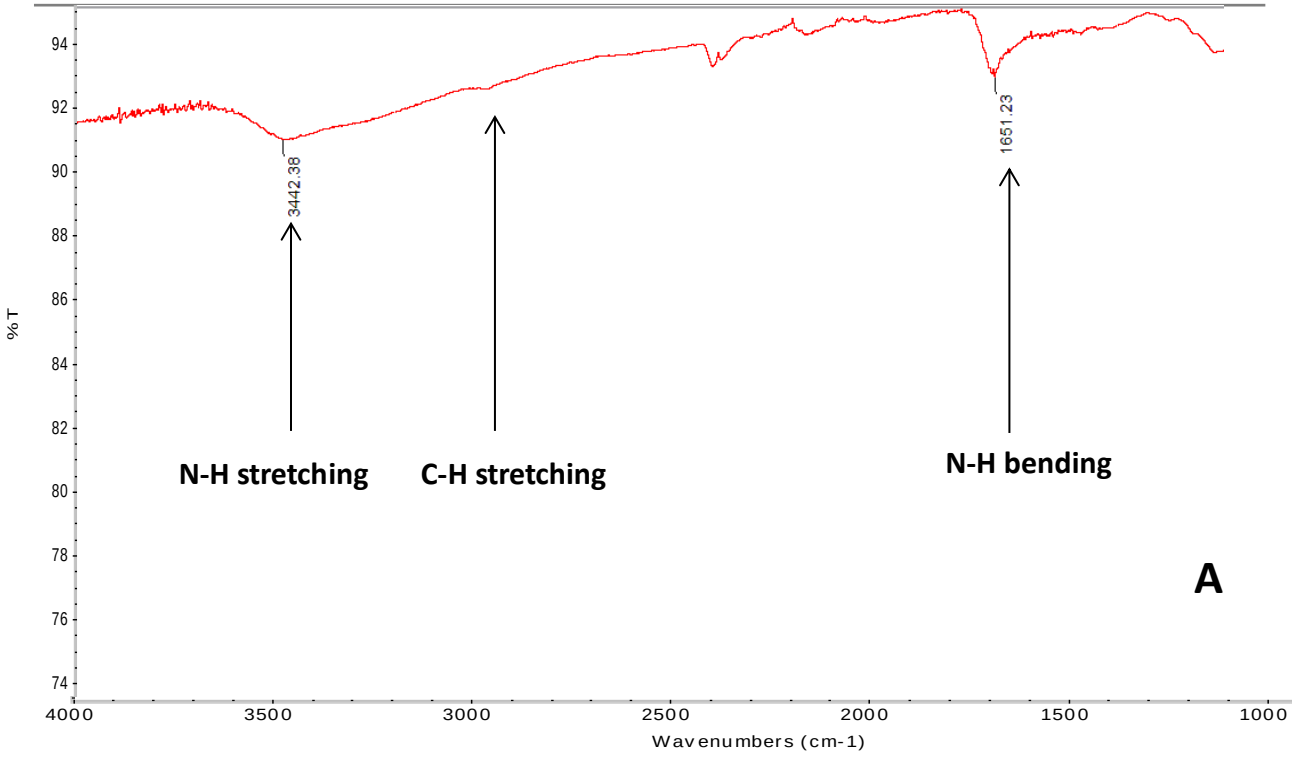

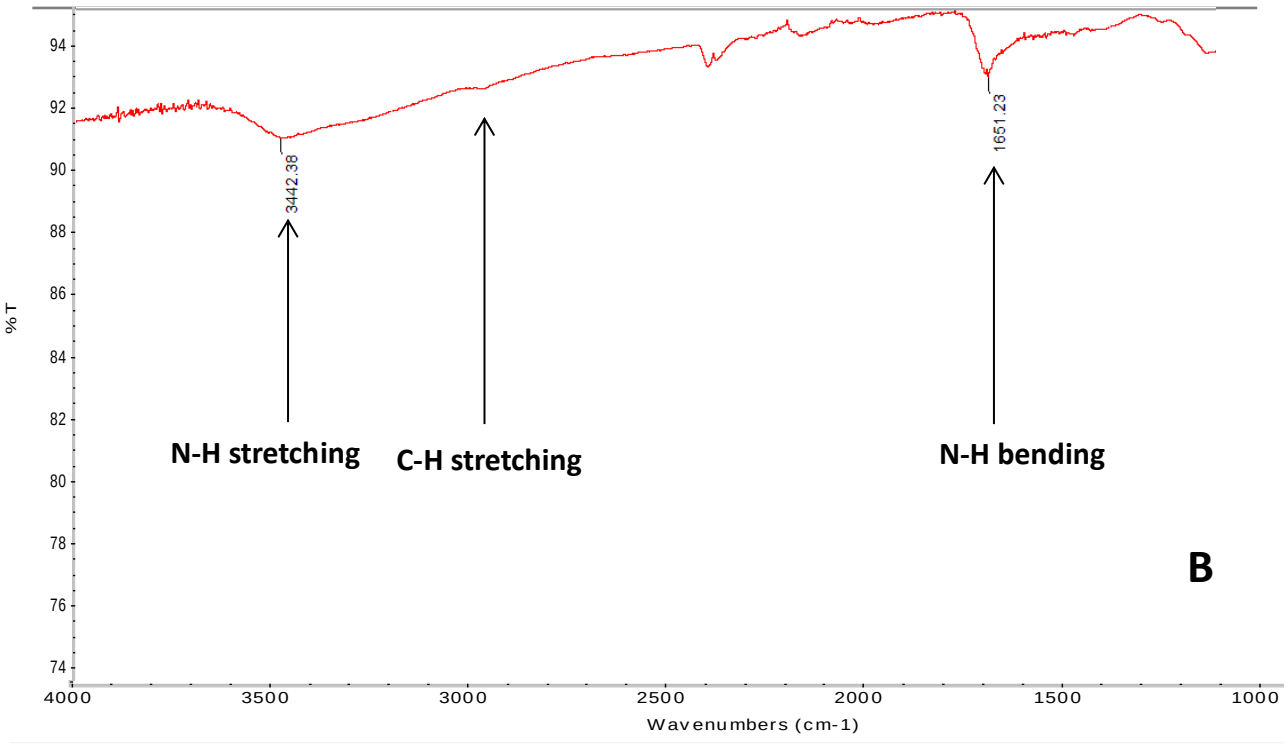

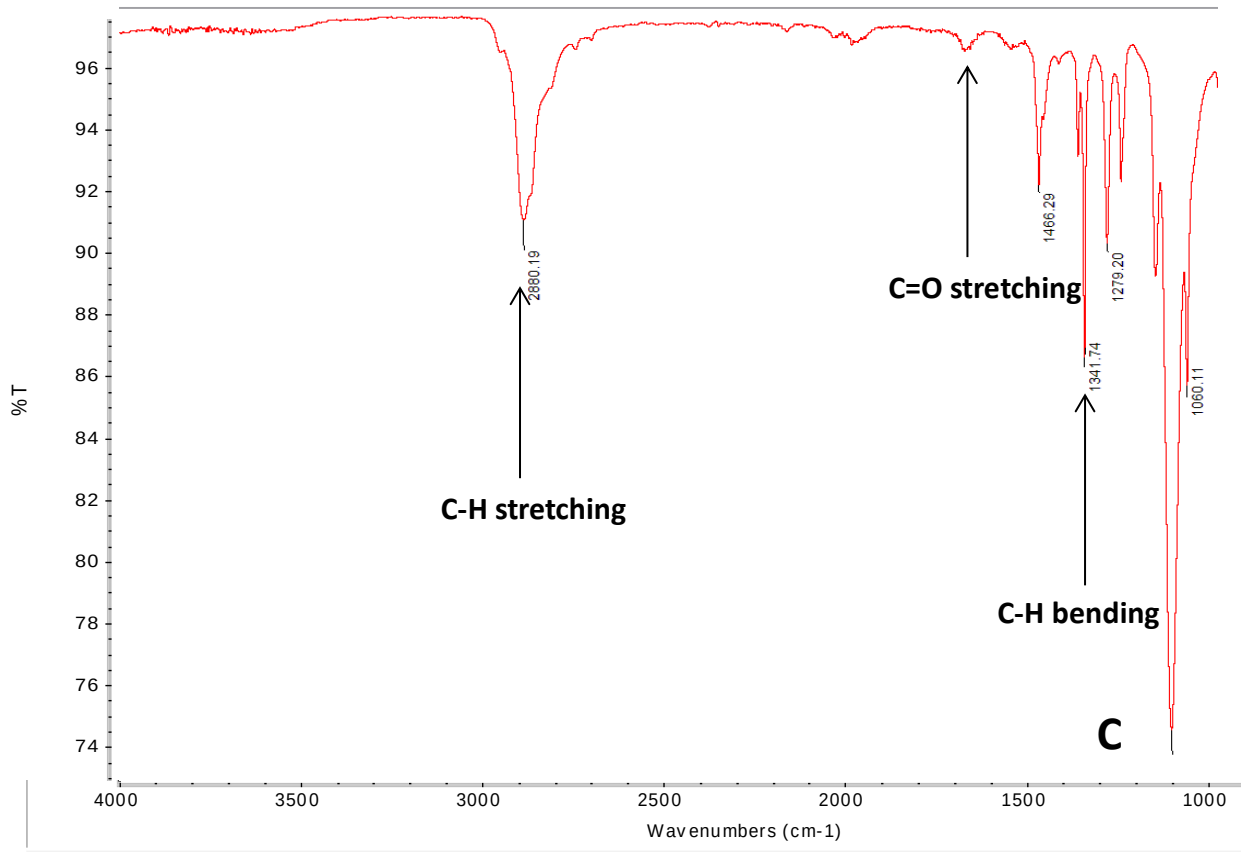

Figure 37. FTIR spectra of A) HNP, B) BNIDi-HNP and C) BNIDi-HNP-PEG, between 1000-4000 cm^{-1}.

Both FTIR spectra of BNIPd-HNP and BNIPd-HNP-PEG confirmed that the drug attachment has been achieved successfully (Figure 38). The series of characteristic IR bands for both formulations are summarised in detail in Table 7. The bands at 1260 cm^{-1} and 1110 cm^{-1} in BNIPd-HNP and BNIPd-HNP-PEG spectra are assigned to aromatic in-plane C-H bending vibrations, respectively. Peaks between 800-700 cm^{-1} are associated with N-H groups (wagging) in both formulations. Bands between 2920-2900 cm^{-1} and at 1600 cm^{-1} are due to alkane C-H stretching and C=O stretching vibrations in both formulations, respectively; presented within the BNIPd structure (Figures 38A and 38B). Peaks observed at 600 cm^{-1} and 2420 cm^{-1} in PEGylated formulation are assigned to C-S stretching and S-H stretching vibrations in PEG-thiol molecule, respectively.

Table 7. Assignment of FTIR spectra for BNIPd-HNP and BNIPd-HNP-PEG.

Samples	IR bands (cm^{-1})	Description
BNIPd-HNP	789	N-H (Wagging)
	900	Aromatic out-of plane C-H (Bending)
	1260	Aromatic in-plane C-H (Bending)
	1600	Aromatic C=C (Stretching)
	1680	C=O (Stretching)
	2915	C-H (Stretching)
BNIPd-HNP-PEG	600	C-S (Stretching)
	780	N-H (Wagging)
	900	Aromatic out-of-plane C-H (Bending)
	1110	Aromatic in-plane C-H (Bending)
	1600	Aromatic C=C (Stretching)
	1646	C=O (Stretching)
	2420	S-H (Stretching)
	2900	C-H (Stretching)

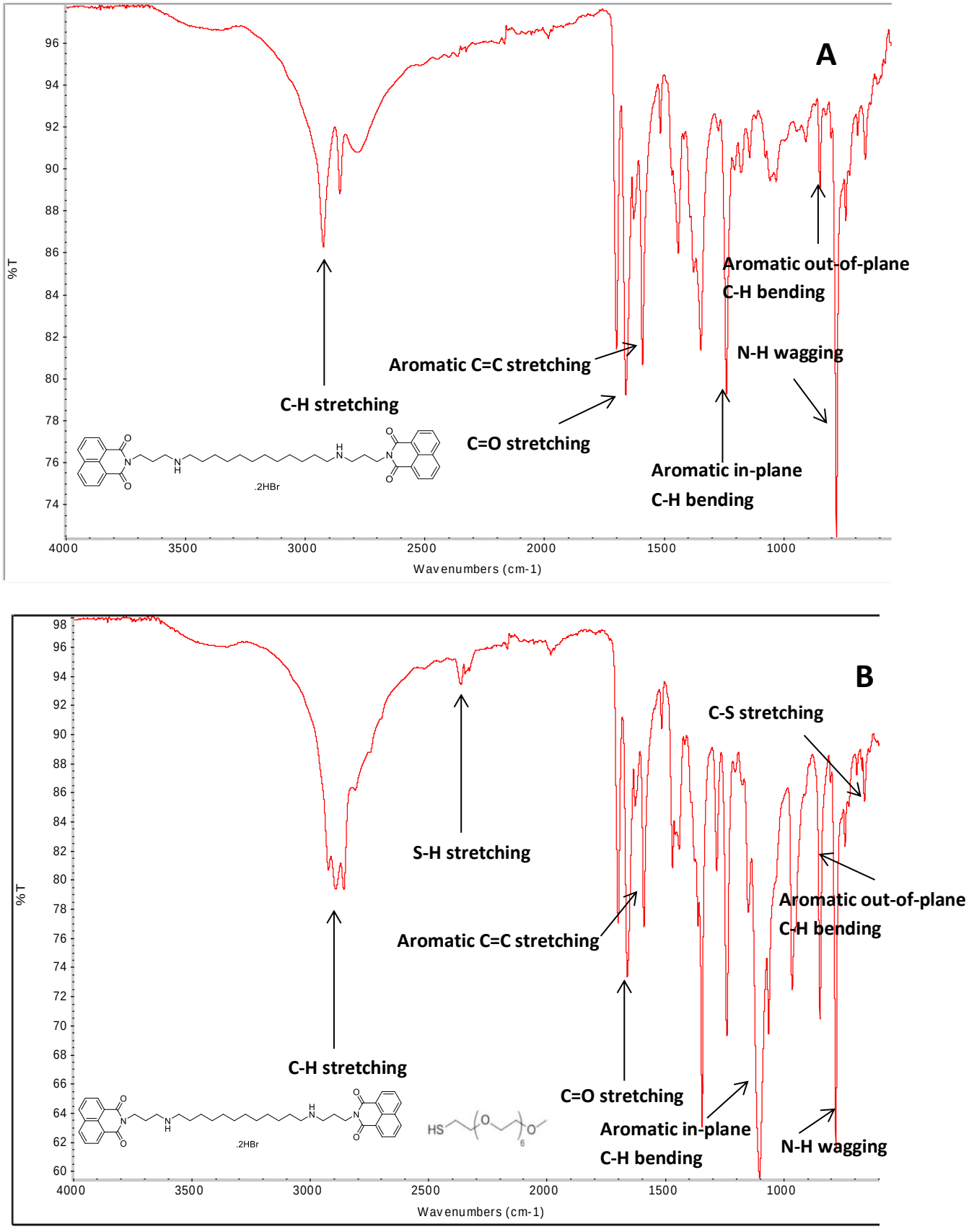

Figure 38. FTIR spectra of A) BNIPd-HNP and B) BNIPd-HNP-PEG between 500-4000 cm^{-1}.

The attachment of BNIPDSpm with HNP and HNP-PEG was proved by FTIR spectra (Figure 39). The series of characteristic IR bands for both formulations are summarised in detail in Tables 8. Bands around 1100 cm^{-1} in BNIPDSpm-HNP and BNIPDSpm-HNP-PEG spectra are assigned to aromatic in-plane C-H bending. Peaks around 2925 cm^{-1}, 1680 cm^{-1} and 1580 cm^{-1} are due to the presence of CH_2 (stretching), C=O (stretching) and aromatic (C=C stretching) groups in both formulations, respectively; presented within the BNIPDSpm structure (Figures 39).

Table 8. Assignment of FTIR spectra for BNIPDSpm-HNP and BNIPDSpm-HNP-PEG.

Samples	**IR bands (cm^{-1})**	**Description**
BNIPDSpm-HNP	1100	Aromatic in-plane C-H (bending)
	1580	Aromatic C=C stretching
	1680	C=O (Stretching)
	2930	C-H (Stretching)
BNIPDSpm-HNP-PEG	1110	Aromatic in-plane C-H (Bending)
	1580	Aromatic C=C stretching
	1674	C=O (Stretching)
	2920	C-H (Stretching)

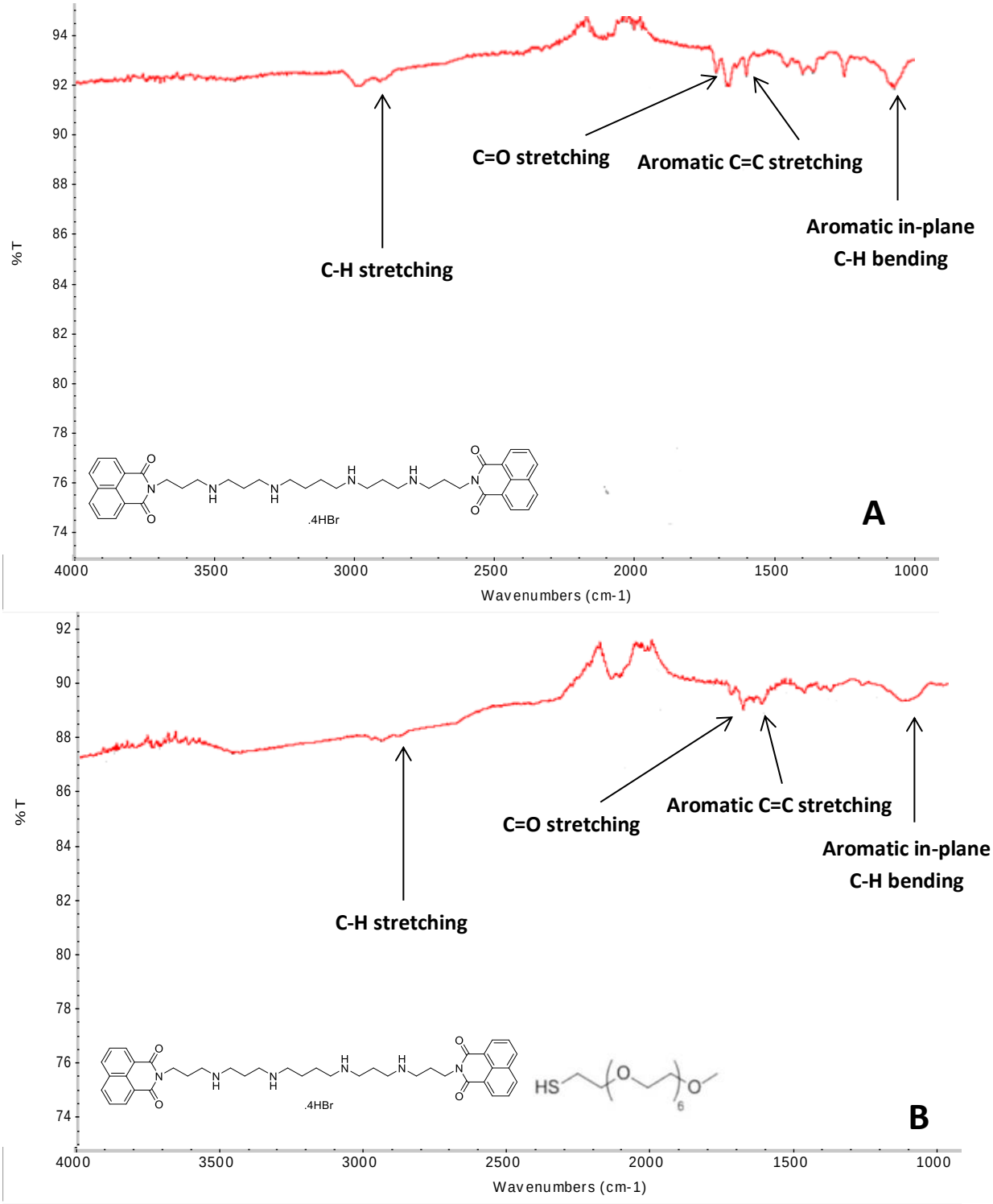

Figure 39. FTIR spectra of A) BNIPDSpm-HNP and B) BNIPDSpm-HNP-PEG, between 1000-4000 cm^{-1}.

FTIR spectra of BNIPds-HNP and BNIPds-HNP-PEG confirmed the conjugation of the drug to the surface of particles (Figure 40). The series of characteristic IR bands for both formulations are summarised in detail in Tables 9. Bands at 900cm^{-1} and around 1240 cm^{-1} in BNIPds-HNP and BNIPds-HNP-PEG spectra are assigned to aromatic out-of-plane and aromatic in-plane C-H bending, respectively. Peaks around 760 cm^{-1} are associated with N-H groups (wagging) in both formulations. The bands around 2935 cm^{-1} and 1600 cm^{-1} are due to the presence of CH_2 (stretching) and C=O (stretching) groups in both formulations, respectively; presented within the BNIPds structure (Figures 40). Small peak was observed around 2400 cm^{-1} in PEGylated formulation, which is assigned to S-H bonds (stretching), presented within PEG-Thiol structure.

Table 9. Assignment of FTIR spectra for BNIPds-HNP and BNIPds-HNP-PEG.

Samples	**IR bands (cm^{-1})**	**Description**
BNIPds-HNP	742	N-H (Wagging)
	900	Aromatic out-of plane C-H (Bending)
	1230	Aromatic in-plane C-H (Bending)
	1590	Aromatic C=C (Stretching)
	1680	C=O (Stretching)
	2930	C-H (Stretching)
BNIPds-HNP-PEG	770	N-H (Wagging)
	900	Aromatic out-of plane C-H (Bending)
	1250	Aromatic in-plane C-H (Bending)
	1600	Aromatic C=C (Stretching)
	1670	C=O (Stretching)
	2410	S-H (Stretching)
	2940	C-H (Stretching)

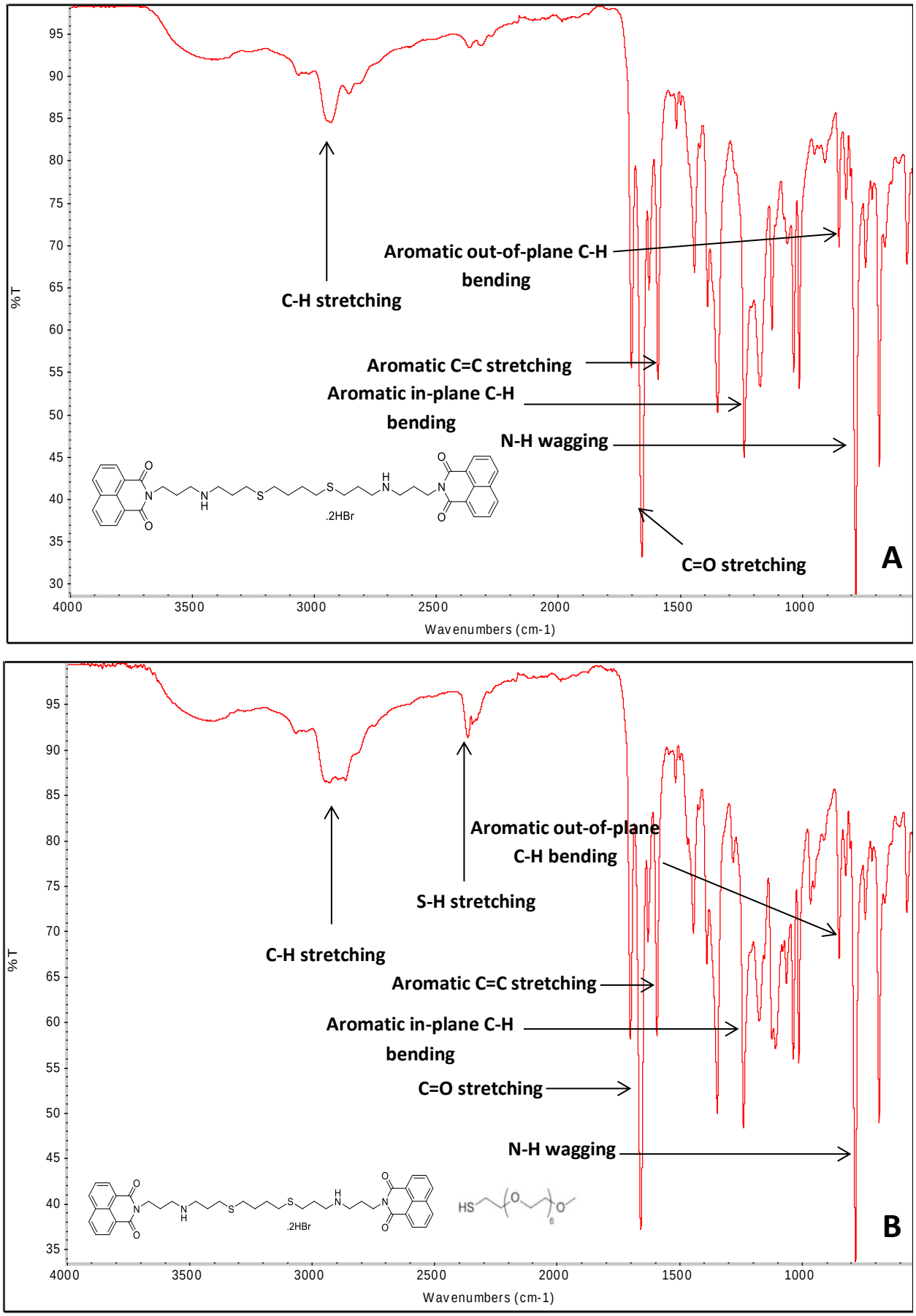

Figure 40. FTIR spectra of A) BNIPds-HNP and B) BNIPds-HNP-PEG between 500-4000 cm^{-1}.

3.3.2.3. Fluorescence spectrometry of formulations

Fluorescence spectrometry was used to confirm the presence of the drug molecules attached the surface of the HNPs. The HNPs themselves are not fluorescence; however, the aromatic groups in the bisnaphthalimide moieties of the drugs undergo excitation and emission allowing them to be detected. The fluorescent spectra for the drugs alone and the formulations (excluding BNIDi formulations) confirmed drug attachment to the HNPs surface (Figures 42-44).

Fluorescence spectra of BNIDi formulations were in agreement with HPLC and FTIR analysis (Figure 41). While BNIDi alone possessed emission λ_{max} at 508 nm (Figure 41B), HNPs alone (Figure 41A) and BNIDi formulations (Figures 41C and 41D) had featureless spectra between 200-600 nm, indicating the absence of BNIDi in formulations.

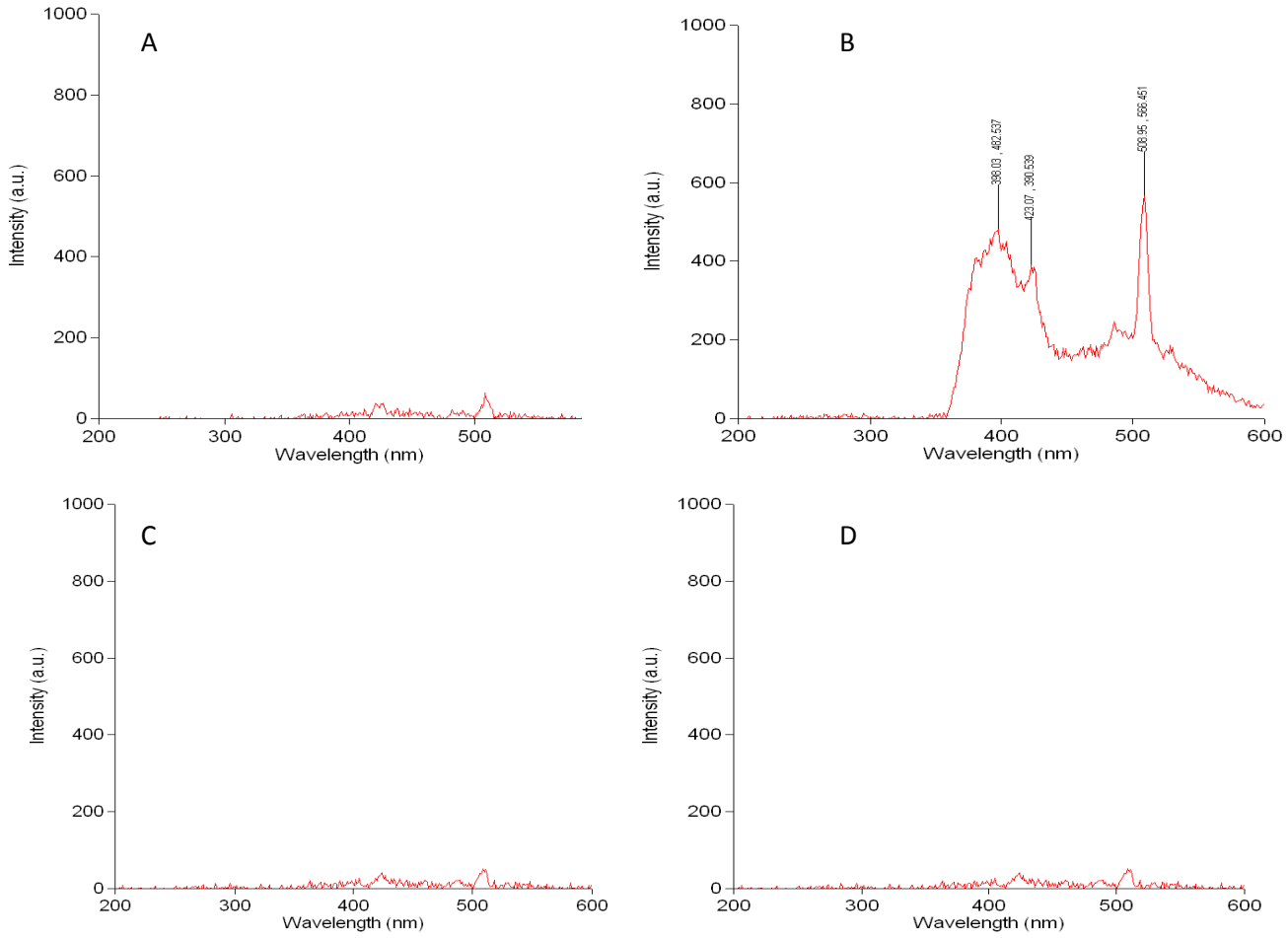

Figure 41. Fluorescence spectrometry of A) HNP, B) BNIDi, C) BNIDi-HNP and D) BNIDi-HNP-PEG (Excitation: 234 nm). Unknown concentration of free drug and conjugated drug was analysed at room temperature.

Fluorescence spectroscopy of BNIPd and its hybrid formulations confirms the presence of drug within the formulations. Free BNIPd (Figure 42A), BNIPd-HNP (Figure 42B) and BNIPd-HNP-PEG (Figure 42C) showed same peaks around 424 nm and 510 nm.

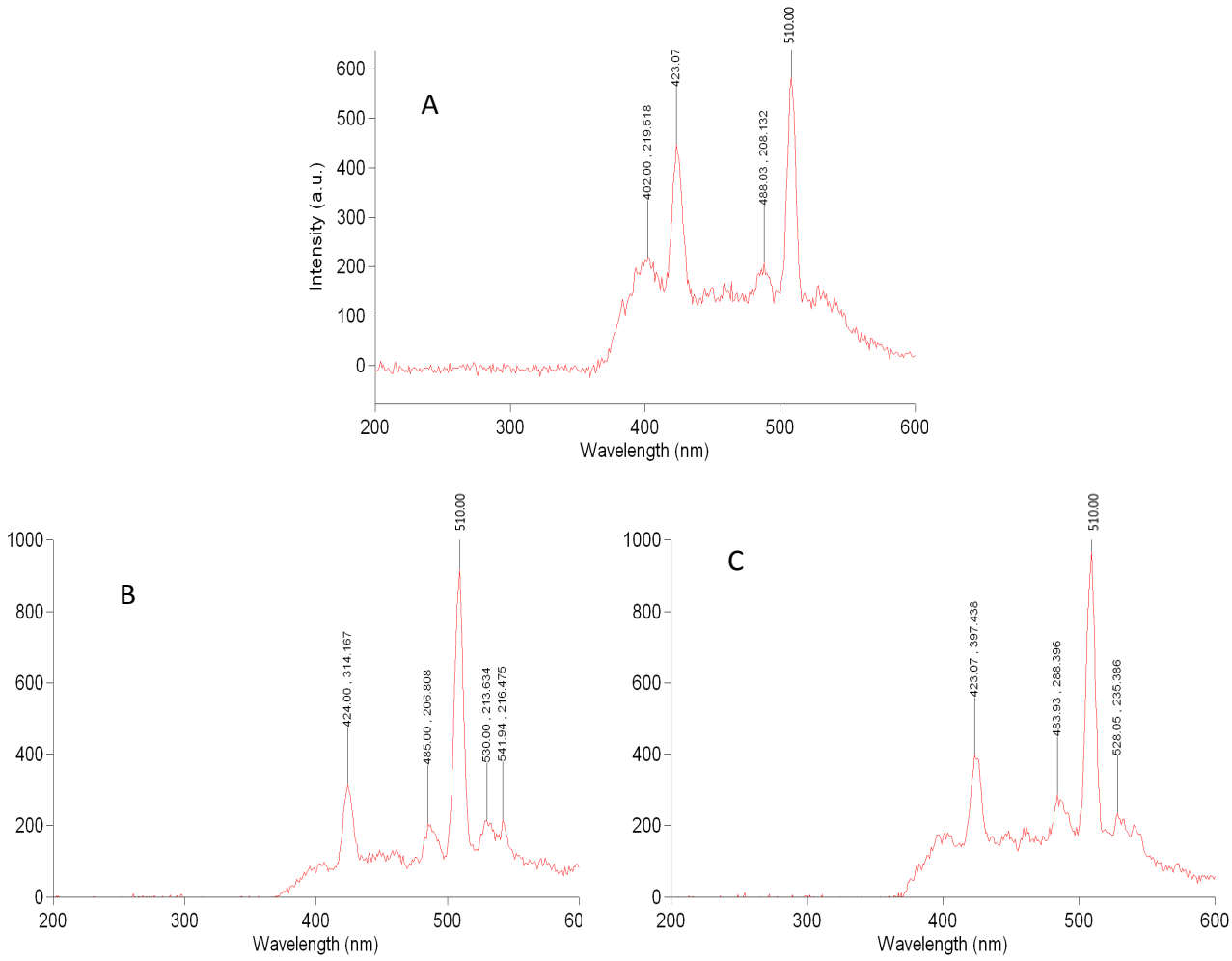

Figure 42. Fluorescence spectrometry of A) BNIPd, B) BNIPd-HNP and C) BNIPd-HNP-PEG (Excitation: 234 nm; Emission: 400 nm). Unknown concentration of free drug and conjugated drug was analysed at room temperature.

Fluorescence spectrometry also validated the conjugation of BNIPDSpm to the surface of particles (Figure 43). A sharp peak within the same wavelenghth (350 nm) was observed for free BNIPDSpm (Figure 43A), BNIPDSpm-HNP (Figure 43B) and BNIPDSpm-HNP-PEG (Figure 43C).

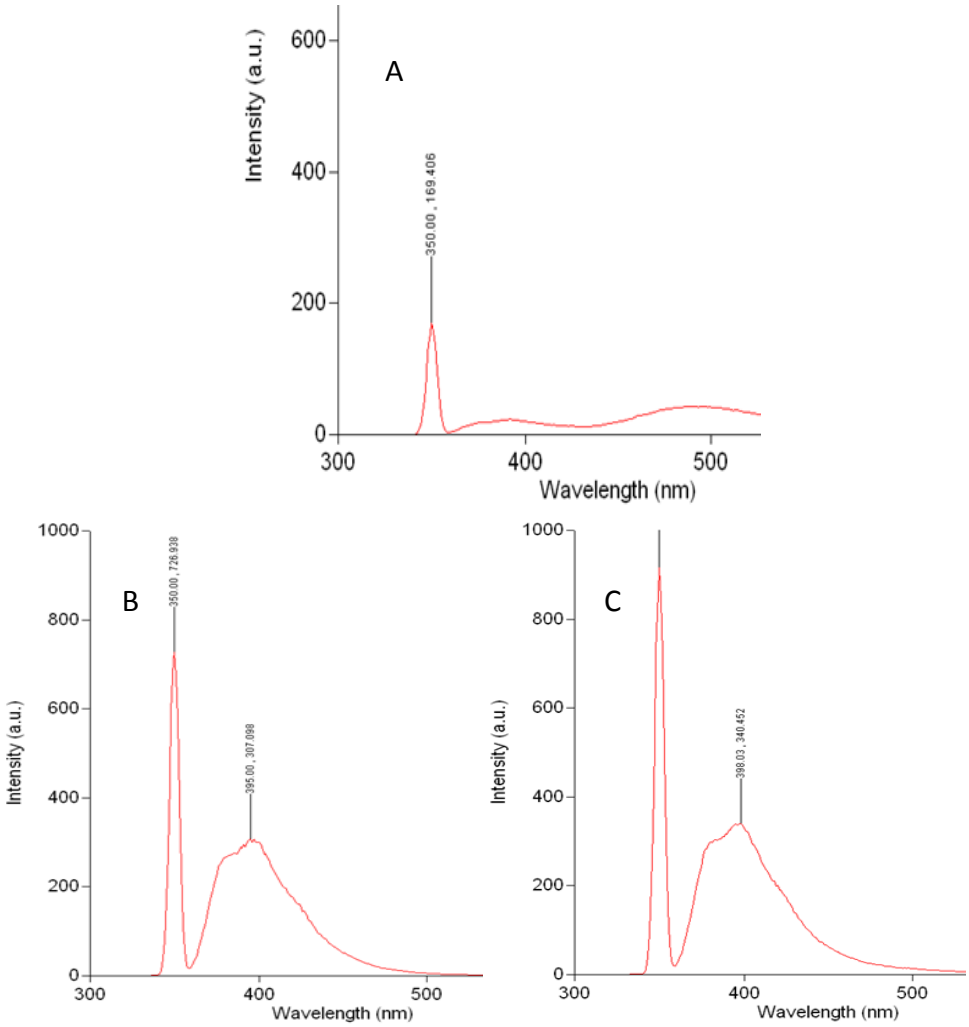

Figure 43. Fluorescence spectrometry of A) BNIPDSpm, B) BNIPDSpm-HNP and C) BNIPDSpm-HNP-PEG (Excitation: 234 nm). Unknown concentration of free drug and conjugated drug was analysed at room temperature.

Figure 44 confirmed the attachment of BNIPds to the surface of HNPs as free BNIPds (Figure 44A) and in conjugation with HNP (Figure 44B) and HNP-PEG (Figure 44C) possessed the same λ_{max} at 508 nm.

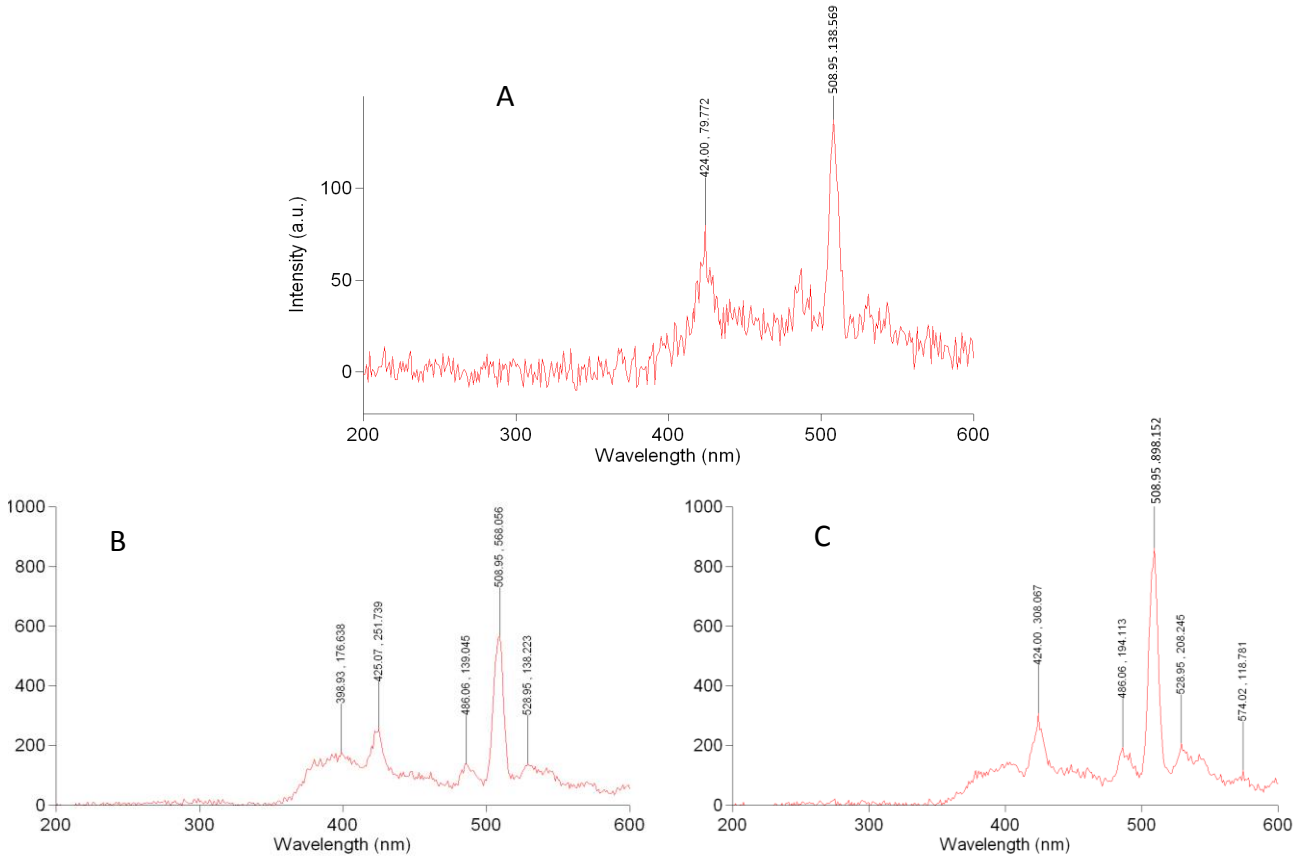

Figure 44. Fluorescence Spectrometry of A) BNIPds, B) BNIPds-HNP and C) BNIPds-HNP-PEG (Excitation: 234 nm; Emission: 400 nm). Unknown concentration of free drug and conjugated drug was analysed at room temperature.

Following the lack of attachment of BNIDi into the surface of HNP and HNP-PEG, it was decided not to continue any further studies with these formulations.

3.3.2.4. Stability tests

The optimal formulations were stored in a dark airtight container at either room temperature (20 °C) or under refrigeration (4 °C) and also in two forms; as liquid formulations and as freeze dried 'cakes' (reconstituted with water and sonicated) for up to 4 weeks (Figures 45 and 46). Both forms (dried and disperse) were sonicated before stability measurement.

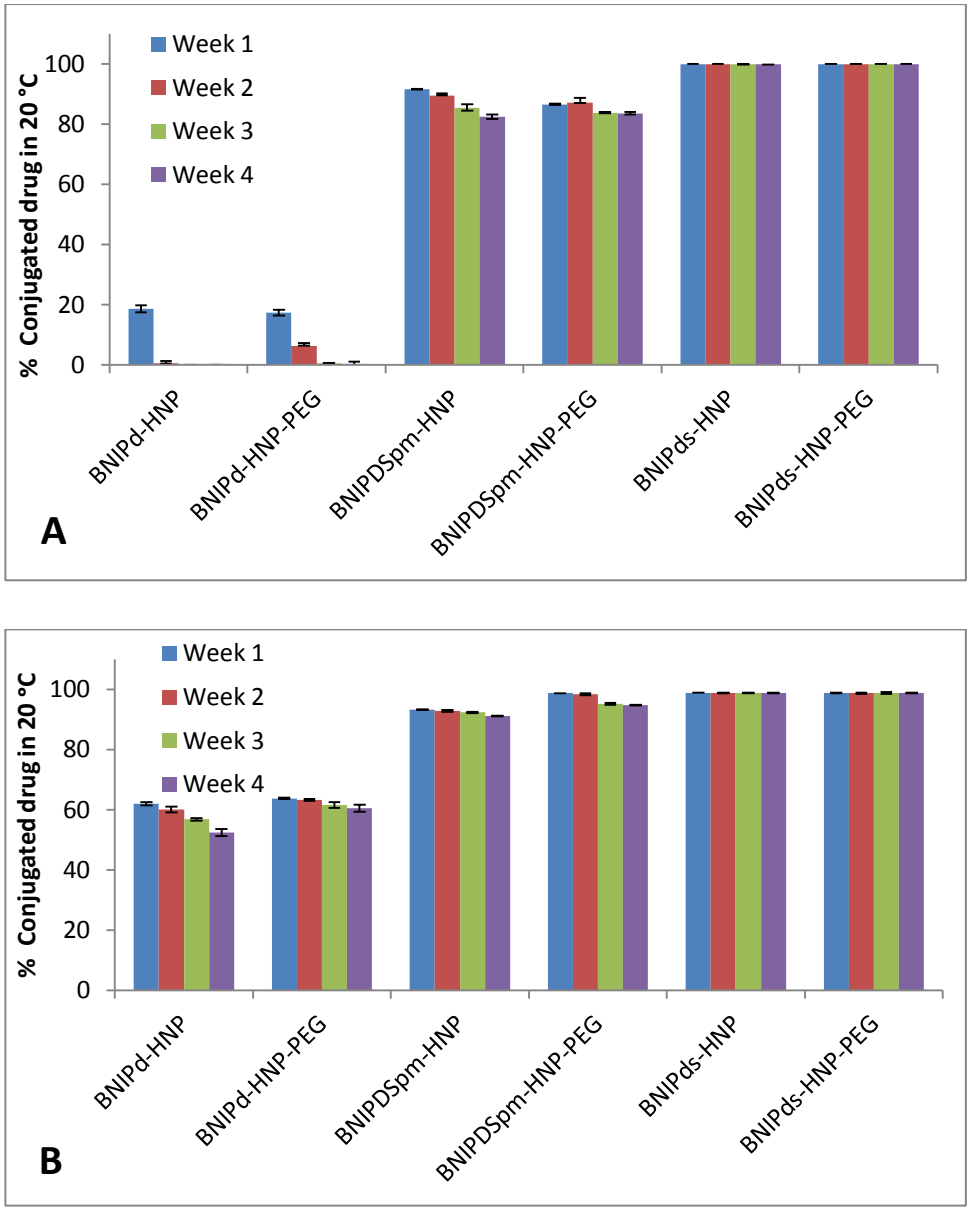

Figure 45. Stability test for novel formulations at 20 °C in the form of A) dispersed in water and B) freeze dried, over the period of 4 weeks (n=3, ave ± SD).

The data suggested that the form of formulation (aqueous / solid) was a more important parameter than the temperature in terms of stability. The samples which were freeze dried possessed a higher degree of stability compared to the liquid preparations. This might be due to the presence of water in in aqueous formulations, which can increase the risk of drug release from the nano-carriers. BNIPd-HNP and BNIPd-HNP-PEG displayed the lowest stability, which might be due to the loose electrostatic interactions between the drug and HNPs, since this drug only possessed two amine groups within its structure. All

aqueous form of BNIPd formulations exhibited less than 20 % stability. As the charge increased in BNIPDSpm, so too did the stability. Presumably due to the stronger electrostatic binding on the HNP surface. Over 80 % and 90 % stability have been achieved for aqueous and freeze dried BNIPDSpm formulations after 4 weeks, respectively. PEGylated formulations exhibited comparable stability to unPEGylated formulations (Figures 45 and 46).

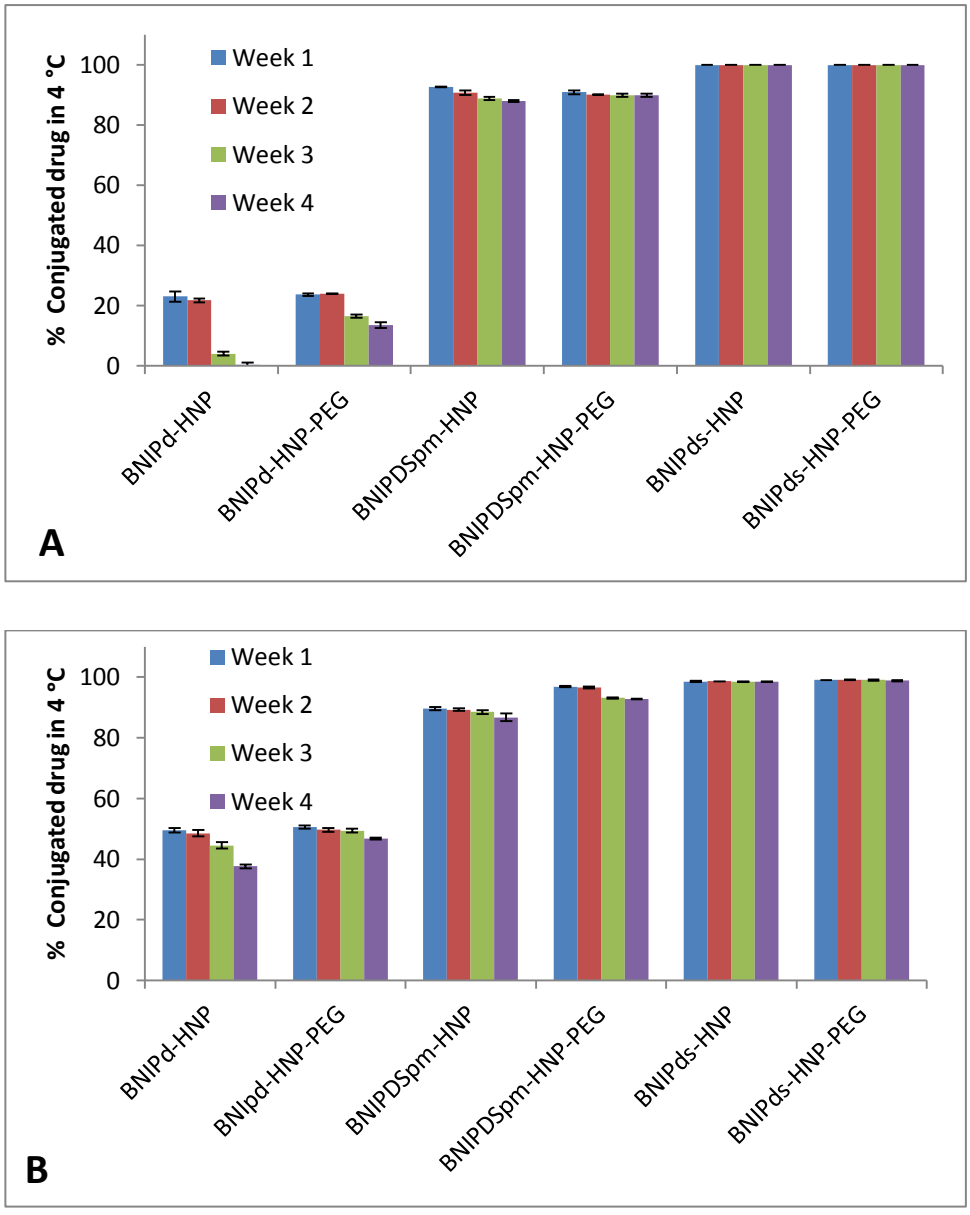

Figure 46. Stability test for novel formulations at 4 °C in the form of A) dispersed in water and B) freeze dried, over the period of 4 weeks (n=3, ave ± SD).

BNIPds formulations were highly stable in both forms and at both temperatures due to the strong covalent binding between the drug and gold at the surface of HNP (Figures 45 and 46). In terms of temperature, decreasing temperature from 20 ºC to 4 ºC increased the stability of the BNIPd and BNIPDSpm aqueous formulations showing that reduced temperature leads to less drug detachment and protects the integrity of the electrostatic bonds.

3.3.3. *In vitro* drug release study

The release of the drugs from the optimal formulations was performed under '*sink*' conditions. We investigated the conditions necessary for drug release in aqueous environment and culturing media (at various temperatures and pH).

3.3.3.1. *In vitro* drug release study in aqueous environments

BNIPd formulations exhibited very low stability (Figures 45 and 46) and the drug attached in lower quantity than other drugs to the surface of HNPs (Figure 36). Therefore, it was decided to start the drug release experiments at room temperature (20 ºC) in water. As expected, the drug release occurred rapidly with 90 % of drug released from PEGylated and unPEGylated formulations within 4 h and 6 h, respectively (Figure 47A). This low stability and fast drug release could be due to the loose electrostatic interactions between the drug and particles, as BNIPd possesses only two amines groups within its structure (Figure 34B). It indicates that these formulations are not stable at all and if they are injected to the body the drug will be released from the particle before reaching to the desired site of action. Following the low stability and fast release of BNIPd from formulations, it was decided not to continue any further drug release studies at different temperatures and/or in biological media with these formulations.

BNIPDSpm-HNP and BNIPDSpm-HNP-PEG were analysed in terms of the amount of BNIPDSpm release in 20, 30, 40, 50 and 60 ˚C (Figures 47B and 47C). BNIPDSpm

release for both formulations measured over 72 h showed a biphasic release profile due to an initial burst, which is followed by a constant release.

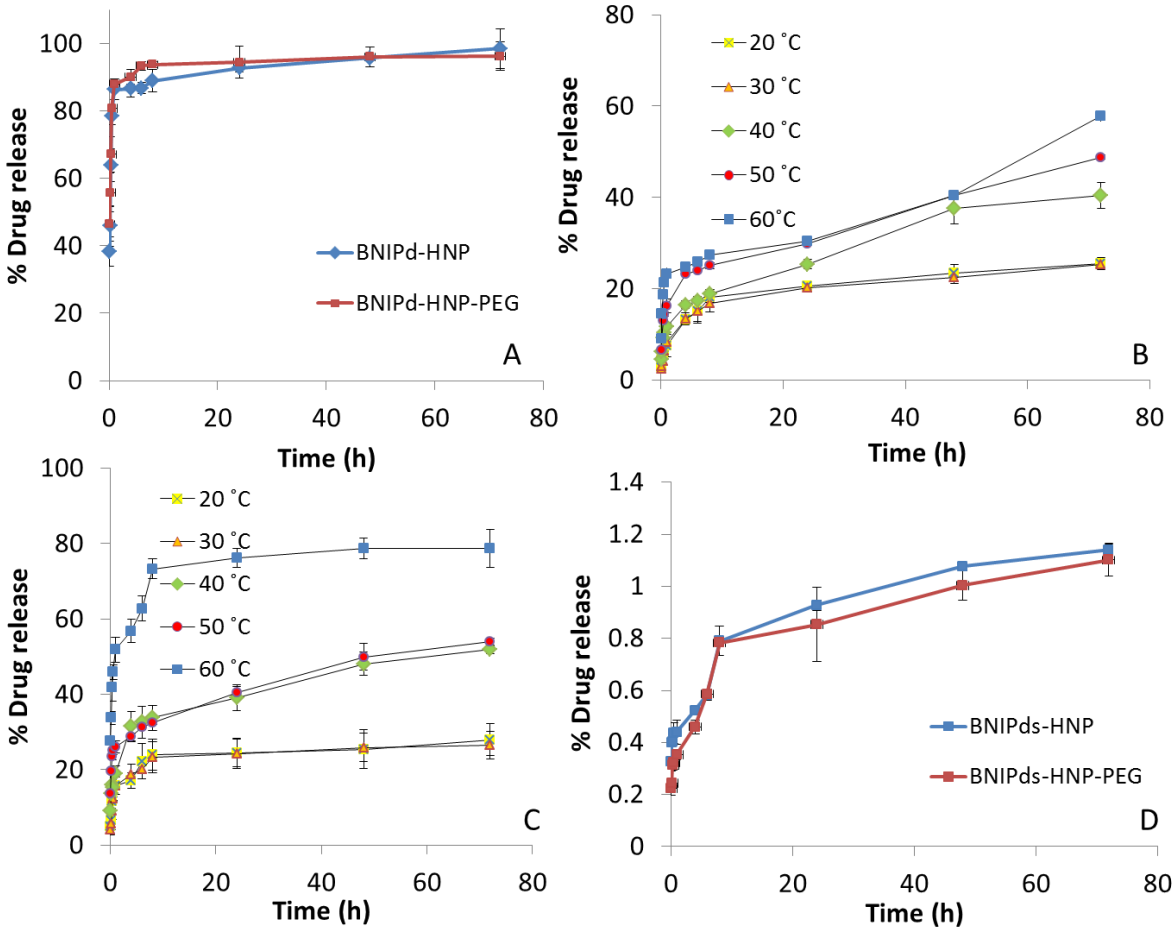

Figure 47. Drug release study of A) BNIPd-HNP and BNIPd-HNP-PEG in 20 ˚C and B) BNIPDSpm-HNP in 20 , 30 , 40 , 50 and 60 ˚C, C) BNIPDSpm-HNP-PEG in 20 , 30 , 40 , 50 and 60 ˚C and D) BNIPds-HNP and BNIPds-HNP-PEG in 60 ˚C. Experiments were performed three times, and data were expressed as mean ± standard errors (n=3, ave ± SD). All statistical analyses were carried out using t.test analysis within the Microsoft Excel software package.

Release of drug from BNIPDSpm-HNP-PEG (Figure 47C) after 20 min was significantly higher than BNIPDSpm-HNP (Figure 47B) in 40, 50 and 60 ˚C ($p < 0.05$). This might be due to the drug position in attachment with the particles. In the absence of PEG BNIPDSpm is flattened at the surface of the particles because of the abundance of free space, thus establishes strong interactions. In the presence of PEG, drug has to compete with the polymer for the particles` surface. As a result this type of interaction is not as

robust as unPEGylated formulation. Analysis of data showed no significant difference in drug release between 20 and 30 ˚C for formulations ($p > 0.05$). After 72 h, nearly 40 %, 50 % and 60 % of drug was released from BNIPDSpm-HNP in 40, 50 and 60 ˚C, respectively (Figure 47B). Interestingly, BNIPDSpm-HNP-PEG showed a different response in 60 ˚C with about 80 % of drug released after 72 h (Figure 47C).

BNIPDSpm drug release pattern was investigated at 44 ºC, as this is the optimum temperature generated by HNPs upon the laser irradiation, described in Chapter Two (Section 2.3.8). BNIPDSpm-HNP and BNIPDSpm-HNP-PEG formulations were able to achieve sustained drug release over 264 h and 336 h, respectively (Figure 48). In this temperature there was a notable difference in drug release between formulations and the amount of drug released from the PEGylated one was significantly higher between 10 min and 24 h ($p < 0.05$).

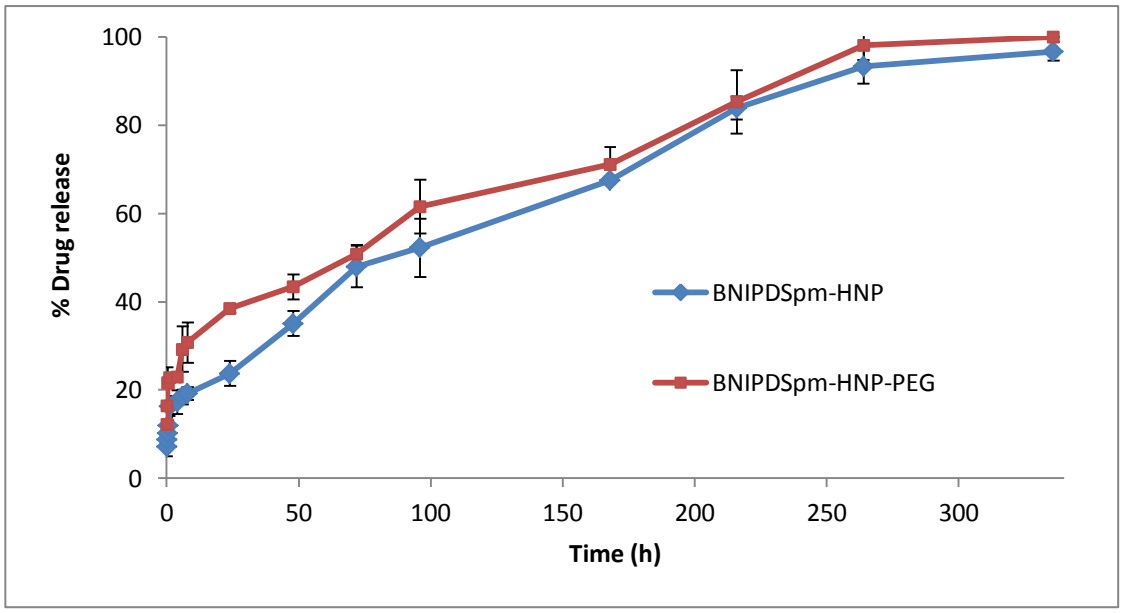

Figure 48. Drug release study for BNIPDSpm-HNP and BNIPDSpm-HNP-PEG at 44 ˚C for the period of 336 h. Experiments were performed three times, and data were expressed as mean ± standard errors (n=3, ave ± SD). All statistical analyses were carried out using t.test analysis within the Microsoft Excel software package.

Due to the permanent covalent binding of BNIPds formulations it was assumed that BNIPds may not be release from the particles, thus drug release experiment was investigated at high temperature (60 ºC) in water, up to 72 h (Figure 47D). The results

showed that less than 1.5 % of drug released from both PEGylated and unPEGylated formulations. This could be associated with the strong covalent dative bond between thiol group of drug and gold coating at the surface of the HNPs. Therefore, if laser irradiation was applied for these formulations, the drug will not be released inside the cells (by the temperate increase achieved through laser irradiation in this study (Figure 30)). However, some studies showed that adjustment of laser power and ionic strength can cleave Au-S bond (Poon *et al*. 2010). Therefore, this formulation may be considered in the future for thermoresposive drug delivery studies. Due to the low release rate of BNIPds from formulations, it was decided not to continue any further drug release studies at different temperatures and/or in biological media with these formulations.

3.3.3.2. *In vitro* drug release in biological media

Release of BNIPDSpm from hybrid formulations was tested in culture media at pH= 7.5, pH=4.6 and pH=3.6 at 37 ºC and 44 ºC up to 312 h to mimic cytoplasm (pHi =7.42), endosome and lysosome environment in pancreatic cancer cells, respectively (Figure 49) (Preissler and Williams, 1981). Release of BNIPDSpm from formulations was time, pH and temperature dependant. In general, like BNIPDSpm release pattern in water (Figures 47B and 47C), formulations showed a biphasic release profile due to an initial burst within 6 h, which is followed by a constant release. The highest release rate occurred in pH=3.6, at 44 ºC for PEGylated formulation (Figure 49B).

In 37 ºC, 50 % release from BNIPSDpm-HNP in pH=3.6, 4.6 and 7.5 occurred after 72 h, 96 h and 144 h, while these amount of drug released from PEGylated formulations after 6 h , 8 h and 24 h with the same pH mentioned above, respectively (Figure 49A). These data suggest that decreasing pH significantly enhanced the release rate of drug from both formulations ($p < 0.05$). Moreover, release rate of BNIPDSpm from PEGylayed formulation is significantly higher than the release from unPEGylated formulation ($p < 0.05$) (Figure 49A). After 312 h the drug completely released from both formulations at 37 ºC.

The same pattern was observed in 44 ºC, and again the higher release occurred in lower pH (Figure 49B). The release from PEGylated formulations was significantly higher than its

unPEGylated counterpart ($p < 0.05$). Half of the drug (0.5 mg) released from BNIPSDpm-HNP in pH=3.6, 4.6 and 7.5 after 24 h, 48 h and 72 h, while these amount of drug released from PEGylated formulations after 4 h , 6 h and 8 h with the same pH mentioned above, respectively (Figure 49B).

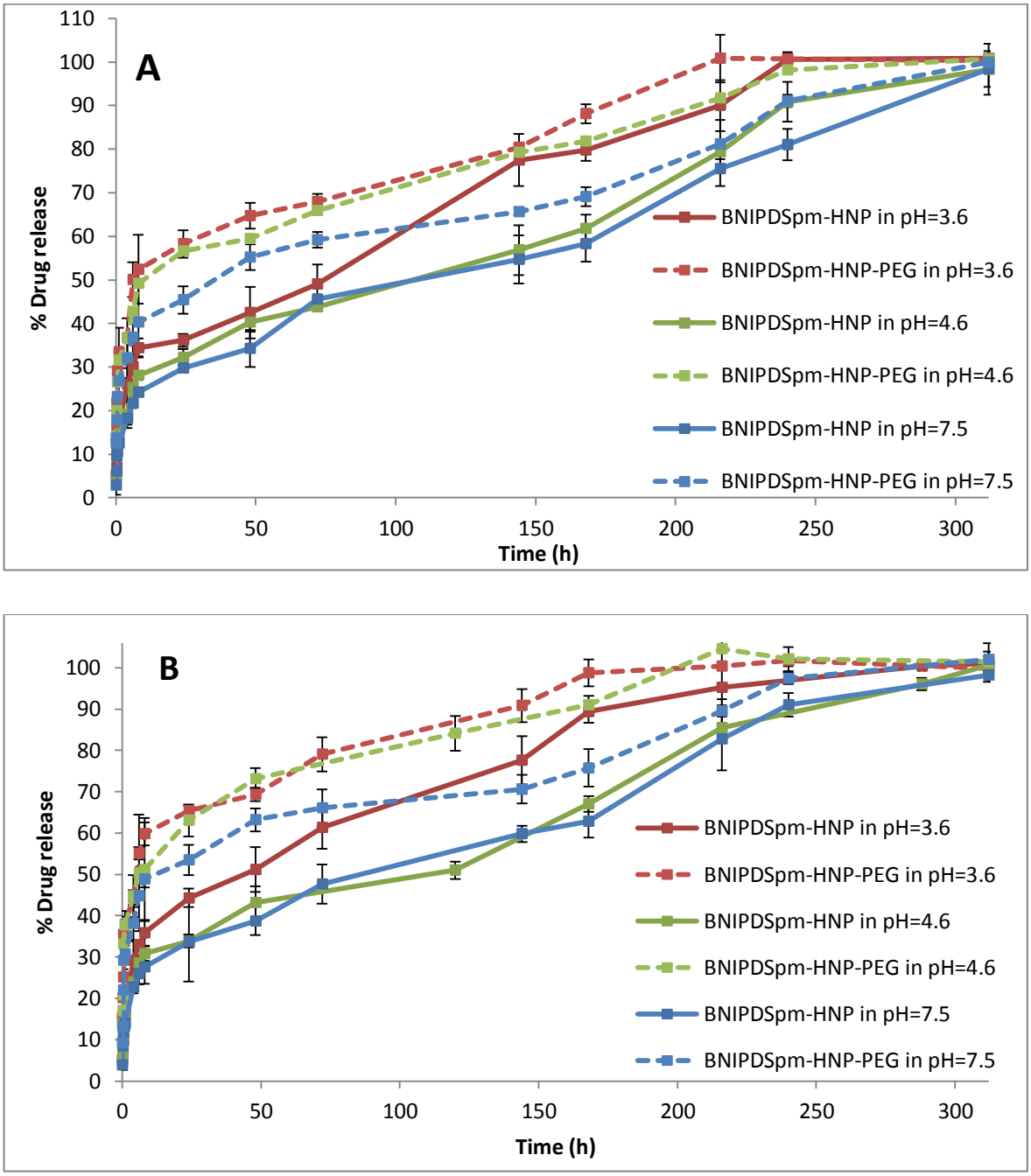

Figure 49. Drug release study for BNIPDSpm-HNP and BNIPDSpm-HNP-PEG at different pH in A) 37 ºC and B) 44 ºC for 312 h. All statistical analyses were carried out using t.test analysis within the Microsoft Excel software package (n=3, ave ± SD).

These data suggest that decreasing pH significantly enhanced the release rate of drug from both formulations as electrostatic interactions can be broken faster in lower pH ($p < 0.05$). After 288 h the drug completely released from both formulations at 44 ºC. The results confirmed that release of BNIPDSpm from the particles was greater/faster at lower pH and PEGylated formulation always possessed faster release compared to the unPEGylated formulation.

By analysing these data we suggest that when the BNIPDSpm-HNP-PEG particles cross the pancreatic cancer cell membrane and accumulate inside the lysosome (pH=3.6), at 44 ºC (achieved by laser irradiation), about 60 % of drug will be released in the first 8 h.

3.4. Discussion

Conjugation of drugs by electrostatic interactions onto the surface of HNPs is a novel strategy to deliver therapeutic agents into their site of action and few investigations have been performed in this area.

Recently, Barnett *et al*. fabricated hybrid iron oxide-gold NPs and a model drug, 6-Thioguanine (6-TG), was successfully conjugated to the surface of these particles with a ratio of 3:1:10 Fe:Au:6-TG. *In vitro* studies were carried out on human pancreatic adenocarcinom (BxPC-3) and differentiated human monocyte cells (U937). The cellular uptake increased with a 10-fold decrease in half maximal inhibitory concentration (IC_{50}) upon the conjugation of the drug with HNPs, compared with the free drug (Barnett *et al*. 2013a). In another study Barnett and co-workers fabricated and evaluated a new class of poly(allylamine) (PAA) polymer conjugated with hydrophobic oxadiazole (Ox) pendant group. They suggested that the thiol-containing pendant group can increase the attachment of HNPs by dative covalent bonding. Different drugs were conjugated via direct conjugation of hydrophilic and encapsulation of hydrophobic drugs. In comparison with the free drug, the conjugated drugs had significant higher drug uptake with decreased IC_{50} (Barnett *et al*. 2013b).

Wagstaff and colleagues reported the conjugation of cisplatin ($\{Pt(NH3)_2\}^{2+}$) via a thiolated polyethylene glycol linker (PEG-thiol) into the surface of iron oxide-gold NPs. The thiol groups in PEG-thiol conjugated to the gold surface by dative covalent bond

(Au-S chemistry), while attaching cisplatin via its terminal carboxylate groups. This novel formulation was up to 110-fold more cytotoxic than the drug alone. Interestingly, they explained that this nano-sized formulation could accumulate in specific regions by using an external magnetic field, which showed cell growth inhibition area for the treated cells by novel formulation (Wagstaff *et al*. 2012).

We have demonstrated the ability of our HNPs to conjugate with different bisnaphthalamide based drugs onto their surface via electrostatic interactions or covalent bonds. Drugs were successfully conjugated to the surface of HNPs and drug content in each formulation was analysed using HPLC. Different loading concentrations for each drug were used and the optimal loading concentration of them was achieved. In general, loading capacity of drugs are affected by a number of factors such as feeding concentration, the number of amine group, the presence of thiol group and PEG and the type of interaction between drug and HNPs (electrostatic or covalent). Data suggested that BNIDi cannot be conjugated to the surface of HNPs (even with the highest loading concentration) due to the lack of amine group which is essential for electrostatic interaction between bisnaphthalamide derivatives and HNPs. Our results demonstrate that between these drugs a significant amount of BNIPDSpm could be loaded on to the HNPs (with linear correlation between the drug feeding and attached concentration) (Figure 36), which is sufficient to achieve drug release in the range of µg with conservative concentration of HNPs. The presence/absence of drug in each formulation has been proved by zeta potential measurement (Table 6), FTIR (Figures 37-40) and fluorescent spectroscopy (Figures 41-44).

In general, number of amine group and the presence of thiol group or PEG in formulation affected particles surface charge. While the presence of amine groups increased the surface charge of the particles (Kardys *et al*. 2013), thiol group and PEG shifted the zeta potential toward negative values (Ku *et al*. 2010). This result is also indirect evidence demonstrating that the amino and thiol group and PEG are conjugated to the surface of HNPs.

FTIR spectra of BNIDi formulations confirmed the lack of drug inside the formulations (Figure 37) which is due to the absence of amine group in this drug discussed before. As a result, it was decided not to further study these formulations.

The conjugation of BNIPd to the HNP is due to the electrostatic interaction of two positive amine groups of this drug with the gold coating, as proved by the peak broadening of N-H

stretching vibrations of drug-HNPs in FTIR spectra (Figure 38). Previously, Selvaraj and colleagues suggested that -NH group of 5-Fluorouracil was involved in binding the drug onto the surface of gold NPs (Selvaraj *et al*. 2007). In another study, Aslam and co-workers explained that gold has a strong affinity towards the amino group (Aslam *et al*. 2004). Although the number of amine group is a crucial factor for electrostatic interaction of bisnaphthalamide derivatives to the surface of HNPs, the two central amines in bisnaphthalmide chain seem to have more affinity to the gold surface as BNIPDSpm with four amines attached significantly more than BNIPd and BNIPds to the surface of HNPs ($p < 0.05$) (Figure 36). Moreover, the stability (Figures 45 and 46) and drug release pattern (Figure 47) of formulations conjugated with BNIPDSpm and BNIPd confirmed that BNIPd formulations were not stable and they possessed fast release pattern. These results associated with the poor interaction of BNIPd with HNPs due to the number of amine group discussed before. Instability and fast drug release from BNIPd formulations made them unsuitable for drug delivery system. BNIPDSpm (with four amine groups) formulations were quite stable for the period of 4 weeks and showed different release pattern at different temperature, solutions and pH.

In general, BNIPDSpm release from formulations in water and culture media showed biphasic patterns, which include a sharp release in the first 10 h following by a gradual release. For drug release in water, PEGylated formulations showed significant higher drug release compared to unPEGylated formulations, especially in 60 ºC, where nearly 73 % of BNIPDSpm was released up to 8 h ($p < 0.05$) (Figure 47C).

BNIPds is conjugated by covalent dative bond through –SH group of the drug with Au at the surface of particles. Au–S bonds are quite strong, approximately 40 kcal mol^{-1} (Ulman, 1996), which is nearly half the strength of a C–H or C–C bond. This strong bond resulted in high optimal loading concentration (Figure 36) and high stability (Figures 45 and 46). But due to this robust interaction, less than 2 % of the drug released in 60 ºC, after 72 h (Figure 47D). This means that BNIPds formulations cannot be used in drug delivery system as the drug will not be release even in high temperature.

In cancer therapy, many drugs such as small molecule chemotherapeutic agents, siRNA, DNA and proteins have to be delivered by a carrier and released into the particular cellular compartments, which is usually cytoplasm or nucleus of cancer cells. Intracellular environment-responsive NPs, which possess high extracellular stability while rapidly

releasing their cargo inside cancer cells have been enormously investigated for improving cancer therapy (Park *et al*. 2006). The pH of cancer cells in the endo/lysosomal compartments is slightly acidic in comparison with normal cells (Figure 50). This naturally existing environment has been vigorously exploited as an internal stimulus to trigger drug release from NPs inside cancer cells. Particularly, these intracellular pH-responsive NPs have shown higher antitumor effects in comparison with non-responsive NPs; as a result of quicker and more efficient drug release in cancerous cells (Meng *et al*. 2009).

However, these NPs have experienced different levels of success *in vitro* and *in vivo*, probably due to the diversities in the responsive compartments such as lysosome, endosome, cytosol and nucleus. Furthermore, for *in vivo* studies, these bio-responsive NPs have to also present high stability in blood circulation system (Lammersa *et al*. 2012).

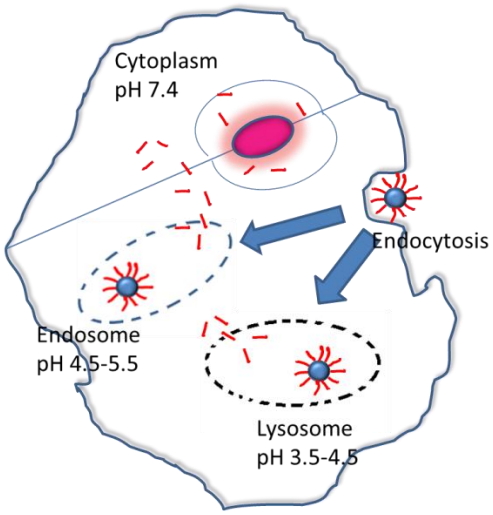

Figure 50. Schematic diagram of intracellular pH-responsive NPs for "active" drug release inside pancreatic cancer cells. The release of drug can be triggered by following two pathways: (i) mildly acidic pH (4.5-5.5) induced drug release in endosomal compartments and (ii) low pH (3.5-4.5) caused drug release in lysosomes.

pH-sensitive NPs that are susceptible to release at endo/lysosomal pH have been fabricated based on formulations possessing protonable amine groups (primary, secondary and tertiary amines). Electrostatic interactions that respond to pH variations can be broken at lower pH. For example, Bae and colleagues suggested that doxorubicins (Dox)-loaded micelles released Dox in a pH-dependent manner and enhanced higher growth inhibition of

human colon tumour at acidic than basic pH. They designed pH responsive drug delivery system in order to release Dox into the cytoplasm via sensing low pH in endosomes (Bae *et al*. 2005).

Recently, Nam *et al*. described a new thermo-pH responsive drug delivery containing 10 nm gold NPs conjugated with Dox, *in vivo*. This novel nanocarrier was able to aggregate in mild acidic environment such as in tumour tissues. By applying laser irradiation, these particles produced heat resulting in Dox release from the particles inside the tumour cells. They revealed that Dox accumulated in tumours up to 17 times over the control due to the enhanced permeation and retention effect (Nam *et al*. 2013).

In our study BNIPDSpm drug release in culture media followed the same pattern of release in water; however, decreasing the pH of media and increasing the temperature (from 37 ºC to 44 ºC) enhanced the drug release rate (Figure 49). These results also showed that BNIPDSpm released in culturing media from HNP-PEG significantly faster than unPEGylated formulation ($p < 0.05$).

Investigation of drug release pattern in culturing media, in 37 ºC and 44 ºC, was crucial for us. Because as described in Chapter Two (Section 2.3.8), 44 ºC would be the temperature of the HNPs upon laser irradiation. Therefore, by *in vitro* drug release investigations in culturing media (in body temperature and 44 ºC), the release pattern of the formulations inside the pancreatic cancer cells, before and after laser irradiation can be predicted.

As a result, BNIPDSpm hybrid formulations showed pH and thermoresponsive drug delivery properties. Therefore, it is assumed that after accumulation of the NPs in endosome and lysosome, the low environmental pH and increasing the temperature through laser irradiation, will result in quick drug release from the particles. Then the free drug can enter cells` nucleus and interact with DNA for anticancer effect.

3.5. Conclusion

It was demonstrated that the type of interaction between bisnaphthalamide derivatives and HNPs had a direct impact on conjugation ability, stability and drug release pattern of hybrid formulations. BNIPDi with no amine group was not able to conjugate with HNP; however, stronger interaction of drug-NPs was achieved by increasing the number of amine from BNIPd to BNIPDSpm. Conjugation of BNIPds with HNPs confirmed that exploiting Au-S chemistry is possible for conjugation of a molecule possessing thiol group to the gold coating surface. This covalent bond resulted in highest stability between bisnaphthalamide hybrid formulations and cannot be broken with the produced heat achieved by laser irradiation in this study. Within four different bisnphthalamide drugs, BNIPDSpm (with four amine groups) formulations possessed the highest loading capacity to the surface of HNP, good stability and thermo-pH responsive drug delivery properties. Drug release study of BNIPDSpm formulations showed that faster release was obtained by increasing the temperature and reducing the pH (close to the pH of intracellular organelles). Moreover, PEGylated formulations mostly revealed greater release of drug in comparison with their unPEGylated counterparts.

Chapter Four

Biological characterisation of novel bisnaphthalmide based formulations

4.1. Introduction

The usual approach in cancer treatment with chemotherapeutic agents comprises of the systemic administration of one or more cytotoxic drugs intravenously which do not possess tumour specificity (Worns, 2013). This lack of specificity results in the normal cells being affected leading to undesirable patient side effects. Various techniques have been reported to enhance the efficacy of anticancer agents such as increasing the solubility or uptake rate of drugs by cancer cells, targeted delivery to tumour (Jeanbart *et al*. 2014) and mitochondria targeted drugs delivery (Modica-Napolitano and Weissig, 2015); however, many of them failed to improve the specific delivery of chemotherapeutic agents. It is estimated that 40 % -70 % of all new compounds identified in drug discovery programs are insufficiently soluble in aqueous media (Lindenberg *et al*. 2004). Some of drug carriers have side effects on normal tissues and organs. Another drawback is the inability of formulation to selectively target tumour cells. Moreover, the resistance of cancer cells to the chemotherapeutic agents remains a significant impediment to successful chemotherapy (Chakraborty and Rahman, 2012). This is particularly true for pancreatic ductal adenocarcinoma (PDAC). PDAC is a deadly disease which is characterised by a dense stroma. Studies have shown that the epithelial and stromal compartments interact to increase the aggressive nature of this cancer (Rasheed *et al*. 2012). Therefore, it is crucial to develop anticancer therapies targeting the stroma and epithelial cells, which may play a prominent role in clinical outcome improvement for patients with this highly lethal disease.

Before a new drug or a novel drug delivery system is deemed clinically suitable and able to be marketed, they have to go through rigorous testing and cost-effectiveness analyses, both in preclinical and clinical studies. Initial characterisations of new compounds are usually followed by *in vitro* (in Latin means within the glass) investigations, where novel formulations are tested on mammalian cells outside their normal biological context. The complexity of cells inside the body is a great obstacle to the determination of interactions between the drug/formulation and biological compartments and the investigation of their basic biological functions. By *in vitro* analyses, *in vivo* fate of the drug/formulation can be estimated. This can be achieved by *in vitro in vivo* correlations (IVIVC) that play a key role in the drug development and optimisation of formulation (Vignais and Vignais, 2010). Therefore, *in vitro* work (tissue culture) offers the potential of avoiding variations

occurring *in vivo* (Freshney, 2005). However, it might be challenging to generalise from the results of *in vitro* work back to the biology of the living organism and give a true representative of *in vivo* conditions (Rothman, 2002). As such these investigations are normally followed by *in vivo* studies using appropriate models in small animals.

4.1.1. Investigation of bioavailability

It is crucial to verify the biocompatibility or cytotoxicity of a novel formulation *in vitro* before introducing to *in vivo* environments. In nano drug delivery systems, bioavailability, uptake and pharmacokinetics of NPs to organisms are key factors to toxicity. Therefore, many *in vitro* assays have been used, such as cytotoxicity assays and drug uptake analysis. These experiments are simple, reproducible and not as expensive or ethically charged as *in vivo* tests. Moreover, NPs as carriers of cytotoxic agents must not be toxic and any increase in cytotoxicity must be due to synergistic effects of chemotherapeutic agents.

4.1.1.1. Cytotoxicity assay

4.1.1.1.1. MTT assay

3-[4,5-dimethylthiazol-2-yl]-2,5-diphenyltetrazolium bromide (MTT) assay is a standard colorimetric assay for assessing cell metabolic activity and verifying the cytotoxic effect of a new compound or formulation when introduced to the cells. The test is based on treating cells in their exponential growth phase with a formulation for a desired period of time (usually between 24-72 h) (Lamprecht *et al.* 2000). Then the formulation is replaced with MTT solution. Inside the cells, NAD(P)H-dependent cellular oxidoreductase enzymes can reflect the number of viable cells present. As these enzymes can reduce the yellow MTT solution to its insoluble formazan, which is identified by a purple colour. Therefore, the percentage of cell viability can be calculated and half maximal inhibitory concentration (IC_{50}) can be determined. This can be achieved by dissolving the formazan crystal in dimethyl sulfoxide (DMSO), following measuring the absorbance formazan solutions by a

microplate reader. It has been reported that 4 h is the optimal time for cells to be incubated with MTT, in order to achieve accurate viability determination (Carmichael *et al*. 1987).

In this study MTT assay was utilised to investigate the toxicity of bisnaphthalamide based drugs, hybrid nanoparticles (HNPs) and novel formulations and comparing them to commercial anticancer drug, gemcitabine.

Microplate reader

Microplate reader (plate readers or microplate photometers) is an instrument which has been used for biological and chemical detections of samples in microtiter plates, usually 96 wells plate (8 by 12 matrixes). They have been enormously utilised in bioassay validation, drug discovery, manufacturing processes and quality control tests in the pharmaceutical companies and research organisations. The volume of sample in each well is usually between 100-200 µL per well. This instrument works by the detection of samples` absorbance, fluorescence intensity, time-resolved fluorescence, luminescence, and fluorescence polarisation (Mosmann, 1983).

4.1.1.1.2. Trypan blue assay

Trypan blue (TB) exclusion assay is one of the oldest and is still one of the most common methods for measuring cell viability. Trypan blue is a vital stain (diazo dye), which is able to stain dead cells blue (due to their more permeable cell membrane). But it cannot colour live cells with intact cell membrane as it is not adsorbed by intact live cell membranes. Therefore, this assay has the potential to identify and enumerate live (unstained) and dead (blue) cells in a given population (Tennant, 1964). The live cells can be counted by an automated cell counter or by a microscope. Then the IC_{50} value can be calculated regarding the number of control cells. In this test, cells in their exponential growth phase are incubated with formulation for a period of time and then treated cells solution will be mixed with trypan blue with the ratio of 1:1 and the number of viable cells is counted.

This assay can be a complimentary test for the MTT results, in order to achieve accurate IC_{50} value.

4.1.2. *In vitro* cellular uptake of formulation

It is important to track a formulation on its cellular journey in order to investigate how the NPs enter the cell and to prove that the site of action for payload release is reached. Many parameters can affect cellular uptake of particles such as shape, stiffness and charge of NP.

The shape of particles is a crucial factor, which can modify the rate of cellular uptake and blood circulation time. Different shapes of NPs have been used in drug delivery systems, such as disk-like, spherical, rod-like, and flexible in shape (Petros and DeSimone, 2010). However, the influences of shape on cellular uptake have been challenging to analyse because most NPs have spherical shape.

The rigidity of NP can also influence distribution and cellular uptake. There are few studies to demonstrate that different types of cells have different preferences for NPs uptake. As an example, while soft NPs such as polymeric NPs can be taken up better than hard NPs (e.g. metalic NPs) by HeLa cells (You and Auguste, 2009), macrophages have the ability to uptake hard ones (Beningo and Wang, 2002).

The NP surface charge can influence the particles distribution, tissue retention and cellular uptake, which has to be well understood to target the delivery of particles. Many studies have been performed to investigate the relation between the surface charge of the particles and their cellular uptake. Most of them proposed that in most cell lines, higher uptake can be achieved by positively charged NPs, which might be due to the charge-charge interaction with the negative cell membrane. However, there are some exceptions for some stem cells such as mesenchymal stem cells (due to the differences in endocytotic/pinocytotic properties of the cell lines) (Lorenz *et al*. 2006) and certain macrophages (macrophage uptake increases with the surface charge increasing (either positive or negative)) (Gratton *et al*. 2008).

The effect of particle size and surface charge on cellular uptake and biodistribution of polymeric NPs was shown in an interesting study by He *et al*. Rhodamine B labeled carboxymethyl chitosan grafted NPs and chitosan hydrochloride grafted NPs were developed as the model negatively and positively charged polymeric NPs, respectively. The result revealed that NPs with large particle size and high surface charge were phagocytised more efficiently by murine macrophage. *In vivo* bio-distribution suggested

that NPs with slight negative charges (-15 mV) and particle size of 150 nm were tended to accumulate in tumour more efficiently. This is positively correlated with *in vitro* murine macrophage uptake assessment. As Rhodamine B labeled carboxymethyl chitosan grafted NPs (-15 mV, 150 nm) possessed the lowest distribution percentage in liver and spleen (He *et al*. 2010).

In this work *in vitro* cellular uptake assay was used to measure the drug accumulation in cells. The concentration of compounds in *in vitro* assays is usually named as the nominal mass dose, which is quoted in units of microgram/picogram of compounds per millilitre (μgmL^{-1}/ $pgmL^{-1}$) (Lison and Huaux, 2011). Therefore, by knowing the number of the cells in each experiment, the concentration of taken up drug in each cell can be calculated.

4.1.3. Atomic Force Microscopy

Atomic force microscopy (AFM) is a kind of scanning probe microscopy (SPM), with very high resolution. SPMs are aimed to identify physical properties, for example height, magnetism and friction with a specific probe. AFMs work through quantifying force between the sample and a probe. Usually, AFMs` probe has a sharp tip, which is like 3-6 micrometres tall pyramid (Figure 51) (Binnig *et al*. 1986). Therefore, information is generated by "feeling" or "touching" the surface with this probe. AFM is capable to scan samples in nanometres and shows the roughness and hardness of a samples surface or cells with very high resolution. Piezoelectric elements, which make really small movements with high accuracy on (electronic) command, are capable to scan samples very precisely (Binnig *et al*. 1986). By using AFM, researchers can distinguish cancer cells from normal cells through the hardness of the cells. Moreover, the interaction between a specific cells and the effect of a chemotherapeutic agent on a certain cell line can be analysed.

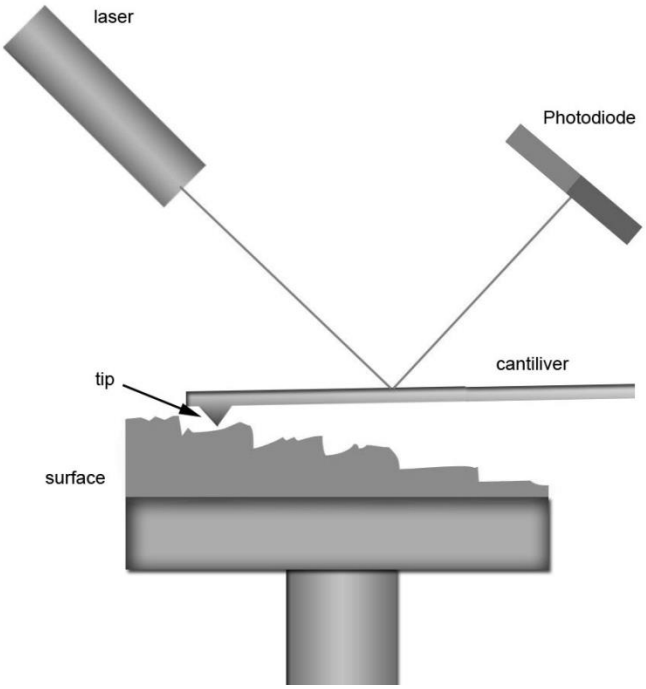

Figure 51. Drawing of basic principle of Atomic Force Microscope (AFM).

Compared to the optical microscope and an electronic microscope, AFM has no lens and beam irradiation. Thus, there is no limitation of space resolution due to a diffraction limit. Moreover, in this technique, there is no need for staining of the sample.

In this study, AFM topography imaging can help to investigate the surface and morphology of the treated cells with different formulations, compared to the control cells.

4.1.4. Arginine-glycine-aspartic acid (RGD) Peptides

In 1999, Buckley and colleagues discovered arginine-glycine-aspartic acid (RGD) peptide as cell attachment site in fibronectin. They found that RGD peptides were able to inhibit tumour metastasis and induce cell apoptosis (Buckley *et al*. 1999). After that, RGD derivatives have been considerably used in studies of cell migration, adhesion, apoptosis and growth by RGD-integrin interactions.

RGD peptides have high affinity to integrin αvβ3, which plays a significant role in tumour angiogenesis. Integrin αvβ3, is a receptor for the extracellular matrix proteins with the exposed RGD tripeptide sequence (Hwang and Varner, 2004). Integrin avβ3 is expressed

on many different types of cancer including pancreatic cancer. However, in this type of cancer, integrin avβ3 is expressed both on primary tumours and on metastatic tumours (Hosotani *et al*. 2002) making it an ideal targeting peptide.

Cyclo(-Arg-Gly-Asp-D-Phe-Cys) peptide or c(RGDfC) (Figure 52) is an RGD tumour-targeting peptide, which can bind to αvβ3 receptors. C(RGDfC) can be easily attached to drugs or surfaces of NPs (Kilian and Mrksich, 2012; Pattillo *et al*. 2005). For example, Pattillo and colleagues incorporated combretastatin into long circulating liposomes. Then c(RGDfC) peptide was conjugated to maleimide functional groups of the liposome on the distal end of PEG chains (Pattillo *et al*. 2005).

In this study, a new approach to link c(RGDfC) peptide to the bis(naphthalimidopropyl) spermine PEGylated hybrid formulation (BNIPDSpm-HNP-PEG) is presented with the goal of targeting integrin avβ3 to increase drug specific delivery and anticancer activity, which will be compared to the formulations without the targeting peptide. This peptide can be conjugated to the surface of HNPs via its thiol group (dative covalent bond) in the cysteine residue in its structure (Figure 52).

Different bisnaphthalamide based drugs alone and in conjugation with HNPs and PEGylated HNPs (HNP-PEG) will be tested *in vitro*, in case of their cytotoxic effects (using MTT assay and trypan blue test). Drug uptake potentials of drug alone and drug-loaded formulations will be analysed on human primary pancreatic adenocarcinoma (BxPC-3), human epithelial-like pancreatic carcinoma (PANC-1) and human monocyte cell line which exhibits macrophage like qualities after differentiation (U937). The latter cell line will be used in order to investigate the cytotoxic effect of drugs and different formulations on immune cells. All results will be compared to the cytotoxic effect of gemcitabine as a control drug.

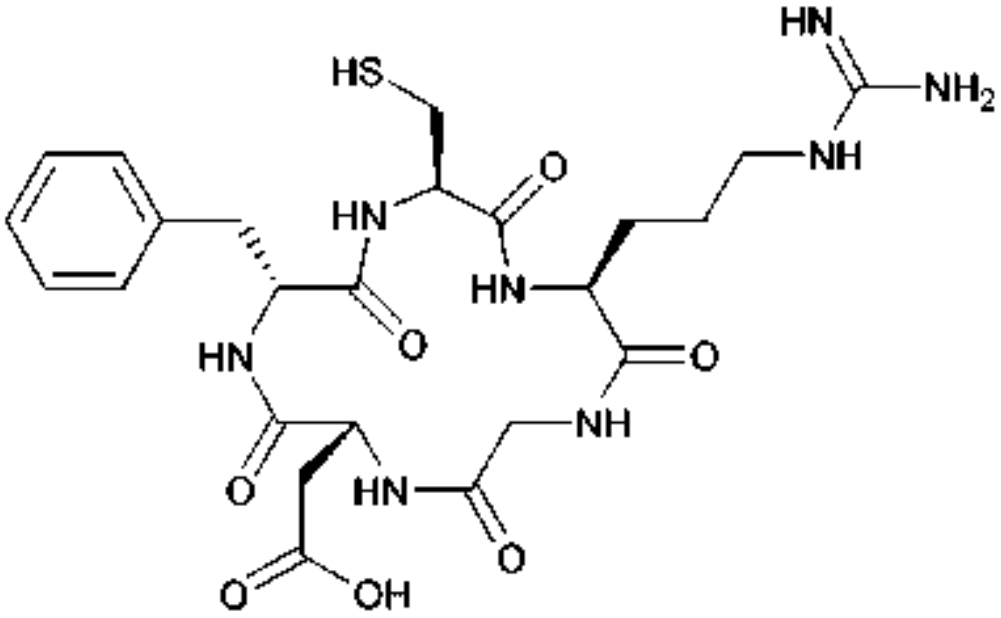

Figure 52. Chemical structure of c(RGDfC)

C(RGDfC) targeting peptide will be conjugated to BNIPDSpm-HNP-PEG to investigate the cytotoxic effects and drug uptake of this novel formulation on all three cell lines, mentioned before. *In vitro* thermoresponsive drug delivery at various temperatures will be carried out to simulate the temperature increase gained upon laser irradiation. AFM topography imaging will be performed to visualise cells surface before and after treatment with drugs and formulations.

4.1.5. Aims and Objectives

The aim of this work is to determine how effective HNPs are as carriers for cytotoxic agents and assess the clinical potential of the bisnaphthalamide formulations in the treatment of pancreatic cancer.

4.2. Materials and Methods

4.2.1. Materials used

Table 10. Materials used in biological investigations.

Materials	Suppliers
Gemcitabine	Sigma-Aldrich Co., UK
Cyclo(-Arg-Gly-Asp-D-Phe-Cys) peptide	Bachem Co., Switzerland
HPLC Grade ethanol	Fisher Scientific, UK
Thiolated poly ethylene glycol (PEG-thiol)	Sigma-Aldrich Co., UK
PRMI culture medium	Life technologies Co., UK
DMEM culture medium	Life technologies Co., UK
Trypsin-EDTA 0.05 %	Life technologies Co., UK
Foetal bovine serum	Fisher Scientific, UK
Phorbol-12-myristate 13-acetate (PMA)	Sigma-Aldrich Co., UK
Phosphate buffered saline	Fisher Scientific, UK
L-glutamine	Sigma-Aldrich Co., UK
Penicillin streptomycin	Life technologies Co., UK
Cell freezing medium-DMSO	Sigma-Aldrich Co., UK
Highly purified water	MillexQ system (UK)
Acetonitrile	Sigma-Aldrich Co., UK
Octane sulfonic acid	Sigma-Aldrich Co., UK
Sodium acetate	ACROS Organics Co., USA
HPLC Grade hydrochloric acid	Sigma-Aldrich Co., UK
HPLC Grade trifluoroacetic acid	Fisher Scientific, UK
HPLC Grade dimethyl sulfoxide	Sigma-Aldrich Co., UK
Glutaraldehyde	Sigma-Aldrich Co., UK
3-[4,5-dimethylthiazol-2-yl]-2,5-diphenyltetrazolium bromide (MTT)	Sigma-Aldrich Co., UK
Bis(naphthalimido)-1,12-diaminododecane (BNIPd)	Synthesised by Keele Nanopharmaceutics Research group
Bis(naphthalimidopropyl)spermine (BNIPDSpm)	Synthesised by Keele Nanopharmaceutics Research group
Bis(naphthamimidopropyl)-3,3`-(butane-1,4-diylbis(sulfanediyl))bis(propan-1-amine) (BNIPds)	Synthesised by Keele Nanopharmaceutics Research group
Hybrid nanoparticles (HNPs)	Synthesised in Chapter Two
BxPC-3 cell line (Passage number:10)	LGC Standards Co., UK
PANC-1 cell line (Passage number:10)	LGC Standards Co., UK
U937 cell line (Passage number:10)	LGC Standards Co., UK

4.2.2. Methods

4.2.2.1. Cytotoxicity Assay

4.2.2.1.1. MTT([3-(4,5-Dimethylthiazol-2-yl)2,5Diphenyltetrazolium Bromide]) cytotoxicity assay

BxPC-3, PANC-1 and U937 cells were cultured in their medium (RPMI medium for BxPC-3 and U937 and DMEM medium for PANC-1) supplemented with 1 % penicillin/streptomycin and 10 % foetal bovine serum (1 % of L-glutamine is also added to PANC-1 and U937 cell culture medium). The maximum passage number of 10 was used for all cell lines during the biological studies and cells were sub cultured when the confluency reached to around 75 %. In order to supply differentiated U937 cell line, 0.02 % of phorbol-12-myristate 13-acetate (PMA) (50 μgmL^{-1} in PBS) was added to the cells suspension. All three different cells (100 µL, 15000 cells/well) in exponential growth phases were seeded into 96 well flat bottomed plate and incubated for 24 h at 37 °C with 5 % CO_2. After 24 h, the media was replaced with various concentrations of gemcitabine, free bisnaphthalamide based drugs, naked HNPs and novel formulations, diluted in cellular growth medium (Table 11). Cells were incubated for further 24 h at the same condition discussed before.

A 20 $mgmL^{-1}$ of each free drug solution was prepared using 50:50 of sterile water:DMSO as the diluent to form a stock solution. From the stock solution, eight dilutions (0.1 - 1×10^{-5} $mgmL^{-1}$) were made using media as the diluent (Table 11). Media and sterile water were the positive and negative controls, respectively (Figure 53). After 24 h, the drug solutions were removed and washed with fresh media to remove any excess drug. Fresh media was replaced into the wells (100 µL). 3-[4, 5-dimethylthiazole-2-yl]-2, 5-diphenyl tetrazolium (MTT, 50 µL, 5 $mgmL^{-1}$ in PBS) was added to the wells and plate was incubated (37 °C with 5 % CO_2) for 4 h. After this time, the MTT solution was removed from the wells. The remaining purple formazan complexes were dissolved in DMSO (100 µL) and the absorbance of the plates was read at 570 nm using a microplate reader (Tecan, infinite 200 pro, GmbH 5082, Australia). Percentage cell viability and IC_{50} was calculated relative to the positive and negative controls (Equation 8) (all biological studies were run in triplicate (n=3) and recorded as average values).

Table 11. Preparation of anticancer drug solutions for MTT assay (0.1 - 1×10^{-5} $mgmL^{-1}$).

*: Sample was made from 0.05 $mgmL^{-1}$ concentration as a stock solution.

Drug concentration ($mgmL^{-1}$)	**Volume of 20 $mgmL^{-1}$ drug stock solution (µL)**	**Volume of media (mL)**
0.1	22.5	4.5
0.05	11.5	4.5
0.025	5.6	4.5
0.01	2.25	4.5
0.005	1.125	4.5
* 0.001	90	4.5
* 0.0001	9	4.5
* 0.00001	1	4.5

In order to prepare the same concentration of drug (Table 11) within hybrid formulations, the initial hybrid formulations were used as a stock solution and the same concentrations of drug discussed in Table 11 were prepared. Moreover, the concentrations made for HNP alone (without drug) indicates the concentration of iron oxide in hybrid formulations (HNP-drug).

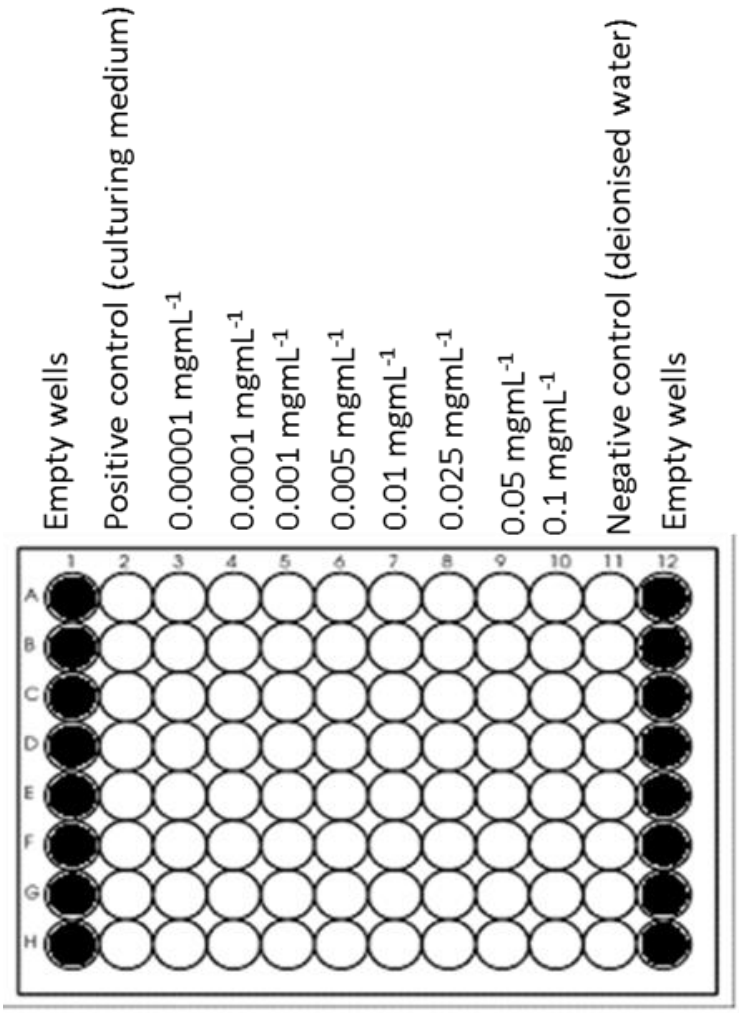

Figure 53. Illustration of different concentrations, positive and negative controls in 96-well plate for MTT assay.

$$\% \text{ Cell viability} = \frac{(\text{Abs of sample - Abs of negative control})}{(\text{Abs of positive control - Abs of negative control})} \times 100 \quad (8)$$

4.2.2.1.2. Trypan blue cytotoxicity test

BxPC-3, PANC-1 and U937 cells (1 mL, 50000 cells/ well) in exponential growth phase were seeded into 12-well flat bottomed plates and incubated for 24 h at 37°C with 5 % CO_2. The media was replaced with drugs, HNPs and novel formulations at various concentrations as previously described. Cells were incubated for 24 h, subsequently the media was removed and cells were washed 3 times with PBS. The cells were trypsinised and re-suspended in fresh media. A mixture of 50 µL of cells and 50 µL of trypan blue solution was placed in an automated cell counter (Invitrogen Countess®, UK) and viable cells were counted. Percentage cell viability and IC_{50} were calculated in relation to the number of control cells as described in Equation 9.

$$\% \text{ Cell viability} = \frac{\text{Number of live cells in sample}}{\text{Number of control cells}} \times 100 \quad (9)$$

4.2.2.2. *In vitro* cellular uptake of formulations

BxPC-3, PANC-1 and U937 cells (3 mL, 150000 cells/ well) in their exponential growth phase were seeded into 6-well plates and incubated for 24 h at 37° C with 5 % CO_2. The media was replaced with 50 µgmL^{-1} & 100 µgmL^{-1} of different bisnaphthalamide based drugs, their hybrid formulations and gemcitabine and incubated for 1 h and 4 h. The medium was removed and each well was washed with 1 mL PBS before the addition of 185 µL trypsin into each well. Cells re-suspended in 1 mL media and viable cells were counted using an automated cell counter (Invitrogen countess®, UK). Cells (100,000) were transferred into the eppendorf tubes and centrifuged (800 rpm, 5 min). The supernatant was removed and cells were resuspended in DMSO:water (1:1) (for samples containing bisnaphthalamide derivatives) or water (for samples containing gemcitabine).

The concentration of bisnaphthalamide derivatives and gemcitabine were quantified using reverse phase high performance liquid chromatography (HPLC) (cells were transferred from 6-well plates into Eppendorf tubes). Characterisation and quantification of bisnaphthalamide derivatives were performed by reverse phase HPLC (Prominence,

Degasser, LC20AD, Shimadzu) using a fluorescent detector at Excitation 234 nm and Emission 394 wavelengths, which discussed in Chapter Three (Section 3.2.2.2.1). For gemcitabine detection, an HPLC with UV detector (Perkin Elmer, Flexar Autosampler, column: SPHERISORB ODS 2 5µm, length 250 mm, internal diameter 4.6 mm) and a mobile phase contained H_2O and acetonitrile (30:70) were used. The standard solutions of gemcitabine were scanned in the range of 200-400 nm against mobile phase as a blank. Gemcitabine showed maximum absorbance at 234 nm. Therefore, samples were detected at 234 nm with flow rate of 1 mL. The limit of detection and limit of quantitation were 0.1498 and 0.4541 μgmL^{-1}, respectively (Rao *et al*. 2007). A calibration was run using gemcitabine solutions, dissolved in H_2O with the concentration of 300-18.75 μgmL^{-1} ($R^2 = 0.999$) (Appendix, Figure 7E). All measurements were run in triplicate and recorded as average values.

In drug uptake method the concentration of drug accumulated in each cell was calculated relative to the total number of cells in each sample (cells were counted by an automated cell counter).

4.2.2.3. Peptide conjugation to PEGylated formulation and characterisation of the new formulation

To a solution of HNPs (1 $mgmL^{-1}$, 5 mL), 25 mg BNIPDSpm (dissolved in 5 mL deionised water), 1 mg c(RGDfC) peptide and 25 mg PEG-thiol were added. The solution was stirred for 3 h before magnetically separating and extensively washing with deionised water. The amount of attached drug and peptide was quantified by RP-HPLC (Prominence, DEGASSER, LC20AD, SHIMADZU) using the same fluorescence detector with the same column discussed in Chapter Three (Section 3.2.2.2.1). c(RGDfC) peptide was detected by a mobile phase containing solvents A and B (50:50). Solvent A was water containing 0.09 % trifluoroacetic acid (TFA) and solvent B was acetonitrile containing 9.91 % H_2O and 0.09 % TFA (Jin *et al*. 2007). The Excitation and Emission wavelengths were 250 nm and 307 nm, respectively. A flow rate of 1 $mLmin^{-1}$ was employed. The aqueous sample (1 mL) was diluted with 1 mL of acetonitrile and 20 µL of the mixture was injected into the HPLC. A calibration was run using drug solutions, dissolved in 50:50 H_2O: acetonitrile with the concentration of 0.312-0.030 μgmL^{-1} ($R^2 = 0.9999$). The amount of attached drug

was calculated from the amount of free drug in waste solution, detected via HPLC. All measurements were run in triplicate and recorded as average values.

4.2.2.4. *In vitro* thermoresponsive cytotoxicity assay

BxPC-3, PANC-1 and U937 cells (3 mL, 150000 cells/ well) in their exponential growth phase were seeded into 6-well plates and incubated for 24 h at 37 °C with 5 % CO_2. Cells treated with 50 μgmL^{-1} of drugs and formulations and incubated for 1 h. Then, cells were further incubated at 25 ºC, 44 ºC and 60 ºC for 0.5 h, in order to investigate the effect of temperature on cell cytotoxicity. Then the drug solutions were removed and cells were washed with fresh media to remove any excess drug. Fresh media was then added to each well. After 24 h incubation (37 °C, 5 % CO_2), media was removed and cells were washed with PBS. The cells were trypsinised and re-suspended in fresh media. A mixture of 50 µL of cells and 50 µL of trypan blue solution was placed in an automated cell counter and viable cells were counted. Percentage of cell viability was calculated regarding to the number of control cells as discussed before (Equation 9). MTT test was not used in this method as the volume (100 µL) in each well (in 96-well plate) was not enough to grow a large number of the cells. Therefore, after heating the cells, the number of the cells might be lower than the minimum limit number of cells counted by automated cell counter ($< 1\times10^{4}$).

4.2.2.5. AFM topography imaging

BxPC-3, PANC-1 and U937 cells (3 mL, 150000 cells/ well) were seeded in 6-well plates containing glass coverslips. Cells were incubated for 24 h at 37 °C and 5 % CO_2. After 24 h the media was replaced with gemcitabine, BNIPDSpm, BNIPDSpm-HNP, BNIPDSpm-HNP-PEG, BNIPDSpm-HNP-PEG-c(RGDfC) and naked HNPs solution (50 μgmL^{-1}) and further incubated for 1 h and 4 h. After abundant washing with PBS, cells were fixed with 1 mL gluteraldehyde (2.5 % in PBS) for 10 min. Fixed cells were washed 5 times with PBS and mounted on glass slides. Cell topography was imaged by a Bruker Catalyst Atomic Force Microscope (Bruker, Germany) using Peak Force Tapping Mode

and a ScanAsyst in contact mode in air (using silicon tip (Bruker, T: 650 nm, L: 115 µm, W: 25 µm) on nitride lever).

4.3. Results

4.3.1. Cytotoxicity of drugs and formulations

Cell viability of BxPC-3, PANC-1 and U937 cells incubated with unloaded HNPs were determined by the MTT cytotoxicity test and trypan blue exclusion assay (Figures 54A and 54B). The concentrations show in the graph for HNP are equal to the concentration of hybrid formulations but obviously without drug (the concentrations of Fe in HNP and hybrid formulations are the same). Generally, both cytotoxic assays exhibited comparable results and the HNPs did not present a remarkable dose responsive effect on cell viability (over the concentration range tested). Cytotoxicity of HNPs was slightly different in each cell line. No significant reduction in viability was observed over the 24 h period up to 25 μgmL^{-1} ($p > 0.05$). HNPs did not show apparent toxicity to all three cell lines after 24 h incubation at concentrations up to 50 μgmL^{-1} ($p > 0.05$). However, after 24 h incubation with the highest concentration of HNPs (100 μgmL^{-1}) a 19-23 % decrease in viability was obtained ($p < 0.05$). This is much more concentrated than would ever be expected to be administered in the drug formulation to a patient in the clinic (Cortajarena *et al*. 2014). Regarding to our biological investigation, which will be discussed in this chapter later, the concentration of iron oxide in a formulation with half maximal inhibitory effect is less than 10 μgmL^{-1}. These findings demonstrated that these particles do not have high toxicity to BxPC-3, PANC-1 and U937 cell lines.

MTT cytotoxicity assay and trypan blue exclusion test were utilised to determine the drug concentration at which only 50 % of the cells population were viable (IC_{50}). Drugs with lower IC_{50} values have a greater cytotoxic effect. The cytotoxicity of different bisnaphthalamide based drugs (BNIPd, BNIPDSpm and BNIPds) was tested against the BxPC-3 cells after 24 h (Figure 54C). The IC_{50} value was analysed by GraphPad Prism 6 software (Figure 54). In general, all three bisnaphthalamide based drugs a presented dose responsive effect on cell viability.

BNIPd possessed the highest cytotoxic effect on BxPC-3 cells and no cells were viable above the concentration of 0.005 $mgmL^{-1}$ (Figure 54C). Therefore, the treated concentrations of BNIPd were modified (0.005 - 1.0×10^{-5} $mgmL^{-1}$) in order to investigate the IC_{50} value accurately (Figure 54D). This drug had a significant reduction on cell viability from 1 μgmL^{-1} treating concentration after 24 h ($p < 0.05$). IC_{50} was achieved around the concentration of 3 μgmL^{-1} and cells viability reached to less than 10 % at the concentration of 5 μgmL^{-1} after 24 h incubation with BNIPd (Figure 54D).

For BNIPDSpm, no significant reduction in viability was observed after 24 h up to 5 μgmL^{-1} ($p > 0.05$) but the cell viability decreased significantly between the concentration of 10 μgmL^{-1} and 25 μgmL^{-1} ($p < 0.05$). IC_{50} was obtained around the concentration of 20 μgmL^{-1}. With 50 μgmL^{-1} incubation concentration of BNIPDSpm, the cell viability declined to less than 10 % (Figure 54C).

For BNIPds, the significant reduction in cell viability started from 1 μgmL^{-1} ($p < 0.05$). IC_{50} was achieved around the concentration of 18 μgmL^{-1} and at the concentration of 50 μgmL^{-1} and 100 μgmL^{-1} the viability of BxPC3 cells was almost zero (Figure 54C).

The result showed that the additional two amine groups or two thiol groups in BNIPDSpm and BNIPds, respectively, decreased their cytotoxic effect in comparison with BNIPd, which possesses only two amines groups. These additional functional groups might affect the 3D shape of these drugs that made them difficult to cross the cells membrane and inhibit DNA replication in cells` nucleus (Ghafoor *et al*. 2012).

The cytotoxic effect of hybrid formulations (conjugated with different type of bisnaphthalamide based drugs) was tested with MTT cytotoxicity test and trypan blue exclusion assay on BxPC-3 cells for 24 h and compared with the cytotoxicity of free drugs.

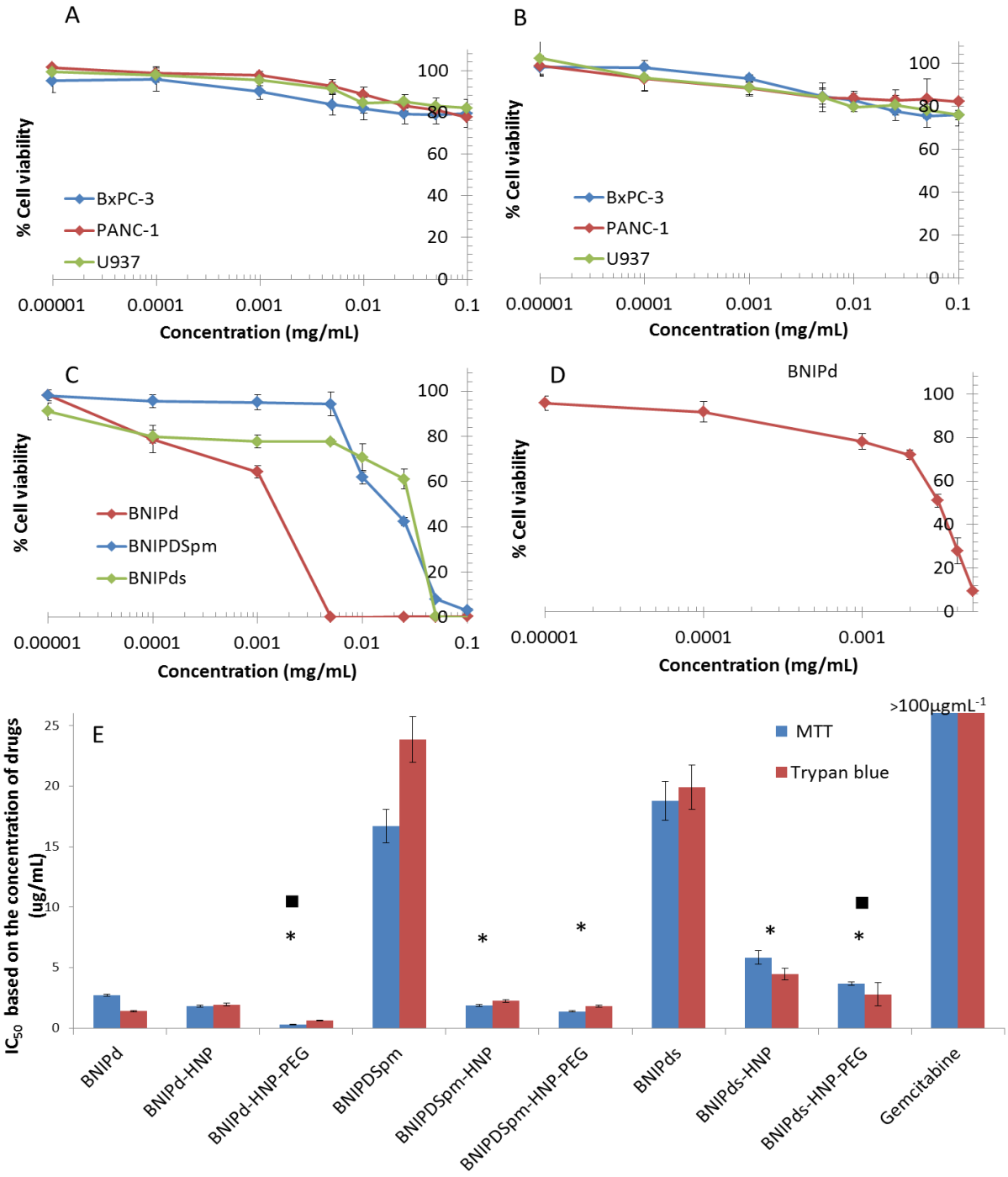

Figure 54. Cell cytotoxicity results of HNPs on BxPC-3, PANC-1 and U937 cell lines, after 24 h ($0.1 – 1.0 \times 10^{-5}$ $mgmL^{-1}$) characterised by A) MTT and B) Trypan blue cytotoxicity assay, C) Cell cytotoxicity results of BNIPd, BNIPDSpm and BNIPds on BxPC-3 cell line by MTT assay, after 24 h ($0.1 – 1.0 \times 10^{-5}$ $mgmL^{-1}$), D) Cell cytotoxicity results of BNIPd on BxPC-3 cell line by MTT assay with revised concentrations, after 24 h ($0.005 – 1.0 \times 10^{-5}$ $mgmL^{-1}$) and E) IC_{50} value of drugs and hybrid formulations on BxPC-3 cells obtained by MTT cytotoxicity test and trypan blue exclusion assay after 24 h. * denotes significant decrease in IC_{50} from hybrid formulations compared with drug alone. ■ denotes significant decrease in IC_{50} from PEGylated formulation compared with unPEGylated formulation at a similar concentration and incubation time ($p < 0.05$) (n=3, ave ± SD). ">100" means that no IC_{50} achieved within the concentrations tested ($0.1 – 1.0 \times 10^{-5}$ $mgmL^{-1}$) and an IC_{50} over 100 μgmL^{-1} was given by GraphPad Prism 6 software.

In general, both cytotoxic assays exhibited comparable results and the IC_{50} of free drugs obtained by both cytotoxic assays decreased significantly ($p < 0.05$) upon the conjugation to the surface of HNPs. BNIPd-HNP-PEG exhibited the lowest IC_{50} value within this group (0.3 μgmL^{-1}), which was significantly less than the IC_{50} of its unPEGylated counterpart ($p < 0.05$). The IC_{50} of hybrid formulations conjugated with BNIPDSpm and BNIPds were around 10 times and 5 times less than that of the free drugs, respectively ($p < 0.05$). The IC_{50} value of BNIPds-HNP decreased significantly from around 5 μgmL^{-1} to around 3 μgmL^{-1} after coating with PEG ($p < 0.05$). Moreover, there was a noticeable decrease on IC_{50} for BNIPDSpm-HNP after PEGylation ($p > 0.05$). These results confirm that the hybrid formulations have significantly higher efficacy compared with free drugs ($p < 0.05$).

The cytotoxic effects of drugs and novel formulations were compared with a commercial chemotherapeutic agent, gemcitabine, as a control using the MTT test and trypan blue exclusion assay (Figure 54E). Generally, both cytotoxic assays exhibited comparable results and gemcitabine presented a dose and time responsive effect on cell viability of BxPC-3 cells. Interestingly, no IC_{50} was observable using both the MTT assay and trypan blue cytotoxicity test for gemcitabine after 24 h (IC_{50} was over the highest incubation concentration (100 μgmL^{-1})).

Development of any formulation is a fine balance between physicochemical properties and biological activity. The data showed that BNIPd possessed the most potent anticancer effects; however, the physicochemical properties and potential use as a triggered system were lacking (outlines in Chapter Three). As described in Chapter Three, the most suitable formulations regarding drug loading, stability and triggered drug release were the BNIPDSpm formulations. Therefore, further cytotoxic studies were focused only on the BNIPDSpm formulations.

The cytotoxicity of BNIPDSpm and its hybrid formulations also evaluated on PANC-1 and U937 cells by MTT and trypan blue assays (Table 12). Similar results achieved by both cytotoxicity tests. U937 cells treated with free BNIPDSpm had lower IC_{50} values than the BxPC-3 and PANC-1 cells, around 6.37 μgmL^{-1}, 16.69 μgmL^{-1} and 28.77 μgmL^{-1}, respectively (achieved by MTT assay). This indicates that free BNIPDSpm is more cytotoxic on U937 cells, compared to BxPC-3 and PANC-1 cells (Table 12). This might be

due to the changes in cell membrane structure and differences in way/rate at which small molecules can be adsorbed by U937 cells in the higher rate, compared with the other cells.

When cells were exposed to BNIPDSpm-HNP formulation, approximately a 9.05-fold and 1.97-fold increase in cytotoxicity were experienced by BxPC-3 and PANC-1 cell lines, respectively (achieved by MTT assay) (Table 12). This indicates that hybrid formulation was able to enhance the therapeutic effect of the drug compared with the free BNIPDSpm. Moreover, it showed that the cytotoxicity of BNIPDSpm-HNP on BxPC-3 is roughly 5 times higher than on PANC-1, which might be due to the higher uptake rate of the drug on BxPC-3 cells.

Table 12. IC_{50} value of BNIPDSpm and hybrid formulations on BxPC-3, PANC-1 and U937 cells achieved by MTT and trypan blue assays. Increasing in cytotoxicity of hybrid formulations was calculated by comparing with the cytotoxicity of free drug (BNIPDSpm) (n=3, ave ± SD).

Drug/ Formulation	BNIPDSpm	BNIPDSpm-HNP	BNIPDSpm-HNP-PEG
IC_{50} value on BxPC-3 by MTT assay (μgmL^{-1})	16.69±1.37	1.84±0.09	1.37±0.07
Increase in cytotoxicity	-	9.05-fold	12.18-fold
IC_{50} value on BxPC-3 by Trypan blue assay (μgmL^{-1})	23.85±1.89	2.23±0.10	1.81±0.09
Increase in cytotoxicity	-	10.57-fold	13.18-fold
IC_{50} value on PANC-1 by MTT assay (μgmL^{-1})	28.77±2.69	14.58±1.24	12.43±1.40
Increase in cytotoxicity	-	1.97-fold	2.31-fold
IC_{50} value on PANC-1 by Trypan blue assay (μgmL^{-1})	23.42±2.51	13.95±1.46	11.50±0.96
Increase in cytotoxicity	-	1.68-fold	2.03-fold
IC_{50} value on U937 by MTT assay (μgmL^{-1})	6.16±0.46	145.50±9.66	150.10±11.01
Decrease in cytotoxicity	-	0.04-fold	0.04-fold
IC_{50} value on U937 by Trypan blue assay (μgmL^{-1})	7.57±1.23	174.80±15.70	150.60±12.24
Decrease in cytotoxicity	-	0.04-fold	0.05-fold

Interestingly, the cytotoxicity of BNIPDSpm on U937 cells decreased significantly; upon the conjugation with HNP (IC_{50} value (by MTT assay) shifted from 6.1 μgmL^{-1} to 160.1 μgmL^{-1}) ($p < 0.05$). Free BNIPDSpm probably enter to the U937 cells through cell membrane pores/ channels and nano-formulations are normally taken up by endocytosis

(Park *et al*. 2006). Therefore, slower proliferation of these cells, in comparison with BxPC-3 and PANC-1 cells, resulted in reduced cytotoxic effect of conjugated drug, compared to free drug.

4.3.2. Drug uptake investigations

4.3.2.1. Drug uptake investigations on BxPC-3 Cell line

BxPC-3 cells were incubated with different bisnaphthalamide based drugs, their hybrid formulations and gemcitabine, as a control anticancer drug, at 50 μgmL^{-1} and 100 μgmL^{-1} concentrations for 1 h and 4 h (Figure 55). The amount of accumulated free drug was quantified by RP-HPLC. In general, cellular uptake appeared to be drug concentration and time dependent. However, there is not enough data to show that the drug is released inside the cells after it was taken up by the cells.

BNIPd and its hybrid formulations possessed low drug uptake value (less than 9 pg) after 1 h incubation time (Figure 55). This low uptake value could be due to the instability of BNIPd formulations, which discussed in Chapter Three (Section 3.3.2). As a result, BNIPd may have been released before the HNPs entered the cells; thus, hindering their uptake. However, the PEGylated formulations showed drug internalisation at concentrations approximately 17-fold higher than the free drug after only 1 h incubation, which is consistent with the use of PEG for transfections, whereby it enables particles to cross the cell membrane and accumulate in intracellular spaces. After 4 h incubation, the uptake value of free drug (with 100 μgmL^{-1} incubation concentration) increased significantly from 3 pg to 6 pg and 35 pg upon the conjugation with HNP and HNP-PEG, respectively (Figure 55).

For BNIPDSpm and its formulations, after 1 h incubation, less than 1.2 pg of BNIPDSpm was taken up from free drug and its formulations. After 4 h incubation, 78 pg and 94 pg of BNIPDSpm-HNP and BNIPDSpm-HNP-PEG were taken up, respectively, while uptake value of free BNIPDSpm (with 100 μgmL^{-1} incubation concentration) stayed around 1.2 pg. These results confirmed the ability of our hybrid formulations to accumulate in BxPC-3 cells more efficiently compared to the free drug.

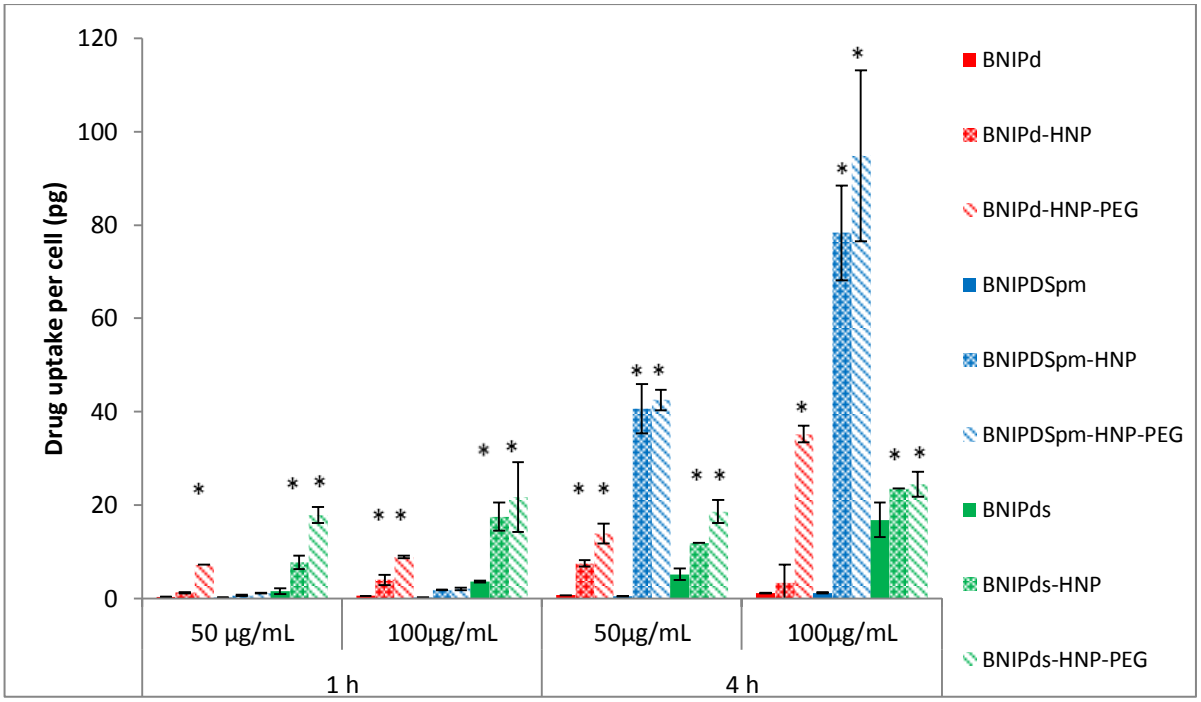

Figure 55. Drug uptake study on BxPC-3 cell line after 1 h and 4 h exposure with BNIPd, BNIPDSpm, BNIPds and their hybrid formulations (n=3, ave ± SD). * denotes significant difference in uptake rate between hybrid formulations and free drug at a similar concentration and incubation time ($p < 0.05$). All statistical analyses were carried out using t.test analysis within the Microsoft Excel software package.

In terms of drug uptake value for BNIPds and its formulations, drug was taken up to a greater extent than BNIPd formulations at both concentrations and incubation times (Figure 55). The initial uptake of BNIPds hybrid formulations after 1 h was significantly higher than BNIPd and BNIPDSpm hybrid formulations ($p < 0.05$). This initial uptake rate of BNIPds formulations might be explained by the burst release of the drug seen in Chapter Three, Section 3.3.3. However, these values stayed around the same level after 4 h incubation with BNIPds hybrid formulations. This could be due to the robust interaction of BNIPds with HNPs (discussed in Chapter Three, Section 3.3.2), which resulted in poor release inside the BxPC-3 cells.

The drug uptake pattern of the hybrid formulations after 4 h incubation was BNIPDSpm formulations > BNIPd formulations > BNIPds formulations. This could be associated with the differences of surface charge between formulations. As BNIPDSpm formulations (with four amine groups in drug`s chemical structure) were more positive (discussed in Chapter Three, Section 3.3.2.2), they were taken up more by BxPC-3 cells which might be

associated with the charge-charge interactions of positive formulation with the negative cell membrane.

Cells incubating with 50 µgmL^{-1} of gemcitabine for 1 h showed the highest drug uptake value within this group (with the same incubation concentration and incubation time) (Figure 56). This might be due to the different mechanism of uptake and type and number of receptor for different type of drug. By increasing the concentration of gemcitabine, drug uptake value after 1 h on BxPC-3 cells did not change significantly and stayed around 99 pg ($p > 0.05$). After 4 h incubation with 50 µgmL^{-1} and 100 µgmL^{-1} of gemcitabine with BxPC-3 cells, 134 pg and 163 pg of drug was taken up by the cells, respectively. Although higher amount of gemcitabine accumulated in BxPC-3 cells compared to the hybrid formulations, the cytotoxicity results in Section 4.3.1 confirmed that BNIPDSpm hybrid formulations possessed a much lower IC_{50}; therefore, even smaller amount of accumulated BNIPDSpm can produce higher cytotoxic effect on BxPC-3 cells, compared with conventional drug, gemcitabine.

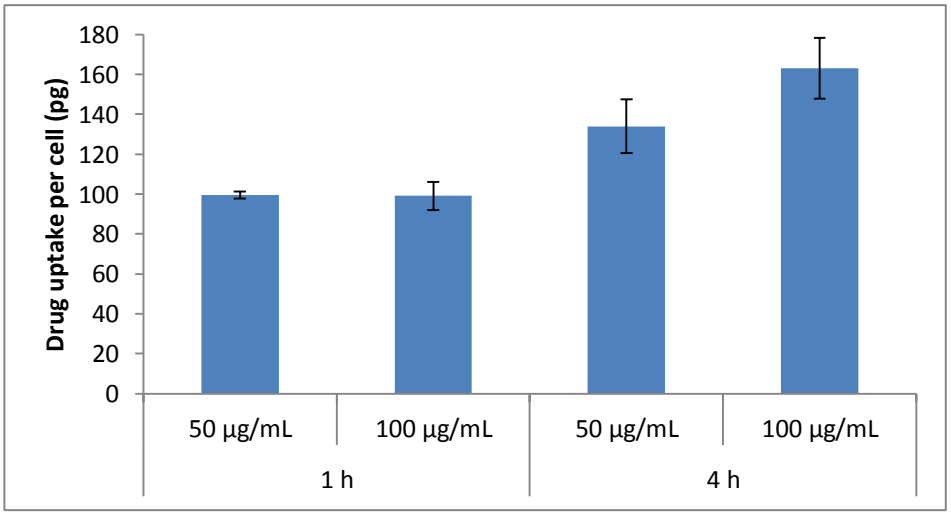

Figure 56. Drug uptake study on BxPC-3 cell line after 1 h and 4 h exposure with gemcitabine (n=3, ave ±SD). All statistical analyses were carried out using t.test analysis within the Microsoft Excel software package.

Due to the poor physicochemical properties and low uptake rate of BNIPd and BNIPds hybrid formulations after 4 h (compared with the BNIPDSpm formulations), it was decided not to continue any further biological experiments for these formulations.

4.3.2.2. Drug uptake investigations on PANC-1 and U937 Cell lines

PANC-1 and U937 cells were incubated with BNIPDSpm, its hybrid formulations and gemcitabine at the concentration of 50 μgmL^{-1} and 100 μgmL^{-1} for 1 h and 4 h.

A similar trend was detected for PANC-1 cells (Figure 57A) as observed for the BxPC-3 cells. However, uptake values for all drugs and formulations were less than 30 pg, which indicate that this cell line did not internalise the drugs/ hybrid formulations at the same rate as BxPC-3 cell line. This could be due to the smaller size of PANC-1 cells (20µm) compared to BxPC-3 cells (30µm) resulting smaller capacity of PANC-1 cells to take up drugs and formulations (size estimation of the cells achieved by AFM, which will be discussed in Section 4.3.7). The data indicates that combination of BNIPDSpm and PEGylated HNPs resulted in significantly ($p < 0.05$) (excluding cells incubated with 100 μgmL^{-1} of formulation for 4 h) higher drug uptake into PANC-1 cells in comparison with BNIPDSpm-HNP, which confirms the ability of PEGylated formulations to act as a transfection agent to increase accumulation in cells.

In U937 cells, the drug uptake pattern was completely different from BxPC-3 and PANC-1 cells, where the highest uptake rates were achieved by the free BNIPDSpm (Figure 57B). There was no significant difference in drug uptake between BNIPDSpm-HNP and BNIPDSpm-HNP-PEG ($p > 0.05$). After 4 h incubation of U937 cells with BNIPDSpm-HNP and BNIPDSpm-PEG (100 μgmL^{-1}) only 2.7 pg and 2.4 pg of drug accumulated in each cell, respectively; while this amount for free drug was 32.9 pg, at a similar incubation concentration and incubation time, which could be due to the different mechanisms of internalisation of drug and NPs. As discussed before, free BNIPDSpm enters to cells through cell membrane pores/channels which is not energy dependant but particles internalise by endocytosis, thus slower proliferation resulted in less uptake of hybrid formulations compared to the free drug ($p < 0.05$).

Drug uptake for gemcitabine on U937 cells was around 11 pg at both incubation concentrations after 1 h, this amount increased to around 17 pg after 4 h incubation with the same incubation concentrations of gemcitabine. It seems that gemcitabine uptake pattern on U937 cells is more time dependant ($p < 0.05$), rather than concentration dependant ($p > 0.05$) (Figure 57B).

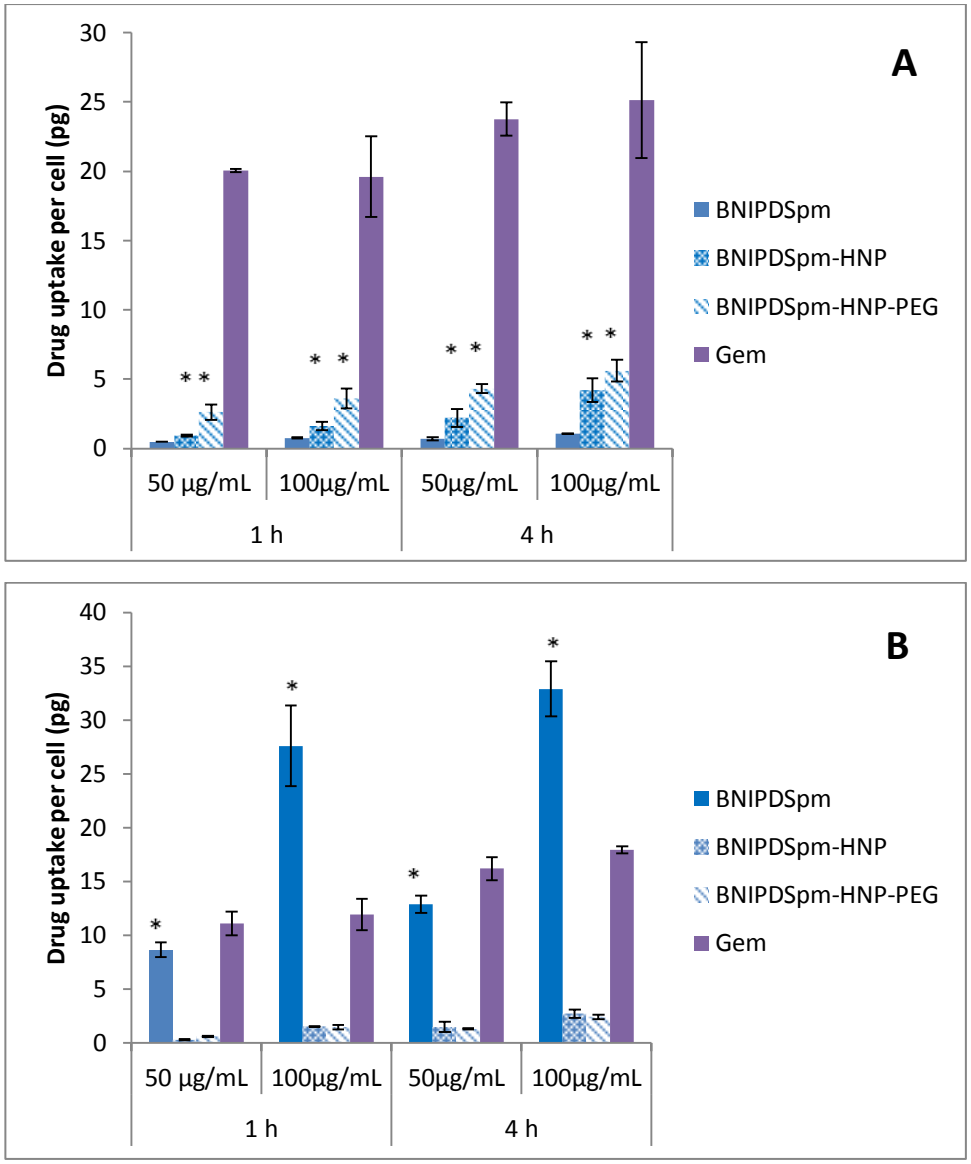

Figure 57. Drug uptake study on A) PANC-1 and B) U937 cell lines after 1 h and 4 h exposure with BNIPDSpm, BNIPDSpm-HNP, BNIPDSpm-HNP-PEG, (n=3, ave ± SD). * denotes significant difference between BNIPDSpm uptake from formulations compared with free BNIPDSpm at a similar concentration and incubation time ($p < 0.05$). All statistical analyses were carried out using t.test analysis within the Microsoft Excel software package.

4.3.3. Cojugation of targeting peptide onto the optimal formulation

The c(RGDfC) peptide, BNIPDSpm and thiolated PEG were simultaneously and successfully conjugated to the HNP and the amount of drug and targeting peptide were analysed by RP-HPLC. The peaks for BNIPDSpm observed at the same time described in Chapter Three (Section 3.3.1). The c(RGDfC) peptide was very sensitive to the HPLC fluorescence detector and a very sharp peak was detected around 17 min at the concentration of 0.156 µgmL^{-1} of c(RGDfC) (Figure 58).

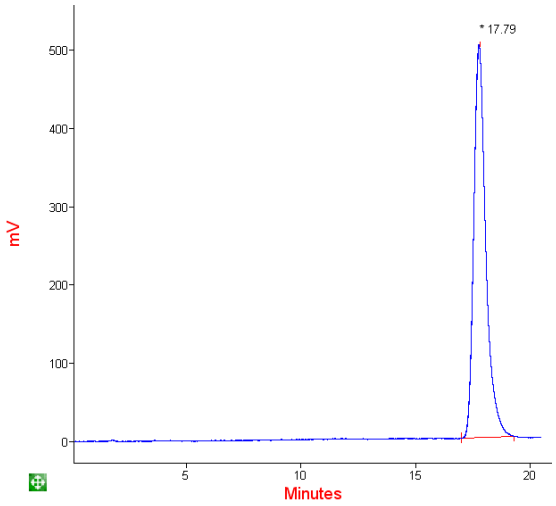

Figure 58. Reverse phase HPLC analysis (with fluorescence detector) of 0.156 µgmL^{-1} c(RGDfC) peptide. Mobile phase contained solvents A and B (50:50). Solvent A was water containing 0.09 % trifluoroacetic acid (TFA) and solvent B was acetonitrile containing 9.91 % H_2O and 0.09 % TFA, Excitation: 250 nm, Emission: 307 nm, flow rate: 1 mLmin^{-1}.

The concentration of the BNIPDSpm and c(RGDfC) peptide in BNIPDSpm-HNP-PEG-c(RGDfC) formulation characterised by HPLC were 3.2 ± 0.0465 mgmL^{-1} (R_2 = 0.9998) and 0.0968± 0.0075 mgmL^{-1} (R_2 = 0.9999), respectively. 48 % of the initial amount of peptide was able to conjugate to the surface of HNPs.

4.3.4. Cytotoxicity of optimal formulation incorporating targeting moieties.

The MTT cytotoxicity test and trypan blue exclusion assay were carried out on BNIPDSpm-HNP-PEG-c(RGDfC) to determine whether this formulations was capable of delivering BNIPDSpm into the BxPC-3 and PANC-1 cancer cells and enhancing the cytotoxic effect of this drug in comparison with non-targeted hybrid formulations. The cytotoxicity of this formulation was also tested on U937 cells to compare the response of the formulation on immune like cells (Figure 59).

After 24 h incubation of BxPC-3 cells with BNIPDSpm-HNP-PEG-c(RGDfC), the IC_{50} was 1.15 μgmL^{-1} and 1.05 μgmL^{-1} achieved by MTT and trypan blue cytotoxicity test, respectively. This was slightly less (but not significantly) than the IC_{50} of PEGylated non-targeted formulation (1.37 μgmL^{-1} and 1.81 μgmL^{-1}, obtained by MTT and trypan blue cytotoxicity test, respectively) ($p > 0.05$). The same result was obtained from PANC-1 cells and notable drop in IC_{50} of targeted formulation was attained, compared with BNIPDSpm-HNP-PEG ($p > 0.05$) (Figure 59). The slight decrease in IC_{50} observed between the targeted and untargeted formulations could to be due to the presence of peptide, which can facilitate the entrance of hybrid formulation inside the pancreatic cancer cells. These results suggest that the BNIPDSpm-HNP-PEG-c(RGDfC) was a more effective delivery vehicle for the delivery of BNIPDSpm to BxPC-3 and PANC-1 cells (although it was not statistically significant ($p > 0.05$)).

Interestingly, while BNIPDSpm-HNP-PEG possessed no IC_{50} on U937 cells after 24 h, the IC_{50} value for targeted formulation was around 57.72 μgmL^{-1} ($p < 0.05$). This shows that U937 cells can recognise targeted formulation better than non-targeted formulations, which could be due the presence of targeting peptide. However, this IC_{50} value is around 10 times higher than the IC_{50} of free BNIPDSpm on U937 cells (Table 12), indicating that targeted formulations appear to be less toxic than the free drug on these cells.

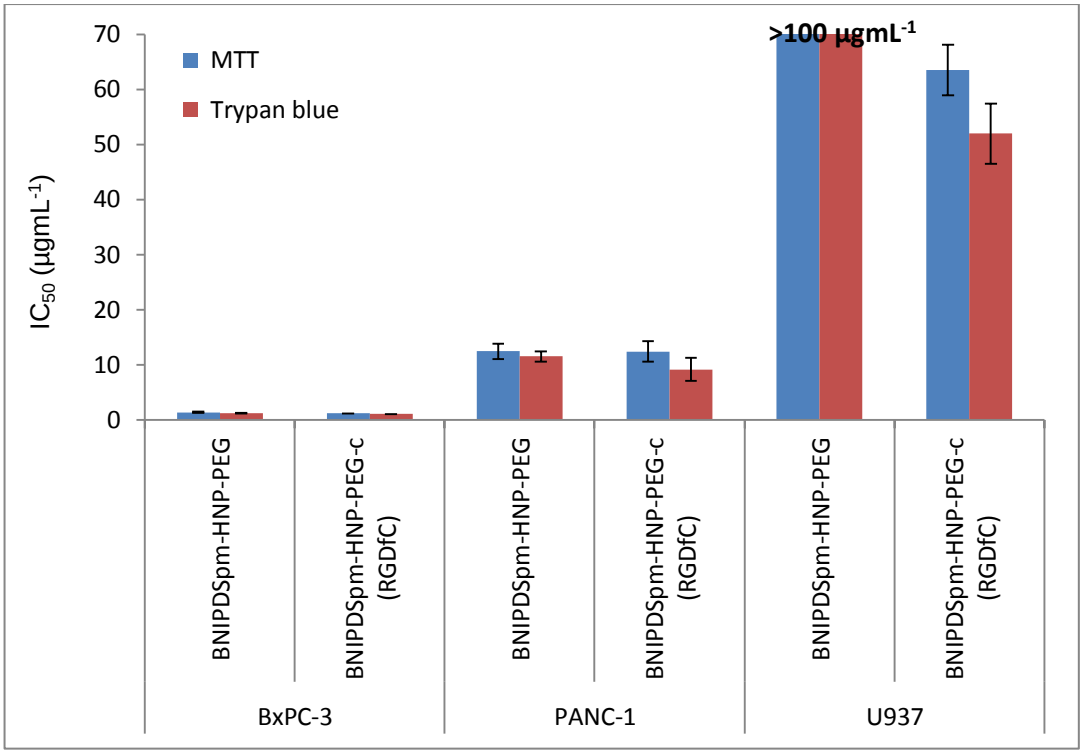

Figure 59. IC_{50} value of BNIPDSpm-HNP-PEG and BNIPDSpm-HNP-PEG-c(RGDfC) achieved by MTT cytotoxicity assay and trypan blue exclusion test on BxPC-3, PANC-1 and U937 cell lines, after 24 h (n=3, ave ± SD). ">100" means that no IC_{50} achieved within the concentrations tested (0.1 – 1.0 × 10^{-5} mgmL^{-1}) and an IC_{50} over 100 µgmL^{-1} was given by GraphPad Prism 6 software.

4.3.5. Drug uptake of optimal formulation incorporating targeting moieties

BxPC-3, PANC-1 and U937 cells were incubated with 50 µgmL^{-1} & 100 µgmL^{-1} of BNIPDSpm-HNP-PEG-c(RGDfC) for 1 h and 4 h and the results were compared with the uptake rate of BNIPDSpm-HNP-PEG on these cells. In general, the uptake rate of BNIPDSpm increased significantly in all cell lines upon the addition of targeting agent (at both concentrations and incubation times) ($p < 0.05$). The greatest uptake rate was achieved by BxPC-3 cells.

After 1 h incubation, while less than 2 pg of BNIPDSpm-HNP-PEG was taken up by these cells, BNIPDSpm-HNP-PEG-c(RGDfC) had uptake value around 109 pg at 100 µgmL^{-1} incubation concentrations (Figure 60). These amounts after 4 h incubation with the same

concentration were 94 pg and 123 pg, respectively ($p < 0.05$). This indicates that the targeted formulation can be taken up faster than non-targeted formulation (especially within 1 h, since the difference of the cellular uptake between formulations was higher after 1 h incubation). The same pattern was observed for PANC-1 and U937 cells. However, the uptake rate of targeted formulation for these cell lines was around five times less than BxPC-3 cells, which was in line with the previous uptake results (Section 4.3.2).

On PANC-1 cells, after 4 h incubation with 100 μgmL^{-1} of hybrid formulations, drug uptake for BNIPDSpm-HNP-PEG-c(RGDfC) reached to 22.5 pg, which was 5 times higher than uptake value of BNIPDSpm-HNP-PEG at a similar concentration and incubation time ($p < 0.05$). This indicates that combination of targeting peptide and PEGylated formulation caused higher uptake rate on PANC-1 cells in comparison with BNIPDSpm-HNP-PEG.

Although, non-targeted formulation showed negligible uptake rate, compared with free drug on U937 cell line (Figure 57B), BNIPDSpm-HNP-PEG-c(RGDfC) possessed comparable uptake rate to BNIPDSpm, since 33 pg and 22 pg of free drug and BNIPDSpm-HNP-PEG-c(RGDfC) accumulated in U937 after 4 h, respectively (incubation concentration: 100 μgmL^{-1}) (Figures 57B and 60). This again indicates that the presence of the targeting ligand can increase the accumulation of the formulations in cells.

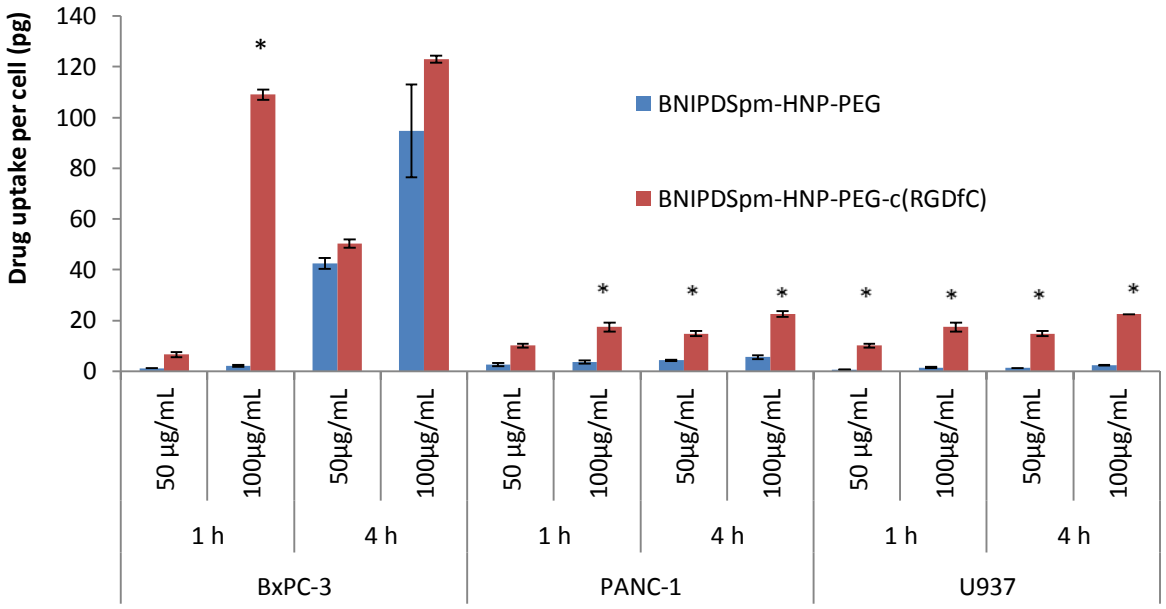

Figure 60. Cellular uptake analysis of BNIPDSpm-HNP-PEG and BNIPDSpm-HNP-PEG-c(RGDfC) after 1 h and 4 h incubation with BxPC-3, PANC-1 and U937 cell lines (n=3, ave ± SD). * denotes significant decrease in IC_{50} from BNIPDSpm-HNP-PEG-c(RGDfC)compared with BNIPDSpm-HNP-PEG in different cell lines ($p < 0.05$).

4.3.6. *In vitro* thermoresponsive cytotoxicity assay

In order to investigate the effect of heat on drug release and overall cytotoxicity of the hybrid formulations, BxPC-3, PANC-1 and U937 cells were treated with 50 μgmL^{-1} of hybrid formulations for 0.5 h at 25 ºC, 44 ºC and 60 ºC (and compared with the free drug and HNPs controls). Treating concentration of 100 μgmL^{-1} was not used as it would be more toxic and a great number of the cells will be killed; thus treated cells cannot be counted by the automated cell counter. In general, the result revealed that increasing the temperature had no remarkable impact on cytotoxicity of HNPs ($p > 0.05$) and the viability of all three types of cells treated with HNPs was more than 80 % at all different incubation temperatures (Figure 61). Increasing the temperature from 25 ºC to 44 ºC decreased the viability of the cells treated with free BNIPDSpm significantly ($p < 0.05$) in all cell lines, which suggests that incubation at 44 ºC increases the action of this anticancer agent. However, upon the incubation of PANC-1 and U937 cells with free drug at 60 ºC, the

viability of the cells increased and changed from 42 % and 14 % viability, respectively (at 44 ºC) to 55 % and 32 % viability, respectively (at 60 ºC) (Figures 61B and 61C). It was postulated that in 60 ºC, the physiochemical properties of BNIPDSpm might be changed (chemical degradation), thus the cytotoxicity of this drug was decreased for PANC-1 and U937 cells. Although this result was observed in triplicate, further investigation is required in order to fully understand if this finding is reliable.

Cytotoxicity of hybrid formulations on BxPC-3 cells significantly increased upon the temperature increase (from 25 ºC to 44 ºC and 60 ºC), compared with free BNIPDSpm ($p < 0.05$), which was more prominent for PEGylated formulations. The viability of BxPC-3 cells treated with BNIPDSpm-HNP at 25 ºC, 44 ºC and 60 ºC were 24 %, 14 % and 9 %, respectively (Figure 61A). These amounts for cells incubated with BNIPDSpm-HNP-PEG at 25 ºC, 44 ºC and 60 ºC were 11 %, 5 % and 3 %, respectively. The results indicate that the PEGylated formulation is significantly more cytotoxic than unPEGylated formulation on BxPC-3 cells, at all temperatures ($p < 0.05$). This could be due to the higher uptake rate of PEGylated formulation discussed before. There was an increase in cell cytotoxicity on BxPC-3 cells treated with BNIPDSpm-HNP-PEG-c(RGDfC) compared with BNIPDSpm-HNP-PEG at different incubation temperatures, though it was not significant ($p > 0.05$) (Figure 61A and Table 13).

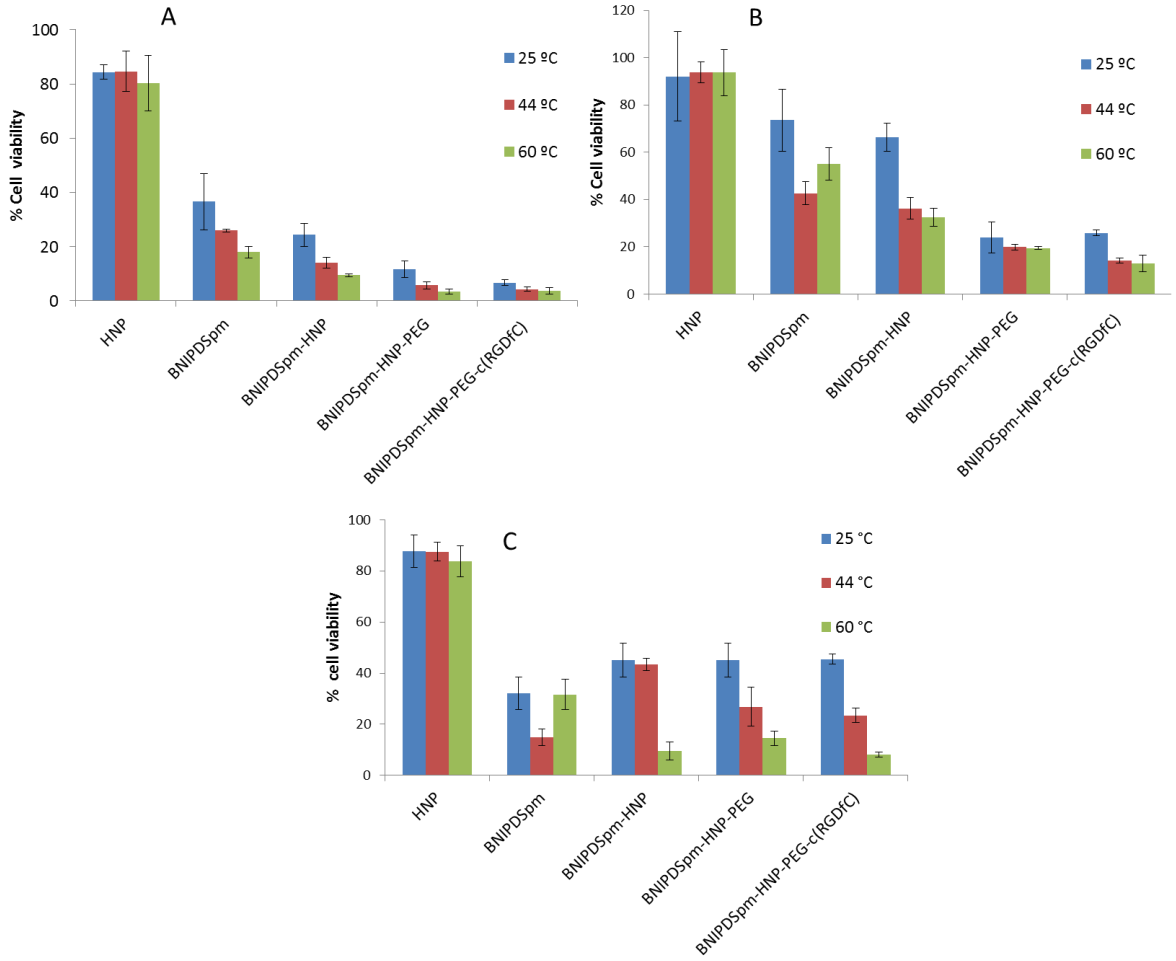

Figure 61. *In vitro* thermoresponsive cytotoxicity test on A) BxPC-3, B) PANC-1 and C) U937 cell lines at 25, 44 and 60 ºC (n=3, ave ± SD).

The same cytotoxicity pattern was observed in PANC-1 cells treated with hybrid formulations (Figure 61B). However, the viability of these treated cells was higher than BxPC-3, with the same incubation temperature and treating agent. This again confirms the cytotoxicity results achieved by MTT and trypan blue cytotoxicity tests whereby the drug and hybrid formulations are more cytotoxic on BxPC-3 cells, in comparison with PANC-1 cells (Table 12).

Table 13. Comparative thermoresponsive cytotoxicity of hybrid formulations at different temperature in comparison with free BNIPDSpm on BxPC-3, PANC-1 and U937 cell lines.

Cell line	Incubation temperature	BNIPDSpm-HNP	BNIPDSpm-HNP-PEG	BNIPDSpm-HNP-PEG-c(RGDfC)
		Cytotoxicity increase from free BNIPDSpm		
BxPC-3	25 ºC	1.50-fold	3.14-fold	5.43-fold
	44 ºC	1.84-fold	4.54-fold	5.31-fold
	60 ºC	1.89-fold	4.77-fold	5.99-fold
PANC-1	25 ºC	1.11-fold	2.15-fold	3.00-fold
	44 ºC	1.17-fold	2.84-fold	3.08-fold
	60 ºC	1.69-fold	2.83-fold	4.22-fold
U937	25 ºC	0.71-fold	0.71-fold	0.70-fold
	44 ºC	0.34-fold	0.55-fold	0.64-fold
	60 ºC	3.31-fold	2.19-fold	3.95-fold

Slight increase ($p > 0.05$) in toxicity achieved upon the treating of U937 with targeted formulations at 25 ºC and 44 ºC in comparison with BNIPDSpm-HNP-PEG. This enhanced cytotoxic effect for cells incubated at 60 ºC was significant ($p > 0.05$). The highest cytotoxic effect on U937 cells received for cells treated with hybrid formulations at 60 ºC (Figure 61C). Cell viability of U937 treated with BNIPDSpm-HNP and BNIPDSpm-HNP-PEG decreased significantly upon incubating at 60 ºC ($p < 0.05$), which might be due to the higher amount of BNIPDSpm being released from the particles at this temperature (Figure 61C).

Table 13 illustrates the increasing cytotoxic effects of drugs upon the conjugation with HNP, HNP-PEG and HNP-PEG-c(RGDfC) with increasing of incubation temperature on BxPC-3 and PANC-1 cell lines. However, this enhanced cytotoxic effect was not observed in U937 cells and increase in toxicity was only achieved for cells treated with hybrid formulations. As it was mentioned before, these cells responded to hybrid formulation at 60 ºC in a different way and an increase in cytotoxicity was attained for cells incubated with hybrid formulation, especially with targeted formulation (4-fold) (Table 13).

While no significant increase in cytotoxicity was observed between U937 cells incubated with BNIPDSpm-HNP at 25 ºC and 44 ºC ($p > 0.05$), the viability of U937 cells treated with BNIPDSpm-HNP-PEG decreased significantly from 45 % (25 ºC) to 26 % (44 ºC) (Figure 61C). U937 cells treated with BNIPDSpm-HNP-PEG-c(RGDfC) showed the same response as PEGylated formulation, however an increase in cell cytotoxicity was observed for the cells incubated with formulation containing targeting peptide in 60 ºC, in comparison with BNIPDSpm-HNP-PEG ($p < 0.05$) (Figure 61C and Table 13).

These results confirm that the cytotoxicity of hybrid formulations on BxPC-3 and PANC-1 cells was significantly enhanced by increasing the incubation temperature *in vitro*, compared with the free drug ($p < 0.05$). Here we used control cells which were not exposed to any formulation, only the temperature increase, as such it may have been more appropriate to compare to cells incubated at physiological temperature for example. In this work it is assumed (in relation to the drug release studies) that by increasing the particles` temperature (accumulated inside the pancreatic cancer cells) via laser irradiation, drug will be released from HNP inside the cells; thus the hybrid formulations are able to kill pancreatic cancer cells in a more efficient way. Therefore, to further investigate this potential in a more appropriate manner future *in vitro* studies are required using laser irradiation as the heating source.

4.3.7. AFM topography imaging

The AFM images were in agreement with the drug uptake study after 1 h and 4 h incubation. In All cell lines, morphological changes appear to have a time dependent manner (Figures 62-64). There was not any remarkable morphological difference between BxPC-3, PANC-1 and U937 control cells and cells incubated with gemcitabine and HNPs, after 1 h and 4 h incubation. This confirms the low cytotoxicity of HNPs and gemcitabine on these cell lines, which was explained before (Section 4.3.1). In BxPC-3 cells, while cells incubated with BNIPDSpm after 1 h were quite healthy (Figure $62D_1$), after 4 h their cellular structures were relatively damaged (Figure $62D_2$). Interestingly, treating these cells with BNIPDSpm-HNP, BNIPDSpm-HNP-PEG and BNIPDSpm-HNP-PEG-c(RGDfC) changed the structure and morphology of BxPC-3 cells completely after 1 h (Figures $62E_1$, $62F_1$ and $62G_1$) and 4 h incubation (Figures, $62E_2$, $62F_2$ and $62G_2$).

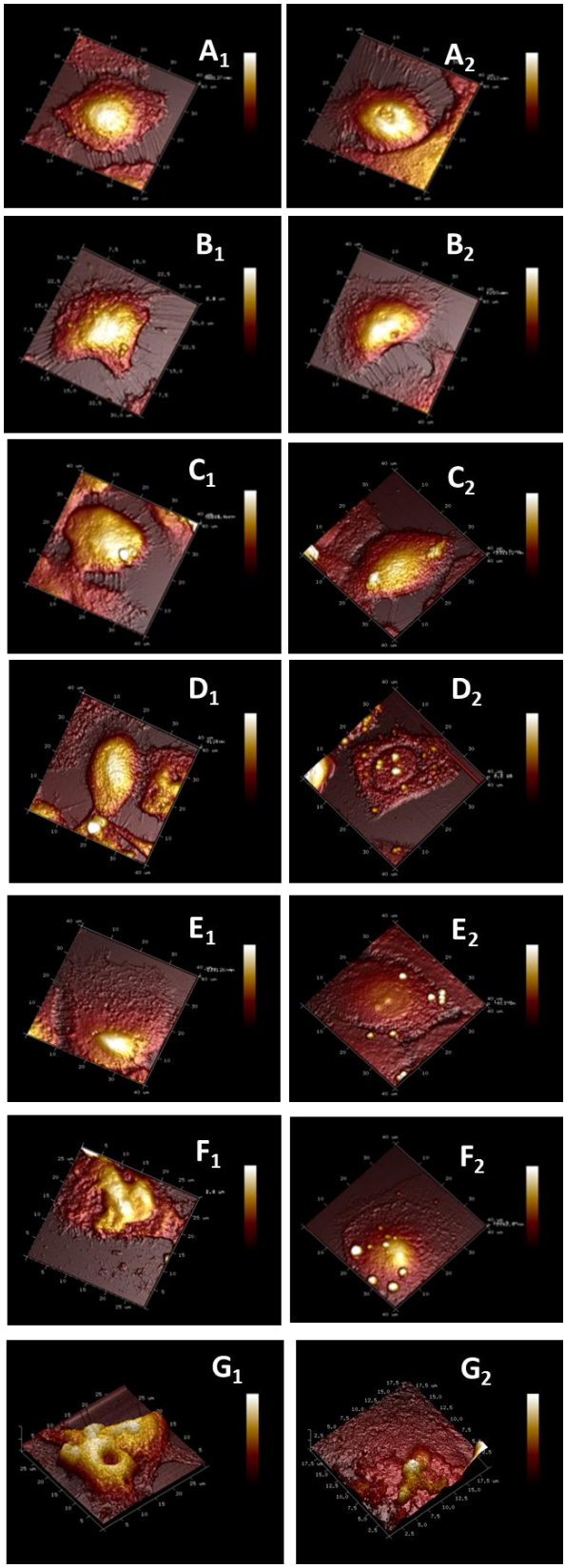

Figure 62. AFM image of BxPC-3 cells: A) Control cells, cells with 50 μgmL^{-1} of B) gemcitabine, C) HNP, D) BNIPDSpm, E) BNIPDSpm-HNP, F) BNIPDSpm-HNP-PEG and G) BNIPDSpm-HNP-PEG-c(RGDfC). All incubated for 1) 1 h & 2) 4 h.

AFM images of PANC-1 cells showed the same result. There was not any significant morphological difference between control cells and cells incubated with gemcitabine and HNPs, after 1 h and 4 h incubation. The circular shape of these cells and the smooth surface of them changed completely upon treating with hybrid formulations (Figures $63E_1$, $63E_2$, $63F_1$, $63F_2$, $63G_1$ and $63G_2$). However, these morphological changes on BxPC-3 cells were more noticeable (Figure 62), confirming the previous biological studies (cytotoxicity tests and drug uptake analyses) on hybrid formulations; where it was suggested that BNIPDSpm and its hybrid formulations possess higher cytotoxic effect and uptake rate on BxPC-3 cells, in comparison with PANC-1 cells.

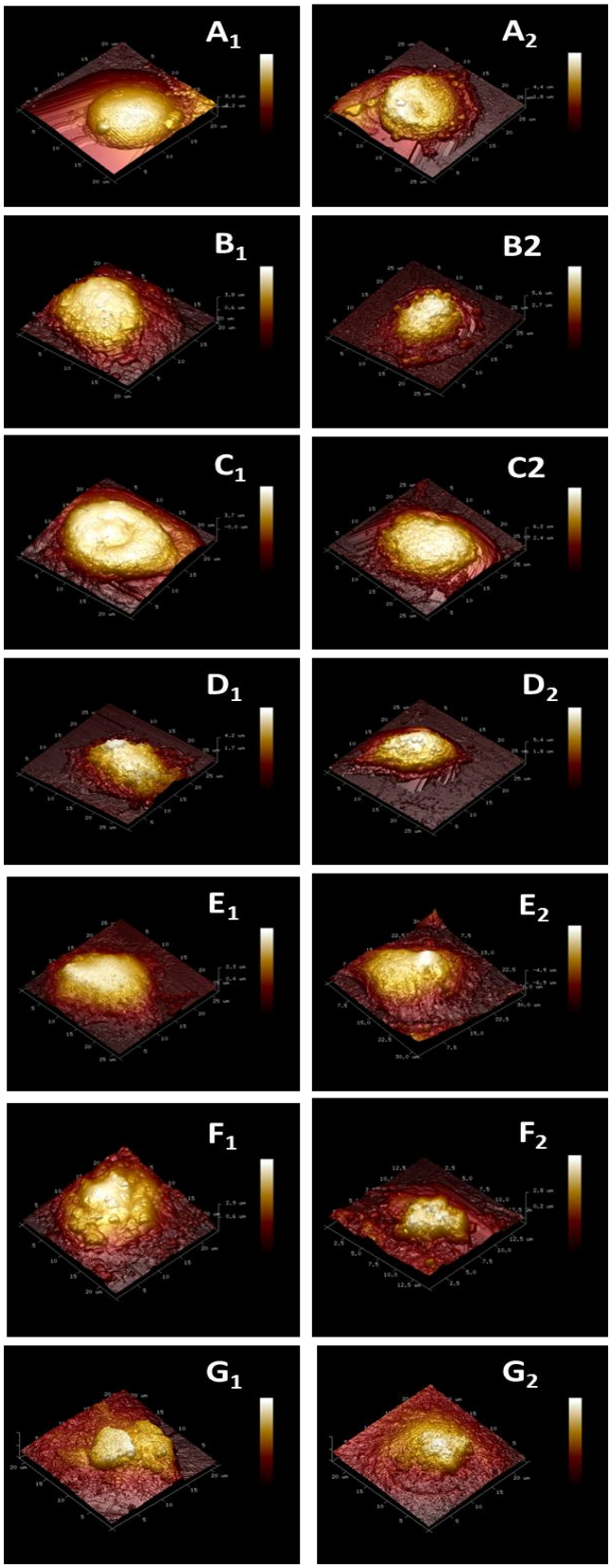

Figure 63. AFM image of PANC-1 cells: A) Control cells, cells with 50 μgmL^{-1} of B) Gemcitabine, C) HNP, D) BNIPDSpm, E) BNIPDSpm-HNP, F) BNIPDSpm-HNP-PEG and G) BNIPDSpm-HNP-PEG-c(RGDfC). All incubated for 1) 1 h & 2) 4 h.

Again in U937 cells, there was not any notable morphological difference between control cells and cells incubated with gemcitabine, HNPs and formulations after 1 h and 4 h incubation. This confirms the low cytotoxicity of HNPs, gemcitabine and formulations on this cell line, which was explained before (Section 4.3.1). U937 AFM images revealed that only free BNIPDSpm resulted morphological changes on U937 cells after 4 h (Figure 64D_2) and other treated U937 cells look similar to the control cells after 1 h and 4 h. These results were in agreement with our cytotoxicity tests and drug uptake analyses; where higher cytotoxicity and drug uptake achieved by U937 cells treated with free BNIPDSpm, compared with cells incubated with hybrid formulations (Table 12 and Figure 57B, respectively).

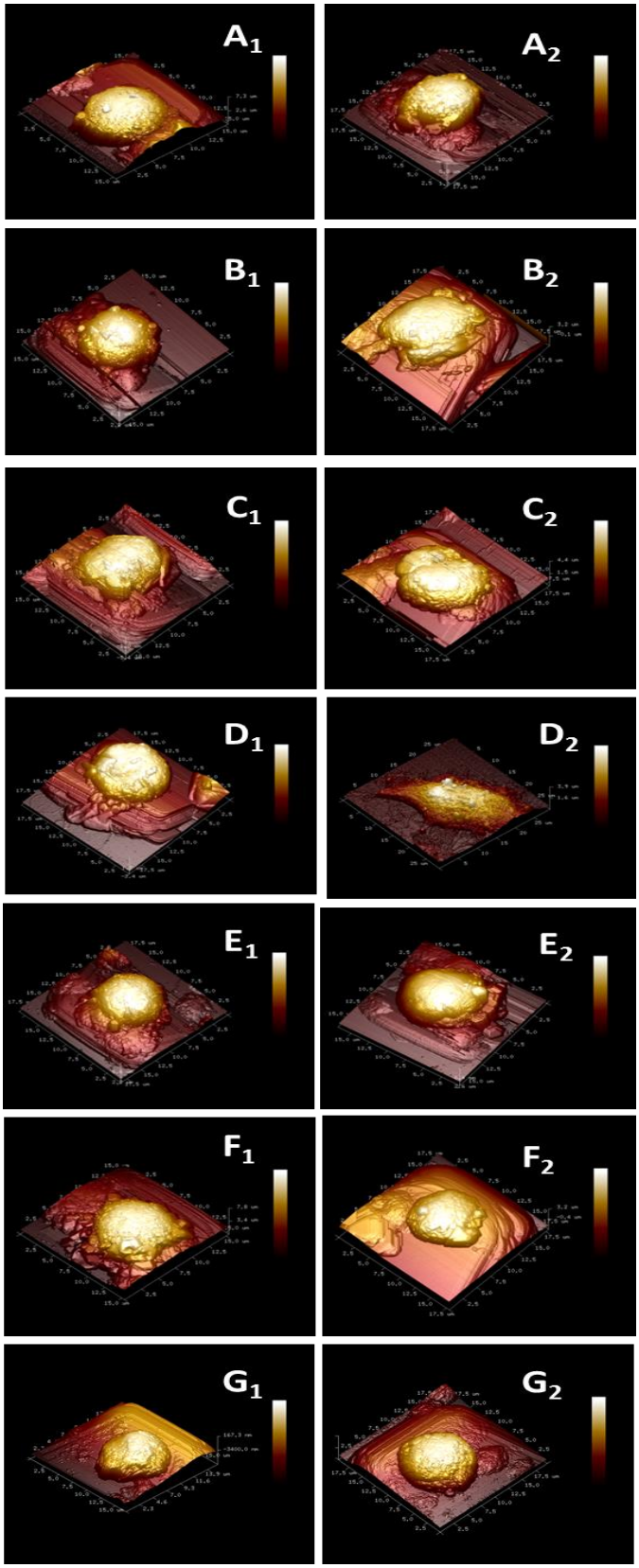

Figure 64. AFM image of U937 cells: A) Control cells, cells with 50 μgmL^{-1} of B) gemcitabine, C) HNP, D) BNIPDSpm, E) BNIPDSpm-HNP, F) BNIPDSpm-HNP-PEG and G) BNIPDSpm-HNP-PEG-c(RGDfC). All incubated for 1) 1 h & 2) 4 h.

4.4. Discussion

Pancreatic cancers are often diagnosed when they have metastasised. Usual treatments for the advanced disease state comprise of radiotherapy and/or chemotherapy approaches. The use of radiotherapy is highly toxic and chemotherapies using gemcitabine and 5-fluorouracil (5-FU) are often ineffective or only effective over short periods. Gemcitabine has been suggested to improve the quality of life in patients (Mignotte and Vayssiere, 1998); however, this drug alone and in combination chemotherapy has failed to achieve great success, which might be explained by the high level of intrinsic resistance of pancreatic cancer tumours to currently available anticancer therapies (Von Wichert *et al.* 2008).

In vitro cytotoxicity tests and basic biological analyses of any drug or formulation are essential before introducing them to animals for *in vivo* studies. General toxicity tests, such as MTT cytotoxicity assay and trypan blue exclusion cytotoxicity test are utilised mainly to detect the biological activity of drugs and formulations, which can be carried out on many cell types.

Possessing high cytotoxicity and specific delivery are essential characteristics of any anticancer drug or formulation. In this study the fabricated HNPs had limited cytotoxic impact on BxPC-3, PANC-1 and differentiated U937 cell lines, over the concentration range tested ($0.1 – 1.0 \times 10^{-5}$ mgmL^{-1}) with less than 30 % cytotoxic activity observed for high HNP concentrations (Figures 54A and 54B). These findings were consistent with other reports of HNP and provide increased confidence for the long term *in vivo* effects of these particles (Barnett *et al*. 2013a; Hoskins *et al*. 2010; Hoskins *et al*. 2012a; Hoskins *et al*. 2012c and Roach *et al*. 2013). Reports have proposed that coating layer of gold protects and shields the iron oxide core from enzymatic degradation, which may result in free radical production. Barnett and colleagues reported no free radical (ROS or LPO) production was detected above basal levels after 72 h incubation of HNPs with both BxPC-3 and differentiated U937 cells. Moreover, there was no significant cytotoxic effect for cells incubated with the high concentration of HNPs (100 µg mL^{-1}) for up to 1 week (Barnett *et al*. 2013a). Hoskins *et al*. also proposed the same cytotoxic effect of HNPs on different cell lines. They reported that after 24 h incubation of iron oxide NPs coated with polyethyleneimine (Fe_3O_4-PEI) (100 µgmL^{-1}) with neuroblast cells (SH-SY5Y), breast adenocarcinoma cells (MCF-7) and U937 cells, up to 30 %, 50 % and 20 % reduction in

viability was detected, respectively. Additionally, they showed that PEGylated Fe_3O_4-PEI experienced only a maximum of 5 % viability reduction across the three cell lines (Hoskins *et al*. 2012a). Moreover, Roach *et al*. investigated cytotoxic effect of HNPs on mouse osteoblast cells (7F2) over 72 h. They found over 80 % of cell viability on 7F2 treated cells with HNP at the highest incubation concentration (100 µg mL^{-1}) (Roach *et al*. 2013).

Recently, a series of bisnaphthalimide polyamine derivatives were synthesised and characterised *in vitro* (Hoskins. 2010; Ralton *et al*. 2009 and Wu *et al*. 2009a). In this study, three different types of bisnaphthalamide based drugs were used (BNIPd, BNIPDSpm and BNIPds). The cytotoxic effects of these bisnaphthalamide derivatives on BxPC-3 cells were characterised. IC_{50} values for BNIPd, BNIPDSpm and BNIPds, achieved by MTT and trypan blue cytotoxicity assays after 24 h, were around 3 μgmL^{-1}, 20 μgmL^{-1} and 19 μgmL^{-1}, respectively (Figure 54C). The high cytotoxicity of BNIPd could be due to its chemical structure and number/ position of amine group (two lateral amines) (Chapter Three, Figure 34) that enables this drug to interact with the DNA of BxPC-3 cells more efficiently. The cytotoxicity results of the hybrid formulations (in conjugation with bisnaphthalamide derivatives) on BxPC-3 cell line revealed significant reduction of cell viability after 24 h (compared with the free drugs), especially for PEGylated formulations, where the cytotoxic effect of PEGylated formulation of BNIPd, BNIPDSpm and BNIPds were about 7, 13 and 6 times greater than the cytotoxicity of free drugs, respectively (Figure 54E). These findings confirm the high efficacy of the hybrid formulations which could be associated with the higher uptake rate of the novel formulations by cells, in comparison with the drugs alone. Cytotoxicity analyses were in agreement with previous study on hybrid formulations.

Previously, Barnett and colleagues conjugated 6-Thioguanine (6-TG) onto the HNPs` surface and incubated with BxPC-3 cells. A 10-fold decrease in IC_{50} was reported with the 6-TG-conjugated with HNPs, in comparison with free drug (Barnett *et al*. 2013b). Wagstaff and co-workers introduced cisplatin conjugated with HNP to ovarian cancer cell lines (A2780 and A2780/cp70). They found that their novel hybrid formulation is up to 110-fold more cytotoxic than free cisplatin on ovarian carcinoma cells (Wagstaff *et al*. 2012).

All cytotoxicity results from the bisnaphthalamide derivatives and their hybrid formulations were compared with commercial anticancer drug, gemcitabine. No IC_{50} achieved for BxPC-3, PANC-1 and differentiated U937 cells treating with gemcitabine within 24 h (Figure 54E). Around 60 %, 80 % and 70 % of cell viability was achieved for BxPC-3, PANC-1 and differentiated U937 cells treated with the highest treating concentration of gemcitabine (100 μgmL^{-1}) after 24 h, respectively. This result confirms that the fabricated formulations were highly cytotoxic to pancreatic cancer cells, in comparison with gemcitabine. These findings were consistent with other report of cytotoxicity of gemcitabine on BxPC-3, human pancreas cells (AsPC-1), homo sapiens pancreatic carcinoma (MiaPaCa-2) and PANC-1 as no IC_{50} was observed after 24 h on these cells (Wu *et al*. 2009b). In another study Wang and colleagues, treated BxPC-3, PANC-1, MiaPaCa-2, AsPC-1 and epithelial ductal adenocarcinoma (PL-45) with gemcitabine over the period of 48 h. They reported over 75 % cell viability analysed with MTT cytotoxicity test over the range of 1 µm (Wang *et al*. 2011). As such, perhaps this study could have benefited from longer incubation times for comparison.

Exploiting targeting peptides for efficient delivery of different materials into cells has a relatively recent history. Integrin αvβ3 receptor is expressed on many different types of cancer cells as for pancreatic cancer cells. This receptor plays key role in tumour development and metastasis. Therefore, by targeting the integrin αvβ3 receptor on pancreatic cancer cells, the efficacy of targeted therapy can be increased with reduced unwanted side effects. Previously, Ji *et al.* conjugated a novel arginine-glycine-aspartic acid (RGD) peptide to bovine serum albumin nanoparticles (BSANPs) to increase the intracellular uptake of gemcitabine into the pancreatic cancer cells (BxPC-3) by receptor-mediated endocytosis. They found that BSANPs accumulate into BxPC3 cells in a time and concentration dependent manner and cellular uptake of gemcitabine for RGD-conjugated BSANPs in BxPC-3 cells was higher than formulation without RGD peptide (Ji *et al*. 2012). In another study, Zuo and colleagues conjugated iRGD peptide (CRGDK/RGPD/EC) to the surface of super paramagnetic iron oxide nanoparticles (SPIONs) to improve labelling of PANC-1 cells in cancer imaging. They proposed that SPIONs with iRGD peptide can increase the uptake and labelling rate of PANC-1 (Zuo *et al*. 2014).

As described in Chapter Three (Section 3.2.2.2) BNIPDSpm formulations showed higher conjugation ability, stability and sustained drug release pattern, thus these formulations were used for further conjugation by c(RGDfC) peptide. In this study, c(RGDfC) peptide was successfully conjugated to the surface of BNIPDSpm-HNP-PEG (PEGylated formulation was used in order to increase biocompatibility) and the amount of attached BNIPDSpm and peptide were analysed by RP-HPLC. Table 12 indicates that the cytotoxicity pattern of free BNIPDSpm was U937 cells > BxPC-3 > PANC-1. Interestingly, the pattern for hybrid formulation was BxPC-3 > PANC-1 > U937, where the cytotoxicity of BNIPDSpm on U937 significantly decreased ($p < 0.05$) upon the conjugation to the surface of HNPs. This indicates that U937 cells internalised the conjugated BNIPDSpm much less than the free drug, which might be due to the difference between drug mechanism of entry (through cell membrane pores/ channels), and hybrid formulations mechanism of entry (endocytosis) as described before. But the IC_{50} of BNIPDSpm-HNP-PEG-c(RGDfC) added to these cells was around half of the IC_{50} achieved by BNIPDSpm-HNP and BNIPDSpm-HNP-PEG. This could be due to the presence of peptide, which can be recognised by the U937 cells.

Cytotoxicity of BNIPDSpm-HNP-PEG-c(RGDfC) (by MTT assay) were 14.51 and 12.4 times higher than free BNIPDSpm on BxPC-3 and PANC-1 cells, respectively; while the increased cytotoxic effect for BNIPDSpm-HNP-PEG was 12.2 and 12.4 times, respectively. It is assumed that a higher toxicity would be experienced with the formulation containing targeting peptide. However, this is not what was observed. The slight (but not significant) increase of cytotoxicity upon the conjugation of targeting peptide could be due to the 2D *in vitro* cytotoxicity analysis (*in vitro* cell culture) and higher cytotoxic effect may be achieved by 3D *in vitro* culturing or *in vivo*.

Drug uptake study of bisnaphthalamide derivatives on BxPC-3 cells showed that hybrid formulations were taken up significantly higher than free drugs ($p < 0.05$) (Figure 55). Within this group BNIPDSpm hybrid formulations, especially the one containing targeting peptide, possessed the highest uptake rate after 4 h incubation (incubation concentration: 100 $\mu g m L^{-1}$). Moreover, the presence of targeting peptide within the formulations resulted in comparable uptake rate to gemcitabine. Due to low stability of BNIPd hybrid formulations and robust interaction of BNIPds with HNPs that resulted poor drug release

in vitro (Chapter Three, Section 3.2.2), hence no further investigation of these formulations on PANC-1 and U937 cell lines was carried out.

Drug uptake results for gemcitabine on BxPC-3 and PANC-1 cell lines were in the range of the drug uptake data previously reported by Paproski *et al* (Paproski *et al*. 2010). Although gemcitabine was taken up mostly in the highest level at all concentration and incubation time by pancreatic cancer cells (Figures 56 and 57A), the cytotoxicity result from gemcitabine showed that this drug did not possess IC_{50} after 24 h. This means that novel BNIPDSpm hybrid formulations are faster acting at killing pancreatic cancer cells, compared with gemcitabine. BNIPDSpm and its hybrid formulations uptake pattern from PANC-1 cells (Figure 57A) were comparable to BxPC-3 cells (Figure 55). However, the uptake rate of drugs (gemcitabine and BNIPDSpm) and hybrid formulations from BxPC-3 cells was around 5 times higher than PANC-1 cells (Figure 57). This might be due to the differences in proliferation of these cells, volume of the cells and/or binding sites for drugs per cell in pancreatic cancer cell lines. In U937 cell line, free BNIPDSpm was accumulated in cells more than hybrid formulations indicating that our hybrid formulations were not recognised by these cells as much as free drug (Figure 57B). The presence of targeting peptide increased uptake rate of BNIPDSpm from the formulations, which means that this formulation was recognised by U937 cells more than other formulations (Figure 60).

In vitro thermoresponsive cytotoxicity result from BxPC-3, PANC-1 and U937 cell lines showed that the viability of treated cells with BNIPDSpm and hybrid formulations mostly decreased by increasing the temperature (Figure 61). Many *in vitro* and *in vivo* studies suggested that the combination of hyperthermia and anticancer drugs has synergistic effect (Hahn, 1982). *In vivo* investigations on animal tumour systems demonstrated by Urano *at al*. showed that some drugs such as cisplatin and bleomycin are more cytotoxic between 40 ºC-45 ºC as the drugs are more active within these temperatures (Urano *et al*. 1999). This is in agreement with BNIPDSpm thermoresponsive cytotoxicity result. Greater cytotoxic effects on BxPC-3, PANC-1 and U937 cells achieved by hybrid formulations incubated in higher temperature could be due to the higher amount of drug being released from the formulations (Figure 61).

AFM topography images of treated cells after 1 h and 4 h were in agreement with drug uptake results, which confirmed the higher cytotoxic effect of hybrid formulations comparing with free BNIPDSpm, especially the PEGylated and targeted formulations

(BNIPDSpm-HNP-PEG-c(RGDfC)) on BxPC-3 and PANC-1 cells (Figures 62 and 63). The enhanced cytotoxic effect of BNIPDSpm hybrid formulations was more prominent on BxPC-3 cells (Figure 62), in comparison with PANC-1 cells (Figure 63), which strengthened our previous results suggesting higher cytotoxic effect (Table 12) and drug uptake rate for our novel formulations on BxPC-3 cells (Figure 55), compared with PANC-1 cells (Figure 57A). Except cells treated with BNIPDSpm for 4 h (Figure $64D_2$), no significant changes in U937 cells morphology was observed upon the incubation with drug and hybrid formulations (Figure 64). This is again in line with the low cytotoxicity (Table 12) and uptake rate (Figure 57B) of BNIPDSpm formulations on these cells. Our results provide evidence that BNIPDSpm delivery with HNPs is highly more efficient compared to the conventional anticancer drug gemcitabine.

4.5. Conclusion

This study shows the ability of BNIPDSpm novel formulations to accumulate and kill pancreatic cancer cells more effectively, compared to the free BNIPDSpm and conventional drug, gemcitabine. The HNPs as carriers showed negligible cytotoxic effect on pancreatic and microphage-like cells over the concentrations tested. The novel hybrid formulations (conjugated bisnaphthalamide derivatives to the surface of HNPs) were capable of increasing cytotoxic effect of free bisnaphthalmides in two pancreatic cancer cell lines (BxPC-3 and PANC-1). *In vitro* drug uptake study also validated that hybrid formulations internalise and accumulate inside pancreatic cancer cells significantly higher than free drugs. The data suggested that the presence of PEG enhances the property of the formulations to internalise inside the BxPC-3 and PANC-1 cells in an efficient way. Moreover, the presence of targeting peptide increased the cytotoxicity and uptake value of the hybrid formulations on pancreatic cancer cells. BNIPDSpm hybrid formulations possessed thermoresponsive drug release potentials *in vitro*. Further research has to be performed *in vitro* and *in vivo* to fully exploit the properties of these nanoparticles for image guided thermally triggered drug delivery.

Chapter Five
General Conclusions and Future Work

5.1. General conclusion

Hybrid iron oxide-gold core shell nanoparticles (HNPs) were successfully synthesised. The physiochemical properties of fabricated particles were characterised by different techniques. Powder x-ray diffraction (PXRD) analysis showed that the diffraction peaks of synthesised iron oxide nanoparticles are closely matched with the reference sample, indicating that our particles have a cubic crystal system with no specific impurities. The ratio of iron: gold within the formulation was around 4: 1, achieved by inductively coupled plasma-optical emission spectroscopy (ICP-OES). UV/Visible spectroscopy, photon correlation spectroscopy and zeta potential measurement confirmed the coating process of particles with polyethylenimine (PEI) and subsequently gold seeding and gold coating steps. HNPs were coated using thiolated poly (ethylene glycol) (PEG-thiol) to increase biocompatibility. The size of HNPs by transmission electron microscopy (TEM) was approximately 40 nm. These HNPs had fairly similar transverse relaxivities (r2) with previously clinically administered Feridex®, indicating the ability of synthesised HNPs to be used in MRI imaging. Iron oxide core of the HNPs was highly crystalline and magnetically ordered at room temperature analysed by superconducting quantum interference device (SQUID). These results suggest that the magnetic characteristics of HNPs after gold coating process are in agreement with clinical standards and therefore have the capacity to be used as contrast agents. These fabricated particles can also act as thermo-seeds due to the presence of gold, since upon laser irradiation for 60 s, HNPs showed a time and concentration dependant heating effect.

Four different bisnaphthalamide derivatives conjugated to the surface of HNP and PEGylated HNP (HNP-PEG) with varied feeding concentrations. As a result, 24 different formulations were synthesised. The difference between these drugs was the number of amine groups presented in carbon chain (between naphthalmaide moieties) and the presence of thiol group, started from bis(naphthalimido)-1,20-diaminoicosane (BNIDi) without any amine to bis(naphthalimido)-1,12-diaminododecane (BNIPd) with two amines, bis(naphthalimidopropyl)spermine (BNIPDSpm) with four amines and bis(naphthamimidopropyl)- 3,3`-(butane-1,4-diylbis(sulfanediyl))bis(propan-1-amine) (BNIPds) with two amines and two additional thiol groups. Our study aimed to investigate the potential of electrostatic interaction of drugs and HNPs (through cationic drug and negatively charged HNPs) as stimuli responsive systems for drug release.

The maximum loading concentration for all drugs was 5 mgmL^{-1} and higher initial feed concentrations were not investigated due to the lack of aqueous solubility of drug compounds over this concentration. Results from high performance liquid chromatography (HPLC) analysis, Fourier Transform Infrared Spectroscopy (FTIR) and fluorescence spectroscopy indicated that BNIDi (without any amine) could not conjugate to the surface of HNP and HNP-PEG at any feeding concentration (Figure 65A). Binding concentration of BNIPd was very low as this drug only possesses two amines in its structure (Figure 65B). BNIPDSpm with the highest number of amine (four amines) conjugated significantly more than other drugs into the particles ($p < 0.05$) (Figure 65C). Although BNIPds was able to conjugate by both electrostatic interactions (through two amines) and dative covalent bond (via two thiols) to the surface of HNP, it did not conjugate as much as BNIPDSpm (Figure 65D). It is proposed that a more rigid binding occurs with less flexibility, utilising greater surface area and hence leading to lower binding concentrations. Increased drug loading feed concentration of BNIPd and specially BNIPDSpm resulted in greater drug attachment onto the HNPs surface. However, the physicochemical properties of the drug in solution hindered further attachment. By increasing the loading concentration of BNIPds from 2.5 mgmL $^{-1}$ to 5 mgmL $^{-1}$ the binding concentration of this drug to the surface of HNPs did not change significantly ($p > 0.05$), indicating that the particle surface was saturated and no more attachment was possible

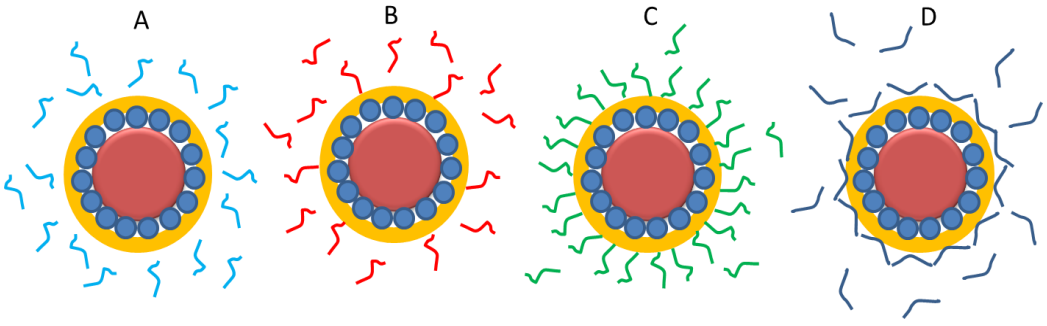

Figure 65. Schematic diagram illustrates conjugation ability of A) BNIDi, B) BNIPd, C) BNIPDSpm and D) BNIPds to the surface of HNP.

PEGylated formulations possessed comparable amount of drugs to unPEGylated formulations; however, slight increase in binding concentration of BNIPd and BNIPDSpm in PEGylated formulations was achieved. We assume that small quantities of drug molecules could have been physically trapped within the polymer framework. The presence of drugs in formulations was also proved by zeta potential measurement, FTIR and fluorescence spectroscopy. Following the lack of attachment of BNIDi into the surface of HNP and HNP-PEG, it was decided not to continue any further studies with these formulations.

Stability studies of the formulations at room temperature (20 ºC) and 4 ºC (in aqueous environment and for freeze dried samples) were in agreement with the conjugation theory since BNIPd formulations with two amines presented very low stability. BNIPDSpm formulations also showed satisfying stability as over 80 % stability was achieved at both temperatures and forms (aqueous and freeze dried forms). BNIPds in conjugation by both covalent (via two thiols) and electrostatic (via two amines) bonds with HNP and HNP-PEG presented the highest stability over the period of four weeks. Moreover, the stability of all formulations increased when samples were kept as a freeze dried powder at both temperatures, indicating that less drug detachment was occurred in the form of powder and liquid environment would increase the risk of drug release from the formulations.

Drug release studies were in line with the conjugation theory (Figure 66). The data showed that the release of BNIPd from formulations in aqueous environment at 20 ºC was very quick due to the loose electrostatic interaction of the drug with HNPs. Around 90 % of BNIPd released from PEGylated and unPEGylated formulations within 4 h and 6 h, respectively. Release of BNIPDSpm from formulations in water showed biphasic patterns, which includes a sharp release in the first 10 h, following by a gradual release. Increasing the temperature had an impact on release of BNIPDSpm from formulations and the highest release rate occurred in 60 ºC, where around 78 % and 57 % of drug released from PEGylated and unPEGylated formulation within 72 h, respectively. Release of BNIPDSpm from PEGylated formulation was higher than unPEGylated formulation which might be due to the small amount of free drug being trapped inside the polymer chain. Release of BNIPds from the formulations in 60 ºC was almost zero which could be due to the robust interaction of the drug with gold at the surface of HNPs.

Release of BNIPDSpm from the formulations was also investigated in culturing medium. Drug release was performed at 37 ºC and 44 ºC with different pH; pH 7.5 as it was close to cytoplasm pH and pH 4.6 and 3.6, which were in the range of endosomal and lysosomal pH, respectively. Drug release in culturing media followed the same pattern; however, decreasing the pH of media and increasing the temperature (from 37 ºC to 44 ºC) enhanced the drug release rate. Results showed that BNIPDSpm released in culturing media from HNP-PEG significantly faster than unPEGylated formulation ($p < 0.05$).

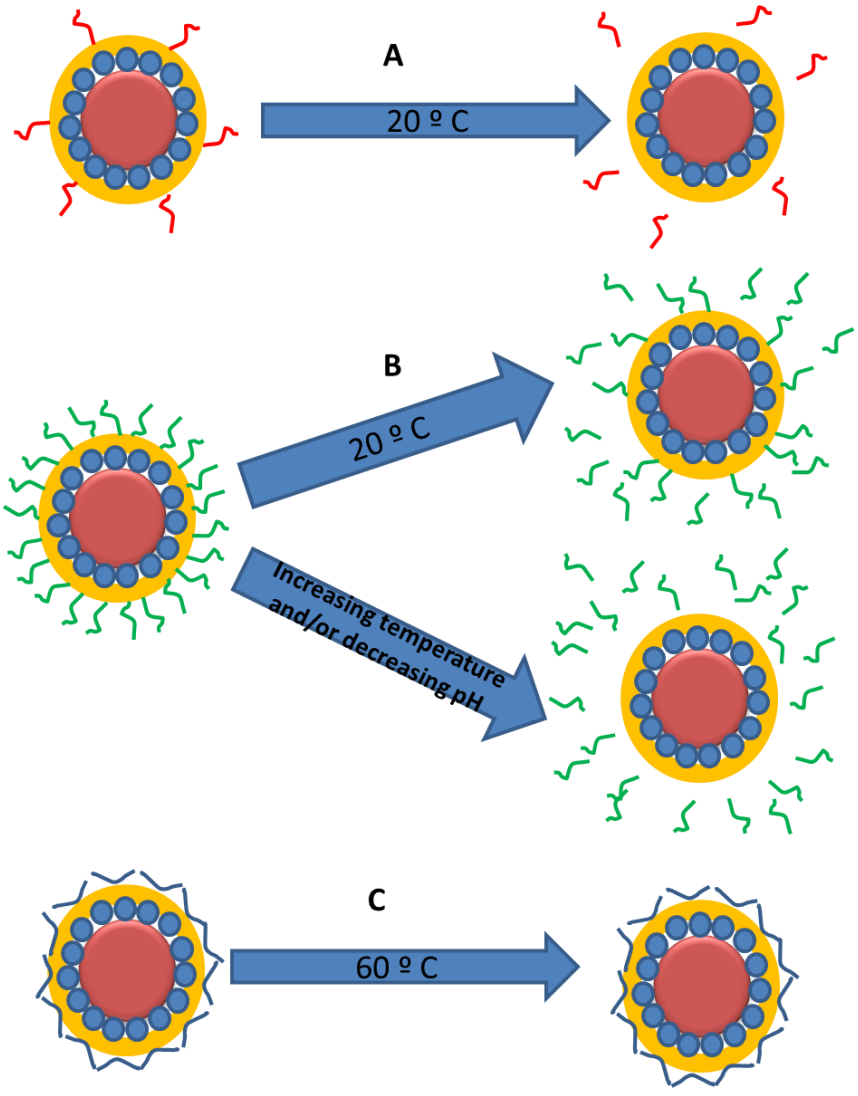

Figure 66. Diagram illustrates drug release pattern from A) BNIPd, B) BNIPDSpm and C) BNIPds formulations.

Drug release rate in culturing media, in 37 ºC and 44 ºC, was important for this study. Because 44 ºC would be the obtained temperature of HNPs upon laser irradiation.

Therefore, by *in vitro* drug release investigations in culturing media (in body temperature and 44 ºC), the release pattern of the formulations inside the pancreatic cancer cells, before and after laser irradiation can be predicted. These novel formulations demonstrated pH and thermoresponsive drug delivery properties. Therefore, it is suggested that when HNPs were taken up by endosome and lysosome, the low environmental pH and increasing the temperature via laser irradiation, would lead to quick drug release from the particles. Then the free drug can enter cells` nucleus and interact with DNA for anticancer effect.

Biological investigations of HNPs, bisnaphthalamide based drugs and their optimal formulations were performed on human primary pancreatic adenocarcinoma (BxPC-3), human epithelial-like pancreatic carcinoma (PANC-1) and human monocyte cell line, which possess macrophage like qualities after differentiation (U937). U937 cell line was applied in order to examine the cytotoxic effect of drugs and different formulations on immune cells. For cytotoxicity evaluation, MTT assay and trypan blue exclusion test were used. Fabricated HNPs incubated with BxPC-3, PANC-1 and U937 cells for 24 h, did not show apparent toxicity, indicating that these particles are not toxic as drug carriers. The cytotoxicity pattern of bisnaphthalamide derivatives was BNIPd > BNIPDSpm ≥ BNIPds. The high cytotoxicity of BNIPd might be associated with its chemical structure and number/ position of amine group (two lateral amines) that enables this drug to interact with the DNA of BxPC-3 cells more efficiently. The cytotoxicity results of hybrid formulations (in conjugation with bisnaphthalamide derivatives) on BxPC-3 cell line revealed significant reduction of cell viability after 24 h (compared with the free drugs), especially for PEGylated formulations. As an example, the cytotoxicity of BNIPDSpm-HNP and BNIPDSpm-HNP-PEG were 9-fold and 12-fold higher than the cytotoxicity of free drug, respectively. These findings confirm the high efficacy of hybrid formulations, compared to the drugs alone, which could be due to the higher uptake rate of the novel formulations by the cells. The cytotoxicity results from bisnaphthalamide derivatives and their hybrid formulations were compared with the conventional anticancer drug, gemcitabine. Interestingly, no IC_{50} achieved for BxPC-3, PANC-1 and differentiated U937 cells treating with gemcitabine within 24 h, which confirms that fabricated formulations were highly cytotoxic on pancreatic cancer cells, in comparison with gemcitabine. Although BNIPd, BNIPds and their formulations possessed potent anticancer effects, their physicochemical properties and potential use as a triggered system were lacking and the most suitable formulations regarding drug loading, stability and triggered drug release were the

BNIPDSpm formulations. Therefore, further cytotoxic studies were focused on BNIPDSpm formulations. The cytotoxicity of BNIPDSpm and its hybrid formulations on PANC-1 followed the same pattern. However, BNIPDSpm-HNP and BNIPDSpm-HNP-PEG were 8 times and 9 times more cytotoxic on BxPC-3 cells, respectively, in comparison with PANC-1 cells. The drug appeared to be more cytotoxic on U937, compared to hybrid formulations, indicating that conjugated BNIPDSpm cannot internalise into U937 cells as much as free drug. Free BNIPDSpm probably enter to the U937 cells through cell membrane pores/channels and nanoformulations are taken up by endocytosis. Therefore, slower proliferation of these cells, in comparison with BxPC-3 and PANC-1 cells resulted in reduced cytotoxic effect of conjugated drug, compared to free drug.

Drug uptake study was investigated for bisnaphthalamide based drugs, their hybrid formulations and gemcitabine within 1 h and 4 h incubation time, which was drug concentration and time dependent. Hybrid formulations possessed significant higher drug uptake ($p < 0.05$), especially PEGylated formulations, on BxPC-3 cells, at all incubation concentrations and times. Gemcitabine showed the highest uptake rate in this group, but the cytotoxicity result from gemcitabine showed that this drug did not possess IC_{50} after 24 h. This means that novel BNIPDSpm hybrid formulations are more efficient to kill pancreatic cancer cells, compared with gemcitabine. Due to the poor physicochemical properties and low uptake rate of BNIPd and BNIPds hybrid formulations after 4 h (compared with the BNIPDSpm formulations), it was decided not to continue any further biological experiments for these formulations. Cellular uptake pattern from PANC-1 cells were comparable to BxPC-3 cells. However, the uptake rate from BxPC-3 cells was around 5 times higher than PANC-1 cells, which might be due to the differences in proliferation of these cells, volume of the cells and/or binding sites for drugs per cell in pancreatic cancer cell lines. In U937 cell line, free BNIPDSpm was accumulated in cells more than hybrid formulations which showed again that hybrid formulations were not recognised by these cells as much as free drug. This could be due to the differences of uptake mechanisms for free drug and particles discussed before.

A c(RGDfC) peptide as a targeting agent was successfully incorporated to BNIPDSpm-HNP-PEG with the goal of targeting integrin avβ3 (receptor for the extracellular matrix proteins with the exposed arginine-glycine-aspartic (RGD) tripeptide

sequence) to increase drug specific delivery and anticancer activity of the hybrid formulation. The cytotoxic effect of PEGylated formulation on all three cell lines increased upon the addition of targeting peptide but this enhanced cytotoxic effect was insignificant on BxPC-3 and PANC-1 cells ($p > 0.05$). It is postulated that this slight increase of cytotoxicity upon the conjugation of targeting peptide could be associated with the 2D *in vitro* cytotoxicity analysis and higher cytotoxic effect may be achieved by 3D *in vitro* culturing or *in vivo* analysis. Targeted formulation was taken up by all cell lines significantly higher than BNIPDSpm-HNP-PEG at all concentrations and incubation times ($p < 0.05$), which confirms that the presence of targeting peptide resulted in higher accumulation of drug in cells.

In vitro thermoresponsive cytotoxicity test at different temperature was performed on BxPC-3, PANC-1 and U937 cell lines to investigate the heating effect on cytotoxicity of the formulations. This experiment was performed to mimic the particles` temperature increase upon the laser irradiation (up to 44 ºC). Our result showed that the viability of treated cells with hybrid formulations mostly decreased by increasing the temperature. This could be due to the higher amount of drug being released from the formulations in higher temperature. Moreover, the targeted formulation possessed comparable cytotoxic effect to BNIPDSpm-HNP-PEG at different temperatures.

Control and treated cells with different drugs and formulations (all three cell lines), were imaged by atomic force microscopy (AFM), after 1 h and 4 h incubation. The results were in agreement with drug uptake results, confirming higher cytotoxic effect of hybrid formulations comparing with free BNIPDSpm, especially the PEGylated formulation and targeted formulation, on BxPC-3 and PANC-1 cells as these formulations changed the structure and morphology of the cells significantly, after 1 h and 4 h. Except cells treated with BNIPDSpm for 4 h, no significant changes in the morphology of U937 cells was observed upon the incubation with drug and hybrid formulations, which is in line with the low cytotoxicity and uptake rate of BNIPDSpm formulations from these cells. These results provide evidence that BNIPDSpm delivery with HNPs is highly more efficient compared to the conventional anticancer drug, gemcitabine.

In conclusion, this is the first time novel HNPs, conjugated with bisnaphthalamaide derivatives, have been shown for pancreatic cancer therapy. BNIPDSpm novel

formulations possessed interesting potential to act as thermoresponsive drug carriers. The data suggested that the presence of PEG and RGD targeting peptide enhances the ability of the BNIPDSpm-HNP to act as biocompatible multimodal platforms with higher affinity to pancreatic cancer cells as an anticancer formulation.

5.2. Future work

The work describes the synthesis and evaluation of novel HNPs. These particles are designed such that they can produce heat on laser irradiation and load cytotoxic drugs to treat pancreatic cancer. Upon the gold coating of iron oxide core and incorporation of different bisnaphthalamide based drugs, multifunctional hybrid formulations have shown their superb application capability in diagnosis and therapeutics. Several hybrid nanoparticles have already exhibited promising application potential during clinical trials (Min *et al*. 2015). For example, functionalised iron oxide NPs such as dextran-coated iron oxide NPs (Sienna+®) for the detection of sentinel lymph nodes, aminosilane-coated iron oxide NPs (MFL AS1®) for hyperthermia therapy, and siloxane-coated iron oxide NPs (Ferumoxsil®) as efficient oral MRI contrast agents have presented clinical utility (Nguyen and Zhao, 2015). These encouraging results are driving the research field forward quickly. In view of the significant research efforts being dedicated to the field, it could be expected that humanity will greatly benefit from nanomedicine in the near future.

Despite all of the advantages of NP-based systems discussed in this account, there is always room for further improvements in this field. For example, in this study, laser irradiation was only performed in agar gel and raw chicken breast. It would be beneficial to study the actual temperature increase in cells *in vitro* and *in vivo*. Determination of surface temperature upon laser irradiation by fluorescent markers would also be useful to achieve better understanding about the actual temperature changes.

We investigated physiochemical and biological effect of four bisnaphthalamide derivatives in conjugation with HNPs. Further modification of the bisnapthalamide chain to increase drug loading capacity would be desirable. We performed a short term stability test (4 weeks) by storing liquid and freeze-dried preparations of the formulations. Long term stability testing of BNIPDSpm hybrid formulations in the future would be advantageous in

order to evaluate their potential as pharmaceutical formulations. More drug release studies involving laser irradiation at appropriate wavelength, i.e. closer wavelength to lambda max of HNP would also be beneficial.

Further cytotoxicity test is required on normal pancreatic cell lines, in order to compare with our cytotoxicity results on pancreatic cancer cells. It would also be beneficial to perform further *in vitro* intracellular trafficking to analyse the mechanism of cellular uptake in pancreatic cancer cells and to visualise exactly where particles reside, which can be carried out by staining the organelles in the cell e.g. cell membrane, nucleus, mitochondria, etc. (Savic *et al*. 2003). It would also be desirable to utilise different inhibitors such as cytochalasin D (endocytosis inhibitor) or sodium azide (metabolic inhibitor) to verify the mechanism of cellular uptake and fate of the particles such as active transport, endocytosis or a different type of transport (Maysinger *et al*. 2007).

It would be beneficial to image treated cells with fluorescent microscopy to show the accumulation of BNIPDSpm inside pancreatic cancer cells as the bisnaphthalamide derivatives are fluorescent chemicals. TEM imaging of accumulated particles inside the pancreatic cancer cells would also be desirable. Moreover, it may be valuable to repeat the AFM topography imaging of the formulations in cells, as the images could be improved upon.

In vivo study is also required to inject the formulation into the pancreatic tumour and investigate reduced growth in xenograft mice over longer time periods to validate the potential of the novel formulation for pharmaceutical therapies. All these studies must be carried out with the aim of bringing the work forward before being considered for clinical investigation.

References

ACS, Siegel, R., Jemal, A. (2014). **Cancer Facts & Figures**. *American Cancer Society, Atlanta, GA*

ACS, Blecher, E., Chaney-Graves, K., DeSantis, C., Edwards, B., *et al.* (2011). **Global Cancer Facts & Figures.** *American Cancer Society*. 2nd Edition. Atlanta.

Albanese, A., Chan, WCW. (2011). **Effect of Gold Nanoparticle Aggregation on Cell Uptake and Toxicity**, *ACS Nano*, 5:5478-5489.

Alexakis, N., Halloran, C., Raraty, M., Ghaneh, P., Sutton, R., Neoptolemos, JP. (2004). **Current standards of surgery for pancreatic cancer**. *Br J Surg*, 91:1410-27.

Alliain, LR., Vo-Dinh, T. (2002). **Surface-enhanced Raman scattering detection of the breast cancer susceptibility gene BRCA1 using a silver-coated microarray platform**. *Anal.Chim. Acta*, 469(1):149-154.

Alliain, LR., Vo-Dinh, T., Stokes, DL. (2002). **Cancer gene detection using surface-enhanced Raman scattering (SERS)**. *J. Raman Specpectrosc*, 33:511-516.

Amstad, E., Zurcher, S., Mashaghi, A., Wong, JY., Textor, M., Reimhult, E. (2009). **Surface functionalization of single superparamagnetic iron oxide nanoparticles for targeted magnetic resonance imaging**. *Small*, 5(11):1334-1342.

Andra, W., d'Ambly, CG., Hergt, R., Hilger, I., Kaiser, WA. (1999). **Temperature distribution as function of time around a small spherical heat source of local magnetic hyperthermia**. *J Magn Magn Mater*, 194: 197–203.

Andrén-Sandberg, A. (2012). **Review of literature on clinical panratology**. *Department of Surgery, Karolinska University Hospital at Huddinge.*

Ansari, SA., Hussain, Q. (2011). **Immobilization of kluyveromyces lactis b galactosidase on concanavalin A layered aluminium oxide nanoparticles—its future aspects in biosensor applications**. *J Mol Catal B Enzymatic*, 70:119-126.

Ansari, SA., Hussain, Q., Qayyum, S., Azam, A. (2011). **Designing and surface modification of zinc oxide nanoparticles for biomedical applications**. *Food Chem Toxicol*, 49:2107-2115.

Aoki, H., Aoki, H., Kutsuno, T., Li, W., Niwa, M. (2000). **An in vivo study on the reaction of hydroxyapatite-sol injected into blood**. *J. Mater.Sci Mater. Med*, 11:67-72.

Arruebo, M., Fernández-Pacheco, R., Ibarra, MR., Santamaría, J. (2007). **Magnetic nanoparticles for drug delivery**. *Nanotoday*, 2(3):22-32.

Aslam, M., Fu, L., Su, M., Vijayamohanan, K., Dravid VP. (2004). **Novel one-step synthesis of amine-stabilized aqueous colloidal gold nanoparticles**. *J. Mater. Chem,* 14:1795-1797.

Aubin-Tam, ME. (2013). **Conjugation of nanoparticles to proteins**. *Methods Mol Biol,* 1025:19-27.

Auffan, M., Rose, J., R. Wiesner, M., Bottero, J. (2009). **Chemical stability of metallic nanoparticles: A parameter controlling their potential cellular toxicity in vitro**. *Environmental Pollution,* 157:1127-1133.

Bae, KH., Lee, K., Kim, C., Park, TG. (2011). **Surface functionalized hollow manganese oxide nanoparticles for cancer targeted siRNA delivery and magnetic resonance imaging**. *Biomaterials,* 32:176-184.

Bae, YH., and Park, K. (2011). **Targeted drug delivery to tumors: Myths, reality and possibility.** *J Control Release***,** 153(3):198-205.

Bae, Y., Nishiyama, N., Fukushima, S., Koyama, H., Yasuhiro, M., Kataoka, K. (2005). **Preparation and biological characterization of polymeric micelle drug carriers with intracellular pHtriggered drug release property: tumor permeability, controlled subcellular drug distribution, and enhanced in vivo antitumor efficacy**. *Bioconjug Chem,*16:122-130.

Banerjee, S., B. Veale, E., M. Phelan, C., A. Murphy, S., M. Tocci, G., J. Gillespie, L., O. Frimannsson, D., M. Kelly, J., Gunnlaugsson, T. (2013). **Recent advances in the development of 1,8-naphthalimide based DNA targeting binders, anticancer and fluorescent cellular imaging agents**. *Chem. Soc. Rev*, 42:1601-1618.

Banwell, CN., McCash, EM. (1994). **Fundamentals of Molecular Spectroscopy**, *4th Edition, UK, McGraw-Hill International.*

Bard, AJ., Faulkner, LR. **Electrochemical Methods: Fundamentals and Applications**. (2001). *New York, NY, USA: John Wiley & Sons Inc,* 2.

Barenholz, Y. (2012). **Doxil ®--the first FDA approved nanodrug: lessons learned**. *J Control Release,* 160(2):117-134.

Barnett, C., Gueorguieva, M., Lees, M., Darton, R., McGarvey, D., Hoskins, C. (2012). **Effect of hybrid composition on physicochemical properties and morphology of iron oxide-gold nanoparticles.** *Journal of Nanoparticle Research,* 14:1170-1174.

Barnett, C., Gueorguieva, M., Lees, M., McGarvey, D., Hoskins, C. (2013a). **Physical stability, biocompatibility and potential use of hybrid iron oxide-gold nanoparticles as drug carriers**. *J Nano Res*, 15(6):1076.

Barnett, C., Lees, M., Curtis, ADM., Kong Thoo Lin, P., Cheng, WP., Hoskins, C. (2013b). **Poly(allylamine) magnetomicelles for image guided drug delivery**. *Available from OpenAIR@RGU*.

Barron, GA. (2010). **Novel bisnaphthalimidopropyl polyamine derivatives: their mode of action in a breast cancer cell system**. *Available from OpenAIR@RGU.*

Basel, MT., Balvida, S., Wang, H., Shresth, TB., Seo, GM., *et al.* (2012). **Cell-delivered magnetic nanoparticles caused hyperthermiamediated increased survival in murine pancreatic cancer model**. *Int J Nanomedicine*, 7:297-306.

Bate, G. (1980). **Recording Materials Chapter 7, in Ferromagnetic Materials.** *Wohlfarth, Elsevier, North Holland*, 2:381-507.

Bean, CP. (1956). **Magnetic Granulometry and Superparamagnetism.** *J Appl Phys*, 27:1448-1452.

Bekyarova, E., Ni, Y., Malarkey, EB. *et al*. (2005). **Applications of carbon nanotubes in biotechnology and biomedicine**. *J. Biomed Nanotechnol*, 1(1):3-17.

Beningo, KA., Wang, YL. (2002**). Fc-receptor-mediated phagocytosis is regulated by mechanical properties of the target**. *J Cell Sci*, 115:849-856.

Berne, BJ., Pecora, R. (2000). **Dynamic Light Scattering. Courier Dover Publications**. ISBN 0-486-41155-9.

Bhadra, D., Bhadra, S., Jain, P., Jain NK. (2002). **Pegnology: a review of PEG-ylated systems.** *Pharmazie*, 57:5-29.

Bianco, A., Kostarelos, K., Partidos, DC., Prato, M. (2005). **Biomedical applications of functionalized carbon nanotubes**. *Chem. Commun*, 5:571-577.

Binnig, G., Quate, CF., Gerber, C. (1986). **Atomic Force Microscope**. *Physical Review Letters*, 56:930-933.

Birks, JB. (1975). **Excimers, Reports on Progress in Physics**, 38:903-974.

Bonnemain, B. (1995). **Superparamagnetic agents in magnetic resonance imaging: Physicochemical characteristics and clinical applications - A review**. *Journal of Drug Targeting*, 6:167-174.

Bose, A., Wui, WT. (2013). **Convolution and validation of in vitro-in vivo correlation of water-insoluble sustained-release drug (domperidone) by first-order pharmacokinetic one-compartmental model fitting equation.** *Eur J Drug Metab Pharmacokinet*, 38(3):191-200.

Bouguer, P. (1729). **Essai d'optique sur la gradation de la lumière**. *Paris, France: Claude Jombert*, 16-22.

Brana, MF., Castellano, JM., Moran, M., Perea de vega, MJ., Qjan, XD., Romerdahl, CA., Keilhauer, G. (1995). **Bisnaphthalimides. 2. Synthesis and Biological Activity of 5, 6-acenaphthalimidoalkyl-1, 8-naphthalimidoalkyl amines**. *European Journal of Medicinal Chemistry*, 30:235-239.

Brana, MF., Castellano, JM., Moran, M., Perez de vega, MJ., Romerdahl, CR., Qjan, XD., *et al*. (1993). **Bis-naphthalimides: A New Class of Antitumour Agents**. *Anti-Cancer Drug Design*, 8: 257-268.

Brana, MF., Castellano, JM., Roldan, CM., Santos, A., Vazquez, D., Jimenez, A. (1980). **Synthesis and Mode(s) of Action of a New Series of Imide Derivatives of 3-nitro-1,8 naphthalic Acid**. *Cancer Chemotherapy and Pharmacology*, 4 (1):61-66.

Brana, MF., Ramos, A. (2001). **Naphthalimides as Anticancer Agents: Synthesis and Biological Activity**. *Current Medicinal Chemistry – Anti-Cancer Agents*, 1:237-255.

Britton, MM. (2010). **Magnetic resonance imaging of chemistry.** *Chem Soc Rev*, 39(11):4036-4043.

Bruchez JR, M., Moronne, M., Gin, P., Wwiss, S., Alivisatos, AP. (1998). **Semiconductor nanocrystals as fluorescent biological labels**. *Science*, 281 (5385): 2013-2016.

Buckley, CD., Pilling, D., Henriquez, NV., Parsonage, G., Threlfall, K., Scheel-Toellner, D., *et al*. (1999). **RGD-peptides induce apoptosis by direct caspase-3 activation**. *Nature*, 397:534-539.

Bystrejewski, M., Cudzilo, S., Huczko, A., Lange, H., Soucy, G., CotaSanchez, G., Kaszuwara, W. (2007). **Carbon encapsulated magnetic nanoparticles for biomedical applications @ thermal stability studies**. *Biomol Eng*, 24: 555–558.

Cai, W., Chen, X. (2007). **Nanoplatforms for targeted molecular imaging in living subjects**. *Small*, 3(11): 1840-1854.

Cai, W., Gao, T., Hong, H., Sun, J. (2008). **Applications of gold nanoparticles in cancer nanotechnology**. *Nanotechnology, Science and Applications*, 1:17-32.

Cai, W., Hsu, AR., Li, ZB. *et al*. (2007). **Are quantum dots ready for in vivo imaging in human subjects?** *Nanoscale Res Lett*, 2:265-281.

Cancer Research UK, (2014), **Pancreatic cancer**.

Cardot, JM., Beyssac, E., Alric, M. (2007). **In Vitro–In Vivo Correlation: Importance of Dissolution in IVIVC**. *Dissolution Technologies*, 15-19.

Carmichael, J., DeGraff, WG., Gazdar, AF., Minna, JD., Mitchell, JB. (1987). **Evaluation of a Tetrazolium-based Semiautomated Colorimetrie Assay: Assessment of Chemosensitivity Testing.** *Cancer* research, 47:936-942.

Carpenter, EE., Sangregorio, C., O'Connor, CJ. (1999). **Effects of shell thickness on blocking temperature of nanocomposites of metal particles with gold shells.** *IEEE Trans. Magn*, 35:3496- 3498.

Castner, DG., Hinds, K., Grainger, DW. (1996). **X-ray photoelectron spectroscopy sulfur 2p Study of organic thiol and disulfide binding interactions with gold surfaces**. *Langmuir*, 12: 5083-5086.

Chakraborty, S and Rahman, T. (2012). **The difficulties in cancer treatment.** *Ecancermedicalscience*, 6(16).

Chan, WCW. (2007). **Bio-applications of nanoparticles**. *Advances in experimental medicine and biology*, 620.

Chan, WCW., Nie, S. (1998). **Quantum dot bioconjugates for ultrasensitive nonisotopic detection**. *Science*, 281 (5385):2016-2018.

Chaudhuri, R.G., Paria, S. (2012). **Core/shell nanoparticles: Classes, properties, synthesis mechanisms, characterization, and applications**. *Chem. Rev*, 112:2373-2433.

Chen, DB., Yang, TZ., Lu, WL., Zhang, Q. (2001). ***In vitro* and *in vivo* study of two types of long-circulating solid lipid nanoparticles containing paclitaxel**. *Chem Pharmaceut Bull*, 49:1444-1447.

Chen, S. (2010). **Polymer coated iron oxide nanoparticle for biomedical imaging**. *Massachusetts Institute of Technology*.

Chen, W., Bian, A., Agarwal, A., Liu, L., Shen, H., Wang, L., Xu, C., Kotov, N A. (2009). **Nanoparticle superstructures made by polymerase chain reaction: collective interactions of nanoparticles and a new principle for chiral materials.** *Nano Lett*, 9:2153-2159.

Chen, WH., Xu, XD., Jia, HZ., *et al.* (2013). **Therapeutic nanomedicine based on dual-intelligent functionalized gold nanoparticles for cancer imaging and therapy *in vivo***. *Biomaterials*, 34(34):8798-8807.

Cheong, SJ., Lee, CM., Kim, SL., Jeong, HJ., Kim, EM., Park, EH., Kim, DW., Lim, ST., Sohn, MH. (2009). **Superparamagnetic iron oxide nanoparticles-loaded chitosan-linoleic acid nanoparticles as an effective hepatocyte-targeted gene delivery system.** *Int J Pharm*, 8;372(1-2):169-76.

Cho, SJ., Idrobo, JC., Olamit, J., Liu, K., Browning, ND., Kauzlarich, SM. (2005). **Growth Mechanisms and Oxidation Resistance of Gold-Coated Iron Nanoparticles.** *Chem. Mater*,17: 3181.

Choi, JS., Jun, YW., Yeon, SI., Kim, HC., Shin, JS., Cheon, J. (2006). **Biocompatible heterostructured nanoparticles for multimodal biological detection.** *J Am Chem Soc*, 128:15982-15983.

Ciobanu, CS., Iconaru, SL., Gyorgy, E., Radu, M., Costache, M., Dinischiotu, A., Coustumer, PL., Lafdi, K., Predoi, D. (2012). **Biomedical properties and preparation of ironoxide-dextran nanostructures by MAPLE technique**. Chemistry Central Journal, 6:17.

Comoucka, J., Drbohlavova, J., Huska, D., Adam, V., Kizek, R., Hubalek, J. (2010). **Magnetic Nanoparticles and Targeted Drug Delivering**. *Pharmacol Res*, 62:144-149.

Conde, J., Doria, G., Baptista, P. (2012). **Noble Metal Nanoparticles Applications in Cancer**. *Journal of Drug Delivery*, doi:10.1155/2012/751075.

Cortajarena, AL., Ortega, D., Ocampo, SM., Gonzalez-García,A., Couleaud, P., Miranda, R., Belda-Iniesta, C., Ayuso-Sacido, A. (2014). **Engineering Iron Oxide Nanoparticles for Clinical Settings**. *Nanobiomedicine*, DOI: 10.5772/58841.

Culha, M., Stokes, D., Allain, LR., Vo-Dinh, T. (2003). **Surface-enhanced Raman scattering substrate based on a self-assembled monolayer for use in gene diagnostics**. *Anal. Chem*, 75(22):6196-6201.

Cunha, AS., Rault, A., Laurent, C., Adhoute, X., Vendrely, V., Bellannee, G., Brunet, R., Collet, D., Masson, B. (2005). **Surgical resection after radiochemotherapy in patients with unresectable adenocarcinoma of the pancreas**. *J Am Coll Surg*, 201(3):359-365.

Curtis, A., Malekigorji, M., Holman, J., Skidmore, M., Hoskins, C. (2015). **Heat Dissipation of Hybrid Iron Oxide-Gold Nanoparticles in an Agar Phantom**. *J Nanomed Nanotechnol*, 6:6.

Deeney, RC., Sinclair, R. (1997). **Ultraviolet and Visible Spectroscopy**, *2nd Edition, Thomas.M UK, John Wiley and Sons.*

DeLong, RK., Reynolds, CM., Malcolm, Y., Schaeffer, A., Severs, T., Wanekaya, Ad. (2010). **Functionalized gold nanoparticles for the binding, stabilization, and delivery of therapeutic DNA, RNA, and other biological macromolecules**. *Nanotechnology, Science and Applications*, 3:56-63.

Denkhaus, E., Salnikow K. (2002). **Nickel essentiality, toxicity, and carcinogenicity**. *Crit Rev Oncol Hematol*, 42(1):35-56.

Dong, K., Liu, Z., Li, Z., Ren, J., Qu, X. (2013). **Hydrophobic anticancer drug delivery by a 980 nm laser-driven photothermal vehicle for efficient synergistic therapy of cancer cells *in vivo*.** *Adv Mater*, 25(32):4452-4458.

Dreaden, EC., Mackey, MA., Huang, X., Kang, B., El-Sayed, MA. **Beating cancer in multiple ways using nanogold**. *Chem. Soc. Rev*, 40(7):3391-3404.

Dunlop D. (1973). **Superparamagnetic and single-domain threshold sizes in magnetite**. *J Geophysical Research*, 78(11):1780-1793.

Farokhzad, OC., Langer, R. (2006). **Developing smarter therapeutic and diagnostic modalities**. *Adv. Drug Deliv*. Rev. 58:1456-1459.

Fassel, VA., Kniesley, RN. (1974). **Inductively coupled plasma optical or emission spectroscopy**, *Analytical Chemistry*, 46:1110a-1120a.

Ferlay, J., Soerjomataram, I., Ervik, M., Dikshit, R., Eser, S., Mathers, C., Rebelo, M., Parkin, DM., Forman, D., Bray, F. (2013). **Cancer Incidence and Mortality Worldwide**. *International Agency for Research on Cancer*, 1:11.

Ferrari, M. (2005). **Cancer nanotechnology: opportunities and challenges**. *Nat Rev Cancer*, 5:161-171.

Farrell, JJ., Elsaleh, H., Garcia, M., Lai, R., Ammar, A., Regine, WF., Abrams, R., Benson, AB., *et al*. (2009). **Human equilibrative nucleoside transporter 1 levels predict response to gemcitabine in patients with pancreatic cancer**. *Gastroenterology*, 136(1):187-195.

Feynman, R. (1959). **Engineering and Science**. *California Institute of Technology*.

Fiedler, VU., Schwarzmaier, HJ., Eickmeyer, F., *et al*. (2001). **Laser-induced interstitial thermotherapy of liver metastases in an interventional 0.5 Tesla MRI system: technique and first clinical experiences**. *J Magn Reson Imaging*, 13: 729-737.

Figuerola, A., Di Corato, R., Manna, L., Pellegrino, T. (2010). **From iron oxide nanoparticles towards advanced iron-based inorganic materials designed for biomedical applications.** *Pharmacol Res*, 62(2):126-143.

Freeman, MW., Arrott, A., Watson, JHL. (1960). **Magnetism in medicine**. *J Appl Phys*, 31:S404.

Freshney. R.I. (2005). **Culture of Animal Cells A Manual of Basic Technique**, *5th Edition, Hoboken NJ, John Wiley & Sons Inc.*

Frieboes, HB., Chaplain, MA., Thompson, AM., Bearer, EL., Lowengrub, JS., Cristini, V. (2011). **Physical oncology: a bench-to-bedside quantitative and predictive approach**. *Cancer Res*, 71(2):298-302.

Funkhouser J. (2002). **Reinventing pharma: The theranostic revolution**. *Current Drug Discovery*, 2:17-19.

Gao, W., Xu, K., Ji, L., Tang, B. (2011). **Effect of gold nanoparticles on glutathione depletion-induced hydrogen peroxide generation and apoptosis in HL7702 cells**. *Toxicol Lett*, 205:86-95.

Gao, Y., Li, Y., Wang, Y., Chen, Y., Gu, J., Zhao, W., Ding, J., Shi, J. (2015). **Controlled Synthesis of Multilayered Gold Nanoshells for Enhanced Photothermal Therapy and SERS Detection**. *Small*, 11(1):77-83.

Ghafoor, M. (2012). **NMR Studies of the Structure and Interactions of Novel Bis naphthalimidopropyl Anticancer Drugs**. Faculty of Engineering and Physical Sciences, University of Manchester.

Glazer, E. S ., Cihui, Zhu., Katheryn., Massey, L., Shea Thompson, C., Warna, D., Kaluarachchi Amir, N., Hamir Steven, A., Curley. (2010). **Noninvasive Radiofrequency Field Destruction of Pancreatic Adenocarcinoma Xenografts Treated with Targeted Gold Nanoparticles**. *Clin Cancer Res*, 16(23):5712-5721.

Gneveckow, U., Jordan, A., Scholz, R., Cho CH., FeuBner, A., Eckelt, L., Wust, P. (2005). **Magnetic force nanotherapy.** *Biomed*. Tech, 50:92-93.

Goodwin, S., Peterson, C., Hoh, C., Bittner, C. (1999). **Targeting and retention of magnetic targeted carriers (MTCs) Enhancing intra-arterial chemotherapy**. *J. Magn. Magn. Mater*, 194(1-3):132-139.

Goon, IY., Lai, LMH., Lim, M., Munroe, P., Gooding, JJ., Amal, R. (2009). **Fabrication of gold-shell-protected magnetite nanoparticles: systematic control using polyethyleneimine**. *Chem Mater*, 21:673-681.

Gratton, SE., Napier, ME., Ropp, PA., Tian, S., DeSimone, JM. (2008). **Microfabricated particles for engineered drug therapies: elucidation into the mechanisms of cellular internalization of PRINT particles**. *Pharm Res*, 25:2845-2852.

Gref, R., Lu¨ck, M., Quellec, P., Marchand, M., Dellacherie, E., Harnisch, S., Blunk, T. Mu¨ller, RH. (2000). **'Stealth' corona-core nanoparticles surface modified by polyethylene glycol (PEG): influences of the corona (PEG chain length and surface density) and of the core composition on phagocytic uptake and plasma protein adsorption.** *Colloids Surf*, 18:301-313.

Gregoria, G., Wills, EJ., Swain, CP., Tavill, AS. (1974). **Drug-Carrier Potential of Liposomes in Cancer Chemotherapy**. *Lancet*, 1: 1313-1316.

Griffiths, P., de Hasseth, JA. (2007). **Fourier Transform Infrared Spectrometry**. *(2nd ed.), Wiley-Blackwell*, ISBN 0-471-19404-2.

Grodzinski, P., Silver, M., Molnar, LK. (2006). **Nanotechnology for cancer diagnostics: promises and challenges.** *Expert Rev Mol Diagn*, 6:307-318.

Gu, Z., Jing, C., Ying, YL., 2, He, P., Long, YT. (2015). **In situ High Throughput Scattering Light Analysis of Single Plasmonic Nanoparticles in Living Cells**. *Theranostic*, 5(2):188-195.

Guo,Y., Zhang, Z., Kim ,D., Li, W., Nicolai, J., Procissi, D., *et al*. (2013). **Photothermal ablation of pancreatic cancer cells with hybrid iron-oxide core gold-shell nanoparticles**. *Int J Nanomedicine*, 8:3437-3446.

Gupta, AK., Gupta, M. (2005). **Synthesis and surface engineering of iron oxide nanoparticles for biomedical applications**. *Biomaterials*, 26:3995-4021.

Gurova, K. (2009). **New hopes from old drugs: revisiting DNA-binding small molecules as anticancer agents**. *Future Oncology*, 5(10):1685-1704.

Guzman, KAD., Finnegan, MP., Banfield, JF. (2006). **Influence of surface potential on aggregation and transport of titania nanoparticles**. *Environ. Sci. Technol*. 40:7688-7693.

Häfeli, OU., Riffle, JS., Harris-Shekhawat, l., Carmichael-Baranauskas, A., Mark, F., Dalley, JP., Bardenstein, D. (2009). **Cell uptake and in vitro toxicity of magnetic nanoparticles suitable for drug delivery**. *Mol Pharm*, 6:1417-1428.

Hahn, GM. (1982). **Thermal Enhancement of the Actions of Anticancer Agents**. *Hyperthermia and Cancer*, 55-86.

Harisinghani, MG., Barentsz, J., Hahn, PF., Deserno, WM., Tabatabaei, S., Hulsbergen van de Kaa, C., De la Rosette, J., Weissleder, R. (2003). **Noninvasive detection of clinically occult lymph-node metastases in prostate cancer**. *New England Journal of Medicine*, 348:2491-U5.

Haynes, DR., Crotti, TN., Haywood, MR. (2000). **Corrosion of and changes in biological effects of cobalt chrome alloy and 316L stainless steel prosthetic particles with age**. *J Biomed Mater Res*. 49(2):167-75.

He, C., Hu, Y., Yin, L., Tang, C., Yin C. (2010). **Effects of particle size and surface charge on cellular uptake and biodistribution of polymeric nanoparticles**. *Biomaterials*, 31:3657-3666.

Hedgire, SS., Mino-Kenudson, M., Elmi, A., Thayer, S., Fernandez-del, CC., *et al*. (2014). **Enhanced primary tumour delineation in pancreatic adenocarcinoma using ultra small super paramagnetic iron oxide nanoparticle-ferumoxytol: an initial experience with histopathological correlation**. *Int J Nanomedicine*, 9:1891-1896.

Hainfeld, JF., O'Connor, MJ., Lin, P., Qian, L., Slatkin, DN., Smilowitz, HM., Karathanasis E. (2014). **Infrared-Transparent Gold Nanoparticles Converted by Tumors to Infrared Absorbers Cure Tumors in Mice by Photothermal Therapy**. *PLoS One*, 9(2):e88414.

Hergt, R., Dutz, S., Muller, R., Zeisberger, M. (2006). **Magnetic particle hyperthermia: nanoparticle magnetism and materials development for cancer therapy**. *J Phys: Condens Matter*, 18: S2919-S2934.

Hervault, A and Thanh, NTK. (2014). **Magnetic nanoparticle-based therapeutic agents for thermo-chemotherapy treatment of cancer**. *Nanoscale*, 6:11553-11573.

Hilger, I., Hergt, R., Kaiser, WA. (2005). **Use of magnetic nanoparticle heating in the treatment of breast cancer IEE Proc**. *Nanobiotechnol*, 152:33-39.

Hilger, I., Kaiser, W. (2012). **Iron oxide-based nanostructures for MRI and magnetic hyperthermia**. *Nanomedicine*, 7(9):1443-1459.

Hirsch, LR., Stafford, RJ., Bankson, JA., Sershen, SR., Rivera, B., Price, RE., Haxle, JD., Halas, NJ., West, JL. (2003). **Nanoshell-medicated near-infrared thermal therapy of tumors under magnetic resonance guidance**. *Proc Natl Acad Sci USA*,100:13549-13554.

Hleb, Y., Hafner, J. H., Myers, J. N., Hanna, E. Y., Rostro, B. C., Zhdanok, S. A., Lapotko, DO. (2008). **LANTCET: elimination of solid tumour cells with photothermal bubbles generated around clusters of gold nanoparticles**. *Nanomedicine (Lond.)*, 3:647.

Hoskins, C. (2010). **The use of novel poly(allylamine) based amphiphilic polymers for drug delivery**. *Available from OpenAIR@RGU*.

Hoskins, C., Cuschieri, A., Wang, L. (2012a). **Cytotoxicity of polycationic iron oxide nanoparticles: Common endpoint assays and alternative approaches for improved understanding of cellular response mechanism**. *J Nanobiotechnol*, 10:15.

Hoskins, C., Min, Y., Gueorguieva, M., McDougall, C., Volovick, A., Prentice, P., Wang, Z., Melzer, A., Cuschieri, A., Wang, L. (2012b). **Hybrid gold-iron oxide nanoparticles as a multifunctional platform for biomedical application**. *Journal of Nanobiotechnology*, 10:27.

Hoskins, C., Ouaissi, M., Lima, SC., Cheng, WP., Loureirio, I., *et al*. (2010). **In vitro and in vivo anticancer activity of a novel nano-sized formulation based on self-assembling polymers against pancreatic cancer**. *Pharm Res*, 27(12):2694-2703.

Hoskins, C., Wang, L., Cheng, WP., Cuschieri, A. (2012c). **Dilemmas in the reliable estimation of the in-vitro cell viability in magnetic nanoparticle engineering: which tests and what protocols?** *Nanoscale Res Letts*, 7:77.

Hosotani, R., Kawaguchi, M., Masui, T., Koshiba, T., Ida, J., Fujimoto, K., *et al*. (2002). **Expression of integrin avβ3 in pancreatic carcinoma: relation to mmp-2 activation and lymph node metastasis.** *Pancreas*, 25:30-35.

Hou, X., T. Jones, B. (2000). **Inductively Coupled Plasma/Optical Emission Spectrometry.** *Encyclopedia of Analytical Chemistry*, 9468-9485.

Hu, R., Yong, K., Roy, I., Ding, H., He, S., Prasad, P. (2009). **Metallic Nanostructures as Localized Plasmon Resonance Enhanced Scattering Probes for Multiplex Dark-Field Targeted Imaging of Cancer Cells**. *J. Phys. Chem*, 113(7):2676-2684.

Huang, C., Jiang, J., Muangphat, C., Sun, X., Hao, Y. (2011). **Trapping iron oxide into hollow gold nanoparticles.** *Nanoscale Res Lett*, 6:1-5.

Huang, P., Baob, Le., Zhanga, C., Lina, J., Luoa, T., Yang, D., *et al*. (2011b). **Folic acid-conjugated silica-modified gold nanorods for X-ray/CT imaging-guided dual-mode radiation and photo-thermal therapy**. *Biomaterials*, 32:9796-9809.

Huang, X., Jain, PK., El-Sayed, IH. *et al*. (2007). **Gold nanoparticles: interesting optical properties and recent applications in cancer diagnostics and therapy**. *Nanomed*, 2: 681-693.

Hurtubise, RJ. (1990**). Phosphorimetry: Theory, instrumentation, and applications**, *USA, VCH*.

Hwang, R., Varner, JV. (2004). **The role of integrins in tumor angiogenesis**. *Hematol Oncol Clin North Am,*18:991-1006.

Hwu, JR., Lin, YS., Josephrajan, T., Hsu, MH.,Cheng, FY., Yeh, CS., Su, WC., Shieh, DB. (2009). **Targeted Paclitaxel by Conjugation to Iron Oxide and Gold Nanoparticles**. *J. Am. Chem*, 131:66-68.

Iancu, C. (2013). **Photothermal Therapy of Human Cancers (PTT) Using Gold Nanoparticles.** *Biotechnology, Molecular Biology and Nanomedicine*, 1(1):53-60.

Iglesias-Silvaa, E., Vilas-Vilelaa, JL., López-Quintelab, MA., Rivasb, J., Rodrígueza, M., Leóna, LM. (2010). **Synthesis of gold-coated iron oxide nanoparticles**. *Journal of Non-Crystalline Solids*, 356(25-27):1233-1235.

Ilovitsh, T., Danan, Y., Meir, R., Meiri, A., Zalevsky, Z. (2015). **Cellular imaging using temporally flickering nanoparticles**. *Scientific Reports*, 5:8244.

Itoh, H., Sugimoto, T. (2003). **Systematic control of size, shape, structure, and magnetic properties of uniform magnetite and maghemite particles**. *J Colloid Interface Sci*, 265:283-295.

Jain, S., Hirst, DG., O'Sullivan, JM. (2012). **Gold nanoparticles as novel agents for cancer therapy**. *Br J Radiol*, 85(1010):101-113.

Jain, PK., Lee, KS., El-Sayed, IH., El-Sayed, M.A. (2006). **Calculated absorption and scattering properties of gold nanoparticles of different size, shape, and composition: applications in biological imaging and biomedicine**. *J Phys Chem B*, 110(14):7238-7248.

Jain, TK., Morales, MA., Sahoo, SK., Leslie-Pelecky, DL., Labhasetwar, V. (2005). **Iron oxide nanoparticles for sustained delivery of anticancer agents**. *Mol. Pharmaceutics*, 2:194-205.

Jeanbart, L., Ballester, M., de Titta, A., Corthésy, P., Romero, P., Hubbell, JA., Swartz, MA. (2014). **Enhancing efficacy of anticancer vaccines by targeted delivery to tumor-draining lymph nodes**. *Cancer Immunol Res*, 2(5):436-447.

Jelveh, S., Chithrani, DB. (2011). **Gold Nanostructures as a Platform for Combinational Therapy in Future Cancer Therapeutics**. *Cancers*, 3(1):1081-1110.

Jensen, TR., Duval, ML., Kelly, KL., Lazarides, AA., C. Schatz, GC., P. Van Duyne, RP. (1999). **Nanosphere Lithography: Effect of the External Dielectric Medium on the Surface Plasmon Resonance Spectrum of a Periodic Array of Silver Nanoparticles**. *J. Phys. Chem*. B,103(45):9846-9853.

Jeong, U., Teng, X., Wang, Y., Yang, H., Xia, Y. (2007). **Superparamagnetic Colloids: Controlled Synthesis and Niche Applications.** *Adv. Mater*, 19:33-60.

Ji, S., Xu, J., Zhang, B., Yao, W., Xu, W., Wu, W., Xu, Y., Wang, H., Ni, Q., Hou, H., Yu, X. (2012). **RGD-conjugated albumin nanoparticles as a novel delivery vehicle in pancreatic cancer therapy**. *Cancer Biol Ther*, 15:13(4):206-215.

Jiang, W., Kim, BYS., Rutka, JT., Chan, WCW. (2008). **Nanoparticle-mediated cellular response is size-dependent**. *Nat. Nanotechnol*, 3(3):145-150.

Jiang, X., Weise, S., Hafner, M., Ro¨cker, C., Zhang, F., Parak, WJ., Nienhaus, GU. (2010). **Quantitative analysis of the protein corona on FePt nanoparticles formed by transferrin binding**. *J. R. Soc. Interface*,7:S5-S13.

Jin, ZH., Razkin, J., Josserand, V., Boturyn, D., Grichine, A., Texier, I., Favrot, MC., Dumy, P., Coll, JL. (2007). ***In Vivo*** **Noninvasive Optical Imaging of Receptor-Mediated RGD Internalization Using Self-Quenched Cy5-Labeled RAFT-c(-RGDfK-)4.** *Molecular Imaging*, 6(1):43-55.

Jokerst, JV, Lobovkina, T., Richard, NZ., Gambhir, SS. (2011). **Nanoparticle PEGylation for imaging and therapy**. *Nanomedicine (Lond)*, 6(4):715-728.

Johnston, MJ., Semple, SC., Klimuk, SK., Edwards, K., Eisenhardt, ML., Leng, EC., Karlsson, G., Yanko, D., Cullis, PR. (2006). **Therapeutically optimized rates of drug release can be achieved by varying the drug-to-lipid ratio in liposomal vincristine formulations**. *Biochim Biophys Acta*, 1758(1):55-64.

Joubert, JC., Quim, An. (1997). **Magnetic Microcomposites as Vectors for Bioactive. Agents: The State of Art**. *Anales de Quimica*, Int. Ed: 93 S70.

Kam, NW., O'Connell, M., Wisdom, JA., Dai, H. (2005). **Carbon nanotubes as multifunctional biological transporters and near infrared agents for selective cancer cell destruction**. *Proc Natl Acad Sci USA*, 102(33):11600-11605.

Kandpal, ND., Sah, N., Loshali, R., Joshi, R., Prasad J. (2014). **Co-precipitation method of synthesis and characterization of iron oxide nanoparticles**. *J Scientific & Industrial Research*, 73:87-90.

Karimi Goftar, M., Moradi Kor, N., Moradi Kor, Z. (2014). **DNA intercalators and using them as anticancer drugs**. *Int j Adv Biological and Biomedical Res,* 2:811-822.

Kardys, AY., Bharali, DJ., Mousa, SA. (2013). **Amino-Functionalized Silica Nanoparticles: In Vitro Evaluation for Targeted Delivery and Therapy of Pancreatic Cancer**. *Journal of Nanotechnology*,Article ID 768724, 8 pages.

Kawamura, G., Nogami, M., Matsuda, A. (2013). **Shape-Controlled Metal Nanoparticles and Their Assemblies with Optical Functionalities**. *Journal of Nanomaterials*, 2013:1-17.

Kayal, S., Ramanujan ,R. V. (2010). **Anti-cancer drug loaded iron-oxide core-shell nanoparticles (Fe@Au) for magnetic drug targeting**. *J. Nanosci. Nanotechnol*:5527-5539.

Kazakevich, Y., LoBrutto, R. (2007). **HPLC for Pharmaceutical Scientists**, *John Wiley and Sons Inc., US.*

Keane, MG., Horsfall, L., Rait, G., Pereira, P. (2014). **A case–control study comparing the incidence of early symptoms in pancreatic and biliary tract cancer**. *BMJ*, 4(11).

Kemshead, JT., Ugelstad, J. (1985). **Magnetic separation techniques: their application to medicine**. *Mol Cell Biochem*, 67:11-18.

Kessentini, S., Barchiesi, D. (2013). **Optimized Nanocage for Cancer Photothermal Therapy and Comparison with Other Nanoparticles**. *Electromagnetics Research Symposium Proceedings, Stockholm, Sweden*.

Khan, AK., Rashid, R., Murtaza, G., Zahra, A. (2014). **Gold Nanoparticles: Synthesis and Applications in Drug Delivery**. *Tropical J Pharmaceutical Research*. 13(7):1169-1177.

Kievit, FM., Wang, FY., Fang, C., Mok, H., Wang, K., Silber, JR., Ellenbogen, RG., Zhang M. (2011). **Doxorubicin loaded iron oxide nanoparticles overcome multidrug resistance in cancer in vitro**. *J Control Release*,152(1):76-83.

Kievit, FM., Zhang, M. (2011). **Surface engineering of iron oxide nanoparticles for targeted cancer therapy**. *Acc Chem Res*,18;44(10): 853-862.

Kilian, KA., Mrksich, M. (2012). **Directing stem cell fate by controlling the affinity and density of ligand-receptor interactions at the biomaterials interface**. *Angew Chem Int Ed Engl*, 14;51(20):4891-4895.

Kim, CK., Ghosh, P., Pagliuca, C., Zhu, ZJ., Menichetti, S., Rotello, VM. (2009). **Entrapment of hydrophobic drugs in nanoparticle monolayers with efficient release into cancer cells**. *J. Am. Chem*. Soc,131(4):1360-1361.

Kita, E., Hashimoto, S., Kayano, T., Minagawa, M., Yanagihara, H., Kishimoto, M., Yamada, K., Oda, T., Ohkohchi, N., *et al*. (2010). **Heating characteristics of ferromagnetic iron oxide nanoparticles for magnetic hyperthermia**. *J. Appl. Phys*, 107.

Kodiha, M., Wang, YM., Hutter, E., Maysinger, D., Stochaj, U. (2015). **Off to the Organelles - Killing Cancer Cells with Targeted Gold Nanoparticles**. *Theranostics*, 5(4):357-370.

Kogan, MJ., Olmedo, I., Hosta, L., Guerrero, AR., Cruz, LJ., Albericio, F. (2007). **Peptides and metallic nanoparticles for biomedical applications**. *Nanomedicine (Lond)*, 2(3):287-306.

Kondoh, H., Iwasaki, M., Shimada, T., Amemiya, K.,Yokoyama, T., Ohta, T., Shimomura, M., Kono, S. (2003). **Adsorption of thiolates to singly coordinated sites on Au(111) evidenced by photoelectron diffraction**. *Phys. Rev. Lett*, 90, 066102.

Koppolu, B., Bhavsar, Z., Wadajkar, A., Nattama, S., Rahimi, M., Nwariaku, F., Nguyen, K. (2012). **Temperature-Sensitive Polymer-Coated Magnetic Nanoparticles as a Potential Drug Delivery System for Targeted Therapy of Thyroid Cancer**. *Journal of Biomedical Nanotechnology*, 8(6):983-990.

Kosaka, PM., Pini, V., Ruz, JJ., da Silva, RA., González, MU., Ramos, D., Calleja, M., Tamayo, J. (2014). **Detection of cancer biomarkers in serum using a hybrid mechanical and optoplasmonic nanosensor**. *Nature Nanotechnology*, 9:1047-1053.

Köseoğlu, Y., Yıldız, F., Kim, D.K., Muhammed, M., Aktaş, B. (2004). **EPR studies on Na-oleate coated Fe_3O_4 nanoparticles, Second Seeheim**. *Conference on Magnetism*, 1(12):3511-3515.

Kossatz, S., Ludwig, R., Dahring, H., Ettelt, V., Rimkus, G., *et al.* (2014). **High therapeutic efficiency of magnetic hyperthermia in xenograft models achieved with moderate temperature dosages in the tumour area**. *Pharm Res*, DOI 10.1007/s11095-014-1417-0.

Kruse, AM., Meenach, SA., Anderson, KW., Hilt, JZ. (2014). **Synthesis and characterization of CREKA-conjugated iron oxide nanoparticles for hyperthermia applications**. *Acta Biomater*, 10(6): 2622-2629.

Ku, S., Yan, F., Wang, Y., Sun, Y., Yang, N., Ye, L. (2010). **The blood– brain barrier penetration and distribution of PEGylated fluorescein-doped magnetic silica nanoparticles in rat brain.** *Biochem. Bioph. Res. Co*, 394:871-876.

Lammersa, T., Kiesslinga, F., Henninkb, WE., Stormb, G. (2012). **Drug targeting to tumors: Principles, pitfalls and (pre-) clinical progress**. *J Controlled Release*, 161(2):175–187.

Lamprecht, A., Torres, HR, Schäfer, U., Lehr, CM. (2000). **Biodegradable microparticles as a two-drug controlled release formulation: a potential treatment of inflammatory bowel disease**, *Journal of Controlled Release*, 69:445-454.

Lankisch, PG., Assmus, C., Maisonneuve, P., Lowenfels, AB. (2002). **Epidemiology of pancreatic diseases in Luneburg County**. *Pancreatology*, 2:469-477.

Lapotko, D., Lukianova, E., Oraevsky, A. (2006). **Selective laser nano-thermolysis of human leukemia cells with microbubbles generated around clusters of gold nanoparticles**. *Lasers Surg. Med*, 38:631.

Lawaczeck, R., Bauer, H., Frenzel, T., Hasegawa, M., Ito, Y., Kito, K., Miwa, N., Tsutsui, H., Vogler, H., Weinmann, HJ. (1997). **Magnetic iron oxide particles coated with carboxydextran for parenteral administration and liver contrasting**. *Acta Radiol*, 38:584–597.

Lee, GY., Qian, WP., Wang, L., Wang, YA., Staley, CA., *et al.* (2013). **Theranostic nanoparticles with controlled release of gemcitabine for targeted therapy and MRI of pancreatic cancer**. *ACS Nano*, 7(3):2078-2089.

Lee, JH., Lee, K., Moon, SH., Lee, Y., *et al*. (2009). **All-in-one target-cell specific magnetic nanoparticles for simultaneous molecular imaging and siRNA delivery**. *Angew. Chem. Int. Ed. Engl*, 48:4174-4179.

Lee, K., Lee, H., Bae, KH., Park, TG. (2010). **Heparin immobilized gold nanoparticles for targeted detection and apoptotic death of metastatic cancer cells**. *Biomater*, 31: 6530-6536.

Lee, KH., Galloway, JF., Park, J., Dvoracek, CM., Dallas, M., *et al.* (2012). **Quantitative molecular profiling of biomarkers for pancreatic cancer with functionalized quantum dots**. *Nanomedicine*, 8(7):1043-1051.

Lee, N., Kim, H., Choi, SH., Park, M., Kim, D., Kim, HC., Choi, Y., Lin, S., Kim, BH., Jung, HS., Kim, H., Park, KS., Moon, WK., Hyeon, T. (2011a). **Magnetosome-like ferromagnetic iron oxide nanocubes for highly sensitive MRI of single cells and transplanted pancreatic isltets**. *Proc Natl Acad Sci USA*, 108:2662-2667.

Lee, SK., Han, MS., Asokan, S., Tung, CH. (2011b). **Effective gene silencing by multilayered siRNA-coated gold nanoparticles**. *Small*, 7(3):364–370.

Lee, UY., Youn, YS., Park, J., Lee, and ES. (2014). **Y-Shaped Ligand-Driven Gold Nanoparticles for Highly Efficient Tumoural Uptake and Photothermal Ablation**. *ACS Nano*, 8 (12):12858-12865.

Letsinger, RL., Elghanian, R., Viswanadham, G., Mirkin, CA. (2000). **Use of a steroid cyclic disulfide anchor in constructing gold nanoparticle-oligonucleotide conjugates**. *Bioconjug Chem*, 11(2):289-291.

Levy, L., Sahoo, Y., Kim, KS., Bergey, EJ., Prasad, PN. (2002). **Nanochemistry: Synthesis and characterization of multifunctional nanoclinics for biological application**. *Chem. Mater*, 14:3715-3721.

Li, J., Zhou, J., Jiang, T., Wang, B., Gu, M., Pettic, L., Mormilec, P. (2014). **Controllable synthesis and SERS characteristics of hollow sea-urchin gold nanoparticles**. *Phys. Chem. Chem. Phys*, 16:25601.

Li, Y., Schluesenerb., HJ., Xua, S. (2010). **Gold nanoparticle-based biosensors**. Gold Bulletin, 43(1):29-41.

Liberti, PA., Rao, CG., Terstappen, LW. (2001). **Optimization of ferrofluids and protocols for the enrichment of breast tumour cells in blood**. *J. Magn. Mater*, 225:301-307.

Lin, J., Zhou, W., Kumbhar, A., Wiemann, J., Fang, J., Carpenter, EE., O'Connor CJ. (2001). **Gold-Coated Iron (Fe@Au) Nanoparticles: Synthesis, Characterization, and Magnetic Field-Induced Self-Assembly**. *Solid State Chem*, 159:26-31.

Lin, Y., Taylor, S., Li, H. *et al*. (2004). **Advances toward bioapplications of carbon nanotubes**. *J. Mater. Chem*, 14(4):527-541.

Lin, Z., Monteiro-Riviere, N., Riviere, J. (2014). **Pharmacokinetics of metallic nanoparticles**. *Wiley Interdisciplinary Reviews: Nanomedicine and Nanobiotechnology*, 7(2):189-217.

Lindenberg, M., Kopp, S., Dressman, JB. (2004). **Classification of orally administered drugs on the World Health Organization Model list of Essential Medicines according to the biopharmaceutics classification system.** *Eur J Pharm Biopharm*, 58(2):265-78.

Ling, Y., Wei, K., Luo, Y., Gao, X., Zhong S. (2011). **Dual docetaxel/superparamagnetic iron oxide loaded nanoparticles for both targeting magnetic resonance imaging and cancer therapy**. *Biomaterials*, 32:7139-7150.

Lison, D., Huaux, F. (2011). ***In vitro* studies: Ups and downs of cellular uptake.** *Nature Nanotechnology,* 6:332-333.

Liu, C. (2005). **A study of particle generation during laser ablation with applications**. *Doctoral Thesis, University of California, Berkeley,* 1-189.

Liu, Z., Cai, W., He, L. *et al*. (2007). ***In vivo* biodistribution and highly effi - cient tumour targeting of carbon nanotubes in mice**. *Nat Nanotechnol*, 2:47-52.

Liu, Z., Chen, K., Davis, C., Sherlock, S., Cao, Q., *et al*. (2008). **Drug delivery with carbon nanotubes for in vivo cancer treatment**. *Cancer Res*, 68:6652-6660.

Lockhart, AC., Rothenberg, ML, Berlin, JD. (2005). **Treatment for pancreatic cancer: current therapy and continued progress**. *Gastroenterology*, 128(6):1642-1654.

Loo, C., Lin, A., Hirsch, L., Lee, MH., Barton, J., Halas, N., West, J., Drezek, R. (2004). N**anoshell-enabled photonics-based imaging and therapy of cancer**. *Technol. Cancer Res*, 3:33.

Lorenz, MR., Holzapfel, V., Musyanovych, A., Nothelfer, K., *et al*. (2006). **Uptake of functionalized, fluorescent-labeled polymeric particles in different cell lines and stem cells. Biomaterials**. *Biomaterials*, 27:2820-2828.

Lu, W., Zhang, G., Zhang, R., *et al*. (2010). **Tumour site–specific silencing of NF-κB p65 by targeted hollow gold nanosphere–mediated photothermal transfection**. *Cancer Res*, 70(8):3177-3188.

Lukianova-Hleb, EY., Volkov, AN., Wu, X., Lapotko, DO. (2013). **Transient enhancement and spectral narrowing of the photothermal effect of plasmonic nanoparticles under pulsed excitation.** *Adv Mater*, 25:772-776.

Lyon, JL., Fleming, DA., Stone, MB., Schiffer, P., Williams, ME. (2004). **Synthesis of Fe Oxide Core/Au Shell Nanoparticles by Iterative Hydroxylamine Seeding**. *Nano Lett*, 4(403):719-723.

Mak, SY., Chen, DH. (2005). **Binding and sulfonation of poly(acrylic acid) on iron oxide nanoparticles: a novel, magnetic, strong acid cationnano-adsorbent**. *Macromol Rapid Comm*, 26:1567-1571.

Maleki, H., Simchia, A., Imanic, M., Costad, BFO. (2015). **Size-controlled synthesis of superparamagnetic iron oxide nanoparticles and their surface coating by gold for biomedical applications.** *J Magnetism and Magnetic Materials*, 324(23):3997-4005.

Malekigorji, M., Curtis, ADM., Hoskins, C. (2014). **The Use of Iron Oxide Nanoparticles for Pancreatic Cancer Therapy**. *J Nanomed Res*, 1(1): 00004.

Mandal, M., Kundu, S., Ghosh, SK., Panigrahi, S., Sau, TK., Yusuf, SM., Pal, T. (2005). **Magnetite nanoparticles with tunable gold or silver shell**. *J Colloid Interface Sci*, 286:187-194.

Manfred, Johannsen., Burghard, Thiesen., Peter, Wust., Andreas, Jordan. (2010). **Magnetic nanoparticle hyperthermia for prostate cancer.** *Int. J. Hyperthermia*, 26(8):790-795.

Matsumura, Y., Maeda, H. (1986). **A new concept for macromolecular therapeutics in cancer chemotherapy: mechanism of tumouritropic accumulation of proteins and the antitumour agent smancs**. *Cancer Res*, 46(12):6387-6392.

Maysinger, D., Lovric, J., Eisenberg, A., Savic, R. (2007). **Fate of micelles and quantum dots in cells**. *European Journal of Pharmaceutics and Biopharmaceutics*, 65:270-281.

Mehdorn, HM., Schwartz, F., Dawirs, S., *et al*. (2011). **High-field iMRI in glioblastoma surgery: improvement of resection radicality and survival for the patient?** *Acta Neurochir Suppl*, 109:103-106.

Mendes, RG., Koch, B., Bachmatiuk, A., El-Gendy, AA., Krupskaya, Y., *et al*. (2014). **Synthesis and toxicity characterization of carbon coated iron oxide nanoparticles with highly defined size distributions**. *Biochim Biophys Acta: General Subjects*, 1840(1):160-169.

Meng, F., Zhong, Z., Feijen, Jan. (2009). **Stimuli-Responsive Polymersomes for Programmed Drug Delivery**. *Biomacromolecules*, 10(2):197-209.

Mermet, JM. (2005). **"Is it still possible, necessary and beneficial to perform research in ICP-atomic emission spectrometry?".** *J. Anal. At. Spectrom*. 20:11-16.

Meyers, RH., Cronic, F., Nice, CM. (1963). **Experimental approach in the use and magnetic control of metallic iron particles in the lymphatic and vascular system of dugs as a contrast and isotropic agent.** *Am. J. Roengenol. Radium Ther. Nucl. Med*, 90:1068-1963.

Mie, G. (1908). **Contribution to the optics of turbid media, especially colloidal metal suspensions**. *Ann. Phys*, 25:377-455.

Mignotte, B., Vayssiere, JL. (1998). **Mitochondria and apoptosis**. *Eur. J. Biochem*, 252 :1-15.

Mikami, Y., Dhakshinamoorthy, A., Alvaroa, M., García, H. (2013). **Catalytic activity of unsupported gold nanoparticles**. *Catal. Sci. Technol*, 3:58-69.

Min, Y., Caster, JM., Eblan, MJ., Wang, AZ. (2015). **Clinical Translation of Nanomedicine**. *Chem. Rev*, 115:11147-11190.

Minotti, G., Aust, SD. (1987). **The requirement for Iron(III) in the initiation of lipid peroxidation by Iron(II) and hydrogen peroxide**. *J BiolChem*, 262:1098-1104.

Modi, S and Anderson, BD. (2013). **Determination of Drug Release Kinetics from Nanoparticles: Overcoming Pitfalls of the Dynamic Dialysis Method**. *Mol. Pharmaceutics*, 10 (8):3076–3089.

Modica-Napolitano, JS., Weissig, V. (2015). **Treatment Strategies that Enhance the Efficacy and Selectivity of Mitochondria-Targeted Anticancer Agents.** *Int J Mol Sci*, 16(8):17394-17421.

Moghimi, SM., Hunter, AC., Murray, JC. (2001). **Long-Circulating and Target-Specific Nanoparticles: Theory to Practice**. *Pharmacol Rev*, 53:283-318.

Mohammadi, R., Yousefi, R., Dadkhah Aseman, M., Nabavizadeh. M., Rashidi, M. (2015). **DNA Binding and Anticancer Activity of Novel Cyclometalated Platinum (II) Complexes**. *Anti-Cancer Agents in Medicinal Chemistry (Formerly Current Medicinal Chemistry - Anti-Cancer Agents)*, 15(1):107-114(8).

Morales, CS., Valencia, P., Thakkar, A., Swanson, E., Langer, R. (2012). **Recent developments in multifunctional hybrid nanoparticles: opportunities and challenges in cancer therapy**. *Frontiers in Bioscience*, 4:529-545.

Moses, MA., Brem, H., Langer, R. (2003). **Advancing the field of drug delivery: taking aim at cancer**. *Cancer Cell*, 4:337-341.

Mosmann, T. (1983). **Rapid colorimetric assay for cellular growth and survival: application to proliferation and cytotoxicity assays**. *Journal of Immunological Methods*, 65(1-2):55-63.

Nam, J., La, WG., Hwang, S., Ha, YS., Park, N., Won, N., Jung, S., Bhang, SH., *et al* (2013). **pH-responsive assembly of gold nanoparticles and "spatiotemporally concerted" drug release for synergistic cancer therapy**. *ACS Nano*, 7(4):3388-3402.

Neesse, A., Michl, P., Frese, KK., Feig, C., Cook, N., Jacobetz, MA., *et al*. (2011). **Stromal biology and therapy in pancreatic cancer**. *Gut*, 60(6):861-868.

Nel, A., Xia, T., Ma¨dler, L., Li, N. (2006). **Toxic potential of materials at the nanolevel**. *Science*, 311:622-627.

Neuberger, T., Schopf, B., Hofmann, H., Hofmann, M., von Rechenberg, B. (2005). **Superparamagnetic Nanoparticles for Biomedical Applications: Possibilities and Limitations of a New Drug Delivery System**. *Journal of Magnetism and Magnetic Materials*, 293(1): 483-496.

Nguyen, KT., Zhao, Y. (2015). **Engineered Hybrid Nanoparticles for On-Demand Diagnostics and Therapeutics.** *Acc. Chem. Res,* 48 (12):3016–3025.

Norrish, K., Taylor, RM. (1962). **Quantitative analysis by x-ray diffraction**. *Division of Soils, C.S.I.R.O., Adelaide, South Australia*, 98-109.

Nuzzo, RG., Zegarski, BR., Dubios, LH. (1987). **Fundamental studies of the chemisorption of organosulfur compounds on Au(111). Implications for molecular self-assembly on gold surfaces**. *J. Am. Chem. Soc*, 109:733-740.

Ochi, M., Takahashi, R. (2001). **Phase Structure and Thermomechanical Properties of Primary and Tertiary Amine-Cured Epoxy/Silica Hybrids**. *Journal of Polymer Science Part B: Polymer Physics*, 39:1071-1084.

O'Sullivan, A., Kocher, HM. (2007). **Pancreatic cancer**. *Br Med J Clin Evid*, 11:409-437.

Pankhurst, QA., Connolly, J., Jones, SK., J, Dobson. (2003). **Applications of magnetic nanoparticles in biomedicine**. *J. Phys. D: Appl. Phys*, 36:167-181.

Pantarotto, D., Singh, R., McCarthy, D., Erhardt, M., *et al*. (2004). **Functionalized carbon nanotubes for plasmid DNA gene delivery**. *Angew. Chem. Int. Ed Engl*, 43:5242-5246.

Paproski, RJ., Young, JD., Cass, CE. (2010). **Predicting gemcitabine transport and toxicity in human pancreatic cancer cell lines with the positron emission tomography tracer 3′-deoxy-3′-fluorothymidine**. *Biochemical Pharmacology*, 79(4):587-595.

Park, JH., Gu, L., Maltzahn, G., Ruoslahtiet, E., *et al*. (2009). **Biodegradable luminescent porous silicon nanoparticles for in vivo applications**. *Nat. Mater*, 8:331-336.

Park, JS., Han, TH., Lee, KY., Han, SS., Hwang, JJ., Moon, DH., *et al*. (2006). **N-acetyl histidineconjugated glycol chitosan self-assembled nanoparticles for intracytoplasmic delivery of drugs: endocytosis, exocytosis and drug release**. *J Control Release*, 115:37-45.

Park, JW., Benz, CC., Martin, FJ. (2004). **Future directions of liposomeand immunoliposome-based cancer therapeutics**. Semin Oncol, 31:196-205.

Pathak, Y and Benita, S. (2012). **Antibody-Mediated Drug Delivery Systems: Concepts, Technology, and Applications.**

Pattekari, P., Zheng, Z., Zhang, X., Levchenko, T., Torchilinb, V., Lvov, Y. (2011). **Top-down and bottom-up approaches in production of aqueous nanocolloids of low solubility drug paclitaxel.** *Phys Chem Chem Phys*, 13:9014-9019.

Pattillo, CB., Sari-Sarraf, F., Nallamothu, R., Moore, BM., Wood, GC., Kiani, MF. (2005). **Targeting of the antivascular drug combretastatin to irradiated tumors results in tumor growth delay.** *Pharm Res*, 22(7):1117-1120.

Petros, RA., DeSimone JM. (2010). **Strategies in the design of nanoparticles for therapeutic applications**. *Nat Rev Drug Discov*, 9:615-627.

Pissuwan, D., Valenzueka, SM., Cortie, MB. (2006). **Therapeutic possibilities of plasmonically heated gold nanoparticles.** *Trends Biotechnol*, 24:62-67.

Pitsillides, CM., Joe, E., Wei, X., Anderson, R., Lin, C. (2003). **Selective Cell Targeting with Light-Absorbing Microparticles and Nanoparticles**. *Biophys J*, 84(6):4023-4032.

Poon, L., Zandberg, W., Hsiao, D., Erno, Z., Sen, D., Gates, BD., Branda, NR. (2010). **Photothermal release of single-stranded DNA from the surface of gold nanoparticles through controlled denaturating and Au-S bond breaking**. *ACS Nano*, 4(11):6395-403.

Popp, MK., Oubou, I., Shepherd, C, Nager, Z., Anderson, C., Pagliaro, L. (2014). **Photothermal Therapy Using Gold Nanorods and Near-Infrared Light in a Murine Melanoma Model Increases Survival and Decreases Tumour Volume**. *J Nanomaterials*, 450670:8 pages.

Poste, G., Kirsh, R. (1983). **Site-Specific (Targeted) Drug Delivery in Cancer Therapy.** *Nat. Biotechnol*, 869-878.

Prabhu, VM., Hudson, SD. (2009). **Nanoparticle assembly: DNA provides control**. *Nat. Mater*, 8:365-366.

Preissler, M., Williams, JA. (1981). **Pancreatic acinar cell function: measurement of intracellular ions and pH and their relation to secretion**. *J. Physiol*, 321:437-448.

Prodan, E., Radloff, C., Halas, NJ., Nordlander, P. (2003). **A hybridization model for the plasmon response of complex nanostructures.** *Science*, 302(5644):419-422.

Provenzano, R., Schiller, B., Rao, M., Coyne, D., Brenner, L., Pereira, B. (2009). **Ferumoxytol as an Intravenous Iron Replacement Therapy in Hemodialysis Patients.** *Clin J Am Soc Nephrol*, 4:386-393.

Puvanakrishnan, P. (2011). **Near-infrared narrowband imaging of tumours using gold nanoparticles**. *Dissertation presented to the Faculty of the Graduate School of The University of Texas at Austin.*

Qian, X., Peng, XH., Ansari, DO., Yin-Goen, Q., Chen, GZ., Shin, DM., Yang, LA., Young, N., Wang MD., Nie, S. (2008**). *In vivo* tumour targeting and spectroscopic detection with surface-enhanced Raman nanoparticle tags**. *Nat. Biotechnol*, 26:83-90.

Quaresma, P., Osorio, I., Doria, G., Carvalho, PA., Pereira, A., *et al*. (2014). **Star-shaped magnetite@gold nanoparticles for protein magnetic separation and SERS detection**. *RSC Adv*, 4:3659.

Ralton, LD., Bestwick, CS., Milne, L., Duthie, S., Kong Thoo Lin, P. (2009). **Bisnaphthalimidopropyl spermidine induces apoptosis within colon carcinoma cells**. *Chem Biol Interact*, 177:1-6.

Rao, JS., Krishna, MM., Prakash, B., Kumar, PR. (2007). **RP-HPLC Analysis of Gemcitabine in Pure Form and in Pharmaceutical Dosage Forms**. *Asian J. Chem*, 19(5):3399-3402.

Rayavarapu, RG., Petersen, W., Ungureanu, C., Post, JN., Leeuwen, TG., Manohar, S. (2007). **Synthesis and Bioconjugation of Gold Nanoparticles as Potential Molecular Probes for Light-Based Imaging Techniques**. *Hindawi Publishing Corporation*, 29817:10 pages.

Rasheed, ZA., Matsui, W., Maitra, A. (2012). **Pathology of pancreatic stroma in PDAC**. *Pancreatic Cancer and Tumor Microenvironment*, Chapter 1.

Rausch, K., Reuter, A., Fischer, K., Schmidt, M. (2010). **Evaluation of nanoparticle aggregation in human blood serum.** *Biomacromolecules*, 11:2836-2839.

Ren, G., Hu, D., Cheng, EWC., Vargas-Reu,s MA., Reip, P., Allaker, RP. (2009). **Characterisation of copper oxide nanoparticles for antimicrobial applications**. *Int J Antimicrob Agents*, 33:587-590.

Rivera, G., Oberdörster, G., Puntes, V., Parak, WJ. (2010). **Correlating physico-chemical with toxicological properties of nanoparticles: the present and the future**. *ACS Nano*, 4: 5527-5531.

Roach, P., McGarvey, DJ., Lees, M., Hoskins, C. (2013). **Remotely Triggered Scaffolds for Controlled Release of Pharmaceuticals**. *Int J Mol Sci*, 14(4):8585-8602.

Robinson, I., Tung, LD., Maenosono, S., Walti, C., Thanh, NTK. (2010a). **Synthesis of core-shell gold coated magnetic nanoparticles and their interaction with thiolated DNA**, *Nanoscale*, 2:2624-2630.

Robinson, JT., Welsher, K., Tabakman, SM., et al. (2010b). **High performance in vivo near-IR (>1µm) imaging and photothermal cancer therapy with carbon nanotubes**. *Nano Res*, 3(11):779-793.

Roper, MG., Skegg, MP., Fisher, CJ., Lee, JJ., Dhanak, VR., Woodruff, DP., Jones, RG. (2004). **Atop adsorption site of sulfur head groups in gold-thiolate self-assembled monolayers**. *Chem. Phys. Lett*, 389:87-91.

Rosensweig, R. E. (2002). **Heating magnetic fluid with alternating magnetic field.** *J. Magn. Magn. Mater*, 252:370-374.

Rothman, S. (2002). **Lessons from the living cell: the culture of science and the limits of reductionism.** *New York: McGraw-Hill*, ISBN 0-07-137820-0.

Roy, I., Ohulchanskyy, T., E. Pudavar, H., J. Bergey, E., *et al*. (2003). **Ceramic-based nanoparticles entrapping water-insoluble photosensitizing anticancer drugs: a novel drug-carrier system for photodynamic therapy**. *J. Am. Chem. Soc*, 125:7860-7865.

Sailor, MJ., Park, JH. (2012). **Hybrid Nanoparticles for Detection and Treatment of Cancer**, *Advanced Material*, 24(28):3779-3802.

Saini, S., Stark, DD., Hahn, PF., Wittenberg, J., Brady, TJ., Ferrucci, JT. (1987). **Ferrite particles: a superparamagnetic MR contrast agent for the reticuloendothelial system**. *Radiology*, 162:211-216.

Sami, SM., Dorr, RT., Alberts DS., Solyom, AM., Remers WA. (2000). **Analogues of amonafide and azonafide with novel ring systems**. *J. Med. Chem*, 43:3067-3073.

Santra, S., Tapec, C., Theodoropoulou, N., Dobson, J., Hebard, A., Tan, W. (2001). **Synthesis and characterization of silicacoated iron oxide nanoparticles in microemulsion: The effect of non-ionic surfactants.** *Langmuir*, 17:2900-2906.

Savic, R., Luo, L., Eisenberg, A., Mayasinger, D. (2003). **Micellar Nanocontainers Distribute to Defined Cytoplasmic Organelles**. *Science*, 300:615-618.

Savla, R., Taratula, O., Garbuzenko, O., Minko, T., *et al*. (2011). **Tumor targeted quantum dot-mucin 1 aptamer-doxorubicin conjugate for imaging and treatment of cancer**. *J. Contr. Release*, 153:16-22.

Schadt, W., Cheung, J., Luo, C., J. Zhong *et al*. (2006). **Molecularly Tuned Size Selectivity in Thermal Pro cessing of Gold Nanoparticles**. *Chem. Mater*, 18(22):5147-5149.

Schleich, N., Po, C., Jacobs, D., Ucakar, B., Gallez, B., et al. (2014). **Comparison of active, passive and magnetic targeting to tumours of multifunctional paclitaxel/SPIO-loaded nanoparticles for tumour imaging and therapy**. *J Control Release*, 194:82-91.

Schwedt, G., Haderlie, B. (1997). **The Essential Guide to Analytical Chemistry**, *2nd Edition, UK, John Wiley and Sons.*

Shultz, MD., Reveles, JU., Khanna, SN., Carpenter, EE. (2007). **Reactive Nature of Dopamine as a Surface Functionalization Agent in Iron Oxide Nanoparticles**. *J. Am. Chem. Soc*, 129:2482-2487.

Seied Sajadi, M., Fathi, F., Farhadyar, N. (2014). **Synthesis and Surface modification of Iron Oxide Nanoparticles for Drug Delivery**. *IJCPS*, 2(4):760-764.

Selvaraj, V., Muthukaruppan, A. (2007). **Analytical detection and biological assay of antileukemic drug 5-fluorouracil using gold nanoparticles as probe**. *Int. J. Pharm*, 337(1-2):275-281.

Senft, C., Franz, K., Blasel, S., *et al*. (2010). **Influence of iMRI-guidance on the extent of resection and survival of patients with glioblastoma multiforme**. *Technol. Cancer Res. Treat*, 9:339-346.

Shukla, R., Bansal, V., Chaudhary, M., Basu, A., Bhonde, RR., Sastry M. (2005). **Biocompatibility of gold nanoparticles and their endocytotic fate inside the cellular compartment: a microscopic overview**. *Langmuir*, 21:10644-10654.

Sibilia. JP. (1996). **A Guide to Materials Characterization and Chemical Analysis**. *2nd Edition, USA, VCH.*

Smith, AL. (1979). **Applied Infrared Spectroscopy**. *John Wiley & Sons, New York.*

Smolensky, ED., Neary, MC., Zhou, Y., Berquo, TS., Pierre, VC. (2011). **Fe3O4@organic@Au: core-shell nanocomposites with high saturation magnetisation as magnetoplasmonic MRI contrast agents.** *Chem Commun*, 47:2149-2151.

Sokolov, K., Aaron, J., Hsu, B. *et al.* (2003). **Optical system for *in vivo* molecular imaging of cancer.** *Technol. Cancer Res. Treat*, 2(6):491-504.

Stewart, B., Wild, C. (2014). **World Cancer Report**.

Stroh, A., Zimmer, C., Gutzeit, C., Jakstadt, M., Marschinke, F., Jung, T, *et al*. (2004). **Iron oxide particles for molecular magnetic resonance imaging cause transient oxidative stress in rat macrophages**. *Free Radic Biol Med*, 36:976-84.

Stuart, B., George, B., McIntyre, P. (1996). **Modern Infrared Spectroscopy**, *UK, John Wiley and Sons*.

Sumer, B., Gao J. (2008). **Theranostic nanomedicine for cancer**. *Nanomedicine (Lond)*, 3(2): 137-140.

Štarha, P., Smola, D., Tuček, J., and Trávníček, Z. (2015). **Efficient Synthesis of a Maghemite/Gold Hybrid Nanoparticle System as a Magnetic Carrier for the Transport of Platinum-Based Metallotherapeutics**. *Int. J. Mol. Sci*, 16:2034-2051.

Takeuchi, N., Maejima, S., Hasebe, O., Matsuda, Y., Hanazaki, K., Kajikawa, S., Mukawa, K., *et al*. (2004). **Clinical problems in gemcitabine treatment for unresectable pancreatic cancer in the elderly--a multicentric retrospective study of 53 cases**. *Gan To Kagaku Ryoho*, 31(12):1987-1991.

Tanaka, Y., Matsuo, K., Yuzuriha, S. (2011). **Objective assessment of skin rejuvenation using near-infrared 1064-nm neodymium: YAG laser in Asians.** *Clin Cosmet Investig Dermatol*, 4:123-130.

Tartaj, P., Morales, MD., Veintemillas-Verdaguer, S., Gonzalez-Carreno, T., Serna, CJ. (2003). **The Preparation of Magnetic Nanoparticles for Applications in Biomedicine**. *Journal of Physics D-Applied Physics*, 36(13):R182-R197.

Taylor, SA., Rankin, C., Townsend, JJ., Craig, JB., Vance, RB., Solank, DL., Brown, TD., Jaeckle, K. (2002). **Phase II trial of amonafide in central nervous system tumors: a Southwest Oncology Group study**. *Invest. New Drugs*, 20:113-115.

Tennant, JR. (1964). **Evaluation of the trypan blue technique for determination of cell viability**. *Transplantation*, 2:685-694.

Thompson, CJ., Ding, CX., Qu, XZ., Yang, ZZ., Uchegbu, IF., Tetley, L., Cheng, WP. (2008). **The effect of polymer architecture on the nano self-assemblies based on novel comb-shaped amphiphilic poly(allylamine)**. *Colloid and Polymer Science*, 286(13):1511-1526.

Thompson, H. (1988). **Exocrine Pancreatic Cancer**. *Journal of Clinical Pathology*, 41(2):237.

Thorek, DL., Chen, AK., Czupryna, J. *et al.* (2006). **Superparamagnetic iron oxide nanoparticle probes for molecular imaging**. *Ann Biomed Eng*, 34: 23-38.

Tiefenthaler, M., Hohla, F., Irschick, E., *et al*. (2003). ***In vitro* studies on the immunosuppressive effect of 2',2'-difluorodeoxycytidine (dFdC) and its metabolite 2',2'-difluorodeoxyuridine (dFdU).** *Immunobiology*, 207(2):149-157.

Tomassetti, P., Campana, D., Piscitelli, L., Casadei, R., Santini, D., Nori, F. Morselli-Labate, A. M., Pezzilli, R., Corinaldesi, R. (2005). **Endocrine pancreatic tumours: factors correlated with survival**. Annals of oncology, 16(11):1806-1810.

Torchilin, VP. (2006). **Multifunctional nanocarriers**. *Advanced Drug Delivery Reviews*, 58(14):1532-1555.

Torchilin, VP., Rammohan, R., Weissig, V., Levchenko, TS. (2001). **TAT peptide on the surface of liposomes affords their efficient intracellular delivery even at low temperature and in the presence of metabolic inhibitors**. *Proc. Natl Acad. Sci.* USA, 98(15):8786-8791.

Ulman A. (1996). **Formation and structure of self-assembled monolayers.** *Chem. Rev*, 96(4):1533-1554.

Urano, M., Kuroda, M., Nishimura, Y. (1999). **For the clinical application of thermochemotherapy given at mild temperatures**. *Int J Hyperthermia*, 15(2):79-107.

Václav, Š., Zdeňka, K., Ondřej, K., Jakub, S., Alena, Ř., Pavel, Ř., Kamil, Z. (2011). **"Soft and rigid" dithiols and Au nanoparticles grafting on plasma-treated polyethyleneterephthalate**. *Nanoscale Research Letters*, 6:607.

Vasir, JK., Reddy, MK., Labhasetwar, VD. (2005). **Nanosystems in Drug Targeting: Opportunities and Challenges**, *Current Nanoscience*, 1:47-64.

Veltkamp, SA., Pluim, D., van Eijndhoven, MA., *et al.* (2008). **New insights into the pharmacology and cytotoxicity of gemcitabine and 2',2'-difluorodeoxyuridine**. *Mol Cancer Ther*, 7(8):2415-2425.

Vignais, PV., Vignais, PM. (2010). **Discovering Life, Manufacturing Life: How the experimental method shaped life sciences**. *Berlin: Springer*, ISBN 90-481-3766-7.

Vittorio, O., Voliani, V., Faraci, P., Karmakar, B., Iemma, F., *et al*. (2014). **Magnetic catechin-dextran conjugate as targeted therapeutic for pancreatic tumour cells**. *J Drug Target*, 22(5):408-415.

Vogl, TJ., Straub, R., Eichler, K., Sollner, O., Mack, MG**.** (2004). **Colorectal carcinoma metastases in liver: laser-induced interstitial thermotherapy--local tumour control rate and survival data.** *Radiology*, 230: 450-458.

Von Wichert, G., Seufferlein, T., Adler, G. (2008). **Palliative treatment of pancreatic cancer**. *J Dig Dis*, 9:1-7.

Vu-Quang, H., Muthiah, M., Lee, HJ., Kim, YK., Rhee, JH., *et al*. (2012). **Immune cell-specific delivery of beta-glucan-coated inron oxide nanoparticles for diagnosing liver metastasis by MR imaging.** *Carbohydrate Polymers*, 87(2):1159-1168.

Wabler, M., Zhu, W., Hedayati, M., Attaluri, A., Zhou, H., Mihalic, J., Geyh, A., DeWeese, TL., Ivkov, R., Artemov, D. (2014). **Magnetic resonance imaging contrast of iron oxide nanoparticles developed for hyperthermia is dominated by iron content**. *Int J Hyperthermia*, 30(3):192-200.

Wagstaff, AJ., Brown, SD., Holden, MR., Craig, GE., Plumb, JA., *et al*. (2012). **Cisplatin drug delivery using gold-coated iron oxide nanoparticles for enhanced tumour targeting with external magnetic fields**. *Inorganica Chimica Acta*, 393:328-333.

Wahajuddin., Arora, S. (2012). **Superparamagnetic iron oxide nanoparticles: magnetic nanoplatforms as drug carriers**. *Int J Nanomedicine*, 7:3445-3471.

Walker, E., Ko, A. (2014). **Beyond first-line chemotherapy for advanced pancreatic cancer: An expanding array of therapeutic options?** *World J Gastroenterol*, 7, 20(9): 2224-2236.

Wallace, SJ., Li, J., Nation RL., Boyd, BJ. (2012). **Drug Release from Nanomedicines: Selection of Appropriate Encapsulation and Release Methodology**. *Drug Delivery Transl. Res*, 2:284-292.

Wang, H., Word, BR., Lyn-Cook, BD. (2011). **Enhanced Efficacy of Gemcitabine by Indole-3-carbinol in Pancreatic Cell Lines: The Role of Human Equilibrative Nucleoside Transporter 1**. *Anticancer Research*, 31(10):3171-3180.

Wang, J., Han, S., Ke, D., Wang, R. (2012). **Semiconductor Quantum Dots Surface Modification for Potential Cancer Diagnostic and Therapeutic Applications**. *Journal of Nanomaterials*, 129041:8 pages.

Wang J., Örnek-Ballanco, C., Xu, J., Yang, W., Yu, X. (2013). **Preparation and characterization of vinculin-targeted polymer–lipid nanoparticle as intracellular delivery vehicle**. *Int J Nanomedicine*, 8:39-46.

Wang, L., Luo, J., Fan, Q., Suzuki, M., Suzuki, IS., Engelhard, MH., Lin, Y., Kim, N., Wang, JQ., Zhong, CJ. (2005a). **Monodispersed core-shell Fe3O4@Au nanoparticles**. *J Phys Chem B*, 109: 21593-21601.

Wang, L., Luo, J., Maye, MM., Fan, Q., Rendeng, Q., Englehard, MH., Wang, C., Lin, Y., Zhong, CJ. (2005b). **Iron oxide-gold core-shell nanoparticles and thin film assembly**. *J Mater Chem*, 15:1821-1832.

Wang, L., Park, H., Lim, Stephanie I., Schadt, MJ., Mott, D., Jin, L., Wang, X., Chuan-Jian, Z. (2008). **Core@shell nanomaterials: gold-coated magnetic oxide nanoparticles**, *J. Mater. Chem*, 18:2629-2635.

Wang, P., Yoo, B., Yang, J., Zhang, X., Ross, A., *et al*. (2014). **GLP-1R-targeting magnetic nanoparticles for pancreatic islet imaging**. *Diabetes*, 63(5):1465-1474.

Wang, X., Xing, X., Zhang, B., Liu, F., Cheng, Y., *et al.* (2014b). **Surface engineering antifouling optomagnetic SPIONs for bimodal targeted imaging of pancreatic cancer cells**. *Int J Nanomedicine*, 9:1601-1615.

Wang, X., Zhou, L., Ma, Y., Li, X., Gu H. (2009). **Control of aggregation size of polyethyleneimine-coated magnetic nanoparticles for magnetofection**. *Nano Res*, 2:365-372.

Wang, YX., Hussain, SM., Krestin, GP. (2001). **Super paramagnetic iron oxide contrast agents: physicochemical characteristics and applications in MR imaging**. *Eur Radiol*, 11(11):2319-2331.

Warheit. DB. (2008). **How Meaningful are the Results of Nanotoxicity Studies in the Absence of Adequate Material Characterization?** *Toxicological Sciences*, 101(2):183-185.

Wei, K., Li, J., Liu, J., Chen, G., Jiang, M. (2012). **Reversible vesicles of supramolecular hybrid nanoparticles**. *Soft Matter*, 8:3300-3303.

Weissleder, R. (2001). **A clearer vision for in vivo imaging**. *Nat Biotechnol*, 19:316-317.

White, CE., Argauer, RJ. (1970). **Fluorescence Analysis: A Practical Approach**. *USA, Marcel Dekker Inc*.

Willems, PW., Taphoorn, MJ., Burger, H., *et al*. (2006). **Effectiveness of neuronavigation in resecting solitary intracerebral contrast-enhancing tumours: a randomized controlled trial**. *J. Neurosurg*, 104:360-368.

World Cancer Report. (2014). **World Health Organization**. *Chapter 1.1. ISBN 9283204298*.

Worns, MA. (2013). **Systemic therapy and synergies by combination**. *Dig Dis*, 31(1):104-111.

Woods, E. (2010**). Laser ablation of the prostate: a safe effective treatment of obstructive benign prostatic disease**. *Can Urol Assoc J*, 4:344-346.

Wootton, CA., Sanchez-Cano, C., Liu, HK., Barrow, MP., Sadler, PJ., O'Connor, PB. (2015). **Binding of an organo-osmium(ii) anticancer complex to guanine and cytosine on DNA revealed by electron-based dissociations in high resolution Top-Down FT-ICR mass spectrometry**. *Dalton Trans*, 44(8):3624-3632.

Wu, A., Xu, Y., Qian, X., Wang, J., Liu, J. (2009a). **Novel naphthalimide derivatives as potential apoptosis-inducing agents: design, synthesis and biological evaluation**. *Eur J Med Chem*, 44:4674-4680.

Wu, CY., Pu, Y., Liu, G., Shao, Y., Ma QS., *et al.* (2012). **MR imaging of human pancreatic cancer xenograft labelled with superparagmagnetic iron oxide in nude mice**. *Contrast Media Mol Imaging*, 7(1):51-58.

Wu, H., Liang, Z., Shi, X., Ren, X., Wang, K., Liu T. (2009b). **Intrinsic chemoresistance to gemcitabine is associated with constitutive and laminin-induced phosphorylation of FAK in pancreatic cancer cell lines**. *Molecular Cancer*, 8:125.

Wu, W., He, Q., Jiang, C. (2008). **Magnetic Iron Oxide Nanoparticles: Synthesis and Surface Functionalization Strategies**. *Nanoscale Res Lett*, 3:397-415.

Xu, C., Wang, B., Sun, S. (2009). **Dumbbell-like Au-Fe3O4 Nanoparticles for Target-Specific Platin Delivery.** *Am. J. Chem. Soc*, 131:4216-4217.

Yallapu, MM., Ebeling, MC., Khan, S., Sundram, V., Chauhan, N., *et al*. (2013). **Novel curcmin-loaded magnetic nanoparticles for pancreatic cancer treatment.** *Mol Cancer Ther*, 12(8):1471-1480.

Yang, H., Liu, C., Yang, D., Zhang, H., Xi, Z. (2009). **Comparative study of cytotoxicity, oxidative stress and genotoxicity induced by four typical nanomaterials: The role of particle size, shape and composition.** *J. Appl. Toxicol*, 29, 69-78.

Yang, X., Grailer, JJ., Rowland, IJ., Javadi, A., *et al*. (2010). **Multifunctional SPIO/DOX-loaded wormlike polymer vesicles for cancer therapy and MR imaging**. *Biomaterials*, 31:9065-9073.

Yen, SK., Padmanabhan, P., Selvan, ST. (2013). **Multifunctional Iron Oxide Nanoparticles for Diagnostics, Therapy and Macromolecule Delivery**. *Theranostics*, 3(12):986-1003.

Yoshida, M., Takimoto, R., Murase, K., Sato, Y., Hirakawa, M., Tamura, F., Sato, T., Iyama, S., Osuga, T., Miyanishi, K., Takada, K., *et al*. (2012). **Targeting Anticancer Drug Delivery to Pancreatic Cancer Cells Using a Fucose-Bound Nanoparticle Approach**. *PLoS ONE*, 7(7):39545.

You, JO., Auguste, DT. (2009). **Nanocarrier cross-linking density and pH sensitivity regulate intracellular gene transfer**. *Nano Lett*, 9:4467-4473.

Yu, K., Park, J., Jon, S. (2012). **Targeting Strategies for Multifunctional Nanoparticles in Cancer Imaging and Therapy**. *Theranostics*, 2(1):3-44.

Yu, MK., Jeong, YY., Park, J., Park, S., Kim, JW., Min, JJ., Kim, K,. Jon, S. (2008). **Drug-loaded superparamagnetic iron oxide nanoparticles for combined cancer imaging and therapy in vivo.** *Chem. Int. Ed*, 47:5362-5365.

Yuan, J., Guo, W., Yang, X., Wang, E. (2009). **Anticancer drug-DNA interactions measured using a photo induced electron-transfer mechanism based on luminescent quantum dots**. *Anal. Chem*, 81:362-368.

Zeng, L., An, L., Wu, X. (2011). **Modeling Drug−Carrier Interaction in the Drug Release from Nanocarriers**. *J. Drug Delivery*, 370308.

Zhang, LW., Monteiro-Riviere, NA. (2009a). **Mechanisms of Quantum Dot Nanoparticle Cellular Uptake**. *Toxicological Sciene*, 110(1):138-155.

Zhang, J., Liu, B., Liu, H., Zhang, X., Tan, W. (2013). **Aptamer-conjugated gold nanoparticles for bioanalysis**. *Nanomedicine (Lond)*, 8(6):983-993.

Zhang, L., Gu, FX., Chan, J M., Wang, A., Langer, Z., Farokhzad, OC. (2008). **Nanoparticles in medicine: therapeutic applications and developments**. *Clin Pharmacol Ther*, 83(5):761-769.

Zhang, P., Ling, G., Pan, X., Sun, J., Zhang, T., Pu, X., Yin, S., He, Z. (2012). **Novel nanostructured lipid-dextran sulfate hybrid carriers overcome tumor multidrug resistance of mitoxantrone hydrochloride**. *Nanomedicine*,8(2):185-193.

Zhang, Q., Ge, J., Goebl, J., Hu, Y., Sun, Y., Yin, Y. (2010). **Tailored synthesis of superparamagnetic gold nanoshells with tunable optical properties.** *Adv Mater*, 22:1905-1909.

Zhang, Q., Iwakuma, N., Sharma, P., Moudgil, M., Wu, C., McNeill, J., Jiang, H., Grobmyer, SR. (2009b). **Gold nanoparticles as a contrast agent for in vivo tumour imaging with photoacoustic tomography**. *Nanothechnology*, 30;20(39):395102.

Zhang, XQ., Xu, X., Lam, R., Giljohann, D., Ho, D., Mirkin, CA. (2011). **Strategy for increasing drug solubility and efficacy through covalent attachment to polyvalent DNA–nanoparticle conjugates**. *ACS Nano*, 5(9):6962-6970.

Zhang, Y., Kohler, N., Zhang, MQ. (2002). **Surface Modification of Superparamagnetic Magnetite Nanoparticles and Their Intracellular Uptake**. *Biomaterials*, 23:7.

Zharov, VP., Mercer, KE., Galitovskaya, EN., Smeltzery, M. (2006). **Photothermal Nanotherapeutics and Nanodiagnostics for Selective Killing of Bacteria Targeted with Gold Nanoparticles**. *Biophysical J*, 90:619-627.

Zhigilei, LV., Lin, Z., Ivanov, DS. (2009). **Atomistic Modeling of Short Pulse Laser Ablation of Metals: Connections between Melting, Spallation, and Phase Explosion**. *J. Phys. Chem*, 113: 11892-11906.

Zijlstra, P., Orrit, M. (2011). **Single metal nanoparticles: optical detection, spectroscopy and applications**. *Rep Prog Phys*, 74:106401-106456.

Zsigmondy, R. (1926). **Properties of colloid**. *Nobel Foundation.*

Zuo, HD., Yao, WW., Chen, TW., Zhu J., Zhang, JJ., Pu, Y., Liu, G., Zhang, XM. (2014). **The effect of superparamagnetic iron oxide with iRGD peptide on the labeling of pancreatic cancer cells in vitro: a preliminary study**. *Biomed Res Int.* 2014:852352 (8 pages).

Appendix

1.0. Standard calibration curves in ICP-OES analysis

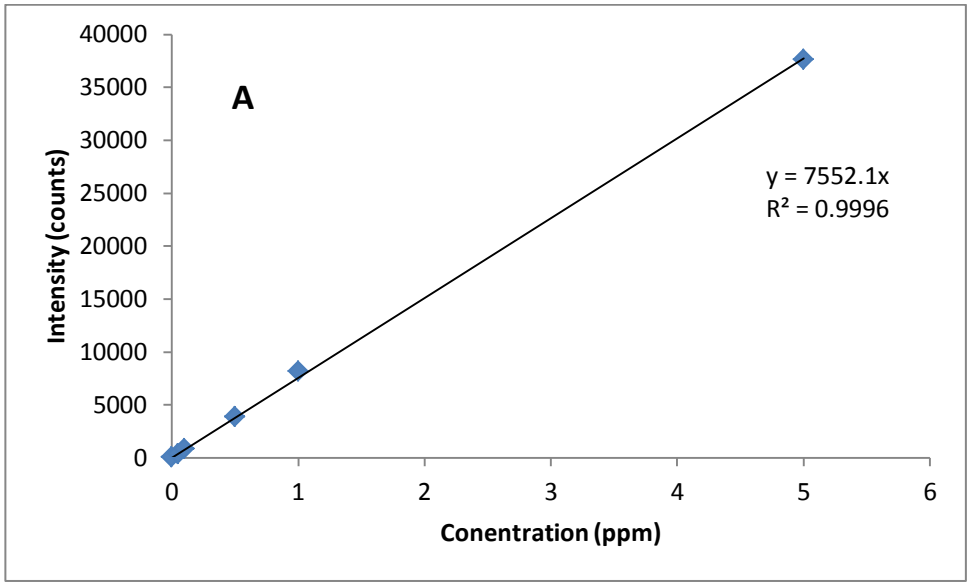

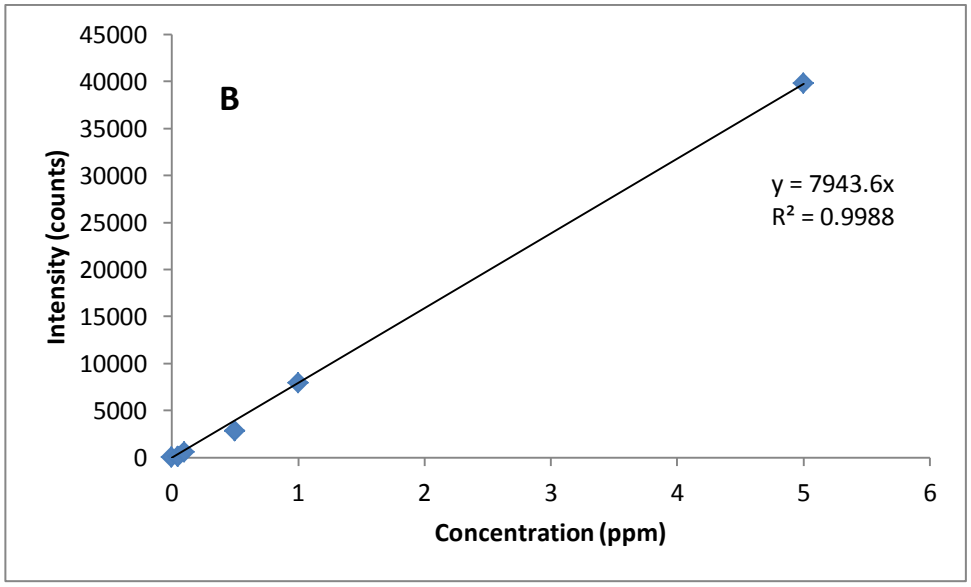

Figure 1. Standard calibration curve of A) Standard Iron and B) standard Gold, analysed by ICP-OES.

1.1. Histogram of frequency distribution (temperature increase by laser irradiation)

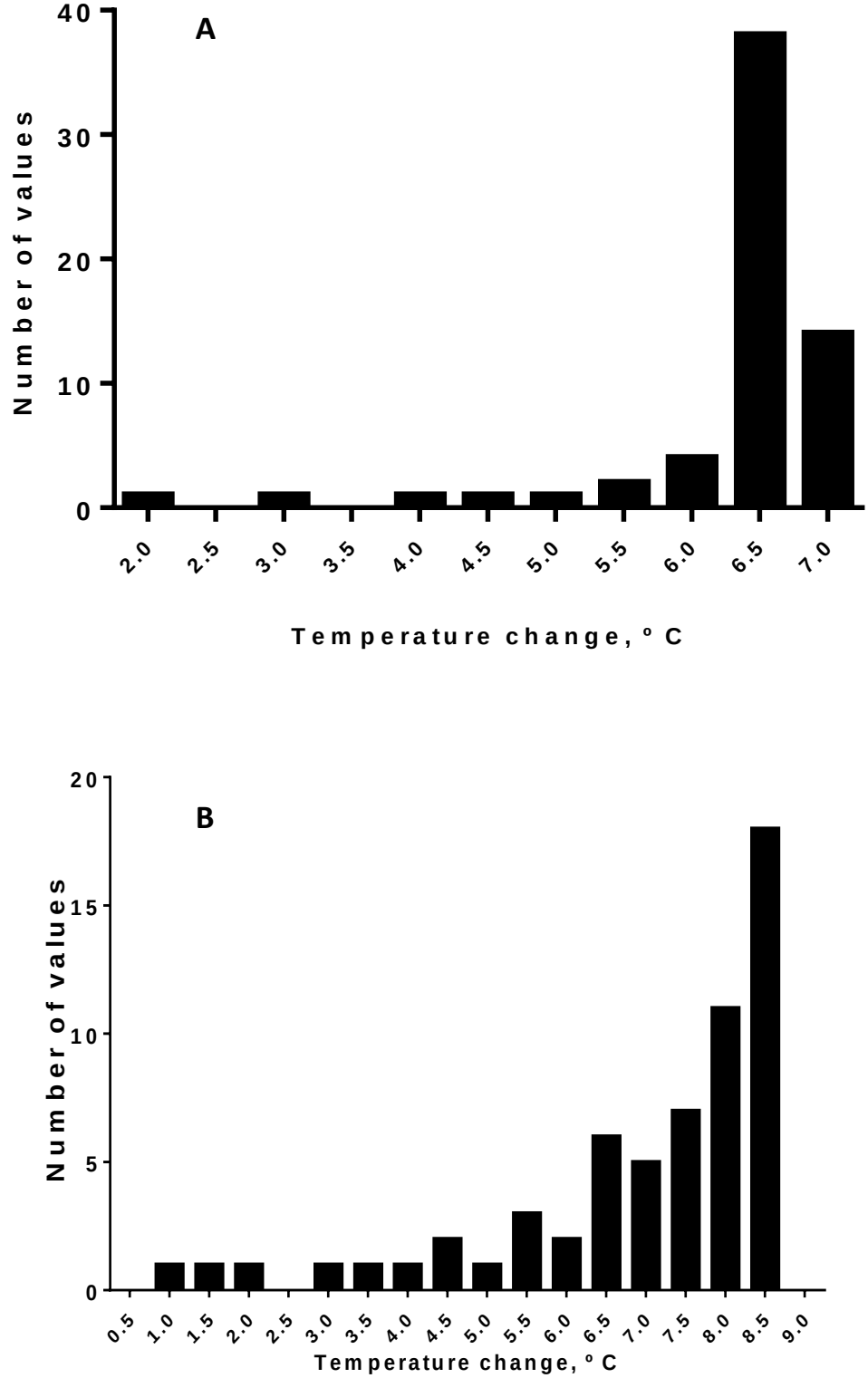

Figure 2. Histogram of frequency distribution of temperature increase for A) 50 μgmL^{-1} and B) 100 μgmL^{-1} of HNPs upon laser irradiation for 60 s at room temperature.

1.2. NMR spectra of bisnaphthalamide based drugs

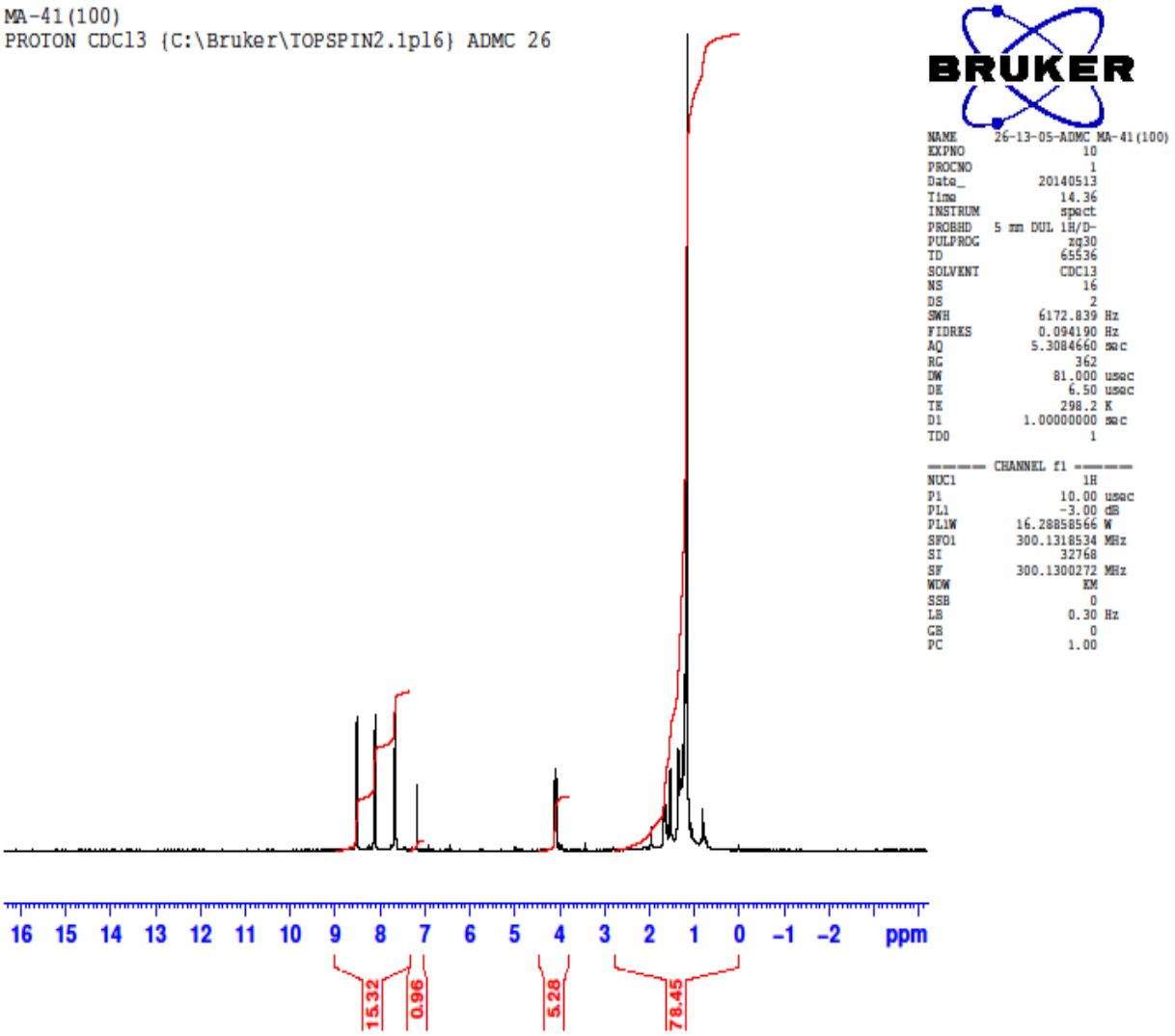

Figure 3. NMR spectrum of BNIDi.

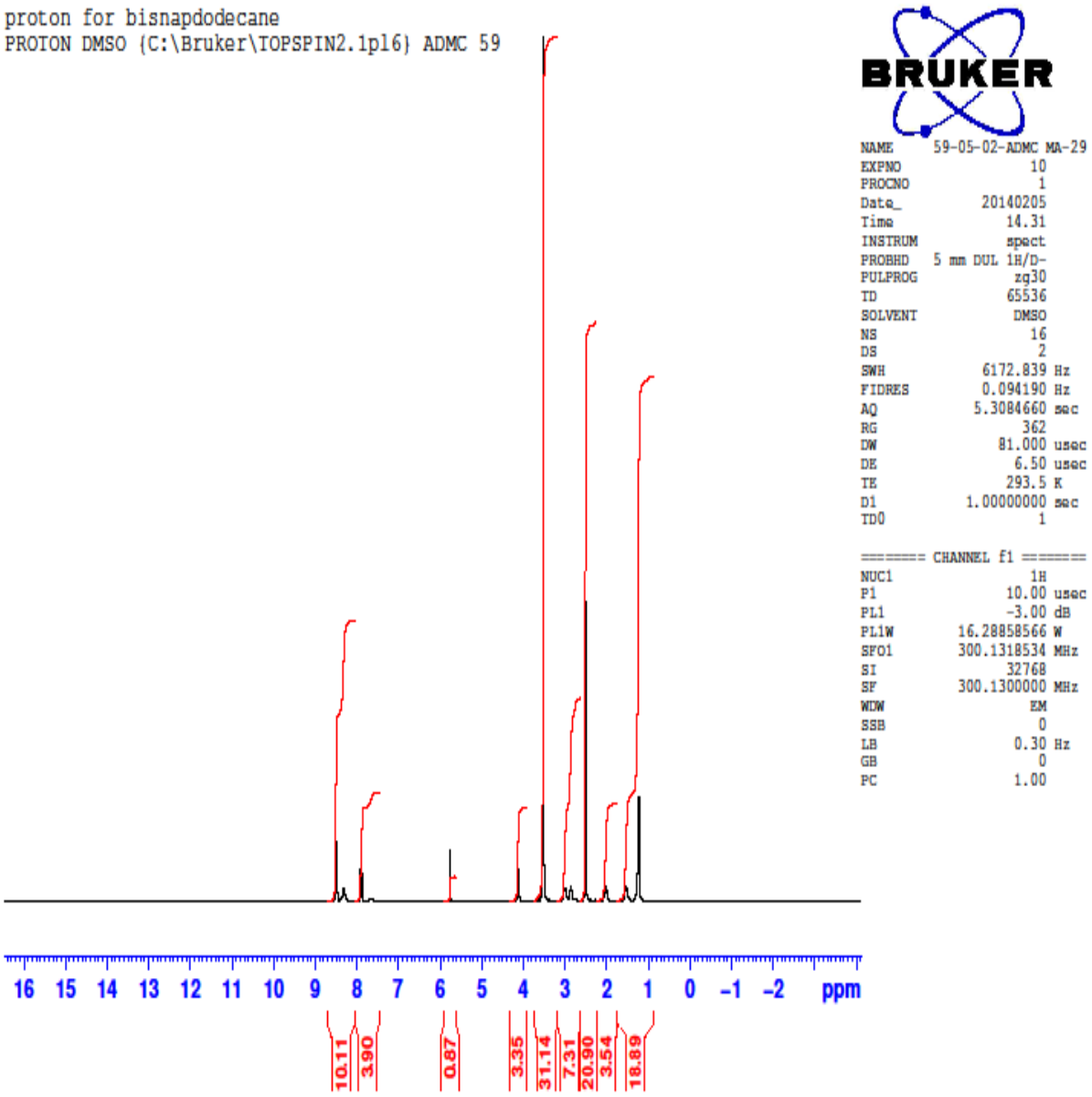

Figure 4. NMR spectrum of BNIPd.

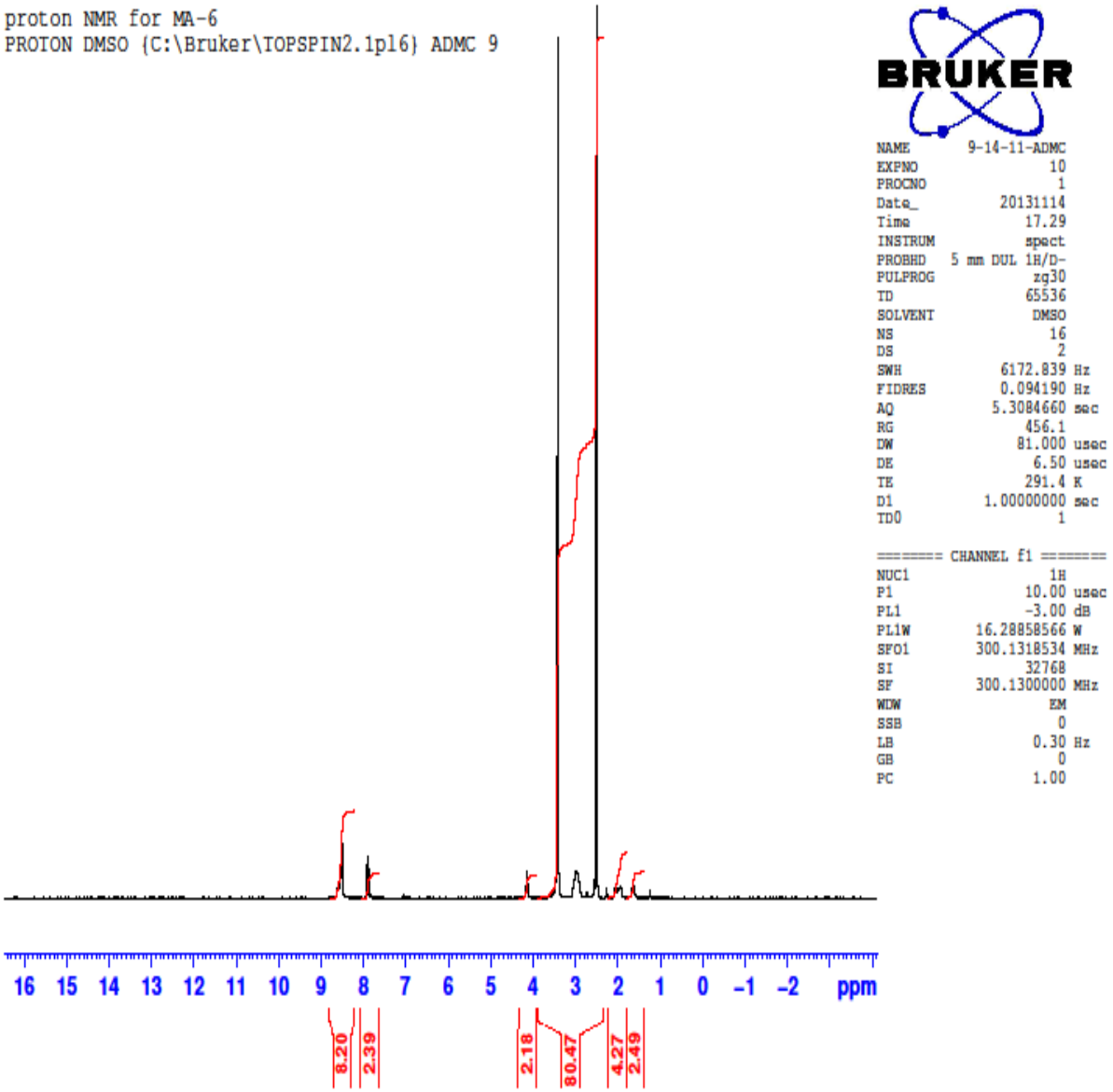

Figure 5. NMR spectrum of BNIPDSpm.

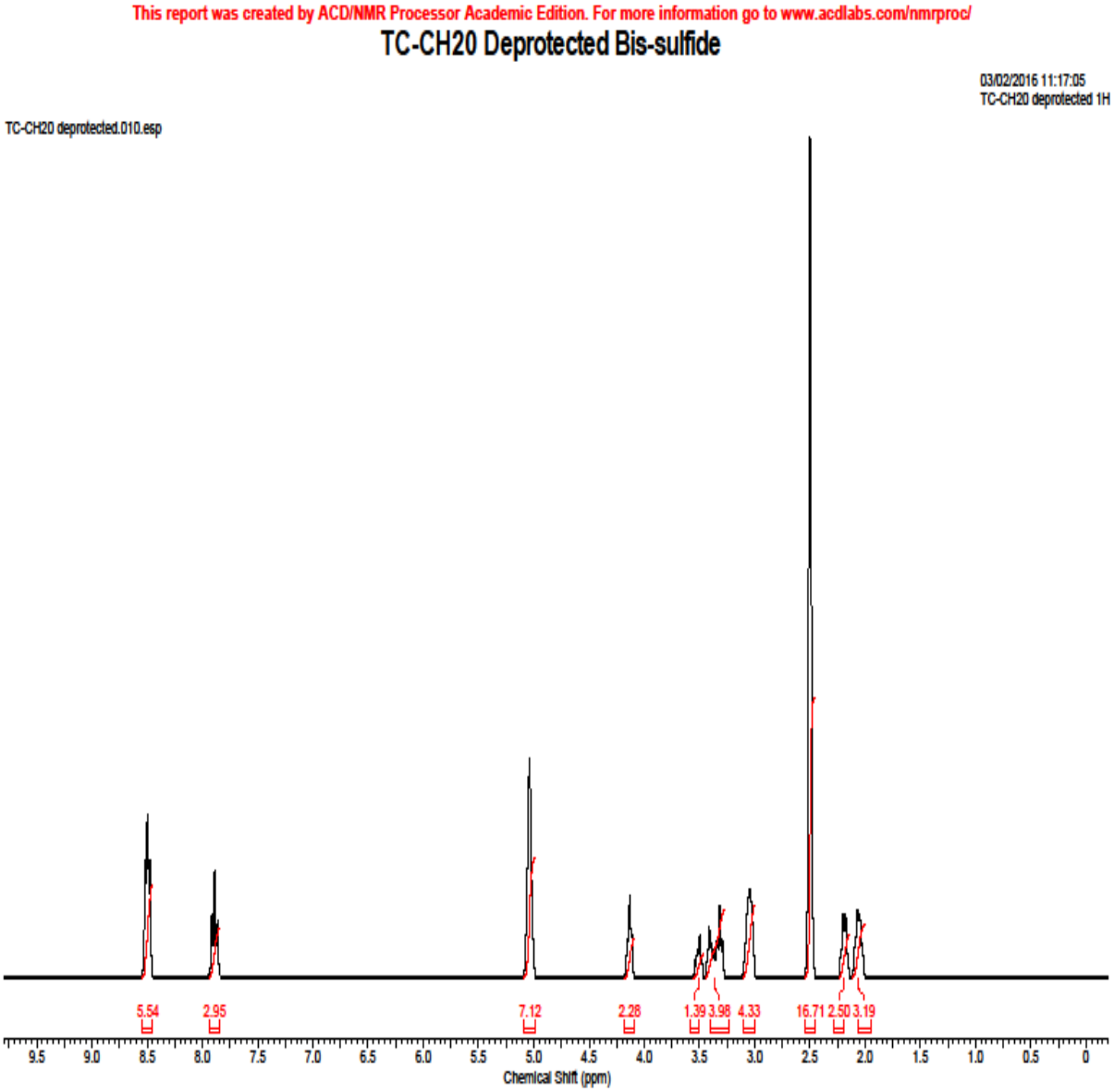

Figure 6. NMR spectrum of BNIPds.

1.3. Calibration graphs of bisnaphthalamide based drugs and gemcitabine

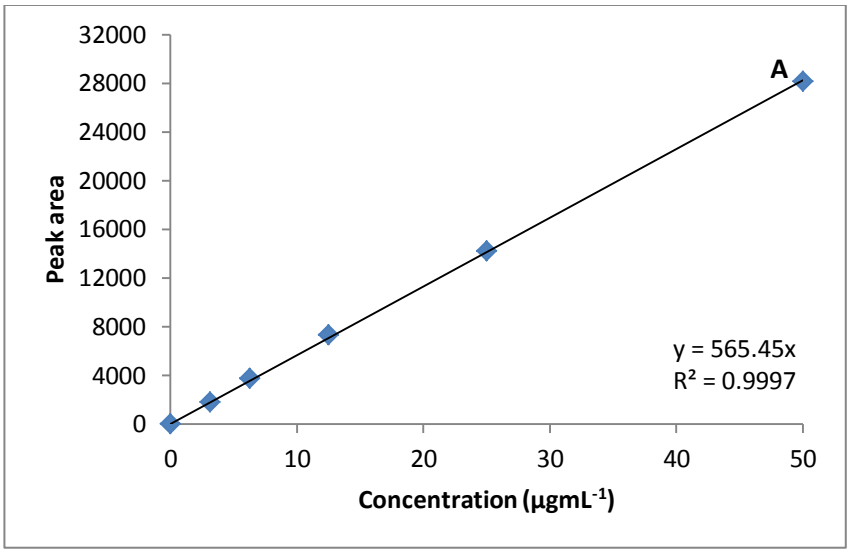

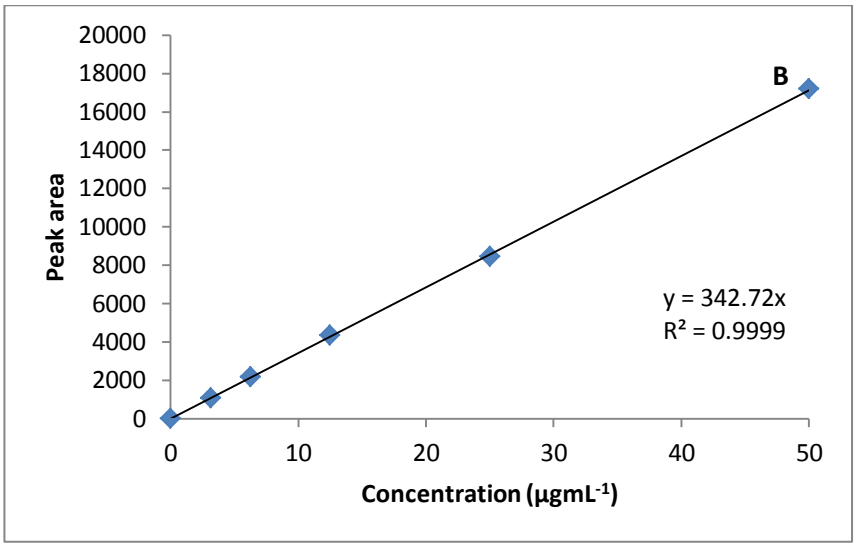

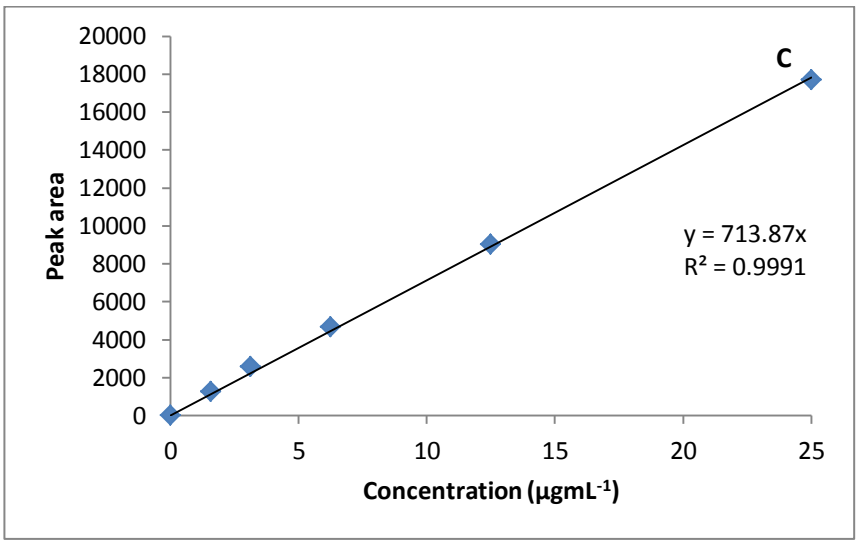

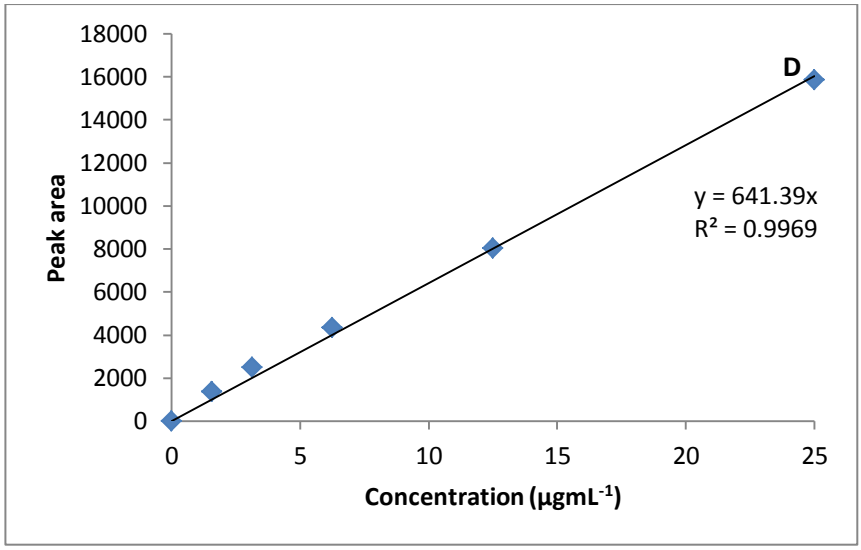

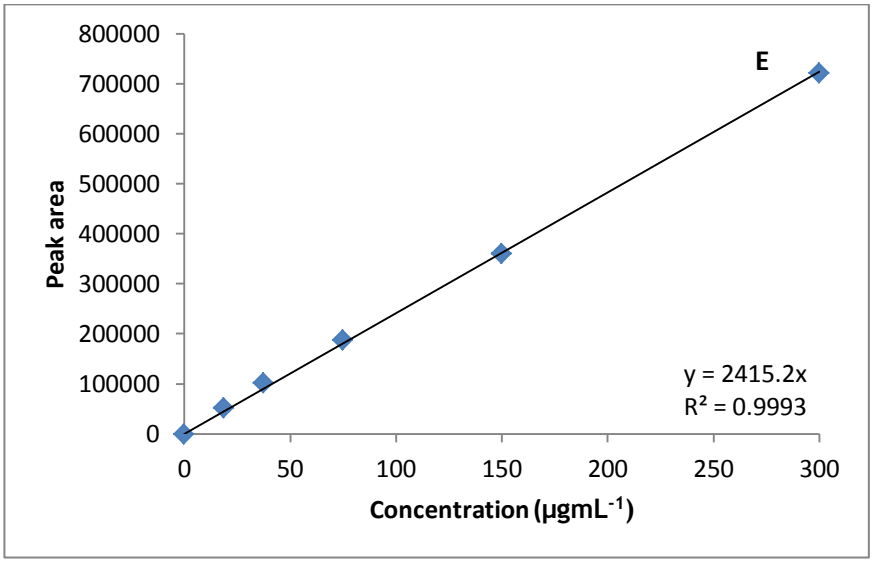

Figure 7. Calibration graph of A) BNIDi, B) BNIPd, C) BNIPDSpm, D) BNIPd and E) Gemcitabine by RP-HPLC analysis detected at 394 nm and 234 nm Emission for bisnaphthalamide based drug and gemcitabine, respectively. Binaphthalamide derivatives were dissolved in DMSO/H2O (50:50 v/v) and gemcitabine was dissolved in water.